

XIX.

BALKAN CONGRESS OF RADIOLOGY



ABSTRACT BOOK

OCTOBER 23-26, 2024
ALTIN YUNUS HOTEL, ÇEŞME
izmir



INDEX

INVITATION	9
2024 BSR COMMITTEE MEMBERS	10
2024 BCR COMMITTEE MEMBERS.....	14
ORAL PRESENTATIONS	18
CORRELATION OF SKELETAL MUSCLE INDEX WITH T-SCORE TO DETERMINE THE BONE MINERAL DENSITY	24
ACROMION–GREAT TUBERCULOUS IMPINGEMENT INDEX MAY PREDICT THE SUSCEPTIBILITY TO ROTATOR CUFF TEARS AND SPORTS INJURY IN CHILDREN.	26
EVALUATION OF THE EFFICACY OF DEEP TRANSVERSE FRICTION MASSAGE IN LATERAL EPICONDYLITIS USING SUPERB MICROVASCULAR IMAGING ON COMMON EXTENSOR TENDON VASCULARISATION	28
IMAGING FINDINGS AND COMPLICATIONS IN ANTERIOR CRUCIATE LIGAMENT RECONSTRUCTION.....	30
ASSESSMENT OF LATERAL PTERYGOID MUSCLE SIGNAL AND MANDIBULAR CONDYLE MORPHOLOGY WITH ANTERIOR DISC DISLOCATION OF THE TEMPOROMANDIBULAR JOINT ON 3T MRI.....	32
EVALUATION OF LATERAL PTERYGOID MUSCLE SIGNAL AND MANDIBULAR CONDYLE MORPHOLOGY WITH ANTERIOR DISC DISLOCATION OF THE TEMPOROMANDIBULAR JOINT IN ADOLESCENTS	35
“RADIOLOGICAL AND CLINICAL EVALUATION OF ENCHONDROMAS: A RETROSPECTIVE STUDY OF 112 CASES”	38
A HIGH ACROMION-GREATER TUBEROSITY IMPINGEMENT INDEX INCREASES THE RISK OF LABRAL TEAR	39
MRI-BASED COMPARATIVE ASSESSMENT OF CAM AND Pincer TYPE HIP MORPHOLOGY BETWEEN SEMI-PROFESSIONAL SOCCER PLAYERS AND NON-ATHLETE CONTROLS	40
PANCREATIC NEUROENDOCRINE TUMORS: A STEPWISE APPROACH TO DIFFERENTIAL DIAGNOSIS.	45
INVESTIGATION OF THE EFFECT OF BODY COMPOSITION MEASUREMENTS DEFINED BY COMPUTED TOMOGRAPHY BEFORE TREATMENT ON DISEASE PROGNOSIS IN PATIENTS WITH METASTATIC COLON CANCER AND COMPARISON WITH OTHER CLINICOPATHOLOGICAL PROGNOSTIC PARAMETERS.....	47
CORRELATION BETWEEN CT LIVER DENSITY (HU VALUES) AND LABORATORY VALUES IN HEPATOSTEATOSIS	51
KEYWORDS: NONENHANCED CT, FATTY LIVER, LIVER FUNCTION TEST, ALANINE TRANSAMINASE	53
THE IMPACT OF DEFECT SIZE ON HERNIA SAC CONTENTS AND THE DEVELOPMENT OF ILEUS IN ABDOMINAL WALL HERNIAS	54
ILEOCOLIC AND COLOCOLIC INTUSSUSCEPTION IN ADULTS: CT FEATURES AND PATHOLOGICAL CORRELATION	57
KEYWORDS: INTUSSUSCEPTION, ILEOCOLIC, COLOCOLIC, COMPUTED TOMOGRAPHY, MALIGNANCY	59
NORMAL LIVER STIFFNESS VALUES MEASURED WITH MR ELASTOGRAPHY AND 2-D SHEAR WAVE ELASTOGRAPHY IN CHILDREN (9-17 AGES).....	60

GD-EOB-DTPA-ENHANCED MRI WITH T1 MAPPING VERSUS FIBROSIS-4 INDEX FOR STAGING LIVER FIBROSIS	63
COMPARATIVE DIAGNOSTIC PERFORMANCE OF TWO ABBREVIATED MRI PROTOCOLS FOR HEPATOCELLULAR CARCINOMA.....	65
EVALUATING THE POTENTIAL OF ABBREVIATED MRI PROTOCOLS FOR LIVER METASTASIS DETECTION: A STUDY IN COLORECTAL CANCER PATIENTS.....	68
QUANTITATIVE EVALUATION OF LIVER STEATOSIS USING ULTRASOUND ATTENUATION IMAGING: A COMPARISON WITH MRI.....	69
NORMATIVE CHOROIDAL PLEXUS APPARENT DIFFUSION COEFFICIENT VALUES IN THE PEDIATRIC POPULATION.....	71
NEUROPSYCHIATRIC LUPUS OR MULTIPLE SCLEROSIS? DIFFERENTIAL DIAGNOSIS USING MYELIN CONTENT INDICES OF NORMAL APPEARING WHITE MATTER: A MYELIN WATER IMAGING STUDY.....	74
EFFECT OF CHEMOTHERAPY ON HIPPOCAMPAL VOLUME: A PRELIMINARY STUDY	76
COMPARATIVE ANALYSIS OF BRAIN VOLUME DIFFERENCES BETWEEN PUBERTY PRECOCIOUS AND NORMAL PUBERTY GIRLS	77
EXCITOTOXIC WHITE MATTER INJURY ON DIFFUSION-WEIGHTED IMAGING: A REVIEW OF PEDIATRIC CAUSES	79
THE ROLE OF APPARENT DIFFUSION COEFFICIENT ASSESSMENT IN WILSON DISEASE WITH NEUROLOGICAL INVOLVEMENT	82
COMPARISON OF T1A POST-CONTRAST AND FLAIR IMAGING METHODS IN THE DIAGNOSIS OF NON-ENHANCING LEPTOMENINGEAL METASTASES: FLAIR HYPERINTENSITY AS AN EARLY FINDING	84
PATTERNS OF NASAL AND PARANASAL SINUS INJURIES IN MAXILLOFACIAL TRAUMA: A RETROSPECTIVE ANALYSIS OF ETIOLOGIES AND FRACTURE LOCATIONS.....	85
IMAGING OF CONGENITAL PYRIFORM SINUS FISTULA IN CHILDREN: A REVIEW OF SIX CASES	87
COMPARISON OF PET/CT AND CT TEXTURE ANALYSIS IN PATIENTS WITH STAGE III-IV LUNG CANCER RECEIVING CHEMORADIOTHERAPY: CAN WE PREDICT THE TREATMENT RESPONSE OF THE TUMOR?.....	90
EVALUATION OF THE VARIABILITY OF AXILLARY ARTERY AND INTERNAL MAMMARY ARTERY DIAMETERS ACCORDING TO INTRAMAMMARY TUMOR LOCATION IN BREAST CANCER PATIENTS WITH MAGNETIC RESONANCE IMAGING	92
EVALUATION OF PNEUMOTHORAX PREDICTIONABILITY BY DEEP LEARNING METHOD BEFORE TRANSTHORACIC FINE NEEDLE ASPIRATION BIOPSY (TTIAB) IN LUNG MASSES	93
COMPARISON OF A DEEP LEARNING RECONSTRUCTION METHOD WITH OTHER RECONSTRUCTION METHODS IN CORONARY CT ANGIOGRAPHY	98
IS THERE A CORRELATION BETWEEN CORONARY ARTERY CALCIUM SCORE AND EPICARDIAL/PARACARDIAL ADIPOSE TISSUE QUANTIFICATION	100
EVALUATION OF THE RELATIONSHIP BETWEEN COINCIDENTALLY DETECTED NON-COMPACTION CARDIOMYOPATHY ON CORONARY CT ANGIOGRAPHY AND THE LEVEL OF CORONARY ARTERY DISEASE AND THE PATIENT'S SYMPTOMS; A RETROSPECTIVE STUDY..	102
RELATIONSHIP BETWEEN THE ANGLE OF POPLITEAL ARTERY TRIFURCATION BRANCHES AND ATHEROSCLEROSIS BURDEN IN CHRONIC PERIPHERAL ARTERIAL DISEASE	104

EFFICACY OF US-GUIDED PERCUTANEOUS FINE NEEDLE ASPIRATION BIOPSY IN PATIENTS WITH PAROTID GLAND MASSES	107
PERCUTANEOUS CHOLECYSTOSTOMY AND ITS IMPACT ON SUBSEQUENT SURGICAL INTERVENTIONS IN ACUTE CHOLECYSTITIS	110
THE ROLE OF KAISER SCORING SYSTEM IN BREAST MRI FOR RISK STRATIFICATION OF INTRADUCTAL PAPILLOMA	112
RELATIONSHIP BETWEEN ADC VALUES AND HISTOPATHOLOGIC PROGNOSTIC MARKERS OF BREAST CARCINOMA	113
THE EFFECTIVENESS OF ULTRASOUND-GUIDED PERCUTANEOUS TPA INJECTION IN THROMBOSED ARTERIOVENOUS FISTULA	115
EFFICACY OF ULTRASOUND-GUIDED MICROWAVE ABLATION IN THE TREATMENT OF BREAST FIBROADENOMAS: A FOLLOW-UP STUDY	116
DIGITAL BREAST TOMOSYNTHESIS-GUIDED BIOPSY: INITIAL EXPERIENCE	119
ULTRASOUND-GUIDED THROMBIN INJECTION FOR THE TREATMENT OF ARTERIAL PSEUDOANEURYSM	120
EFFICACY AND SAFETY OF ENDOVASCULAR EMBOLIZATION WITH N-2-BUTYL-CYANOACRYLATE IN PATIENTS WITH MASSIVE HEMOPTYSIS: RESULTS OF A SINGLE-CENTER EXPERIENCE	121
COMPARISON OF TEMPOROMANDIBULAR JOINT DISC IN CHRONIC RENAL FAILURE PATIENTS AND HEALTHY ADULTS WITH SHEAR WAVE ELASTOGRAPHY	122
THE RADIOLOGICAL-PATHOLOGICAL CORRELATION IN BREAST CANCER CASES WITH NEOADJUVANT CHEMOTHERAPY	125
DETECTION OF URGENT PATHOLOGY IN PEDIATRIC EMERGENCY ULTRASOUND REPORTS USING LARGE LANGUAGE MODELS	127
DETECTION OF BRAIN ANEURYSMS ON T2W IMAGES BY USING ARTIFICIAL INTELLIGENCE	128
CORRELATION OF HISTOPATHOLOGICAL AND RADIOLOGICAL RESPONSE PATTERNS AND THEIR PROGNOSTIC IMPLICATIONS IN BREAST CANCER AFTER NEOADJUVANT CHEMOTHERAPY	129
CLASSIFICATION OF BRAIN CT REPORTS BY EMERGENCY LEVEL USING ARTIFICIAL INTELLIGENCE	132
AUTOMATED CLASSIFICATION OF THE PHASECASE SCALE IN MRI USING DEEP LEARNING METHODS	134
US-GUIDED PERCUTANEOUS TRANSABDOMINAL TRU-CUT BIOPSY IN PATIENTS WITH OVARIAN TUMORS	135
IS IT FEASIBLE TO ESTABLISH A STROKE UNIT IN THE REMOTEST CORNER OF TÜRKİYE? A CASE SERIES FROM HAKKARİ	139
EVALUATING SPECIMEN ADEQUACY IN THYROID FNAB: A COMPARISON OF TRANSFER TECHNIQUES	141
DIAGNOSTIC UTILITY OF QUANTITATIVE AND SEMI-QUANTITATIVE PARAMETERS FROM MULTIPARAMETRIC MRI IN PROSTATE CANCER DETECTION: A RETROSPECTIVE STUDY	142
THE UTILITY OF QUANTITATIVE ADC AND T2 VALUES, ENHANCEMENT PATTERN, AND LESION SHAPE CHARACTERISTICS IN DIFFERENTIATING TRUE POSITIVE FROM FALSE POSITIVE LESIONS ON MULTIPARAMETRIC PROSTATE MRI	144
MAGNETIC RESONANCE IMAGING FINDINGS OF NEONATAL OVARIAN TORSION	147

PREOPERATIVE PREDICTION OF SEROUS AND MUCINOUS BORDERLINE OVARIAN TUMORS ACCORDING TO MRI FEATURES.....	149
A COMPREHENSIVE REVIEW OF POST-TREATMENT IMAGING IN GYNECOLOGIC MALIGNANCIES: CASE-BASED TIPS AND TRICKS FOR DETECTING POTENTIAL COMPLICATIONS AND AVOIDING PITFALLS	152
POSTER PRESENTATIONS.....	155
RADIOLOGICAL DIFFERENCES BETWEEN NEUROBLASTOMA AND WILMS TUMOR.....	167
BRONCHIOLITIS OBLITERANS SECONDARY TO GRAFT VERSUS HOST DISEASE IN A CHILD WITH ACUTE MYELOID LEUKEMIA	169
POLYOSTOTIC FIBROUS DYSPLASIA ISOLATED TO THE THORACOLUMBOSACRAL SPINE IN A CHILD	172
NEGATIVE MULTIPARAMETRIC PROSTATE MRI IN BIOPSY-NAÏVE MEN - DYNAMIC OF THE PROSTATE VOLUME AND PROSTATE-SPECIFIC ANTIGEN DENSITY DURING FOLLOW-UP	174
PEDIATRIC NEURO BEHÇET DISEASE PRESENTING WITH LONGITUDINALLY EXTENSIVE MYELITIS: THE BAGEL SIGN ON MRI.....	176
TORSION IN A BIPARTITE SPLEEN: IMAGING FINDINGS IN A CHILD.....	178
IMAGING FINDINGS OF PRIMARY PERITONEAL RHABDOMYOSARCOMATOSIS IN A CHILD ..	180
MAGNETIC RESONANCE IMAGING OF CHEMOTHERAPY TREATMENT-RELATED INTRACRANIAL COMPLICATIONS IN CHILDREN WITH HEMATOLOGIC MALIGNANCIES	182
BRAIN ARTERIOVENOUS MALFORMATIONS	185
IGG4 RELATED CORONARY ARTERY PERIARTERITIS IN A PATIENT WITH CORONARY ARTERY ANOMALY: A CASE REPORT	187
PRIMARY SYNOVIAL SARCOMA OF THE CRANIAL VAULT.....	189
IMAGING FINDINGS OF CHRONIC RECURRENT MULTIFOCAL OSTEOMYELITIS AND ITS MIMICS IN CHILDREN.....	191
PULMONARY ARTERIOVENOUS MALFORMATIONS	195
COULD CARDIAC MAGNETIC RESONANCE IMAGING HELP IN THE ASSESSMENT OF THE UNDERLYING CAUSE OF THE SIGNIFICANTLY IMPROVED CONGESTIVE HEART FAILURE?... ..	197
DOUBLE BUBBLES BEYOND THE NEONATAL PERIOD: IMAGING FINDINGS OF DUODENAL OBSTRUCTION IN CHILDREN	199
COLLISION TUMORS OF THE OVARY: “TWO IN ONE”	202
INTERVENTIONAL RADIOLOGY MANAGEMENT OF SPLENIC ABSCESS DUE TO SALMONELLA ENTERITIDIS FOLLOWING ABDOMINAL TRAUMA – CASE REPORT	203
A CASE OF PULMONARY ALVEOLAR MICROLYTICOSIS	205
THE IMPACT OF BODY FAT DISTRIBUTION AND SARCOPENIA ON NAC REACTION AND RECURRENCE IN LABC PATIENTS DEPENDING ON MOLECULAR SUBTYPES.....	206
FROM HEADACHES TO OBSTRUCTIVE ILEUS: FOLLOWING THE DOTS	208
SUBCLAVIAN ARTERY DISSECTION: THE VISIBLE TIP OF THE AORTIC ICEBERG!	209
GOSSYPBOMA: A DIAGNOSIS TO BE REMEMBERED	211
A RARE SESAMOID BONE OF THE FOOT; OS VESALIANUM	213
GASTROPANCREATIC FISTULA: A RARE COMPLICATION OF RECURRENT PANCREATITIS.....	215

MAYER-ROKITANSKY-KÜSTER-HAUSER SYNDROME WITH SUPERNUMERARY OVARY: VERY RARE CONGENITAL CO-OCCURRENCE	217
OVERLOOKED SMALL BOWEL MASS: GASTROINTESTINAL STROMAL TUMOR	219
DANGEROUS COMPLICATION OF ACUTE CHOLECYSTITIS: GALLBLADDER PERFORATION ..	222
UTERINE SMOOTH MUSCLE TUMORS OF UNCERTAIN MALIGNANT POTENTIAL (STUMP): A REPORT OF TWO CASES	224
WHAT IF IT IS NOT JUST WALL THICKENING?	226
DELAYED DIAGNOSIS OF SUBCLAVIAN ARTERY PSEUDOANEURYSM FOLLOWING SUICIDE ATTEMPT IN MAJOR DEPRESSION: THE CRITICAL ROLE OF DETAILED ULTRASOUND IMAGING	228
INTRAPERITONEAL PREGNANCY: A TICKING TIME BOMB IN THE ABDOMEN - A CRITICAL DIAGNOSTIC CHALLENGE	230
AN UNCOMMON CAUSE OF ABDOMINAL PAIN: HUGE GASTRIC BEZOAR	232
LUNG INVOLVEMENT IN RHEUMATOID ARTHRITIS: RADIOLOGICAL APPROACH.....	234
GASTRIC DIVERTICULUM.....	236
PRIMARY PATHOLOGY OR SECONDARY? DISSEMINATED INTRAVASCULAR COAGULOPATHY WITH DIFFERENTIAL DIAGNOSIS	238
HEPATIC GAS GANGRENE: TWO CASES OF A RARE POST - OPERATIVE COMPLICATION	240
PANCREATIC DUCTAL ADENOCARCINOMA AND MIMICS: TIPS TO AVOID MISDIAGNOSIS IN COMPUTED TOMOGRAPHY	241
ACUTE AORTIC SYNDROME: GENERAL RADIOLOGICAL OVERVIEW WITH CASES	243
PROXIMAL STENT HOLDER FRACTURE: A RARE COMPLICATION OF ENDURANT II® AORTIC STENT-GRAFT	245
LEFT ATRIAL BAND; A RARE CONGENITAL ANOMALY	247
EXTENSOR DIGITORUM BREVIS MANUS MUSCLE; A RARE VARIANT	249
INFERIOR VENA CAVA DUPLICATION – A CASE REPORT	250
MRI DIAGNOSIS OF OVARIAN MASSES: MAKE THIS PUZZLE EASY	251
A RARE CAUSE OF ILEUS IN ADULTS: INTUSSUSCEPTION-CASE REPORT	253
MECKEL DIVERTICULUM PATHOLOGIES IN PEDIATRIC PATIENTS; CASE-BASED APPROACH	255
ACCESSORY EXTENSOR CARPI RADIALIS LONGUS TENDON	257
THE ACCESSORY EXTENSOR CARPI RADIALIS INTERMEDIUS TENDON	258
RADIOLOGICAL FEATURES OF PLACENTAL MESENCHYMAL DYSPLASIA	259
THE ACCESSORY EXTENSOR CARPI RADIALIS LONGUS AND BREVIS COINCIDENCE.....	260
ABSENCE OF EXTENSOR CARPI RADIALIS LONGUS TENDON	261
RADIOLOGICAL FEATURES OF BORDERLINE SEROUS OVARIAN TUMOR.....	263
INTRACRANIAL LESIONS TUBEROUS OF SCLEROSIS.....	265
IMAGING FINDINGS OF GRANULOSA CELL TUMOR: OVARIAN MASS AND ENDOMETRIAL HYPERPLASIA.....	267
TETRALOGY OF FALLOT (TOF) AND MAJOR AORTOPULMONARY COLLATERAL ARTERIES (MAPCAS).....	268

A CURIOUS TWIST: THE DISCOVERY OF EXTENSIVE CALCINOSIS UNIVERSALIS REVEALED IN A CASE OF RECTUS SHEATH HEMATOMA	270
SITUS INVERSUS AND AUTOSOMAL DOMINANT POLYCYSTIC KIDNEY DISEASE IN AN ADULT PATIENT	272
INFERIOR MESENTERIC VEIN THROMBOPHLEBITIS SECONDARY TO ACUTE DIVERTICULITIS	274
ISOLATED LIVER HERNIATION TO POSTERIOR MEDIASTINUM THROUGH GASTROESOPHAGEAL HIATUS.....	276
THE IMPORTANCE OF DORSAL (SUPINE) DECUBITUS X-RAY IN PNEUMOPERITONEUM.....	277
HERLYN-WERNER-WUNDERLICH SYNDROME	278
AI IN RADIOLOGY: A ROBUST ASSISTANT OR A MISLEADING TOOL? PRIMARY RESULTS	280
A CASE OF SUSPECTED FOREIGN BODY SWALLOWING: THE USE OF X-RAY AND ULTRASOUND AS SCREENING METHODS	281
RICE BODIES IN THE WRIST	282
SOLITARY FIBROUS TUMOR IN THE CENTRAL NERVOUS SYSTEM: TWO CASES	284
ISCHEMIC STROKE AS A RARE COMPLICATION OF A BEE STING: A CASE REPORT	286
A RARE CORONARY ARTERY ANOMALY: CONGENITAL ABSENCE OF THE LCX	288
DOMINANT LCX ORIGINATING FROM THE RIGHT SINUS OF VALSALVA	289
A RARE CASE: UNROOFED CORONARY SINUS ASD AND PERSISTENT LEFT SUPERIOR VENA CAVA	291
A RARE CORONARY ARTERY ANOMALY: LEFT MAIN CORONARY ARTERY ORIGINATING FROM RIGHT SINUS VALSALVA	293
A RARE CASE: PULMONARY CEMENT EMBOLISM	294
NEONATAL OSTEOMYELITIS: PLAIN RADIOGRAPHY AND ULTRASOUND FINDINGS.....	295
A RARE CASE; TRIGEMINAL NERVE ROOT INVOLVEMENT OF SINONASAL MUCORMYCOSIS IN AN IMMUNOCOMPROMISED PATIENT	297
LUMBAR MRI FINDINGS IN CHILDREN AND ADOLESCENTS PRESENTING WITH NON-SPECIFIC LOW BACK PAIN.....	299
FIBROUS TALOCALCANEAL COALITION ON MRI.....	301
A RARE ANOMALY: PARTIAL PERICARDIAL AGENESIS IMAGING FINDINGS.....	303
ORBITAL TUMORS	305
THE MAMMOGRAPHIC AND MRI APPEARANCES OF ULTRASONOGRAPHIC VISIBLE MALIGNANT BREAST MICROCALCIFICATIONS	307
RADIOLOGICAL IMAGING CHARACTERISTICS OF TERATOMAS DETECTED DURING THE PRENATAL PERIOD	309
TART (TESTICULAR ADRENAL REST TUMORS)	311
LIPOMA ARBORESCENS OF THE KNEE ON MRI: A RARE CASE REPORT.....	312
MRI OF OVARIAN CYSTADENOMAS	314
ADENOMA MALIGNUM OF UTERIN CERVIX: MAGNETIC RESONANCE IMAGING FINDINGS ..	316
RARE ACCESSORY BONE OF THE FOOT; OS CALCANEUS SECUNDARIS.....	318

RARE INVOLVEMENT OF SARCOIDOSIS: INTRAMAMMARIAN AND BILATERAL AXILLARY MULTIPLE LYMPHADENOPATHIES	320
A RARE AND INTERESTING CASE REPORT: INVASIVE BREAST CARCINOMA WITH SPONTANEOUS REGRESSION AFTER LABOUR	322
LEFT CIRCUMFLEX AORTA -CASE REPORT	324
A RETROSPECTIVE ANALYSIS OF CASES AND RADIOLOGICAL EVALUATION OF PATHOLOGICAL FINDINGS BASED ON 13 YEARS OF EXPERIENCE IN FETAL MRI AT A TERTIARY CARE CENTER.	325
A RARE UROGENITAL ANOMALY: ZINNER SYNDROME	327

INVITATION

Dear Colleagues,

I am honored to invite you to the XIX Balkan Congress of Radiology (BCR) in Cesme, Türkiye. Last year's BCR was a success, just like its predecessors, and the executive board of the Balkan Society of Radiology and the scientific planning committee of this year's congress are trying to do their best to reach the same scientific level in 2024.

Just like in the past, also this year, BCR aims to provide an effective and collegial platform for the exchange of knowledge and scientific experience. It also seeks to tighten the bonds between our colleagues from the Balkan Congress by providing a social environment suitable for scientific networking. The topics are selected regarding the needs of experienced radiologists and our colleagues in training. Thus, the congress will be a unique opportunity to review your knowledge in different aspects of radiology and to catch up with the current trends that will shape the future of our profession. Our speakers are experienced scientists with global achievements. We also have an ESOR course on oncologic imaging embedded in our congress. You will benefit from the outstanding ESOR faculty joining us in Cesme.

The Balkans, a unique geographic area in southeastern Europe, is steeped in history, natural beauty, and culture. Bordered by the Adriatic Sea, the Ionian Sea, the Aegean Sea, the Turkish Straits, and the Black Sea, our region is a testament to the richness of our world. We are fortunate to live in a place where myths are not just stories but lived experiences, where civilizations have flourished, declined, and risen again with renewed strength.

Solidarity between Balkan countries is not just a concept, but a crucially important reality. People living on these soils are like each other, sharing a common past and, indeed, an archetypical one. We laugh at the same jokes and dine very similarly, and similar things make us cry. We are sisters and brothers who speak different languages but share the same mindset. I believe that if we can give our cooperation, generally, and our society, specifically, a run, there are many things we can achieve together. Together, we will be stronger. This sense of unity and shared purpose is what makes our conference and our profession so special.

Cesme is a district of Izmir and used to be one of the twelve Ionian colonies in history. Today, it is one of the pupils of the Turkish tourist scene. And please remind yourself that beautiful Cesme will become even more stunning in autumn.

See you in Cesme soon, and let's discuss the bright future of the BSR together.

Prof. Nevra Elmas
President, BSR

Prof. Şükrü Mehmet Ertürk
President, BCR 2024

2024 BSR COMMITTEE MEMBERS

Nevra Elmas

President

nevraelmas@gmail.com

Nicholas Gourtsoyiannis

Honorary President, Chairperson of the Nominations Committee

gournick@gmail.com

Miloš Lučić

1st Vice President

milos.a.lucic@gmail.com

Charina Triantopoulou

2nd Vice President

ctriantopoulou@gmail.com

Ružica Maksimović

Past President

rmaksimovic@yahoo.com, ruzica.maksimovic@med.bg.ac.rs

Nadica Mitreska

Treasurer

mitreska_nadica@hotmail.com

Cem Calli

Secretary General

cem.calli@gmail.com

G. Hadjidekov

Chairperson of the Membership Committee

jordiman76@yahoo.com

D. Cokkinos, Greece

demoscokkinos@gmail.com

Nikoleta Traikova

Chairperson of the Bylaws Committee

nikoletatraikova@gmail.com

Vasileios Rafailidis

billraf@hotmail.com

Mustafa Seçil

drmustafasecil@gmail.com

Council of National Representatives

Achilleas Chatziioannou. Greece

achatzi@med.uoa.gr

Nicholas Gourtsoyiannis

Chairperson of the Nominations Committee
gournick@gmail.com

OkanAkhan, Turkey

akhano@tr.net, oakhan@hacettepe.edu.tr

Vasil Hadjidekov, Bulgaria

hadjidekov@yahoo.com

AndrasPalko, Hungary

palkoand@gmail.com

Panos Prasopoulos; Greece

pprasopo@auth.gr, pprasopo@gmail.com

RužicaMaksimović

rmaksimovic@yahoo.com, ružica.maksimovic@med.bg.ac.rs

Junior Forum Committee

Mehmet Şükrü Ertürk, TUR

smerturk@gmail.com

**2024 BCR- 24-26 October 2024 / Çeşme-İZMİR /TR
PROGRAM PLANNING COMMITTEE-**

Chairperson

Efrosini Papadaki

fpapada@ote.net

Members

Deniz Akata, TR

akataaden@gmail.com dakata@hacettepe.edu.tr

Andras Palko, Hungary

palkoand@gmail.com

I. Lupescu, Romania

ilupescu@gmail.com

Vesna Sarajlic , BiH

vesnasarajlic8@gmail.com

Miloš Gašić, RS

gasic.milos@yahoo.com milosgasic1985@gmail.com

Svetlana Antevska Grujevska , NM

svetlana.antevskagrujoska@gmail.com

October 23-26, 2024
Balkan Congress of Radiology
Altın Yunus Hotel, Çeşme

Dora Zlatareva, Bulgaria
dorazlat@yahoo.com

Main Topics:

- **Oncologic Imaging,**
- **Emergency Radiology,**
- **Artificial intelligence**

2024 BCR COMMITTEE MEMBERS

BALKAN SOCIETY OF RADIOLOGY BOARD OF DIRECTORS

Nevra Elmas

Chair

Nicholas Gourtsoyiannis

Honorary Chair

Miloš Lučić

First Vice Chair

Charina Triantopoulou

Second Vice Chair

Ružica Maksimović

Former Chair

Nadica Mitreska

Treasurer

Cem Çallı

Secretary General

CONGRESS ORGANIZING COMMITTEE

Şükrü Mehmet Ertürk

Congress Chair

Cem Çallı

Congress Secretary

SCIENTIFIC PROGRAM ORGANIZING COMMITTEE

Efrosini Papadaki

Chair

Deniz Akata

Miloš Gašić

Ioana Gabriela Lupescu

Vesna Sarajlic

Gasic Milos

Stevlana Antevska Grujevska

Dora Zlatareva

Members

LOCAL ORGANIZING COMMITTEE

Canan ALTAY	Mustafa HARMAN
Levent ALTUN	Mecit KANTARCI
Nurhan Sabir AKKOYUNLU	Ayşenur OKTAY
Ali BALCI	İsmail ORAN
Funda BARLIK	Şebnem ÖRGÜÇ
Yaşar BÜKTE	Mustafa ÖZMEN
Can ÇEVİKOL	Yelda ÖZSUNAR
Nezahat ERDOĞAN	Recep SAVAŞ
Erkan GÖKÇE	Mustafa SEÇİL
Serkan GÜNEYLİ	Turgut TALI

October 23-26, 2024
Balkan Congress of Radiology
Altın Yunus Hotel, Çeşme

SCIENTIFIC PROGRAM



OCTOBER 23-26, 2024
ALTIN YUNUS HOTEL, ÇEŞME
izmir

XIX. BALKAN CONGRESS OF RADIOLOGY



WEDNESDAY, OCTOBER 23, 2024			
08:00 - 08:45	Registration		
08:45 - 09:00	Welcoming Introduction		
09:00 - 09:30	How to characterize liver tumors? G. Brancatelli (IT)		
09:30 - 10:00	Diagnoses and staging of pancreatic adenocarcinoma S. Gourtsoyianni (GR)		
10:00 - 10:30	Image-guided prostate interventions Jurgen Fütterer (NL)		
10:30 - 10:50	COFFEE BREAK		
10:50 - 13:00	Workshops Speakers: G. Brancatelli (IT), S. Gourtsoyianni (GR), J. Fütterer (NL)		
13:00 - 14:00	LUNCH BREAK		
14:00 -14:30	Diagnoses and staging of rectal cancer S. Gourtsoyianni (GR)		
14:30 - 15:00	How to use PI-Rads? Jurgen Fütterer (NL)		
15:00 - 15:30	Diagnosis and staging of Hepatocellular carcinoma G. Brancatelli (IT)		
15:30 - 15:50	COFFEE BREAK		
15:50 - 18:00	Workshops Speakers: S. Gourtsoyianni (GR), J. Fütterer (NL), G. Brancatelli (IT)		
18:00 - 18:15	Certificate of attendance		
18:30	OFFICIAL OPENING CEREMONY Moderators: Nevra Elmas (TR), Okan Akhan (TR) Prof. Nevra Elmas President, BSR Lal Denizli - Çeşme Municipality Mayor Prof. Hadi Özer - Honorary Guest Prof. Şükrü Mehmet Ertürk President, BCR 2024		
18:45 - 19:00	In The Memories of Prof. Totev & Prof. Tsetis Vassil Hadjidekov (BU), Nicholas Gourtsoyiannis (GR)		
19:00 - 19:20	Opening lectures: "New horizons of radiology". Andras Palko (HU)		
THURSDAY, OCTOBER 24, 2024			
	Scientific session / Hall 1	Scientific session / Hall 2	Scientific session / Hall 3
08:30 - 10:00	ABDOMINAL RADIOLOGY Moderators: C. Triantopoulou, Silvija Lucic (Online)	NEURORADIOLOGY Moderators: Efrasini Papadaki, Zulejha Merhemic	EMERGENCY RADIOLOGY Moderators: Vesna Sarajlic, Nadika Mitreska
08:30 - 08:52	Dilated pancreatic duct. Is it always a tumor? C. Triantopoulou (GR)	Genetics in stroke – what is the role of imaging Dora Zlatoreva (BU)	Imaging in pulmonary emergencies. S. Tavernarakis (GR)
08:52 - 09:12	CT colonoscopy in clinical practice S. Papaioannou (GR)	Neuroimaging research of headache disorders (fMRI and DTI) Tamas Kincses (HU)	Acute aortic syndrome Vesna Sarajlic (BiH)
09:12 - 09:33	Imaging of diffuse liver disease Mehmet Şükrü Ertürk (TR)	An Update on Brain Metastases Imaging Milos Lucic (SR) (Online)	Imaging of emergencies in neuroradiology Marijana Karlovic Vidakovic (BiH) (Katilamayacak)
09:33 - 10:00	Hybrid imaging – abdominal incidental findings Silvija Lucic (SR) (Online)	CEST imaging in Neuroradiology Gökşen Çoban Çiftçi (TR)	Not only appendicitis! Transabdominal ultrasound images diverse pathology in the iliac fossae. D. Kokkinos (GR) (Online)
	Scientific session / Hall 1	Scientific session / Hall 2	Scientific session / Hall 3
10:00 - 11:30	ADVANCES AND CHALLENGES IN ARTIFICIAL INTELLIGENCE FOR RADIOLOGY Moderators: Milos Lucic (Online), Michael Klontzas	ONCOLOGIC IMAGING Moderators: L. Moulapoulou, Dragos Cuzino	IMAGING OF INCIDENTAL LESIONS Moderators: S. Gourtsoyianni, Mustafa Harman
10:00 - 10:22	Chasing the black swan: AI in imaging Mehmet Şükrü Ertürk (TR)	Update in lymphomas imaging. Dragos Cuzino (RO)	Incidental Lesions of the Brain Cenk Eraslan (TR)
10:22 - 10:44	Radiomics and clinical applications Firat Atak (TR)	Whole Body Imaging in Multiple Myeloma L. Moulapoulou (GR)	Incidental Lesions of the Lung Akin Çinkoğlu (TR)
10:44 - 11:06	How to ensure reproducibility in AI applications for radiology Michael Klontzas (GR)	Imaging of abdominal lymphoma G.Pekindil (TR)	Incidental nodule in the liver Gülbiz Dağoğlu Kartal (TR)
11:06 - 11:29	Social and Global Impact of AI in Radiology Milos Lucic (SR) (Online)	Benign or malignant? Imaging hepatic vessels thrombosis with Contrast Enhanced Ultrasound. D. Kokkinos (GR) (Online)	Incidentals lesion of the pancreas: C. Triantopoulou (GR)
11:30 - 12:00	COFFEE BREAK		
	Scientific session / Hall 1	Scientific session / Hall 2	Scientific session / Hall 3
12:00 - 13:30	AI IN CLINICAL PRACTICE Moderators: Panagiotis Papadopoulos (Online), Gökşen Çoban Çiftçi	TRAUMA Moderators: Andras Palko, Mehmet Ruhi Onur	PEDIATRIC IMAGING Moderators: Irmira Sefic Pasic, Roxana Papa Stanila
12:00 - 12:22	AI in Neuroradiology Gökşen Çoban Çiftçi (TR)	Imaging of retroperitoneal injury: Vesna Sarajlic (BiH)	Comparison between lung ultrasound and chest x-ray in evaluation of RDS: Irmira Sefic Pasic (BiH/SLO)
12:22 - 12:44	AI in MSK Radiology: Michael Klontzas (GR)	Imaging of pregnant trauma patients Andras Palko (HU)	Spectrum of extracranial MR fetal abnormalities: George Hadjidekov (BU)
12:44 - 13:06	AI in mammographic Breast Density and Risk assessment: M. Ioannidou (GR)	The role of imaging in polytrauma patients: Mehmet Ruhi Onur (TR)	Imaging biomarkers in pediatric solid tumors: Irmira Sefic Pasic (BiH/SLO)
13:06 - 13:30	AI in interventional radiology Panagiotis Papadopoulos (GR) (Online)	Advances on endovascular treatment of subdural hematomas: M. Mantatzis (GR) (Online)	Contribution of fetal MRI in the Prenatal Diagnosis of CNS Anomalies: Roxana Papa Stanila (RO)
13:30 - 14:30	LUNCH BREAK		

October 23-26, 2024
Balkan Congress of Radiology
Altın Yunus Hotel, Çeşme

	Scientific session / Hall 1	Scientific session / Hall 2	Scientific session / Hall 3
14:30 - 16:00	CASES FOR ACES IN ABDOMINAL RADIOLOGY <i>Moderator:</i> Lukas Dagdilelis <i>Speakers:</i> Lukas Dagdilelis (GR), Katerina Xinou (GR), Vesna Sarajlic (BIH)	CASES FOR ACES IN MSK RADIOLOGY <i>Moderator:</i> Dragos Cuzino <i>Speakers:</i> Milos Gasic (SR), Adalet Elçin Yıldız (TR), Dragos Cuzino (RO)	SCIENTIFIC PRESENTATIONS <i>Moderators:</i> D.Kokkinos (Online), Mehmet Ruhi Onur
	Scientific session / Hall 1	Scientific session / Hall 2	Scientific session / Hall 3
16:00 - 17:30	ONCOLOGIC IMAGING AFTER TREATMENT <i>Moderators:</i> P. Prassopoulos, Funda Barlık	SCREENING IN RADIOLOGY <i>Moderators:</i> Oğuz Dicle, N. Dimitropoulos	ONCOLOGIC IMAGING <i>Moderators:</i> Mustafa Seçil, Olivera Nikolic (Online)
16:00 - 16:22	Post surgical imaging evaluation and follow up of patients with gastric cancer. P. Prassopoulos (GR)	Performance of AI in mammographic (FFDM and DBT) screening N. Dimitropoulos (GR)	Imaging of prostate cancer: Milena Spirovski (SR) (Online)
16:22 - 16:44	Post neoadjuvant chemoradiotherapy evaluation of rectal cancer: Andras Palko (HU)	Screening for coronary artery disease: Selin Ardalı Düzgün (TR)	Diagnosis and staging of cholangiocarcinoma Ezgi Güler (TR)
16:44 - 17:06	Monitoring response of neoadjuvant chemotherapy in breast cancer patients with MR mammography. E. Panourgia (GR) (Online)	Screening for lung cancer: Akin Çinkooğlu (TR)	Imaging of testical tumors Mustafa Seçil (TR)
17:06 - 17:30	MRI in treatment of diffuse astrocytoma: Marija Jovanovic (SR)	Role of AI in radiology screening: Oğuz Dicle (TR)	Acute abdominal conditions of the oncology patients Devrim Karaosmanoğlu (TR)
17:30 - 18:00	COFFEE BREAK		
	Scientific session / Hall 1	Scientific session / Hall 2	Scientific session / Hall 3
18:00 - 19:30	SESSION FOR BULGARIAN RADIOLOGY <i>Moderators:</i> Nevra Elmas, Nikoleta Traikova (Online)	SCIENTIFIC PRESENTATIONS <i>Moderators:</i> Dragos Cuzino, Adalet Elçin Yıldız	SCIENTIFIC PRESENTATIONS <i>Moderators:</i> Dora Zlatareva, Cenk Eraslan
18:00 - 18:30	Bulgarian Association of Radiology: Nikoleta Traikova (BU) (Online)		
18:30 -19:00	The Journey of Endovascular Aneurysm and AVM's Treatment in Bulgaria: Stanimir Sirakov (BU)		
19:00 - 19:30	The perspectives in Interventional radiology in St Marina University Hospital Varna, Bulgaria: Chavdar Bachvarov (BU)		
19:30 -20:30	Hall 1 BSR Executive Committee Meeting & General Assembly		
FRIDAY, OCTOBER 25, 2024			
	Scientific session / Hall 1	Scientific session / Hall 2	Scientific session / Hall 3
08:30 - 10:00	MSK RADIOLOGY <i>Moderators:</i> Milos Gasic, Anesa Cengic	IMAGING OF PELVIS <i>Moderators:</i> Deniz Akata, Gökhan Pekindil	INTERVENTIONAL RADIOLOGY IN ONCOLOGY <i>Moderators:</i> Okan Akhan, Dimitrios Filippiadis (Online)
08:30 - 08:52	MRI importance in SLAP lesions of the shoulder joint: Milos Gasic (SR)	Adnexal masses (O-RADS score) Deniz Akata (TR)	The role ablation according to BCLC. Dimitrios Filippiadis (GR) (Online)
08:52 - 09:14	Hoffa's fat pad pathology : imaging findings and differential diagnosis: Anesa Cengic (BIH)	MRI staging of endometrial cancer: an update Bourgioti (GR) (Online)	The role of TACE and TARE for BCLCB Alexandar Gjoreski (NMA) (Online)
09:14 - 09:36	Imaging findings of plantar aponeurosis disorders: Anesa Cengic (BIH)	Vulvar and cervical cancer Olivera Nikolic (SR) (Online)	The role of Ablation for icCCA Okan Akhan (TR)
09:36 - 10:00	Synovioentheseal complex: Pivotal role in imaging approach to arthritis: Adalet Elçin Yıldız (TR)	Preoperative imaging in Peritonitis carcinomatosa Fundu Barlık (TR)	The role of TACE and TARE for icCCA Aytaç Gülcü (TR)
	Scientific session / Hall 1	Scientific session / Hall 2	Scientific session / Hall 3
10:00 - 11:30	SAFETY AND QUALITY ASSURANCE IN RADIOLOGY <i>Moderators:</i> Andras Palko, Boris Brkjacic (Online)	QUANTITATIVE MRI <i>Moderators:</i> Efrasini Papadaki, Mehmet Şükrü Ertürk	MSK RADIOLOGY <i>Moderators:</i> Remide Arkun, Şebnem Örgüç
10:00 - 10:22	Justification of CT examinations in Europe: Boris Brkjacic (CR) (Online)	Organ-Specific Fat Quantification: Liver & Pancreas Ilkay Idilman (TR)	Bone Tumors- Pitfalls and mimics: Remide Arkun (TR)
10:22 - 10:44	CT dose management in practice: Chryssa Paraskevopoulou (GR) (Online)	Organ-Specific iron Quantification: Liver and heart Selin Ardalı Düzgün (TR)	Muscle Tumors: Berna Dirim Mete (TR)
10:44 - 11:07	MR safety: Tamas Kincses (HU)	Myelin water imaging: Efrasini Papadaki (GR)	Groin pain-extraarticular disorders: Remide Arkun (TR)
11:07 -11:30	Peer review of radiology reports and clinical audits in radiology departments: Athanasia Papachristodoulou (GR)	SWI and QSM: applications in CNS disorders: Efrasini Papadaki (GR)	Wrist imaging-pitfalls, variants and common pathologies in Athletes: Berna Dirim Mete (TR)
11:30 - 12:00	COFFEE BREAK		
	Scientific session / Hall 1	Scientific session / Hall 2	Scientific session / Hall 3
12:00 - 13:30	FILM READING SESSION <i>Moderators:</i> Mustafa Seçil	SCIENTIFIC PRESENTATIONS <i>Moderators:</i> Sandy Tavernarakis, Selin Ardalı Düzgün	SCIENTIFIC PRESENTATIONS <i>Moderators:</i> Dimitrios Filippiadis (Online), Aytaç Gülcü
12:00 - 12:15	Abdomen Uluç Özkızıltan (TR)		
12:15 - 12:30	Female pelvis Duygu Doğa Ekizlioğlu (TR)		
12:30 - 12:45	MSK Michael Klontzas (GR)		
12:45 - 13:00	Cardiovascular Dora Hantosi (HU)		
13:00 - 13:15	Cardio Olga Nedeljkovic (SR)		
13:15 - 13:30	Neuro Ali Murat Koç (TR)		
13:30 - 14:30	LUNCH BREAK		
	Scientific session / Hall 1	Scientific session / Hall 2	Scientific session / Hall 3
14:30 - 16:00	CASES FOR ACES IN NEURORADIOLOGY <i>Moderator:</i> Cem Çallı <i>Speakers:</i> Cem Çallı (TR), Efrasini Papadaki (GR), Dora Zlatareva (BU)	CASES FOR ACES IN CARDIAC, PEDIATRIC AND INTERVENTIONAL RADIOLOGY <i>Moderator:</i> Okan Akhan <i>Speakers:</i> Milena Spirovski (SR) (Online), Roxana Popa Stanila (RO), Okan Akhan (TR)	SCIENTIFIC PRESENTATIONS <i>Moderators:</i> Michael Klontzas, Fırat Atak
	Scientific session / Hall 1	Scientific session / Hall 2	Scientific session / Hall 3
16:00 - 17:30	NEURO AND HEAD AND NECK RADIOLOGY <i>Moderators:</i> Turgut Talı (Online), Nikoleta Traikova (Online)	BREAST AND CARDIAC IMAGING <i>Moderators:</i> Ayşenur Oktay, Olga Nedeljkovic	SCIENTIFIC PRESENTATIONS <i>Moderators:</i> Milena Spirovski (Online), Gökhan Pekindil
16:00 - 16:22	Sellar and juxtasellar masses Zulejha Merhemic (BIH)	Radiological assessment of neoadjuvant chemotherapy in breast cancer: Vanessa Beslogic (BIH)	
16:22 - 16:44	Temporal bone pathology Nikoleta Traikova (BU) (Online)	Pitfalls and limitations of breast MRI: Özge Aslan (TR)	
16:44 - 17:06	Imaging of skull brain tumors Zulejha Merhemic (BIH)	Nodal assessment and management in breast cancer: Merve Gürsoy Bulut (TR)	
17:06 - 17:30	Nontraumatic spinal injuries Turgut Talı (TR) (Online)	Cardiac magnetic resonance in the diagnosis of paracardial and cardiac masses Olga Nedeljkovic (SR)	
17:30 - 18:30	Hall 1 Closing Ceremony and Awarding		

ORAL PRESENTATIONS

XIX. BALKAN CONGRESS OF RADIOLOGY SCIENTIFIC PRESENTATION LIST

24 October 2024 - Hall 2

18:00 - 19:30	SCIENTIFIC PRESENTATIONS Moderators: Dragos Cuzino, Adalet Elçin Yıldız
18:00 - 18:09	Correlation of skeletal muscle index with T-score to determine the bone mineral density Ceren Aydın
18:09 - 18:18	Acromion-great tuberculous impingement index may predict the susceptibility to rotator cuff tears and sports injury in children Fatma Zeynep Arslan
18:18 - 18:27	Evaluation Of The Efficacy Of Deep Transverse Friction Massage In Lateral Epicondylitis Using Superb Microvascular Imaging On Common Extensor Tendon Vascularisation Seda Soğukpınar Karaağaç
18:27 - 18:36	Imaging Findings and Complications in Anterior Cruciate Ligament Reconstruction Fatih Ateş
18:36 - 18:45	Assessment of Lateral Pterygoid Muscle Signal and Mandibular Condyle Morphology with Anterior Disc Dislocation of the Temporomandibular Joint on 3T MRI Abdi Gürhan
18:45 - 18:54	Evaluation of Lateral Pterygoid Muscle Signal and Mandibular Condyle Morphology with Anterior Disc Dislocation of the Temporomandibular Joint in Adolescents Abdi Gürhan
18:54 - 19:03	Radiological and Clinical Evaluation of Enchondromas: A Retrospective Study of 112 Cases Nicon Nita
19:03 - 19:12	A High Acromion-Greater Tuberosity Impingement Index Increases the Risk of Labral Tear Fatma Zeynep Arslan
19:12 - 19:21	MRI-based Comparative Assessment of Cam and Pincer Type Hip Morphology Between Semi-Professional Soccer Players and Non-Athlete Controls Yasemin Küçükçiloğlu
19:21 - 19:30	The Relationship Between Spondylolisthesis And Osteoporosis: A Whole-Body Dual-Energy X-Ray Absorptiometry Study Ahmet Nedim Kahraman

24 October 2024 - Hall 3

14:30 - 16:00	SCIENTIFIC PRESENTATIONS Moderators: D.Kokkinos, Mehmet Ruhi Onur
14:30 - 14:39	Pancreatic Neuroendocrine Tumors: A Stepwise Approach To Differential Diagnosis Anna Simichanidou
14:39 - 14:48	Investigation Of The Effect Of Body Composition Measurements Defined By Computed Tomography Before Treatment On Disease Prognosis In Patients With Metastatic Colon Cancer And Comparison With Other Clinicopathological Prognostic Parameters İrfan Durmuş
14:48 - 14:57	Correlation Between CT Liver Density (HU values) and Laboratory Values in Hepatosteatosi Mesut Furkan Yazar
14:57 - 15:06	The impact of defect size on hernia sac contents and the development of ileus in abdominal wall hernias İsmail Furkan Şimşek
15:06 - 15:15	Ileocolic and colocolic intussusception in adults: CT features and pathological correlation Hilal Şahin
15:15 - 15:24	Normal Liver Stiffness Values Measured with MR Elastography and 2-D Shear Wave Elastography in Children (9-17 ages) Osman Kahraman
15:24 - 15:33	Gd-EOB-DTPA-enhanced MRI with T1 mapping versus fibrosis-4 index for staging liver fibrosis Esin Cibiroğlu
15:33 - 15:42	Comparative Diagnostic Performance of Two Abbreviated MRI Protocols for Hepatocellular Carcinoma Sezer Nil Yilmazer Zorlu
15:42 - 15:51	Evaluating the Potential of Abbreviated MRI Protocols for Liver Metastasis Detection: A Study in Colorectal Cancer Patients Sevde Nur Emir
15:51 - 16:00	Quantitative Evaluation of Liver Steatosis Using Ultrasound Attenuation Imaging: A Comparison with MRI Celal Caner Ercan

24 October 2024 - Hall 3	
18:00 - 19:30	SCIENTIFIC PRESENTATIONS Moderators: Dora Zlatareva, Cenk Erarslan
18:00 - 18:09	Normative Choroidal Plexus Apparent Diffusion Coefficient Values in the Pediatric Population Abdi Gürhan
18:09 - 18:18	Neuropsychiatric Lupus Or Multiple Sclerosis? Differential Diagnosis Using Myelin Content Indices Of Normal Appearing White Matter: A Myelin Water Imaging Study Anna Simichanidou
18:18 - 18:27	Effect Of Chemotherapy On Hippocampal Volume: A Preliminary Study Kubilay Kağan Budak
18:27 - 18:36	Comparative Analysis of Brain Volume Differences Between Puberty Precocious and Normal Puberty Girls Hanife Gülten Düzkalır
18:36 - 18:45	Excitotoxic White Matter Injury on Diffusion-Weighted Imaging: A Review of Pediatric Causes Çiğdem Öztunalı
18:45 - 18:54	The role of apparent diffusion coefficient assessment in Wilson disease with neurological involvement Abdi Gürhan
18:54 - 19:03	Comparison of T1A Post-Contrast and FLAIR Imaging Methods in the Diagnosis of Non-Enhancing Leptomeningeal Metastases: FLAIR Hyperintensity as an Early Finding Fatma Zeynep Arslan
19:03 - 19:12	Patterns of Nasal and Paranasal Sinus Injuries in Maxillofacial Trauma: A Retrospective Analysis of Etiologies and Fracture Locations Gülşen Yücel Oğuzdoğan
19:12 - 19:21	Imaging of congenital pyriform sinus fistula in children: A review of six cases Çiğdem Öztunalı
25 October 2024 - Hall 2	
12:00 - 13:30	SCIENTIFIC PRESENTATIONS Moderators: Sandy Tavernarakı, Selin Ardalı Düzgün
12:00 - 12:09	Comparison of PET/CT and CT Texture Analysis in Patients with Stage III-IV Lung Cancer Receiving Chemoradiotherapy: Can We Predict The Treatment Response of The Tumor? Nilufar Gasimli
12:09 - 12:18	Evaluation of the Variability of Axillary Artery and Internal Mammary Artery Diameters According to Intramammary Tumor Location in Breast Cancer Patients with Magnetic Resonance Imaging Deniz Esin Tekcan Şanlı
12:18 - 12:27	Evaluation of Pneumothorax Predictionability by Deep Learning Method Before Transtoracic Fine Needle Aspiration Biopsy (TTIAB) in Lung Masses Nilufar Gasimli
12:27 - 12:36	Computed tomographic pulmonary angiography in the assessment of severity of acute pulmonary embolism and right ventricular dysfunction İrfan Durmuş
12:36 - 12:45	Comparison of a Deep Learning Reconstruction Method With Other Reconstruction Methods In Coronary CT Angiography Eda Cingöz
12:45 - 12:54	Is There A Correlation Between Coronary Artery Calcium Score And Epicardial/Paracardial Adipose Tissue Quantification Osman Konukoğlu
12:54 - 13:03	Evaluation of the relationship between coincidentally detected non-compaction cardiomyopathy on coronary CT angiography and the level of coronary artery disease and the patient's symptoms ; a retrospective study Serhat Akış

25 October 2024 - Hall 3	
12:00 - 13:30	SCIENTIFIC PRESENTATIONS Moderators: Dimitrios Filippiadis, Aytaç Gülcü
12:00 - 12:09	Relationship between the angle of popliteal artery trifurcation branches and atherosclerosis burden in chronic peripheral arterial disease Ali Alkaş
12:09 - 12:18	Efficacy of US-guided Percutaneous Fine Needle Aspiration Biopsy in Patients with Parotid Gland Masses Berat Acu
12:18 - 12:27	Percutaneous Cholecystostomy and Its Impact on Subsequent Surgical Interventions in Acute Cholecystitis Emir Hüseyin Nevai
12:27 - 12:36	The Role Of Kaiser Scoring System In Breast MRI For Risk Stratification Of Intraductal Papilloma Ayşe Şilan Kapuci
12:36 - 12:45	Relationship Between ADC Values And Histopathologic Prognostic Markers of Breast Carcinoma Ayşegül Taşdöğen
12:45 - 12:54	The Effectiveness of Ultrasound-Guided Percutaneous tPA Injection in Thrombosed Arteriovenous Fistula Ahmet Taha Kayaoğlu
12:54 - 13:03	Efficacy of Ultrasound-Guided Microwave Ablation in the Treatment of Breast Fibroadenomas: A Follow-Up Study Eda Cingöz
13:03 - 13:12	Digital Breast Tomosynthesis-Guided Biopsy: Initial Experience Umur Anıl Pehlivan
13:12 - 13:21	Ultrasound-Guided Thrombin Injection for the Treatment of Arterial Pseudoaneurysm Aslı Aras
13:21 - 13:30	Efficacy And Safety Of Endovascular Embolization With N-2-Butyl-Cyanoacrylate In Patients With Massive Hemoptysis: Results Of A Single-Center Experience Merve Solak
25 October 2024 - Hall 3	
14:30 - 16:00	SCIENTIFIC PRESENTATIONS Moderators: Michael Klontzas, Fırat Atak
14:30 - 14:39	Comparison of Temporomandibular Joint Disc in Chronic Renal Failure Patients and Healthy Adults with Shear Wave Elastography Abdi Gürhan
14:39 - 14:48	The Radiological-Pathological Correlation in Breast Cancer Cases with Neoadjuvant Chemotherapy Merve Kurt Koçak
14:48 - 14:57	Detection of Urgent Pathology in Pediatric Emergency Ultrasound Reports Using Large Language Models Hafsa Kolluk
14:57 - 15:06	Detection of Brain Aneurysms on T2W Images by Using Artificial Intelligence Hamza Eren Güzel
15:06 - 15:15	Correlation of Histopathological and Radiological Response Patterns and Their Prognostic Implications in Breast Cancer After Neoadjuvant Chemotherapy Ahmet Bozer
15:15 - 15:24	Classification of Brain CT Reports by Emergency Level Using Artificial Intelligence Hamza Eren Güzel
15:24 - 15:33	Automated Classification Of The Phasescale Scale In Mri Using Deep Learning Methods Zülküf Akdemir

25 October 2024 - Hall 3	
16:00 - 17:30	SCIENTIFIC PRESENTATIONS Moderators: Milena Spirovski, Gökhan Pekindil
16:00 - 16:09	US-guided Percutaneous Transabdominal Tru-cut Biopsy in Patients with Ovarian Tumors Berat Acu
16:09 - 16:18	Is It Feasible to Establish a Stroke Unit in the Remotest Corner of Türkiye? A Case Series from Hakkari Eyüp Kızıl
16:18 - 16:27	Evaluating Specimen Adequacy in Thyroid FNAB: A Comparison of Transfer Techniques Fatma Zeynep Arslan
16:27 - 16:36	Diagnostic Utility of Quantitative and Semi-Quantitative Parameters from Multiparametric MRI in Prostate Cancer Detection: A Retrospective Study Gülşen Yücel Oğuzdoğan
16:36 - 16:45	The Utility of Quantitative ADC and T2 Values, Enhancement Pattern, and Lesion Shape Characteristics in Differentiating True Positive from False Positive Lesions on Multiparametric Prostate MRI Selahattin Durmaz
16:45 - 16:54	Magnetic Resonance Imaging Findings of Neonatal Ovarian Torsion Umur Anıl Pehlivan
17:03 - 17:12	Preoperative prediction of serous and mucinous borderline ovarian tumors according to MRI features Tuğçe Hancıoğlu
17:12 - 17:21	A comprehensive review of post-treatment imaging in gynecologic malignancies: case-based tips and tricks for detecting potential complications and avoiding pitfalls Yeşim Yekta Yürük

CORRELATION OF SKELETAL MUSCLE INDEX WITH T-SCORE TO DETERMINE THE BONE MINERAL DENSITY

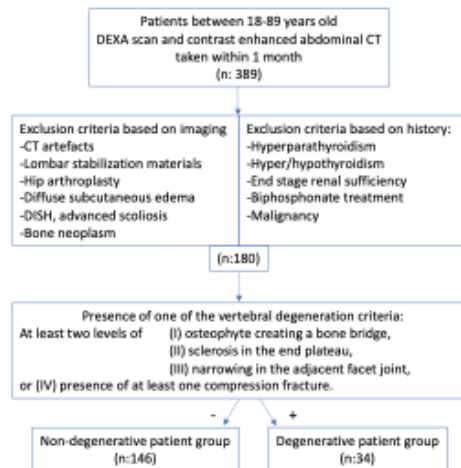
Ceren Aydın¹, Nurdan Çay²

¹Antalya Kemer State Hospital

²Ankara Yıldırım Beyazıt University

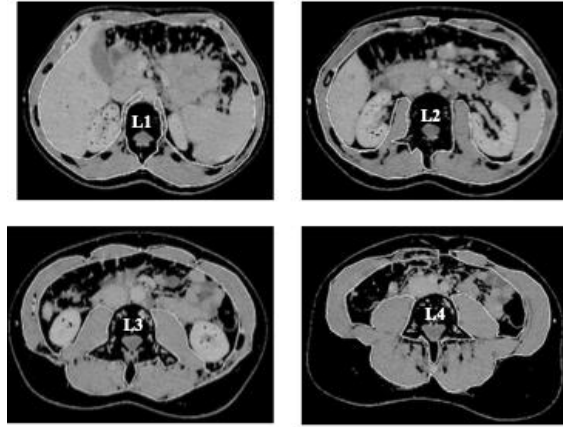
Abstract: Objective: In this study, our aim is to reveal the correlation between sarcopenia and bone mineral density (BMD) and to determine the contribution of the skeletal muscle index (SMI), which is used in the definition of sarcopenia, to the diagnosis of osteoporosis. Materials and Methods: Among the patients who underwent Dual-energy X-ray absorptiometry (DEXA) those who had an abdominal computed tomography (CT) scan at most one month apart were determined. Degeneration criteria were defined as the presence of at least one of the signs of osteophyte creating a bone bridge, sclerosis at the end plateau, narrowing of the adjacent facets in at least two levels, or at least one compression fracture. For degenerative (n: 34) and non-degenerative (n: 146) groups, BMD and T scores in DEXA, SMI values and bone densities at lumbar levels 1-4 in CT were recorded. Results: Positive correlations were found for each level between SMI and lumbar BMD measurements for 180 patients ($p<0,05$). When the degenerative patient group was examined separately, there was no significant correlation between lumbar BMD and SMI values; while there was a positive correlation between BMD and SMI in nondegenerative patients. ($r=0,234-0,317$, $p<0,05$). The correlation between SMI and BMD in nondegenerative patients over 60 years of age was moderately positive ($r=0,408$, $p<0,05$). There was also a positive correlation between bone densities and femoral BMD and SMI values for the two groups ($p<0,05$). SMI for each lombar level had high correlation among themselves ($r=0,86-0,92$, $p<0,05$). Conclusion: Since there is a correlation between SMI and BMD, that is sarcopenia and osteoporosis, treatment for osteoporosis may be considered in patients with sarcopenia. Lumbar BMD values measured by DEXA in patients with vertebral degeneration are misleading, presence of sarcopenia in these patients may be a guide in the diagnosis of osteoporosis.

Patient Selection



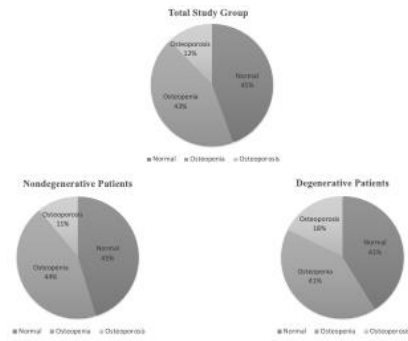
Inclusion and exclusion criteria for the study

Skeletal muscle area calculations



Skeletal muscles were drawn in axial sections at the specified lumbar levels and the HU level was selected between -29 and +150.

Group distributions



Bone mineral density distributions according to patient groups

Keywords: Sarcopenia, Osteoporosis, DEXA, Bone mineral density, Skeletal muscle index

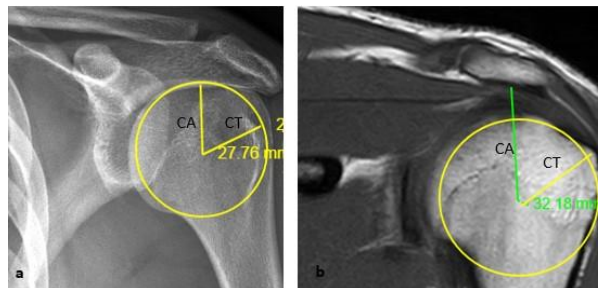
ACROMION–GREAT TUBERCULOUS IMPINGEMENT INDEX MAY PREDICT THE SUSCEPTIBILITY TO ROTATOR CUFF TEARS AND SPORTS INJURY IN CHILDREN.

Oner Ozbey¹, Fatma Zeynep Arslan¹

¹Basaksehir Cam and Sakura City Hospital

Abstract: Introduction: The Acromion–Greater Tuberosity Impingement Index (ATI) is a newly defined angle and there are only a few articles available in the literature. In this study, the relationship between ATI and a series of shoulder pathologies and morphometric measurements was evaluated using shoulder MRI and X-ray in children. Materials and Methods: The relationship between the ATI and classical pathologies and measurements (including acromion type, presence of rotator cuff tear, acromiohumeral distance (AHD), acromion index (AI), lateral acromion angle (LAA), critical shoulder angle (CSA) in our pediatric patients under 18 years of age included in our study was examined. The values obtained from both MRI and X-ray images were compared. Results: A total of 64 pediatric patients were evaluated, and the mean age was 11.77 years. Acromion types 3 and 4 were significantly higher in children with higher ATI values on MRI and X-ray ($p < 0.005$). A statistically significant relationship was found between the MRI-measured ATI values and rotator cuff tears ($p < 0.005$), while no significant relationship was found with X-ray ATI values ($p = 0.27$). While ATI on MRI shows a significant positive correlation with AI, LAA, and CSA ($p < 0.005$), it represents a negative insignificant relationship with AHD ($p = 0.025$). Similarly, ATI on X-ray shows a significant positive correlation with AI, LAA, and CSA ($p < 0.005$), but demonstrates a positive insignificant relationship with AHD ($p = 0.015$). Conclusion: Children with higher ATI values tend to have a wider AI, as well as a higher incidence of type 3 and 4 acromion, and are more likely to have supraspinatus tendon tears. This can serve as a marker for rotator cuff tears and sports injuries that are rarely seen in the children.

Figure 1



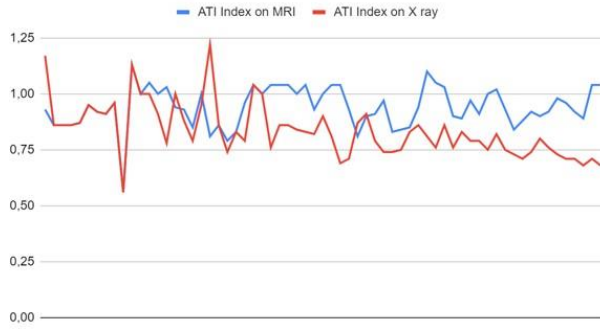
The schematic representation of the acromion-greater tuberosity relationship. The diagram illustrates the anatomical landmarks used to measure the Acromion-Greater Tuberosity Impingement Index (ATI). The measurement is obtained by dividing the distance from the center of rotation of the humeral head to the greater tuberosity by the distance from the center of rotation of the humeral head to the inferior surface of the acromion. ATI calculations were conducted using both lateral shoulder X-ray (a) and axial MRI scans (b). On X-ray CA (center of rotation of the humeral head- the distance of the acromion) is 27 mm and CT (center of rotation of the humeral head- the distance of the greater tuberosity) is 25 mm. On MRI; CA is 32 mm and CT is 24,89 mm.

Figure 2



: a) The critical shoulder angle (CSA) is defined as the angle formed between the superior and inferior bone margins of the glenoid and the most lateral edge of the acromion. b) The lateral acromial angle (LAA) is determined by the angle between a line through the midpoint of the glenohumeral joint and the line along the inferior border of the acromion. c) Acromiohumeral distance (AHD) is quantified as the distance measured between the humeral head and the undersurface of the acromion. d) The acromion index (AI) is derived from the ratio of the distance from the glenoid cavity to the lateral edge of the humerus compared to the distance from the glenoid cavity to the lateral edge of the acromion.

Figure 3



MRG'de ölçülen ATI ile X-ray'de ölçülen ATI arasında 0.906'lık bir Pearson korelasyon katsayısı bulunmaktadır. Bu, yüksek derecede pozitif bir ilişkiyi göstermekte olup, istatistiksel olarak anlamlıdır (p-değeri: 0.0001). Bu bulgular, MRG ve X-ray yöntemlerinin ATI ölçümlerinin benzerliğini destekleyerek klinik değerlendirmelerde uyumlu sonuçlar elde edileceğini göstermektedir.

Keywords: Acromion–great tuberculous impingement index, Shoulder, Pediatric

EVALUATION OF THE EFFICACY OF DEEP TRANSVERSE FRICTION MASSAGE IN LATERAL EPICONDYLITIS USING SUPERB MICROVASCULAR IMAGING ON COMMON EXTENSOR TENDON VASCULARISATION

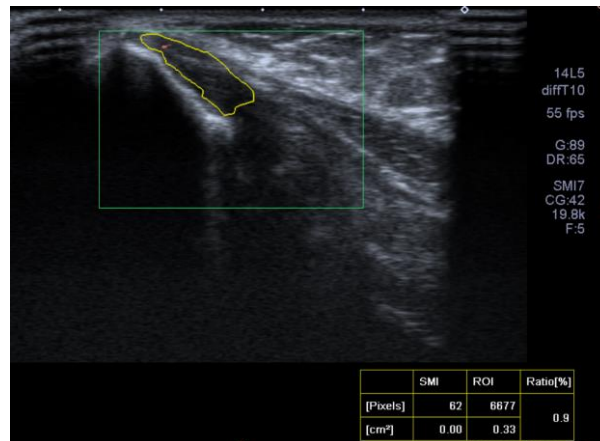
Seda Sogukpınar Karaagac¹, Nevzat Yesilmen²

¹Department of Radiology, Faculty of Medicine, Firat University, Elazığ, Turkey

²Department of Physical Therapy, Fethi Sekin City Hospital, Elazığ, Turkey

Abstract: Lateral epicondylitis, also referred to as tennis elbow, represents the most prevalent form of elbow discomfort among adults. The objective of this study is to evaluate the vascularity of the common extensor tendon (CET) using superb microvascular imaging (SMI) before and after deep transverse friction massage, and to compare the effects of the treatment on tendon vascularity. The study included 4 male and 16 female patients diagnosed with lateral epicondylitis who had been experiencing symptoms for a minimum of two months. A total of two months treatment was administered, comprising two sessions per week of deep transverse friction massage of the common extensor tendons. Tendon AP diameters, Visual Analogue Scale (VAS) scores and superb microvascular imaging (SMI) vascularisation values were recorded at the outset of the study and at one and two months thereafter. A statistically significant reduction in VAS score was observed following treatment compared to the pre-treatment value ($P < 0.05$). The mean value of tendon AP diameters was observed to increase from 4.76 mm prior to treatment to 5.58 mm in the second month following treatment, a change that was statistically significant. A statistically significant difference was observed between the CET SMI values following treatment, as determined by the Wilcoxon test ($P < 0.05$). The mean SMI vascularisation index (VI) value of CET was 1.32% in the pre-treatment period, 3.18% in the first month after treatment and 5.06% in the second month post-treatment, with a statistically significant difference ($P < 0.05$). The SMI method represents a promising new avenue for evaluating CET vascularisation in lateral epicondylitis, offering a potential diagnostic tool for comparing the efficacy of different therapeutic modalities.

Image 1a



Vascular index measurement with superb microvascular imaging of the common extensor tendon before treatment

Image 1b



Increase in vascular index observed in second month after treatment

Keywords: Superb Microvascular Imaging, Deep Transverse Friction Massage, Lateral Epicondylitis, Common Extensor Tendon

IMAGING FINDINGS AND COMPLICATIONS IN ANTERIOR CRUCIATE LIGAMENT RECONSTRUCTION

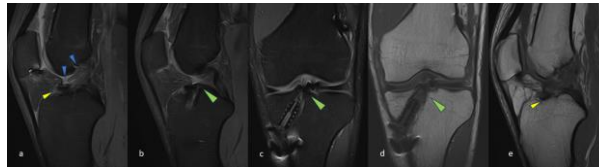
Fatih Ateş¹

¹Konya City Hospital, Radiology Department

²Selçuk University, Faculty of Medicine, Radiology Department

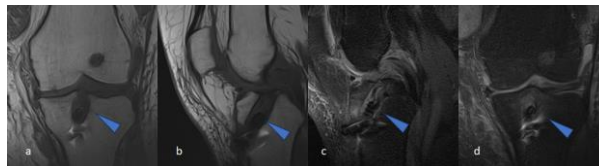
Abstract: Introduction and Objective: Anterior cruciate ligament (ACL) tears are the most common ligament injuries in the knee [1,2]. In recent years, there has been an increase in the number of patients undergoing knee surgery due to ACL ligament tears. This increase is attributed to difficulties in postoperative recovery, recurrence of symptoms, or new injuries, leading to a rise in the number of patients seeking Magnetic Resonance Imaging (MRI) [3]. Verifying the accuracy of ACL graft placement and investigating postoperative complications are common scenarios in postoperative knee imaging. MRI serves as the primary imaging modality in these cases [4]. Our study aims to describe MRI findings postoperatively for both ACL graft reconstructions and complications. Materials and Methods: The study included 124 patients who underwent cruciate ligament reconstruction and presented to the radiology department between 2019 and 2024. Imaging findings for these patients were retrospectively assessed using the hospital's PACS (Picture Archiving and Communication System). Results: 30 of the patients exhibited normal findings for cruciate ligament reconstruction. Specific complications identified were as follows: 33 patients had roof impingement, 18 had cystic enlargement of the tunnel, 16 had partial ACL graft rupture, 15 had arthrofibrosis, 11 had total ACL graft rupture, 11 had lateral wall impingement, 9 had associated bone fragments, 7 had anteriorly positioned tibial tunnels, 6 had pericruciate fat pad impingement, 3 had laxity, 3 had both femoral and tibial tunnels, 2 had iliotibial band syndrome, and 1 had material dislocation. Three patients had normal findings for ACL grafts. Some patients exhibited multiple findings simultaneously. Discussion and Conclusion: MRI is an effective imaging modality for evaluating the position of the ACL graft, tunnels, and fixation materials, as well as for investigating the causes of postoperative pain and functional loss [5,6]. The frequency of ACL reconstruction surgery is increasing over time. Therefore, it is crucial for radiologists to be familiar with MRI findings, common complications, and procedural details associated with ACL reconstruction surgeries. This paper aims to present normal MRI findings and the appearance of common complications that may arise following ACL graft reconstruction surgery.

Figure 1



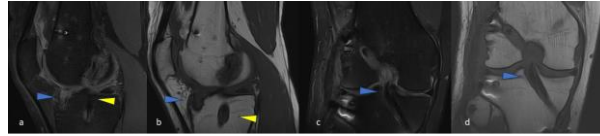
In a young male patient, a partial rupture of the ACL with a wrinkled appearance was observed (a; blue triangles). In the same patient, a hypointense appearance adjacent to the anterior ACL on both T1 and T2-weighted images was evaluated as arthrofibrosis (a, e; yellow triangles). Additionally, there was narrowing at the tibial tunnel exit, which was reported as lateral wall impingement. This patient has undergone reoperation.

Figure 2



In the T1-weighted coronal and sagittal images (a, b) and proton density sagittal and coronal sections (c, d), as indicated by the blue arrows, there is an enlargement of the tibial tunnel.

Figure 3



The anterior cruciate ligament tibial tunnel appears prominently vertical and anterior on imaging. This has been reported as roof impingement secondary to increased intensity in the ACL (a: sagittal proton density; b: sagittal T1-weighted; c: coronal proton density; d: coronal T1-weighted; blue triangles). Additionally, there are findings of posterior cruciate ligament (PCL) reconstruction in the patient, with the PCL graft evaluated as normal (yellow triangles).

Table:

Results	Normal ACL graft	Roof impingement	Tunnel cystic enlargement	Partial ACL rupture	Arthrofibrosis	Total ACL rupture	Side wall impingement	Bone fragment	Anterior tibial tunnel	Pericruciate impingement	Laxity	Double femoral and tibial tunnels	Iliotibial band syndrome	Material dislocation	Normal PCL graft
Number	30	33	18	16	15	11	9	7	6	3	3	3	2	1	3

Total ACL Reconstruction Patients and Findings

Keywords: Anterior Cruciate Ligament Reconstruction, Impingement, Graft rupture, Arthrofibrosis

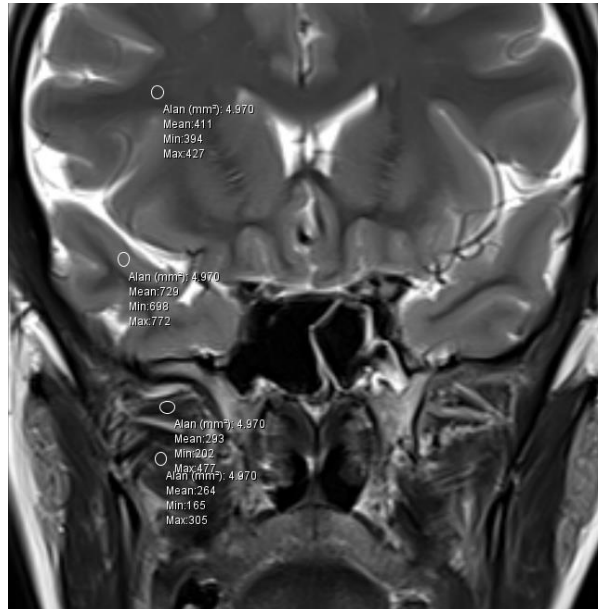
ASSESSMENT OF LATERAL PTERYGOID MUSCLE SIGNAL AND MANDIBULAR CONDYLE MORPHOLOGY WITH ANTERIOR DISC DISLOCATION OF THE TEMPOROMANDIBULAR JOINT ON 3T MRI

Seyit Erol¹, Halil Özer¹, Abdi Gürhan¹, Mustafa Koplay¹, Mehmet Öztürk¹

¹Selcuk University, Faculty of Medicine

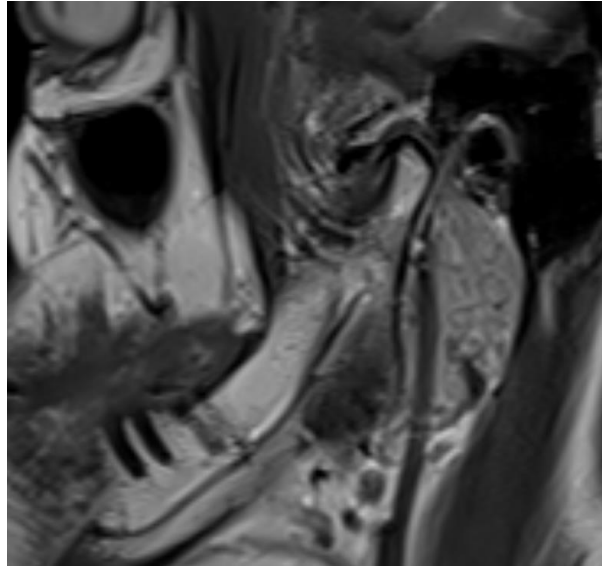
Abstract: Anterior dislocation of the temporomandibular (TMJ) disc is a condition manifested by impaired chewing function and severe pain, and Magnetic Resonance Imaging (MRI) is very important in its diagnosis. Patients over the age of 18 who underwent TMJ MRI in our hospital between January 2019 and April 2024 were included in this study. Anterior dislocation with reduction (ADwR), anterior dislocation without reduction (ADwoR), and normal TMJ discs were identified on MRI. The anteroposterior diameter and medial-lateral diameter of the mandibular condyle were measured and the condyle was categorized as straight, rounded, or beaked. On MRI, TMJ disc morphologies were determined as biconcave, thickening anterior, thickening posterior, biplanar, and folded. Signal intensities from the the upper-lower heads of the lateral pterygoid muscle and gray-white matter of the brain were evaluated, and the lateral pterygoid muscle signal intensity ratio (SIR) was calculated. The study included 112 patients and 224 temporomandibular joints, with 70.5% females, a mean age of 35.55±14.89 years. In 224 TMJ discs, 139(62.1%) were normal, 48(21.4%) were ADwR, and 37(16.5%) were ADwoR. Condyle morphologies were found as 143(63.8%) round, 56(25%) flat, and 25(11.2%) beak. Disc morphologies were found as 138(61.6%) biconcave, 40(17.9%) thickening posterior, 17(7.6%) thickening anterior, 16(7.1%) biplanar, and 13(5.8%) folded. Beak-shaped condyles and folded discs were more commonly found in cases with ADwoR ($p < 0.001$). A significant difference was found between normal disc and ADwR and ADwoR in AP and ML diameter measurements of the condyle ($p < 0.001$). The lateral pterygoid muscle signal intensity ratios did not differ significantly within disc pathology groups ($p > 0.05$). In the ROC analysis the condyle AP and ML diameters showed fair performance for classification of disc pathology. The condyle AP diameter AUC was 0.610 ($P < 0.001$), with a sensitivity of 59.5% and a specificity of 58.8% at a cut-off value of 5.86 mm. The condyle ML diameter AUC was 0.722 ($P < 0.001$), with a sensitivity of 64.9% and a specificity of 63.9% at a cut-off value of 18.02 mm. The LPM SIR showed poor performance for classification of disc pathology. Consequently, condyle morphology, condyle AP, and ML diameters offer important information in identifying the disease of the TMJ disc.

Signal measurement



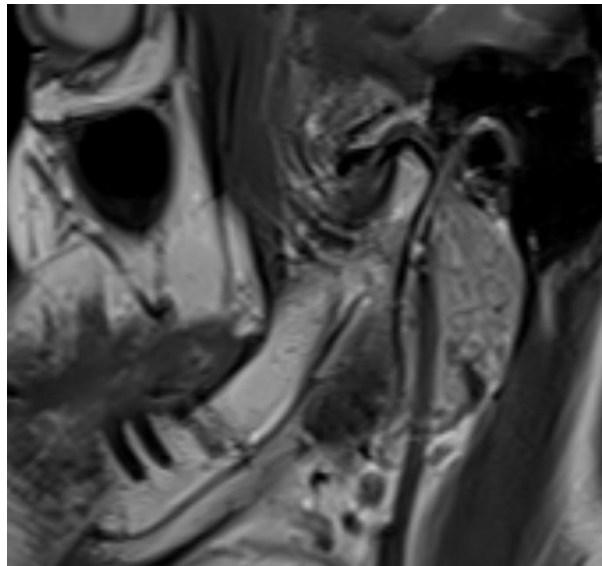
Intensity measurement with ellipsoid ROI in the superior and inferior heads of the lateral pterygoid muscle and the white and gray matter of the brain is shown.

Closed mouth, Anterior dislocation without Reduction



Anteriorly dislocated disc is observed in the right temporomandibular joint in the mouth closed position.

Open mouth, Anterior Dislocation without Reduction



Anteriorly dislocated without reduction disc is observed in the right temporomandibular joint in the open mouth position.

Table 1: Comparison of condyle diameters and lateral pterygoid muscle signal intensity ratio according to the disc pathology (n=224)

		N	Mean	SD	F	p	Sig.
Condil AP measurement	Normal (1)	139	6.43	1.16			
	ADwR (2)	48	5.79	1.19	7.75	<0.001	1-2; 1-3
	ADwoR (3)	37	5.73	1.42			

Condil ML measurement	Total	224	6.18	1.25	17.20	<0.001	1-2; 2-3; 1-3
	Normal (1)	139	19.11	2.22			
	ADwR (2)	48	18.08	2.54			
	ADwoR (3)	37	16.49	3.17			
	Total	224	18.46	2.64			

ANOVA, data are presented as mean \pm standard; ADwR: Anterior dislocation with reduction; ADwoR: Anterior dislocation without reduction, AP: antero-posterior, ML: medio-lateral, LPM: lateral pterygoid muscle.

Table 2: Comparison of disc locations with condyle and disc morphology (n=224)

		Normal	ADwR	ADwoR	P-value
Condil Morphology	Round	105 (73.4)	24 (16.8)	14 (9.8)	<0,001
	Flat	29 (51.8)	18 (32.1)	9 (16.1)	
	Beak	5 (20)	6 (24)	14 (56)	
	Biconcave	109 (79)	25 (18.1)	4 (2.9)	<0,001
	Thickening posterior	23 (57.5)	10 (25)	7 (17.5)	
	Thickening anterior	3 (17.6)	6 (35.3)	8 (47.1)	
Disc Morphology	Biplanar	4 (25)	6 (37.5)	6 (37.5)	
	Folded	0 (0)	1 (7.7)	12 (92.3)	

Chi-Square Tests, data are presented as counts, with percentages in brackets; ADwR: Anterior dislocation with reduction; ADwoR: Anterior dislocation without reduction.

Table 3: ROC analysis result of condil AP and ML diameter used for diagnosis of temporomandibular disc dislocation

	AUC (95% CI)	Cut off	p-value	Sensitivity (%)	Specificity (%)
Condil AP	0.610 (0.501-0.720)	>5.86	<0.05	59.5	58.8
Condil ML	0.722 (0.623-0.821)	>18.02	<0.001	64.9	63.9

AUC: Area under the curve, 95% CI: 95% confidence interval. AP: antero-posterior, ML: medio-lateral. LPM: lateral pterygoid muscle. SIR: Signal intensity ratio

Keywords: Temporomandibular joint, Magnetic Resonance Imaging, Musculoskeletal Imaging

EVALUATION OF LATERAL PTERYGOID MUSCLE SIGNAL AND MANDIBULAR CONDYLE MORPHOLOGY WITH ANTERIOR DISC DISLOCATION OF THE TEMPOROMANDIBULAR JOINT IN ADOLESCENTS

Seyit Erol¹, Halil Özer¹, İsmail Dilek¹, Abdi Gürhan¹, Mehmet Öztürk¹

¹Selcuk University, Faculty of medicine

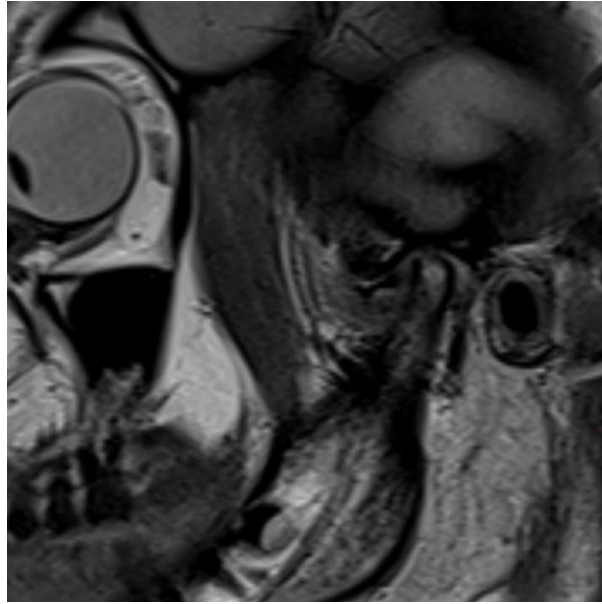
Abstract: Anterior dislocation of the temporomandibular (TMJ) disc is a condition that can be encountered in adolescence, causing serious dysfunction. Magnetic Resonance Imaging (MRI) plays a crucial role in assessing TMJ disc pathology. Patients aged 12-18 years who underwent TMJ MRI in our hospital between January 2018 and February 2024 were included in this study. On MRI, TMJ discs were determined as normal, anterior dislocation with reduction (ADwR), and anterior dislocation without reduction (ADwoR). Signal intensities were measured from the upper and lower heads of the lateral pterygoid muscle and brain gray and white matter. From these measurements, the lateral pterygoid muscle signal intensity ratio (SIR) was obtained. The anteroposterior diameter and medial-lateral diameter of the mandibular condyle were measured and the condyle was categorized as straight, rounded, or beaked. The study included 108 patients and 216 temporomandibular joints, with 74.1% females, a mean age of 15.63 ± 1.32 years. In 216 TMJ discs, 81(37,5%) were normal, 81(37,5%) were ADwR, and 54(25) were AdwoR. Condyle morphologies were found as 109(50,5%) round, 76(35,2%) flat, and 31(14,4%) beak. Beak-shaped condyles were more commonly found in cases with AdwoR ($p < 0,001$). A significant difference was found between normal disc and ADwR, and also between normal disc and ADwoR in AP and ML diameter measurements of the condyle ($p < 0.001$). The lateral pterygoid muscle signal intensity ratios did not differ significantly within disc pathology groups ($p > 0.05$). In the ROC analysis the condyle AP and ML diameters showed fair performance for classification of disc pathology. The condyle AP diameter AUC was 0.644($P=0.001$), with a sensitivity of 61.1 % and a specificity of 63.6% at a cut-off value of 5.71 mm. The condyle ML diameter AUC was 0.647($P=0.001$), with a sensitivity of 64.8 % and a specificity of 63% at a cut-off value of 16.89 mm. The LPM SIR showed poor performance for classification of disc pathology. As a result, condyle morphology, condyle AP and ML diameters provide significant findings in distinguishing TMJ disc pathology.

Signal Measurement



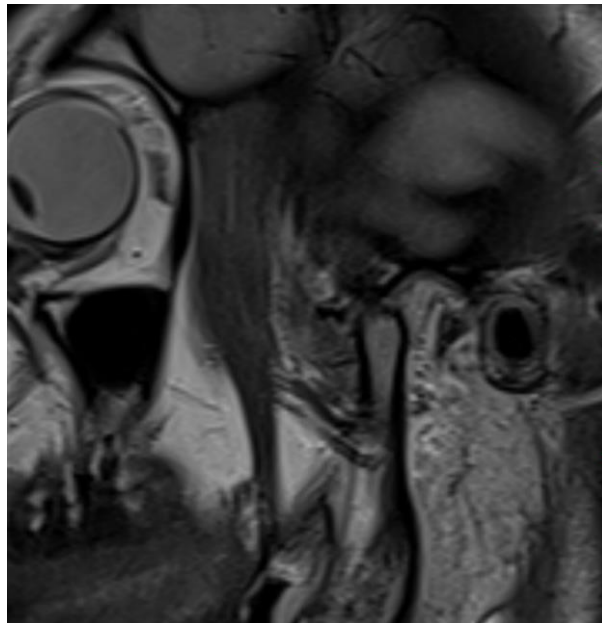
Signal measurements from the superior and inferior head of the lateral pterygoid muscle, brain white and gray matter with ellipsoid ROI are shown.

closed mouth, anterior dislocation without reduction



Anteriorly dislocated disc is observed in the right temporomandibular joint in the mouth closed position.

open mouth,, non-reduced dislocation



In the right temporomandibular joint, an anteriorly dislocated disc without reduction is observed in the open mouth position.

Table 1: Comparison of condyle diameters and lateral pterygoid muscle signal intensity ratio according to the disc pathology (n=216)

		N	Mean	SD	F	p	Sig.
Condil AP measurement	Normal (1)	81	6,27	1,13	8,47	<0.001	1-2; 1-3
	ADwR (2)	81	5,76	1,43			

Condil ML measurement	ADwoR (3)	54	5,35	1,31	10,9	<0.001	1-2; 1-3
	Total	216	5,85	1,34			
	Normal (1)	81	18,3	2,02			
	ADwR (2)	81	17,12	2,29			
	ADwoR (3)	54	16,47	2,83			
	Total	216	17,4	2,45			

ANOVA, data are presented as mean \pm standard; ADwR: Anterior dislocation with reduction; ADwoR: Anterior dislocation without reduction, AP: antero-posterior, ML: medio-lateral, LPM: lateral pterygoid muscle.

Table 2: Comparison of disc locations with condyle morphology (n=216)

Normal	ADwR	ADwoR	p-value	<0.001
Round	54 (49.5)	38 (34.9)	17 (15.6)	
Flat	23 (30.3)	30 (39.5)	23 (30.3)	
Beak	4 (12.9)	13 (41.9)	14 (45.2)	

Chi-Square Tests, data are presented as counts, with percentages in brackets; ADwR: Anterior dislocation with reduction; ADwoR: Anterior dislocation without reduction.

Table 3: ROC analysis result of condil AP and ML diameter used for diagnosis of temporomandibular disc dislocation

	AUC (95% CI)	Cut off	p- value	Sensitivity (%)	Specificity (%)
Condil AP	0.644 (0.557- 0.732)	>5.71	<0.001	61.1	63.6
Condil ML	0.647 (0.557- 0.736)	>16.89	<0.001	64.8	63

AUC: Area under the curve, 95% CI: 95% confidence interval. AP: antero-posterior, ML: medio-lateral. LPM: lateral pterygoid muscle. SIR: Signal intensity ratio

Keywords: Temporomandibular joint, Magnetic Resonance Imaging, Musculoskeletal imaging

“RADIOLOGICAL AND CLINICAL EVALUATION OF ENCHONDROMAS: A RETROSPECTIVE STUDY OF 112 CASES”

Mehmet Demir¹, Nicon Nita¹

¹*Harran University, Faculty Of Medicine , Department Of Radiology*

Abstract: Introduction: Enchondromas are rare but significant benign cartilage tumors that develop within the bone marrow cavity, most commonly affecting the bones of the hands, feet, and long bones. These tumors are typically asymptomatic and are often incidentally detected during imaging studies conducted for other reasons. However, when the tumor grows or poses a risk of malignant transformation, symptoms such as pain, swelling, deformity, and, rarely, pathological fractures may occur. This study aims to examine the clinical and demographic characteristics of enchondromas in 112 patients. Material and Methods: In this retrospective study, 112 patients diagnosed with enchondroma via computed tomography or magnetic resonance imaging between 2015 and 2023 in a radiology clinic were reviewed. The demographic data, clinical findings, and radiological imaging results of the patients were evaluated. Results: A total of 112 patients were evaluated retrospectively. The age range was between 5 and 84 years, with a mean age of 45.35 years. The majority of the patients were female (59%, n=66), while 41% were male (n=46). The most common site of enchondromas was the bones of the hands (36%, n=40), followed by the bones of the feet (21%, n=23), long bones (30%, n=34), and other bones (13%, n=15). Most of the tumors were smaller than 3 cm and asymptomatic, but the likelihood of symptoms increased with tumor size. Discussion: The findings are largely consistent with the literature, confirming that the bones of the hands and feet are the most commonly affected areas. Larger tumors are more likely to be symptomatic and may require intervention. The higher incidence of enchondromas in females may be related to hormonal or genetic factors, but further research is needed in this area. Conclusion: This study provides important insights into the clinical and demographic characteristics of enchondromas. While most tumors are small and asymptomatic, larger tumors tend to be symptomatic and may require surgical intervention. Future studies with larger patient groups are needed to better understand the pathogenesis, clinical course, and treatment of enchondromas. Key words: Enchondroma, Benign cartilage tumor, Magnetic resonance, Computed tomography

Keywords: Enchondroma, Benign cartilage tumor, Magnetic resonance, Computed tomography

A HIGH ACROMION-GREATER TUBEROSITY IMPINGEMENT INDEX INCREASES THE RISK OF LABRAL TEAR

Fatma Zeynep Arslan¹, Sinan Erdemi¹

¹*Basaksehir City Hospital*

Abstract: Background: The Acromion–Greater Tuberosity Impingement Index (ATI) is a recently described measurement that reflects acromial coverage. ATI is calculated by dividing the distance from the rotational center of the humeral head to the greater tuberosity of the humerus by the distance from the rotational center of the humeral head to the undersurface of the acromion (1). This study is the first to compare the relationship between ATI and labral tears. Our aim is to evaluate whether a higher ATI is associated with labral tears using MR arthrography. Methods: A total of 150 shoulder MR arthrography scans were retrospectively evaluated. ATI values obtained from MRI and X-ray images were compared. Intraoperative glenoid labral tears were classified as: anterior labral tears, (2) posterior labral tears, (3) superior labral anterior posterior (SLAP) type II tears (A, B, or C), (4) SLAP type V tears, (5) SLAP type VIII tears, or (6) circumferential labral tears (combined SLAP, anterior, and posterior labral tears). Demographic data, clinical findings, arthroscopy history, and acromion type were also recorded. Results: The mean age was 41.77 years (range 5-17 years, standard deviation ± 3.08 years). SLAP type II lesions were the most common type (53.9%) in the patient group. Acromion type 3 was significantly more prevalent in shoulders with higher ATI values on MRI and X-ray ($p < 0.005$). According to the ROC curves, ATI is a good predictor of SLAP tear lesions on both X-ray (cut-off, 0.887) and MRI (cut-off, 0.986). Patients with SLAP tear lesions had significantly higher mean ATI values compared to those without ($p < 0.001$ for both X-ray and MRI). Conclusion: Numerous anatomical variations of the superior labrum and adjacent structures complicate the interpretation of SLAP tears on imaging and during MR arthroscopy. Patients with SLAP tear lesions have significantly higher ATI values. Higher ATI values may be a risk factor for labral pathologies. This information can be useful in interpreting shoulder MRIs where MR arthrography is not available and there is uncertainty regarding a labral tear.

Keywords: acromion–greater tuberosity impingement index, shoulder, labral tear

MRI-BASED COMPARATIVE ASSESSMENT OF CAM AND Pincer Type Hip Morphology Between Semi-Professional Soccer Players and Non-Athlete Controls

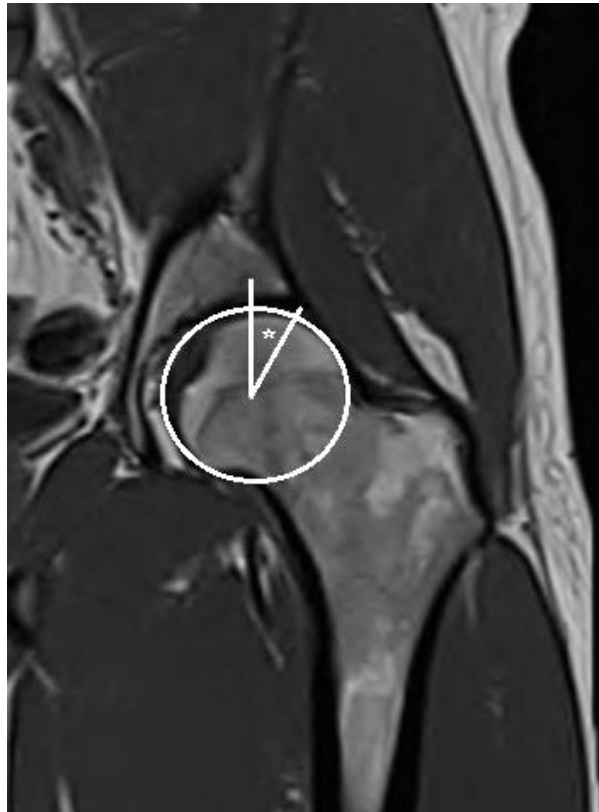
Yasemin Kucukciloglu¹, Deniz Aydin²

¹Near East University, Department of Radiology

²Near East University, Department of Orthopaedics

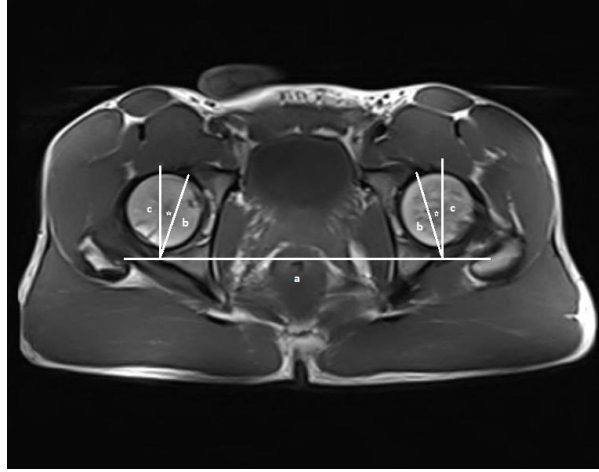
Abstract: Purpose: Femoroacetabular impingement is a condition that can lead to impaired hip function at an early age and is associated with structural differences in hip morphology. The aim of the study was to assess and compare the MRI-based radiological parameters of hip morphology between semi-professional soccer players and non-athlete controls, in young adults who have completed hip development. Methods: MRI scans of young male soccer players and their age- and gender-matched control group were reviewed retrospectively. Lateral center edge angle, acetabular version, alpha angle, collodiaphyseal angle and femoral head coverage ratio were noted and compared between groups. Results: MRI scans of 120 hips of 30 young male soccer players and 30 non-athletes in the control group were included in the study. The mean age of all participants were $24,88 \pm 5,10$ (min:15 , max:34). Anteversion was found statistically higher in non-athlete group ($p=0,02$ for right hip and $p=0,05$ for left hip). The collodiaphyseal angle was found statistically higher in soccer-player group ($p=0,01$ for right hip and $p=0,03$ for left hip). Lateral center edge angle was higher in non-athlete group but it was not significantly different between groups. Femoral head coverage ratio was significantly higher in non-athlete group ($p=0,02$ for right hip and $p=0,01$ for left hip). Alpha angle was not significantly different between groups. Conclusion: This study shows that semi-professional soccer players and non-athletes have a different femoroacetabular morphology. However, no evidence were found indicating that the risk of cam or pincer type morphology increased in semi-professional soccer players.

Figure 1



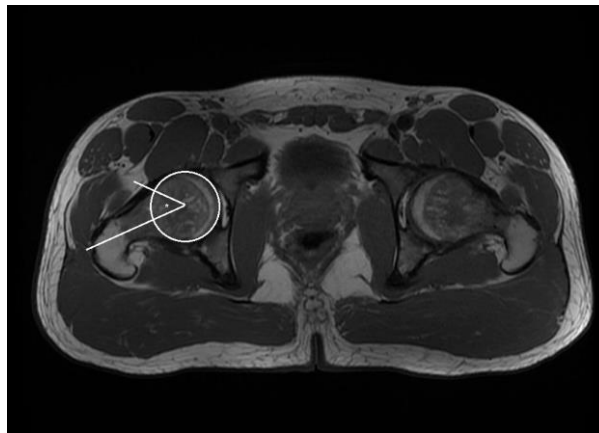
Coronal T1W image shows lateral center edge angle (*), formed by a perpendicular line from the center of the femoral head extending superiorly and a line from the center of the femoral head through the lateral acetabular rim.

Figure 2



Axial T1 W image shows a line drawn between both posterior corners of acetabula (line a), a line (line b) tangential to both anterior and posterior corners of acetabulum, and a third line (line c) perpendicular to line a. Angle of acetabular version (*) is the angle between lines b and c.

Figure 3



Alpha angle was measured by drawing a circle around the axial circumference of the femoral head, a line from center of femoral head through central axis of femoral neck and a second line that extends from the intersection of the first line and the center of the femoral head to the point where the osseous anterior femoral head intersects the circle on axial T1W image. The angle between the two lines was noted (*).

Keywords: Femoroacetabular impingement, Cam type morphology, Pincer type morphology, MRI

THE RELATIONSHIP BETWEEN SPONDYLOLISTHESIS AND OSTEOPOROSIS: A WHOLE-BODY DUAL-ENERGY X- RAY ABSORPTIOMETRY STUDY

Muhammet Mustafa Kaşık¹, Elif Dilara Topcuoğlu¹, Ahmet Nedim Kahraman¹, Esin
Derin Çiçek¹

¹University of Health Sciences Fatih Sultan Mehmet Training and Research Hospital, Department of Radiology

Abstract: Purpose: To determine the relationship between T-scores derived from whole-body dual-energy X-ray absorptiometry (DEXA) and the presence of spondylolisthesis. Materials and Methods: In this single-centre study, patients who underwent whole-body DEXA scan with a prediagnosis of osteoporosis in our Radiology Clinic between September 2022 and August 2024, were retrospectively evaluated. The age, gender, body mass index (BMI) and T-score values of the patients were recorded. The study population consisted of patients who underwent computed tomography (CT) or magnetic resonance imaging (MRI) studies of the lumbar spine before or within two years after the whole-body DEXA scan. The images were evaluated for the presence of spondylolisthesis and spondylolysis. Patients with postoperative spinal changes and poor quality cross-sectional images were excluded. Student-t test and pearson correlation were used for statistical analysis. Results: A total of 363 whole-body DEXA scans were conducted, and 71 patients with lumbar spine cross-sectional imaging were evaluated. The study included 57 patients, comprising 47 women and 10 men, with a mean age of 61.3 ± 14.9 years, who met the inclusion criteria. Seven patients had spondylolisthesis, 10 patients had spondylolysis and six patients had both spondylolisthesis and spondylolysis. The results of the study demonstrated a statistically significant positive correlation between age and BMI ($p=0.027$) and a negative correlation between age and T-score ($p=0.029$). A statistically significant positive correlation was observed between BMI and T-score ($p = 0.001$). Although the mean T-score was -0,77 for the patients with spondylolisthesis, -1,17 for the patients with spondylolysis, -0,85 for the patients with both spondylolisthesis and spondylolysis and -0,22 for the patients without spondylolisthesis or spondylolysis, no statistically significant difference was observed between the groups with respect to T-score. Conclusion: The results of this study indicate that an increase in the prevalence of spondylolisthesis may be attributed to the presence of osteopenia and osteoporosis.

Figure1

Protokol No: 671748

Cinsiyet: Erkek

Doğum Tarihi: 15.04.1948

Muayene Tarihi: 10.11.2022

Boy: 154,0 cm

Kilo: 73,0 kg

DEĞERLENDİRME:

AP Spine L1-L4 bölgesinde ölçülen BMD değeri 1,803 g/cm², T-skoru -1,0 olup OSTEOPENİKTİR.

Femur Boyun bölgesinde ölçülen BMD değeri 0,881 g/cm², T-skoru -1,8 olup OSTEOPENİKTİR.

Femur Toplam bölgesinde ölçülen BMD değeri 0,502 g/cm², T-skoru -1,0 olup OSTEOPENİKTİR.

Bölge	Alan	Yaş	T-Skor	Z-Skor	BMD	BMC
AP Spine	L1-L4	74,5	-1,0	-0,2	1,002 g/cm²	47,06 g
Sol Femur	Boyun	74,5	-1,8	0,0	0,881 g/cm²	4,98 g
Sol Femur	Toplam	74,5	-1,0	0,4	0,502 g/cm²	33,22 g

World Health Organization (WHO) criteria for post-menopausal Caucasian Women

NORMAL: T-skoru ≥ -1 SD ve altı

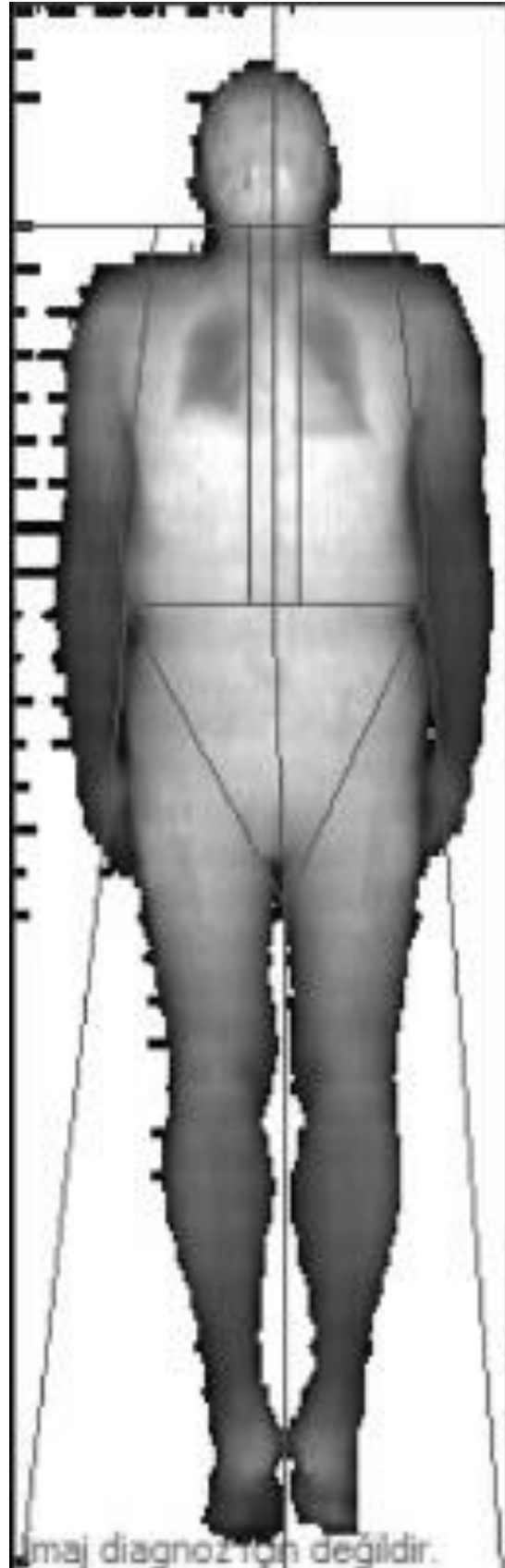
OSTEOPENİ: T-skoru -1 ve -2.5 SD arası

OSTEOPOROSİS: T-skoru < -2.5 SD ve altı

Sıydamında...

Whole-body dual-energy X-ray absorptiometry (DEXA) report of the 74 years old male patient with L4-5 spondylolisthesis

Figure2



Whole-body dual-energy X-ray absorptiometry (DEXA) image of the 74 years old male patient with L4-5 spondylolisthesis

Figure3



The sagittal lumbar CT image of a 74-year-old male patient with osteopenia reveals the presence of L4-5 spondylolisthesis.

Keywords: Osteoporosis, Spondylolisthesis, Dual-Energy X-Ray Absorptiometry

PANCREATIC NEUROENDOCRINE TUMORS: A STEPWISE APPROACH TO DIFFERENTIAL DIAGNOSIS.

Anna Simichanidou¹, Nikolaos Bouras¹, Ekaterini Xinou¹, Anna Paschali², Eleni Karoglou¹

¹Radiology Department, Theagenio Cancer Hospital, Thessaloniki, Greece

²Nuclear Medicine Department, Theagenio Cancer Hospital, Thessaloniki, Greece

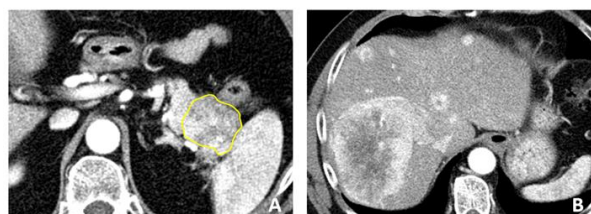
Abstract: Introduction: Pancreatic neuroendocrine neoplasms are rare tumors originating from neuroendocrine cells and consist of two major categories: well – differentiated pancreatic neuroendocrine tumors (pNETs) and poorly – differentiated pancreatic neuroendocrine carcinoma (pNEC). pNETs further exhibit three histological grades according to the degree of cellular proliferation. pNETs and pNEC are characterized by distinct biological behavior, treatment response and prognosis. Imaging plays an important role in differentiating low grade (grade 1 and 2) from high grade (grade 3) pNETs and pNEC, as well as in excluding potential mimickers. Hereby, we present a stepwise approach to differential diagnosis through key findings in multimodality imaging. Results: The location of the tumor is important, since pNETs appear more commonly in the body and tail, whereas pNEC in the head. The size of the lesion must be identified, as low grade pNETs usually measure less than 3cm. Well – differentiated pNETs typically have smooth, clear – cut margins and scarcely cause ductal obstruction, contrary to ill - defined pNECs. Furthermore, low grade tumors appear solid and homogeneous, while inhomogeneous tumors with necrosis, cystic degeneration, hemorrhage and calcification usually account for high grade tumors. Moreover, low grade pNETs typically appear hypervascular in the arterial phase and retain the enhancement in the portal phase. The more aggressive the tumor, the more atypical the enhancement pattern becomes, a general rule that also applies to liver and nodal metastases. Complementary, lower apparent diffusion coefficients in magnetic resonance imaging correspond to more aggressive tumors. Other pancreatic and extrapancreatic findings must be looked for, since 10% of pNETs occur in the setting of hereditary syndromes, such as multiple endocrine neoplasia. Lastly, the value of functional imaging is paramount, since different radiolabeled somatostatin analogues show variable affinity to tumors depending on grade and degree of differentiation. The aforementioned steps also help avoiding pitfalls and facilitate the differential diagnosis, which includes a variety of conditions, such as intrapancreatic splenules, gastrointestinal stromal tumors, hypervascular metastases and solid pseudopapillary epithelial neoplasms. Conclusion: A systematic approach is important to discriminate low from high grade pNETs and pNEC and exclude other pancreatic entities by implementing multiple imaging modalities.

Figure 1



A hyperenhancing small mass (<3cm maximum diameter) with smooth, well - defined borders is observed in the pancreatic head (arrow in A). The mass is not distinguishable from the rest of the pancreatic parenchyma in the portal phase (B), imaging characteristics indicative of a low - grade pancreatic NET.

Figure 2



In the pancreatic tail, a heterogeneous mass with hyperenhancing solid and hypoenhancing necrotic components and a maximum diameter about 5cm can be seen (yellow outline, A). Multiple metastases of various sizes are observed throughout the hepatic parenchyma, most of which with a hyperenhancing rim and a necrotic center (B). Both the primary and secondary sites show characteristics of a high grade pancreatic NET.

Keywords: arterial hyperenhancement, pNEC, pNET

INVESTIGATION OF THE EFFECT OF BODY COMPOSITION MEASUREMENTS DEFINED BY COMPUTED TOMOGRAPHY BEFORE TREATMENT ON DISEASE PROGNOSIS IN PATIENTS WITH METASTATIC COLON CANCER AND COMPARISON WITH OTHER CLINICOPATHOLOGICAL PROGNOSTIC PARAMETERS

İrfan Durmuş¹, Yeliz Aktürk¹, Ebru Çılıbrı¹

¹Ankara Etlik City Hospital

Abstract: Introduction: Sarcopenia is a condition that may occur during the cancer process is often associated with poor prognosis. Skeletal muscle mass area and index (SMA and SMI), total psoas index (TPI) which shows the amount of muscle quantitatively, Hounsfield unit average calculation (HUAC) and multifidus muscle/fat attenuation ratio (MMFAR), which are measurements related to muscle density can be calculated from Computed Tomography (CT) images. In addition, subcutaneous and visceral adipose tissue (SAT and VAT) areas can be calculated with CT. Neutrophil and platelet lymphocyte ratio (NLR and PLR) and prognostic nutritional index (PNI), which are indicators of inflammatory and nutritional status that may cause low muscle mass. The aim: The aim of our study is to show the effect of sarcopenia and body composition parameters on survival in patients diagnosed with metastatic colon cancer (mCC) and their relationship with biochemical values such as NLR, PLR and PNI. Materials and Methods: 173 mCC patients included in the study. SAT-VAT areas and MMFAR value were calculated at the umbilicus level. SMA, TPI and HUAC values were measured at the L3 vertebra level from the abdominal CT images obtained on the date of diagnosis of metastatic disease. According to the SMI cut-off values patients were divided into sarcopenic and non-sarcopenic patients. ROC analysis was performed to determine NLR, PLR and PNI cutoff values. Kaplan-Meier and Cox regression analyzes were performed to determine the effect of sarcopenia, NLR, PLR and PNI on survival. Correlation analyzes were performed to investigate the relationship between sarcopenia with biochemical and pathological data. Results: No significance was found between sarcopenia with PNI, NLR, PLR and other pathological parameters. In the survival analysis, OS were shorter in sarcopenic patients ($p=0.002$), in patients with $PNI \leq 41.5$, $NLR \geq 3.22$ and $PLR \geq 131.14$ ($p=0.001$, $p=0.001$ and $p=0.012$, respectively). In Cox regression analysis, sarcopenia, TPI, HUAC, PLR, PNI and NLR were significant in univariate analysis, while significance was detected for NLR ($p=0.007$) and PNI ($p=0.007$) in multivariate analysis. Conclusion: PNI and NLR are independent prognostic factors in patients with mCC. Sarcopenia, TPI, HUAC, PNI, NLR and PLR are among the parameters affecting survival in patients with mCC.

SAT and VAT measurements

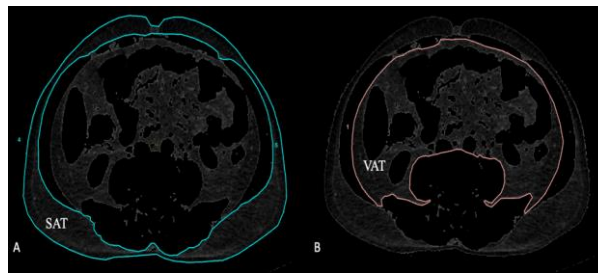


Figure 1. CT axial section image. After setting the density threshold values at the umbilicus level as -190 and -30 HU, the area between the light blue lines was measured for SAT (A) and the area limited by the pink line for VAT (B) was measured in cm².

SMA and Psoas Measurements



Figure 2. CT axial section image. (A) After the density threshold values were set as -30 and +110 HU at the L3 vertebra level the borders of the psoas, erector spinae, quadratus lumborum, transversus abdominis, external and internal oblique abdominal muscles and rectus abdominis were marked with a red line and the area was measured in cm². (B) After marking the borders of both psoas muscles with a blue line at the L3 vertebra level, the areas (cm²) and densities (HU) were recorded.

Multifidus Muscle Fat Attenuation Ratio Measurement

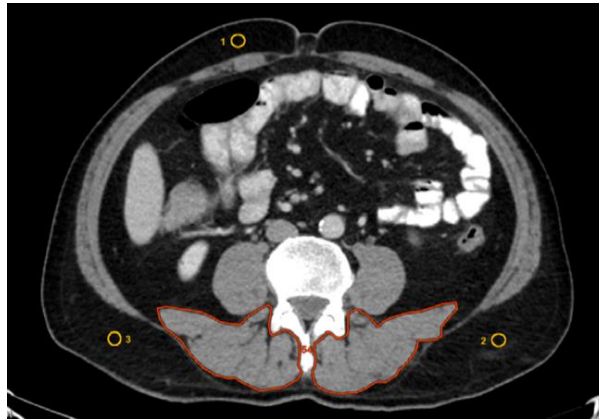


Figure 3. After the boundaries of the multifidus muscle were determined with a red line on both sides at the umbilicus level, muscle density values (HU) were measured. In addition, density values (HU) were measured from three different areas (orange circles) on the same section, within the subcutaneous fat tissue away from the vascular and muscle tissue.

Table 1. Kaplan-Meier Analysis

	n	Died	Alive	Survival Rate	Average Survival Time (Months)	95% Confidence Interval	p
						Lower and Upper Limit	
PNI (≤ 41.5)	59	48	11	18.6%	20.37 \pm 3.74	13.03-27.72	0.001**
PNI (> 41.5)	114	70	44	38.6%	40.88 \pm 4.94	31.18-50.58	
SARCOPENIA (+)	57	45	12	21.1%	21.75 \pm 3.06	15.74-27.75	0.002**
SARCOPENIA (-)	116	73	43	37.1%	42.25 \pm 5.66	31.14-53.35	
NLR (< 3.22)	94	54	40	42.6%	48.24 \pm 6.51	35.48-61.01	0.001**
NLR (≥ 3.22)	79	64	15	19.0%	19.71 \pm 2.33	15.14-24.29	
PLR (< 131.14)	58	31	27	46.6%	51.61 \pm 9.87	32.26-70.95	0.012*
PLR (≥ 131.14)	115	87	28	24.3%	27.09 \pm 2.58	22.02-32.16	

According to Kaplan-Meier analysis, significance was found between the survival rates of the patients in terms of PNI, Sarcopenia, NLR and PLR variables.

Table 2. Cox-Regression Analysis

Variable	Univariate Analysis		Multivariate Analysis	
	HR (95% Confidence Interval) Lower and Upper Limit	p	HR (95% Confidence Interval) Lower and Upper Limit	p
Metastasis Sites				
-Liver Metastasis (+)	1,734 (1,105-2,723)	0.017*	1.455 (0.919-2.302)	0.102
-Lung Metastasis (+)	0.998 (0.692-1.440)	0.993		
-Peritoneum Metastasis (+)	1.469 (0.967-2.231)	0.071		
-Central Nervous System Metastasis (+)	1.499 (0.608-3.693)	0.379		
Metastasis Stage				
-M1a	Reference	0.001**	Reference	0.006**
-M1b	2,273 (1,460-3,538)	0.001**	1,809 (1,126-2,905)	0.014**
-M1c	1,993 (1,239-3,204)	0.004**	1,691 (1,118-2,557)	0.013*
Tumor Histology				
-Other Subtypes	Reference			
-Adenocarcinoma	1.177 (0.531-2.196)	0.609		
Tumor Differentiation				
-Low	2.297 (0.969-5.446)	0.059		
-Moderate	1.490 (0.773-2.873)	0.234		
-Good	Reference	0.167		
NLR (≥ 3.22)	2,493 (1,712-3,630)	0.001**	1,776 (1,169-2,697)	0.007*
PLR (≥ 131.14)	1,667 (1,105-2,515)	0.015*	0.930 (0.574-1.506)	0.744
PNI (≤ 41.5)	2,114 (1,455-3,073)	0.001**	1,776 (1,169-2,697)	0.007**
SAT (cm²)	0.998 (0.996-1.000)	0.056		
VAT (cm²)	1,000 (0.997-1.002)	0.824		
SMA (cm²)	0.995 (0.990-1.000)	0.052		
TPI (cm²/m²)	1,162 (1,047-1,291)	0.005**	0.948 (0.836-1.075)	0.376
HUAC	1.059 (1.016-1.103)	0.006**	0.978 (0.938-1.020)	0.424
MMFAR	1.968 (0.679-5.704)	0.213		
Sarcopenia (+)	1,781 (1,223-2,595)	0.003**	1.101 (0.649-1.869)	0.721

In Cox regression analysis, sarcopenia, TPI, HUAC, PLR, PNI and NLR were significant in univariate analysis while significance was detected for NLR and PNI in multivariate analysis.

Table 3. The Relationship Between Sarcopenia and Other Datas

		Sarcopenia		p
		No (n=116)	Yes (n=57)	
Metastasis Sites	Liver	85 (73.3)	44 (77.2)	^b 0.578
	Lung	46 (39.7)	26 (45.6)	^b 0.455
	Peritoneum	39 (33.6)	12 (21.1)	^b 0.088
	Central Nervous System	2 (1.7)	3 (5.3)	^c 0.333
	Bone	2 (1.7)	1 (1.8)	^c 1,000
	Other Abdominal Organs	26 (22.4)	11 (19.3)	^b 0.483
Metastasis Stage	M1a	49 (42.2)	29 (50.9)	^b 0.275
	M1b	29 (25.0)	16 (28.1)	
	M1c	38 (32.8)	12 (21.1)	
Tumor Localization	Cecum	2 (1.7)	1 (1.8)	^c 1,000
	Right Colon	40 (34.5)	22 (38.6)	^b 0.596

	Left Colon	13 (11.2)	10 (17.5)	^b 0.249
	Sigmoid Colon	51 (44.0)	22 (38.6)	^b 0.502
	Transverse Colon	11 (9.5)	3 (5.3)	^c 0.393
Tumor Histology	Adenocarcinoma	102 (87.9)	54 (94.7)	^b 0.158
	Mucinous	10 (8.6)	1 (1.8)	
	Neuroendocrine	1 (0.9)	0 (0)	
	Signet Ring Cell	3 (2.6)	2 (3.5)	
Tumor Differentiation	Low	8 (7.8)	5 (9.3)	^c 0.511
	Moderate	84 (81.6)	40 (74.1)	
	Good	11 (10.7)	9 (16.7)	
KRAS	Mutant	34 (44.2)	16 (48.5)	^b 0.676
	Wild	43 (55.8)	17 (51.5)	
NRAS	Mutant	1 (1.3)	0 (0)	^c 1,000
	Wild	75 (98.7)	31 (100)	
BRAF	Mutant	1 (1.3)	1 (3.2)	^c 0.497
	Wild	75 (98.7)	30 (96.8)	
NLR	Mean±Sd	4.12±3.52	4.28±4.21	^d 0.730
	Median (Min-Max)	2.9 (0.7-20)	3.2 (0.5-24.1)	
PLR	Mean±Sd	200.28±136.58	227.93±181.27	^d 0.309
	Median (Min-Max)	163.4 (44.6-974.4)	192.6 (68.5-1041.3)	
CEA≥5	Yes	37 (31.9)	22 (38.6)	^b 0.382
	No	79 (68.1)	35 (61.4)	
PNI	Mean±Sd	46.21±8.17	43.86±7.67	^a 0.072
	Median (Min-Max)	46.6 (30-67.5)	44.5 (29-59.2)	
ECOG	Mean±Sd	0.69±0.88	1.12±1.07	^d 0.006**
	Median (Min-Max)	0 (0-4)	1 (0-4)	

There is no significant difference in NLR, PLR, CEA and PNI levels compared to sarcopenia. ECOG performance scores of those with sarcopenia were found to be statistically significantly higher.

Keywords: Metastatic Colon Cancer, Body Composition, Computed Tomography, Sarcopenia, Overall Survival

CORRELATION BETWEEN CT LIVER DENSITY (HU VALUES) AND LABORATORY VALUES IN HEPATOSTEATOSIS

Mesut Furkan Yazar¹, Şevket Kahraman², Hüseyin Aydemir², Mehmet Gündüz², Mecit Kantarcı², Sonay Aydın²

¹Bilecik Training and Research Hospital

²Erzincan Binali Yıldırım University

Abstract: Introduction In the presence of hepatosteatosi, liver parenchymal density values decrease according to the degree of steatosis, and abnormalities can be seen in liver function tests. Our aim with this study is to compare alanine transaminase (ALT), aspartate transaminase (AST), gamma glutamyl transferase (GGT), ALT/AST values between the group with hepatosteatosi and the group without hepatosteatosi. Methods Individuals whose liver function tests AST, ALT and GGT parameters were studied within a maximum of 24 hours with computed tomography (CT) scan were included in the study. Density measurements were made by manually drawing circular ROI from the liver segments 3, 4b, 5, 6 levels and the upper, middle and lower parts of the spleen on the nonenhanced computed tomography (NECT) images. Liver function tests are documented along with density measurements. Results: A total of 1028 individuals were included in the study. Individuals with liver density ≤ 40 HU mean AST 38.29 ± 14.85 , ALT 47.15 ± 19.92 , GGT 50.22 ± 28.79 , ALT/AST 1,29 values were found. Individuals with liver density > 40 HU mean AST 21.77 ± 8.26 , ALT 18.27 ± 8.74 , GGT 20.76 ± 13.65 , ALT/AST 0, 86 values were found. It was observed that the ALT values of individuals with a liver density value in the range of 60 to 80 (16.2 ± 7.12) were significantly lower than those of individuals with a liver density value of 40-60, 20-40 and 0-20 HU. In addition, it was observed that the liver density value increased significantly as the ALT value decreased ($p=0.001$). It was observed that the AST and GGT value tended to decrease significantly as the liver density value increased ($p=0.001$). Conclusion: The frequency of female gender and advanced age was found to be high in the hepatosteatosi group. It was determined that the right lobe of the liver was more fatty than the left lobe in the hepatosteatosi group. ALT, AST, GGT, ALT/AST mean values were found to decrease as the liver parenchyma density value goes from the lowest to the highest group.

Figure 1

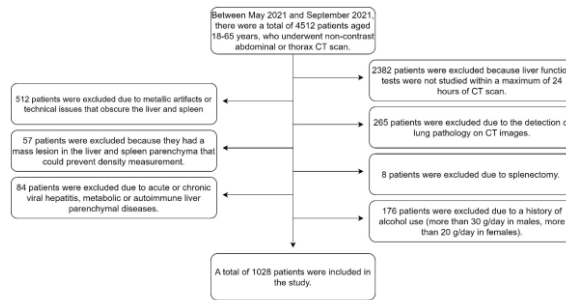
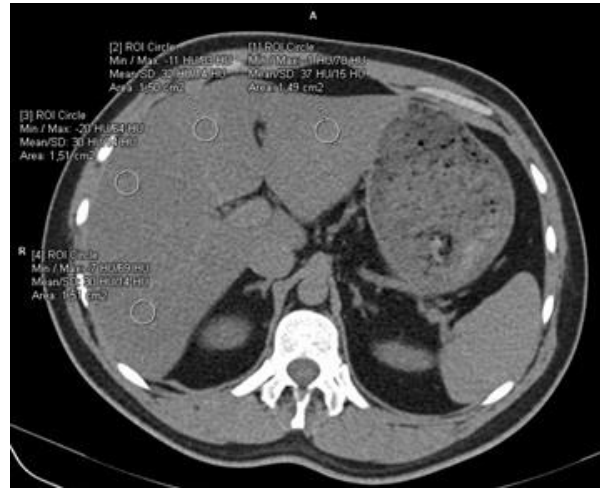


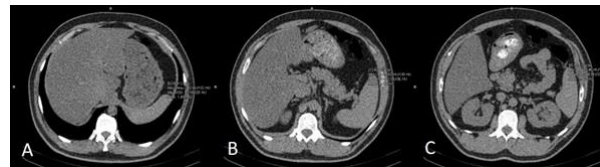
Diagram showing the study population

Figure 2



Density measurements of liver segments 6, 5, 4b, and 3 on the unenhanced CT axial image.

Figure 3



A. Density measurement from the upper 1/3 of the spleen in unenhanced CT axial image B. Density measurement from the hilum of the spleen in unenhanced CT axial image C. Density measurement from the lower 1/3 of the spleen in unenhanced CT axial image

Table 1

Variables (n=1028)	Median	mean \pm SD	minimum- maximum
Age	42	42,44 \pm 12,71	18-65
ALT	19	22,46 \pm 15,03	1-161
AST	22	24,16 \pm 11,13	3-113
GGT	19	25,03 \pm 19,66	1-212
ALT/AST ratio	0,87	0,92 \pm 0,38	0,06-3,32
Liver Density	57	53,72 \pm 13,71	2-79
Liver Density SD	27	28,49 \pm 11,08	8-88
Spleen Density	46	47,22 \pm 7,38	10-75
Spleen Density SD	25	27,34 \pm 10,86	8-70
Liver Density / Spleen Density	1	1,15 \pm 0,32	0-4
Liver Density - Spleen Density	10	6,49 \pm 13,5	-47-35
Gender n (%)			
Male	453 (44,1)		
Female	575 (55,9)		

Distribution of general and demographic characteristics

Table 2

Parameter	Liver Density \leq 40 HU (n=149)			Liver Density >40 HU (n=879)			t / χ^2	p
	median	mean \pm SD	min-max	median	mean \pm SS	min-max		
Age	48,00	46,86 \pm 10,27	22-65	41,00	41,69 \pm 12,93	18-65	5,46	0,001

Female/Male	82/67			371/508			8,50	0,004
ALT	44,00	47,15±19,92	15-161	17,00	18,27±8,74	1-70	17,41	0,001
AST	34,00	38,29±14,85	15-113	20,00	21,77±8,26	3-83	13,24	0,001
GGT	44,00	50,22±28,79	13-212	18,00	20,76±13,65	1-143	12,26	0,001
ALT/AST	1,24	1,29±0,47	0,44-3,32	0,83	0,86±0,33	0,06-2,29	10,83	0,001
Liver left lobe	30,5	27,91±9,67	2-43	59,5	59,21±7,46	41-80	45,21	0,001
Liver right lobe	27,5	25,18±9,87	1-41	57,5	57,43±7,96	37-78,5	44,07	0,001
Segment 3	31	28,35±9,72	3-43	60	59,62±7,66	40-82	44,17	0,001
Segment 4b	30	27,47±9,92	0-43	59	58,81±7,57	40-82	44,51	0,001
Segment 5	28	25,38±9,98	1-42	58	57,89±7,96	36-79	44,31	0,001
Segment 6	27	24,99±10,02	1-40	57	56,97±8,22	34-79	42,46	0,001

Comparison of fatty liver status (Liver Density ≤ 40 HU & Liver Density > 40 HU) in the general characteristics of the cases

Table 3

		Liver density																
		0-20			20-40			40-60			60-80							
		median	mean±SD	min-max	median	mean±SD	min-max	median	mean±SD	min-max	median	mean±SD	min-max	F / χ^2	p			
Age	48	^{bc}	47,12±10,36	26-65	47	^c	45,94±10,01	22-64	43	^{ab}	43,14±12,98	18-65	39	^a	39,59±12,57	18-65	13,10	0,001
Female/Male			17/16			65/51			221/228			150/210					8,79	0,032
ALT	51	^d	53,91±15,49	31-97	41	^c	45,22±20,67	15-161	18	^b	19,71±9,44	1-70	15	^a	16,2±7,12	1-44	312,1	0,001
AST	39	^c	41,18±12,85	23-76	33	^b	37,47±15,32	15-113	21	^a	22,42±8,14	3-60	19	^a	20,82±8,34	6-83	133	0,001
GGT	55	^c	57,03±24,88	19-125	41	^b	48,28±29,62	13-212	19	^a	22,69±15,26	3-143	16	^a	17,99±10,34	1-86	143,1	0,001
ALT/AST	1,33	^c	1,38±0,41	0,58-244	1,22	^b	1,27±0,48	0,44-3,32	0,87	^a	0,9±0,34	0,06-2,29	0,78	^a	0,8±0,3	0,08-1,79	71,36	0,001

Comparison of the general characteristics of the cases in liver density groups

Keywords: nonenhanced ct, fatty liver, liver function test, alanine transaminase

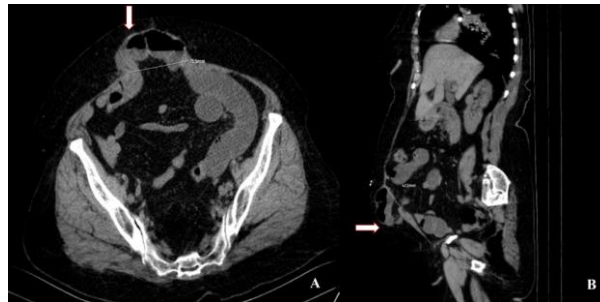
THE IMPACT OF DEFECT SIZE ON HERNIA SAC CONTENTS AND THE DEVELOPMENT OF ILEUS IN ABDOMINAL WALL HERNIAS

İsmail Furkan ŞİMŞEK¹, Hasan ERDOĞAN¹

¹Kayseri City Hospital

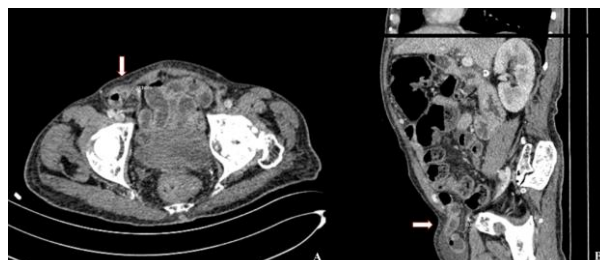
Abstract: Abdominal hernias are defined as the protrusion of intra-abdominal structures through a defect in the abdominal wall. While hernias are often asymptomatic, complications such as obstruction, strangulation, and incarceration may occur. In this study, we aimed to investigate the relationship between hernia defect size and the development of these complications. **Materials and Methods** The study retrospectively included contrast-enhanced and non-contrast abdominal CT images of 500 patients over the age of 18. Radius measurements were obtained from axial and sagittal images using two-dimensional diameter measurements, and defect area was calculated using the formula $r1 \times r2 \times \pi$. Statistical analyses were performed using SPSS version 22.0. ROC analysis was conducted to determine the cut-off value for defect area concerning the development of complications. **Results** Of the patients, 215 (43.3%) were female and 282 (56.7%) were male, with a mean age of 64.5 ± 14.6 years. 39 patients (7.8%) had ileus, while 458 (92.2%) did not. Inflammation within the hernia sac was observed in 158 patients (31.8). The mean defect area was $23.1 \pm 49.2 \text{ cm}^2$ in patients with ileus, compared to $8.5 \pm 21.7 \text{ cm}^2$ in those without. Incisional, parastomal, and paraumbilical hernias were the types most prone to ileus. Ileus occurred in 34.6% of incisional hernias, 28.6% of parastomal hernias, and 20% of paraumbilical hernias. The bowel loops most commonly herniated in patients with ileus were ileal (69.2%) and jejunal (12.8%) loops. Correlation analysis revealed a significant relationship between defect area and both ileus and inflammation. In the ROC analysis (Figure), the cut-off value for hernia defect area predicting ileus was determined to be 5.29 cm^2 , with a sensitivity of 69% and a specificity of 70%. **Conclusion:** No prior study in the literature has specifically investigated the impact of defect area on the development of complications. In this study, examining anterior abdominal wall defects, we found a significant correlation between defect area and the presence of ileus and inflammation. The risk of ileus and inflammation increases notably when the defect area exceeds the identified threshold. Therefore, considering the defect area in clinical practice may provide an opportunity for early intervention before complications arise.

Figure 1



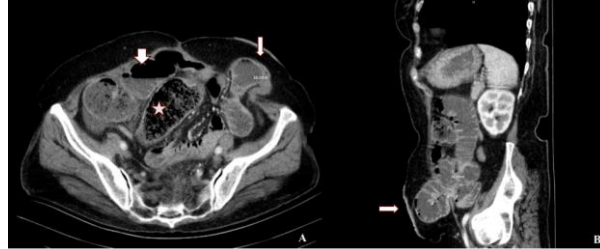
Axial (A) and sagittal (B) images of an umbilical hernia containing ileal loops along the midline of the anterior abdominal wall. At higher levels in the axial images, signs of ileus were more pronounced.

Figure 3



Axial (A) and sagittal (B) images of an indirect inguinal hernia containing ileal loops in the right inguinal region. In Image B, air-fluid levels are observed intermittently (curved arrows). At higher levels in the axial images, signs of ileus were more pronounced.

Figure 2



Axial (A) and sagittal (B) images of a paraostomal hernia containing jejunal loops on the left side of the anterior abdominal wall. In Image A, dilated bowel loops containing air-fluid levels consistent with ileus (bold arrow) and small bowel feces sign (asterisk) are observed.

Table 1

Hernia Type	Frequency	Percent
Indirect inguinal	197	39,6
Umblikal	132	26,6
Paraumblikal	48	9,7
Incisional	35	7
Direct inguinal	27	5,4
Spigelian	18	3,6
Epigastric	13	2,6
Paraostomal	9	1,8
Bochdalek	8	1,6
Femoral	4	0,8
Superior lumbal	3	0,6
Interparietal	2	0,4
Obturator	1	0,2

Abdominal hernia types detected in patients

Table 2

		Age	Ileus	Inflammation
--	--	-----	-------	--------------

Defect Surface Area	Pearson Correlation	-,022	0,156**	0,106*
	Pearson Correlation	0,630	0,000	0,018

Correlation analysis between defect area and other variables

Table 3

			Asymptomatic 95% Confidence Interval	
Area	Std. Error	Significant	Lower Bound	Upper Bound
0,745	0,038	0,000	0,671	0,81

Area under the curve values in calculating the hernia defect area cut-off value for ileus development using ROC analysis

Keywords: abdominal hernia, ileus, cut-off

ILEOCOLIC AND COLOCOLIC INTUSSUSCEPTION IN ADULTS: CT FEATURES AND PATHOLOGICAL CORRELATION

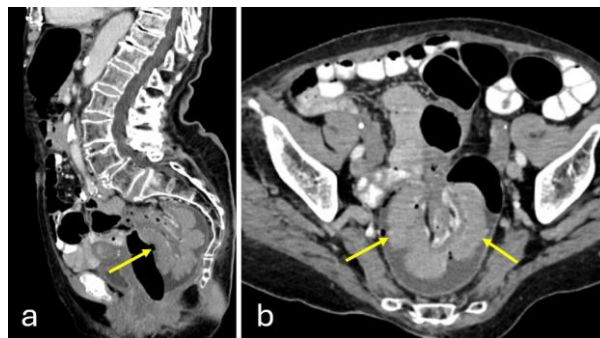
Olgun Şahin¹, Hilal Şahin²

¹*İzmir City Hospital, Department of Radiology, İzmir*

²*University of Health Sciences, İzmir Faculty of Medicine, Department of Radiology, İzmir*

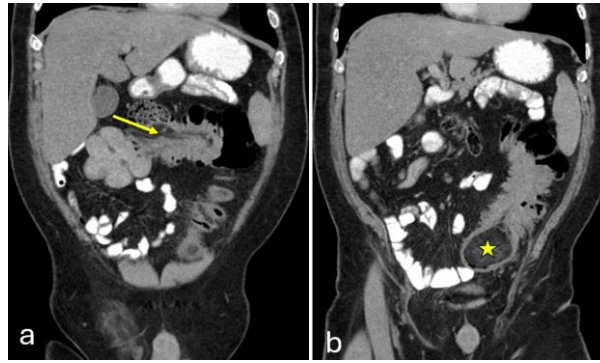
Abstract: Background: Intussusception is the condition in which a part of the intestine invaginates into its distal adjacent bowel segment. Intussusceptions involving the colon are less common contrary to small bowel intussusceptions. Nevertheless, they are rarely transient or idiopathic, and often require surgery due to underlying neoplastic etiology. The aim of this study was to investigate the relationship between CT features and pathology results in intussusceptions involving the colon. Methods: Institutional review board approval was obtained for this single center study. Abdominopelvic CT images of 106 patients who applied to our institution and diagnosed as intussusception between 2017 and 2024 were reviewed retrospectively. Patients with gastroduodenal (n=1), small bowel (n=71) or transient ileocecal (n=1) intussusception, and incorrect reporting (n=5) were excluded from the study. From CT images, the location, length and maximum diameter of the intussuscepted segment, presence of intraabdominal free fluid and presence of ileus were evaluated by two radiologists in consensus. Patient characteristics (age, sex), surgical procedure performed, tumor type and the presence of bowel wall ischemia were noted. For the statistical analysis, Fisher's exact test and Student's T test were performed to determine the relationship between location, length and diameter of the intussuscepted segment, and malignancy and ischemia. Results: In the final cohort, 28 patients (16 male, 12 female, mean age 59,5-years) with histopathological confirmation of ileocolic and colocolic intussusception was included. There were 11 (39%) ileocolic and 17 (61%) colocolic intussusceptions in the study. Only 5 patients had small bowel ileus. 23 patients had different procedures of colon resection whereas 5 patients had colon biopsy or polypectomy by colonoscopy. There was no significant relationship between the maximum diameter of the intussuscepted segment and bowel ischemia ($p>0.05$). However, the length of the intussuscepted segment was significantly related to ischemia ($p=0.02$). There was significant relationship between the malignant tumoral etiology and the distal colocolic intussusception involving descending and sigmoid colon ($p<0.01$). Conclusion: CT has an important role in determining the location of intussusception and associated features. Long segment involvement is related to bowel ischemia. Distal colocolic intussusception is more likely to occur due to malignant colon tumor.

Fig 1



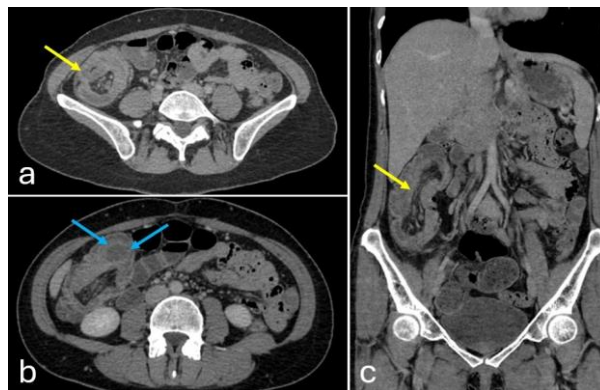
88-years-old woman with colocolic intussusception. Sagittal (a) and axial (b) CT images show a large polypoid lesion originating from distal sigmoid colon and invaginating into the upper rectal lumen. Pathology resulted as adenocarcinoma developing on villous adenoma.

Fig 2



49-years-old man with colocolic intussusception. Coronal reformatted images (a, b) show colocolic intussusception (arrow) starting from transverse colon and extending to the lumen of sigmoid colon. The etiology is consistent with a colonic submucosal lipoma which is seen as a fatty polypoid lesion at the distal part of the intussusception (star). Pathology proved the diagnosis with accompanying ischemic changes.

Fig 3



50- years-old woman with ileocolic intussusception. Axial (a, b) and coronal reformatted (c) CT images show invagination of ileal segment with its mesentery along ascending colon (yellow arrows). A low-density polypoid lesion is visible at the distal part of the intussuscepted segment (blue arrows). Pathology resulted as inflammatory fibroid polyp of the ileum.

Table 1

	Parameters	Right colic (n=18)	Left colic (n=10)	p value
Patient characteristics	Age (years)	53.9	69.8	0.028
	Male	11	5	0.697
	Female	7	5	
CT features	Length (mm)	94.9	50.5	0.002
	Diameter (mm)	58.8	58.5	0.955
Pathology	Benign	12	0	<0.001
	Malignant	6	10	

Ischemia	Present	4	0	0.265
	Absent	14	10	

Demographic data, radiological and pathological features of right colic and left colic intussusceptions according to the start point.

Keywords: Intussusception, Ileocolic, Colocolic, Computed Tomography, Malignancy

NORMAL LIVER STIFFNESS VALUES MEASURED WITH MR ELASTOGRAPHY AND 2-D SHEAR WAVE ELASTOGRAPHY IN CHILDREN (9-17 AGES)

Mehmet Seker¹, Mehmet Sait Dogan¹, Hayrettin Temel², Osman Kahraman¹, Fatma Zeynep Güngören¹, Mehmet Koçak³, Cengiz Erol¹

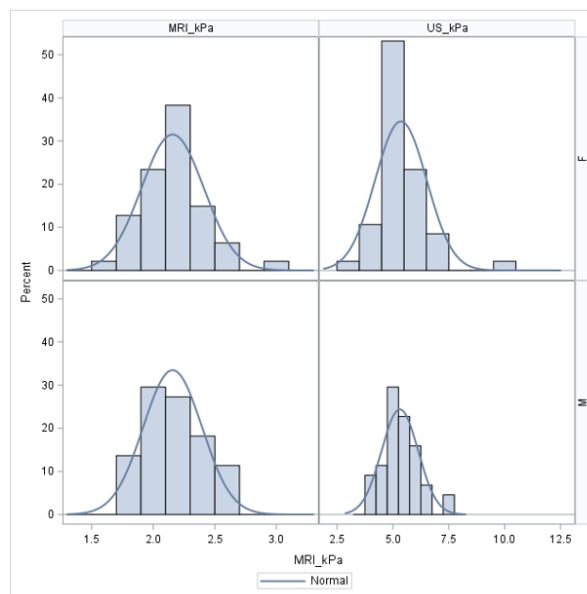
¹Istanbul Medipol University School of Medicine, Department of Radiology

²Istanbul Medipol University School of Medicine, Department of Pediatrics

³Istanbul Medipol University School of Medicine, Department of Biostatistics

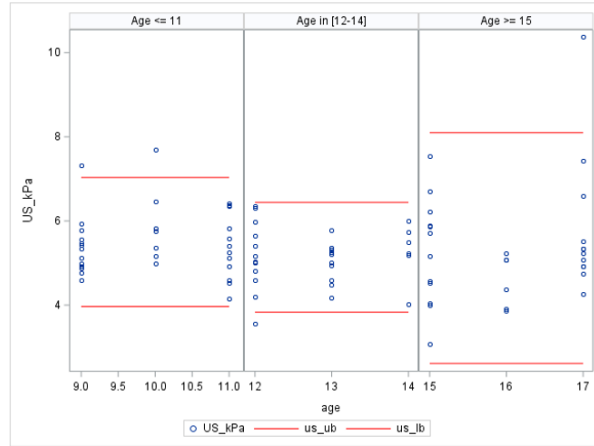
Abstract: Purpose: The aim of this study is to determine the range of normal liver stiffness values for magnetic resonance (MR) and ultrasound (US) elastography in healthy Turkish children aged 9-17 years. Materials and Methods: This was a prospective single-center cohort study. One hundred volunteers without a known history of liver disease were recruited between November 2022 and October 2023. Clinical examination, biochemical and serological analysis, MR, and US exams were performed on the same day. MRI scans obtained at one field strength (3.0 T) were analyzed. R2*, proton density fat fraction (PDFF), MRI stiffness values, and US elastography stiffness values were expressed as means. The age-specific normative ranges of the liver stiffness measures for both modalities were expressed as ± 1.96 standard deviation around the sample average. Comparison of the stiffness measures across age groups and by gender was done using Wilcoxon-Mann-Whitney or Kruskal-Wallis tests, and the correlation of stiffness measures with other continuous markers was measured by Spearman's Rank Correlation. Results: Ninety-one volunteers had complete data and no documented exclusion criteria. The overall mean liver stiffness values for MR and US elastography were 2.16 ± 0.24 kPa (95% normative lower and upper bounds: 1.69-2.63 kPa) and 5.34 ± 1.00 kPa (95% normative lower and upper bounds: 3.38-7.30 kPa) respectively. There was no significant difference between age groups 9-11, 12-14, and 14-17 in terms of liver stiffness regardless of imaging modality. There was a negative correlation between body mass index and liver stiffness values obtained from both MR and US elastography exams ($p = -0.28$, $p = 0.0082$ and $p = -0.22$, $p = 0.039$ respectively.) The mean liver stiffness values did not significantly correlate with age, height, gender, R2*, and PDFF. Conclusion: Mean liver stiffness values and normative ranges were defined by MR and US elastography in children. Liver stiffness was shown to be independent of age and gender. * This study was funded under the "1002-A Rapid Support Program (Project Number: 222S019)" which is conducted by the Scientific and Technological Research Council of Turkey (TÜBİTAK).

Liver Stiffness Values by gender



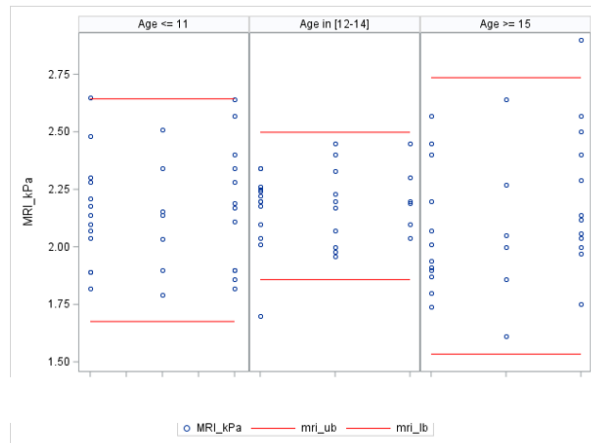
Distribution of liver stiffness values in MRI (MRI_kPa) and ultrasound (US_kPa) by gender (F: female, M: male)

US Stiffness Measurements



US stiffness (US_kPa) by age groups, the upper limit of normal (us_ub), and lower limit of normal (us_lb) are shown in the scatter plot.

MRI Stiffness Measurements



MRI stiffness (MRI_kPa) by age groups, the upper limit of normal (mri_ub), and lower limit of normal (mri_lb) are shown in the scatter plot.

Liver Stiffness Values by Gender

		Case	Minimum	Median	Maximum	Mean	Standard deviation
MR elastography (kPa, p=0.91)	F	47	1.61	2.17	2.90	2.16	0.25
	M	44	1.70	2.15	2.65	2.16	0.24
US elastography (kPa, p=0.85)	F	47	3.07	5.17	10.38	5.36	1.15
	M	44	3.86	5.25	7.70	5.31	0.82

Liver MR-US elastography stiffness values by gender (F: female, M: male)

Liver Stiffness Values by Age Groups

		Case	Mean	Standart deviation	Lower limit of normal	Upper limit of normal
MR_elastography kPa, p=0.46)	Total case	91	2.16	0.24	1.69	2.63
	9-11 age	32	2.16	0.25	1.67	2.65
	12-14 age	29	2.18	0.16	1.87	2.49
	15-17 age	30	2.13	0.31	1.52	2.74
US elastography (kPa, p=0.28)	Total case	91	5.34	1.00	3.38	7.30
	9-11 age	32	5.50	0.78	3.97	7.03
	12-14 age	29	5.14	0.67	3.83	6.45
	15-17 age	30	5.36	1.40	2.62	8.10

Normal liver stiffness values with a 95% confidence interval by age groups

Keywords: normal healthy subjects, liver stiffness measurement, ultrasound elastography, magnetic resonance elastography

GD-EOB-DTPA-ENHANCED MRI WITH T1 MAPPING VERSUS FIBROSIS-4 INDEX FOR STAGING LIVER FIBROSIS

Esin Cibirolu¹, Fatma Kulali¹

¹University of Health Sciences, Umraniye Training and Research Hospital, Department of Radiology

Abstract: Purpose: The staging of liver fibrosis is important for treatment planning in chronic liver disease. In cirrhosis the deposition of collagen fibers in the extracellular space can cause the longer T1 relaxation time. T1 reduction rate was decreased in liver fibrosis. Therefore, we aimed to investigate the relationship between T1 reduction rate and fibrosis-4 index for evaluation and staging of liver fibrosis. Methods: This retrospective study was approved by the institutional ethics committee, and informed consent was waived. The consecutive 84 patients [51 men, 33 women with a mean age of 56±10 years (range 29-76 years)] with chronic liver disease who underwent Gd-EOB-DTPA-enhanced magnetic resonance imaging (MRI) with T1 mapping during a retrospective two years period were included in our study. T1 mapping images were evaluated by two radiologists separately. T1 reduction rate and fibrosis-4 index were estimated. The patients were classified into three groups according to fibrosis-4 index (<1.5, 1.5-3.5, >3.5). The statistical relationship between T1 reduction rate and fibrosis-4 index was analyzed. Results: A total of 84 Gd-EOB-DTPA-enhanced MRI examinations with T1 mapping were reviewed. There were 26, 26, and 32 patients in low-risk (fibrosis-4 index <1.5), moderate risk (fibrosis-4 index 1.5-3.5), and high-risk (fibrosis-4 index >3.5) groups, respectively. The relationship between T1 reduction rate and fibrosis-4 score was found statistically significant ($p < 0.0001$). Patients with lower T1 reduction rate had higher fibrosis-4 index. In comparison of three groups, T1 reduction rate was also correlated ($p < 0.0001$). There was a strong correlation between measurements of two radiologists ($r^2 = 0.87$, $p < 0.0001$). Conclusion: T1 reduction rate which indicates liver function correlates with fibrosis-4 index. The categorization of liver fibrosis as low, moderate and high-risk groups is possible with Gd-EOB-DTPA-enhanced MRI with T1 mapping.

Figure 1

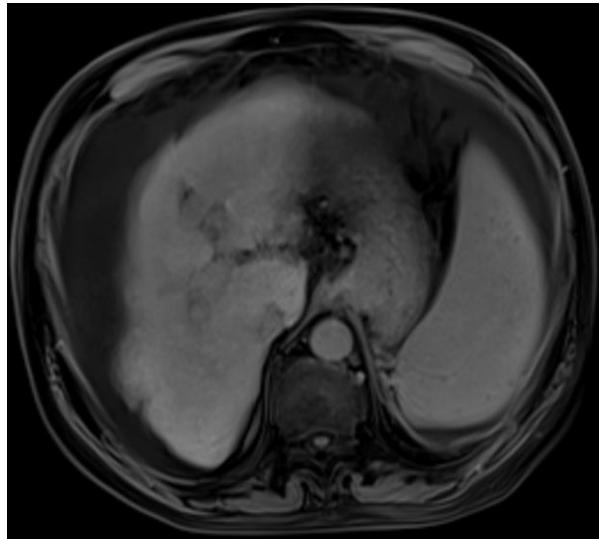


Figure 1: Gd-EOB-DTPA-enhanced T1 3D VIBE image at hepatobiliary phase in 59-year-old male patient with high fibrosis-4 index

Figure 2

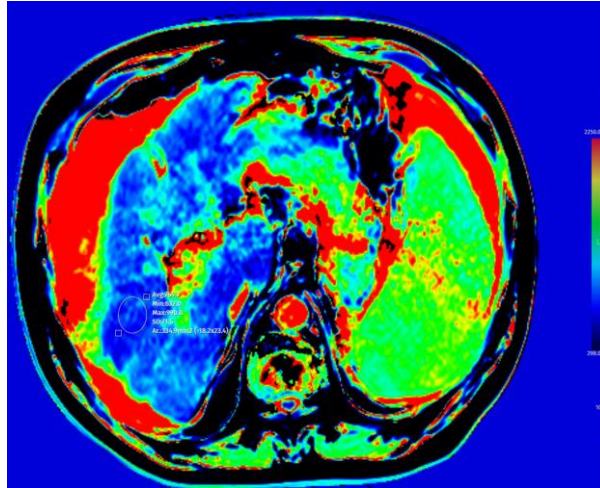


Figure 2: The measurement of ROI in the right lobe of liver at axial pre-contrast T1 mapping image

Figure 3

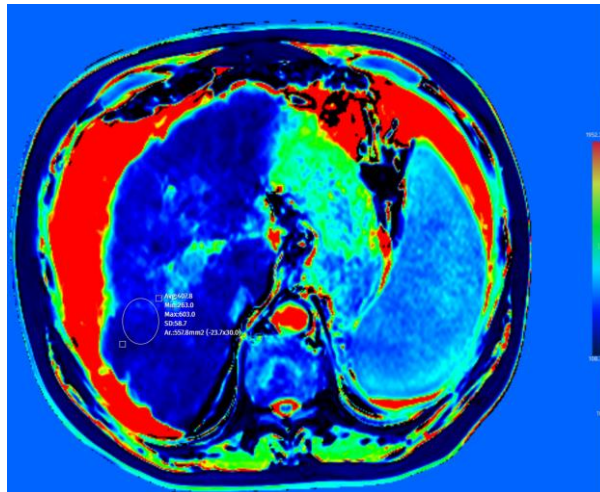


Figure 3: The measurement of ROI in the right lobe of liver at Gd-EOB-DTPA-enhanced T1 mapping image

Keywords: fibrosis-4 index, liver fibrosis, T1 mapping, magnetic resonance imaging, Gd-EOB-DTPA

COMPARATIVE DIAGNOSTIC PERFORMANCE OF TWO ABBREVIATED MRI PROTOCOLS FOR HEPATOCELLULAR CARCINOMA

Sezer Nil YILMAZER ZORLU¹, Ruhi Erdem ERGÜDEN¹, Diğdem KURU ÖZ¹,
Ayşe ERDEN¹

¹Ankara University Faculty of Medicine, Department of Radiology

Abstract: Introduction-Objective: Magnetic resonance imaging (MRI) screening for hepatocellular carcinoma (HCC) in high-risk populations, despite its cost and time commitment, may be a preferable option for select patient groups. The aim of this retrospective study was to evaluate the diagnostic performance of two different abbreviated MRI (abMRI) protocols derived from gadoxetate-enhanced MRI for HCC screening in patients with chronic liver disease. Material-Methods: This retrospective study included consecutive gadoxetate-enhanced liver MRI examinations performed at a single institution over a one-year period. Lesions were categorized using LI-RADSv2018 by an experienced abdominal radiologist and grouped as “benign” (LI-RADS 1-3) or “malignant” (LI-RADS 4-5, M). Two abMRI protocols were evaluated: non-contrast abMRI (NC-abMRI), consisted of axial T2-weighted and diffusion-weighted imaging and hepatobiliary phase abMRI (HB-abMRI), included the precontrast sequences of the NC-abMRI protocol, as well as a hepatobiliary phase obtained at 20 minutes after gadoxetate administration. Two independent, blinded radiologists reviewed the two abMRI sets and categorized patients into four groups based on established criteria; “no lesion”, “benign lesion”, “indeterminate lesion” and “malignant lesion”. The first two groups were also categorized under “routine follow-up”, while the latter two were categorized under “further investigation needed” (figure 1-3). Interobserver agreement measured using Cohen’s κ and the diagnostic performance of the two different abMRI protocols were investigated using the McNemar test. Results: The study included 183 patients (M/F: 134/89; mean age: 60 \pm 10 years) with chronic liver disease. Based on the reference standard, a total of 56 malignant and 68 benign lesions were detected in 84 patients, while no lesions were detected in 99 patients. A per-lesion analysis was conducted to calculate the sensitivities and specificities of the abMRI protocols for each reader (Table 1). The inter-reader agreement for both NC-abMRI and HB-abMRI was excellent in patients who required further assessment and those who did not ($\kappa = 0.85$ and $\kappa = 0.95$ respectively). Conclusion: AbMRI protocols may serve as an acceptable, cost-effective alternative to both ultrasound and standard dynamic contrast-enhanced MRI for the surveillance of HCC. To validate these findings and thoroughly assess the comparative cost-benefit ratio of AbMRI versus ultrasound, a multicenter prospective trial is necessary.

Figure 1

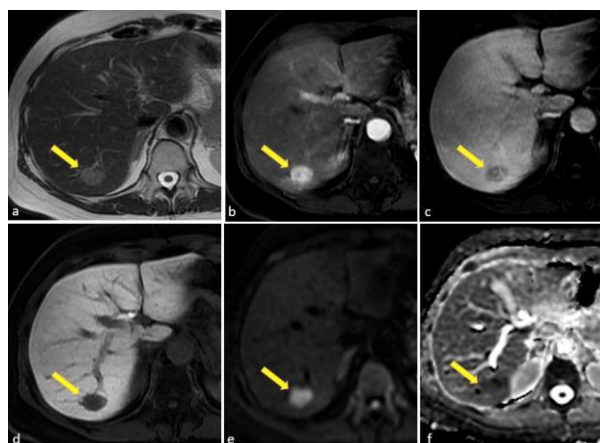


Figure 1: Magnetic resonance imaging (MRI) of a 62-year-old female patient, demonstrating a LI-RADS 5 lesion in segment 7. (a) T2-weighted image demonstrates intermediate signal intensity. (b) Arterial phase reveals hyperenhancement. (c) Venous phase shows washout. (d) Hepatobiliary phase exhibits hypointense signal intensity. (e-f) Diffusion-weighted imaging (DWI) demonstrates restricted diffusion. This lesion is classified as malignant according to both the abbreviated non-contrast MRI (NC-abMRI) and the abbreviated hepatobiliary phase MRI (HB-abMRI) protocols.

Figure 2

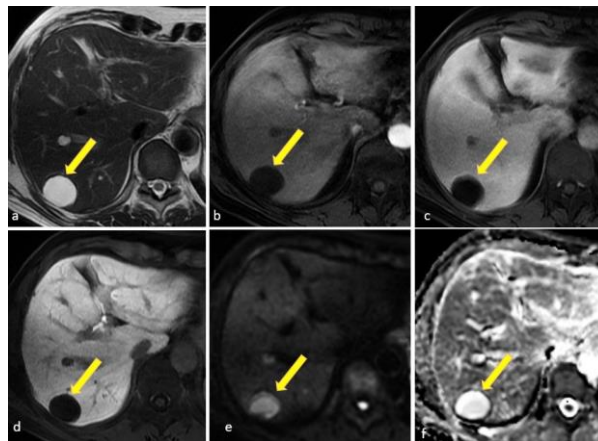


Figure 2: MRI of a 54-year-old male patient with chronic hepatitis B virus infection, demonstrating a 3 cm lesion in segment 7. (a) T2-weighted image shows markedly hyperintense signal. (b-c) Post-contrast arterial and venous phases reveal no enhancement. (d) Hepatobiliary phase exhibits no enhancement. (e-f) DWI demonstrates no restricted diffusion. This lesion was evaluated as a simple cyst based on a complete gadoxetate-enhanced dynamic liver MRI and categorized as LI-RADS 1. The lesion was classified as benign according to both abbreviated non-contrast MRI (NC-abMRI) and the abbreviated hepatobiliary phase MRI (HB-abMRI) protocols.

Figure 3

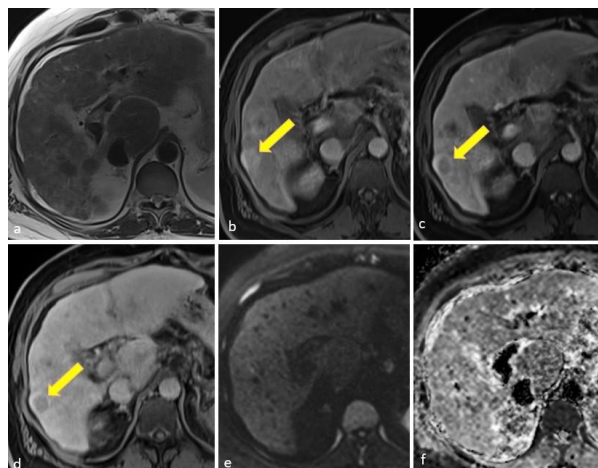


Figure 3: MRI of a 55-year-old male patient demonstrating a 24 mm LI-RADS 5 lesion in segment 6. (a) T2-weighted image demonstrates isointense signal. (b) Arterial phase reveals enhancement. (c) Venous phase shows washout. (d) Hepatobiliary phase exhibits hypointense signal. This lesion was identified in a complete gadoxetate-enhanced dynamic liver MRI examination. Abbreviated non-contrast MRI (NC-abMRI) protocol: The lesion was indistinguishable from surrounding parenchyma on T2-weighted and DWI and classified as ‘routine follow-up’. Abbreviated hepatobiliary phase MRI (HB-abMRI) protocol: The lesion was classified as ‘further investigation needed’ due to hypointensity on hepatobiliary phase imaging.

Table 1

	Reader 1	Reader 1	Reader 2	Reader 2
	NC-abMRI	HB-abMRI	NC-abMRI	HB-abMRI
Sensitivity	82,5 %	93,8 %	81,3 %	93,8 %

	(CI: 72,7-89,3 %)	(CI: 86,2-97,3 %)	(CI: 71,3-88,3 %)	(CI: 86,2-97,3 %)
Specificity	94,4 % (CI: 89,3-97,1 %)	95,1 % (CI: 90,2-97,6 %)	88,8 % (CI: 82,6-93 %)	91,6 % (CI: 85,9-95,1 %)
Positive predictive value	89,2 % (CI: 80,1-94,4 %)	91,5 % (CI: 83,4-95,8 %)	80,2 % (CI: 70,3-87,5 %)	86,2 % (CI: 77,4-91,9)
Negative predictive value	90,6% (CI: 84,8-94,3 %)	96,5 % (CI: 92-98,5 %)	89,4 % (CI: 83,3-93,5 %)	96,3 % (CI: 91,7- 98,4)

Table 1: Per-lesion diagnostic performance of each reader for abbreviated MRI protocols

Keywords: hepatocellular carcinoma, magnetic resonance imaging, chronic liver disease

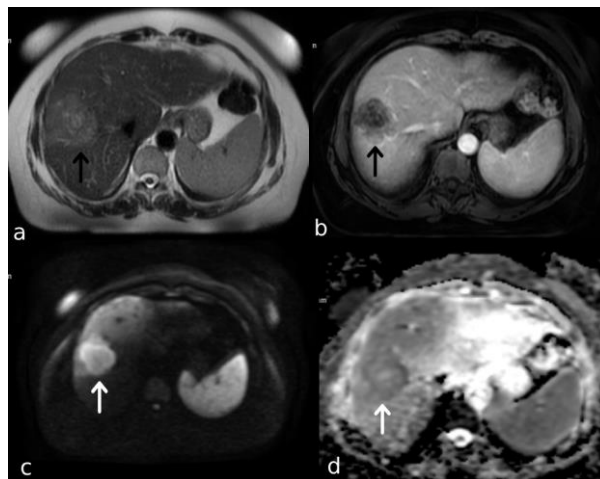
EVALUATING THE POTENTIAL OF ABBREVIATED MRI PROTOCOLS FOR LIVER METASTASIS DETECTION: A STUDY IN COLORECTAL CANCER PATIENTS

Sevde Nur Emir¹, Safiye Sanem Dereli Bulut¹

¹University of Health Sciences, Umraniye Training and Research Hospital

Abstract: Objective: To evaluate the diagnostic accuracy of different abbreviated MRI (AMRI) protocols consisting of dynamic enhanced+T2W and DWI+T2W for the detection and characterization of liver metastases in a patient group with known colorectal cancer. Methods: A total of 197 hepatic lesions were retrospectively analyzed across three different MRI sets: AMRI-1 (dynamic enhanced + T2W), AMRI-2 (DWI+T2W), and a standard MRI protocol. The patient cohort included 100 individuals (63 males, 37 females) with a mean age of 62.6 years (SD: 11.1 years). Lesion characterization was categorized as benign, malignant, or undeterminate based on histopathology, PET-CT and imaging follow-up. Sensitivity, specificity, and area under the receiver operating characteristic curve (AUC) were calculated for each MRI set. Results: The standard MRI protocol identified 197 liver lesions (175 metastatic, 18 benign, and 4 undeterminate); 142 lesions (72.1%) were larger than 10 mm, with the majority being metastatic (140/142). Among the 55 lesions ≤ 10 mm, most were also metastatic (35/55). Reader 1 identified 195 lesions using the AMRI-1 protocol (175 metastatic, 15 benign, and 5 indeterminate), with 5 lesions representing partial volume artifacts (false positives). The sensitivity per lesion was 89.7% (95% CI: 0.85–0.93). Reader 2 identified 183 lesions using the AMRI-2 protocol (169 metastatic, 6 benign, and 8 indeterminate), with 8 lesions representing partial volume artifacts (false positives). The sensitivity per lesion was 92.3% (95% CI: 0.88–0.95). After excluding indeterminate lesions, missed lesions, and false positives, the AUC for characterizing detected liver lesions was 91.0% (95% CI: 0.75–0.98) for Reader 1 (n = 190) and 93.5% (95% CI: 0.85–0.98) for Reader 2 (n = 183) using the AMRI protocols. The standard MRI protocol's AUC was 96.8% (95% CI: 0.90–1.00). No statistically significant difference was found in sensitivity between the AMRI-1 and AMRI-2 and standard MRI protocols ($p > 0.05$). Conclusion: The standard MRI protocol demonstrated the highest sensitivity and specificity for detecting and characterizing liver metastases. However, differences between the protocols were not statistically significant. Abbreviated MRI protocols incorporating dynamic and diffusion-weighted imaging could serve as effective alternatives for routine clinical practice.

59-year-old male with metastatic colorectal cancer.



a. Axial T2W sequence shows a hyperintense lesion in the liver right lobe anterior segment (black arrow). b. Axial T1W contrast-enhanced image shows hypointense lesion with peripheral contrast enhancement (black arrow). c. Axial DWI (b = 800) d. ADC map image shows diffusion restriction (white arrow), both readers characterized this lesion as malignant

Keywords: Liver, Colorectal neoplasms, Magnetic resonance imaging

QUANTITATIVE EVALUATION OF LIVER STEATOSIS USING ULTRASOUND ATTENUATION IMAGING: A COMPARISON WITH MRI

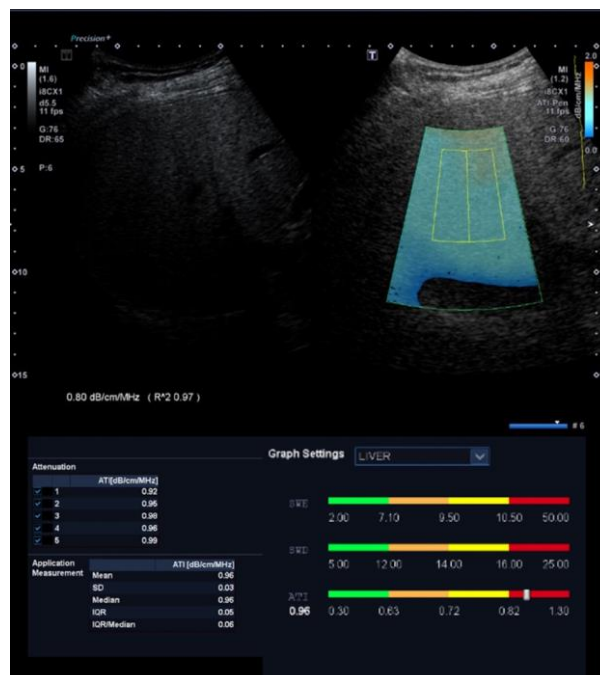
Celal Caner Ercan¹, Edanur Karapınar¹, Asli Ciftcibasi Ormeci², Mesut Bulakci¹

¹Istanbul University, Medical Faculty of Istanbul, Department of Radiology

²Istanbul University, Medical Faculty of Istanbul, Department of Gastroenterology

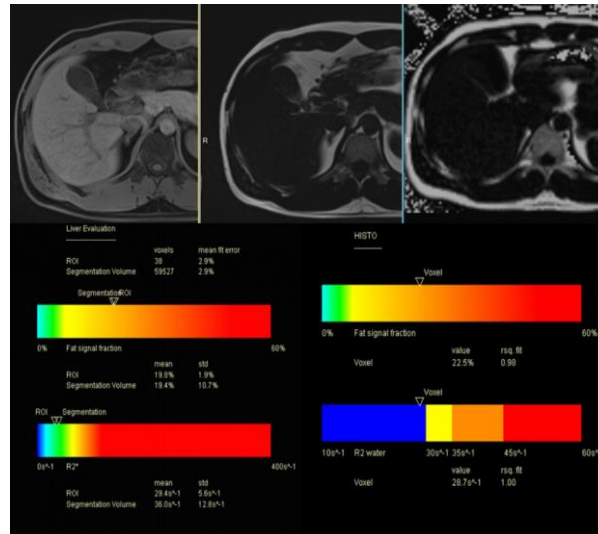
Abstract: Introduction: Fatty liver disease, characterized by fat accumulation exceeding 5-10% of liver weight, is increasingly common in both adults and children. Proton density fat fraction MRI (MRI-PDFF), a quantitative liver fat measurement technique, shows strong correlation with histopathology. This study compares ultrasound attenuation imaging (ATI), which quantifies steatosis by measuring the attenuation coefficient in liver tissue, with MRI-PDFF, the gold standard in quantitative imaging. Materials and methods: The study included 257 patients who underwent both ATI and MR-PDFF. Fatty liver was categorized into mild (S1, $\geq 5.2\%$ steatosis), moderate (S2, $\geq 11.3\%$ steatosis), and severe (S3, $\geq 17.1\%$ steatosis) based on MRI-proton density fat fraction. Ultrasound assessments were independently performed by two radiologists, each blinded to both the MRI findings and each other's evaluations. Results: Steatosis was absent in 116 (45.1%) cases, while MRI-proton density fat fraction identified S1 steatosis in 60 patients (23.3%), S2 in 40 patients (15.6%), and S3 in 41 patients (16%). There was a strong correlation between the attenuation coefficient and MRI-PDFF ($r=0.88$, 95% CI 0.85-0.90). ROC analysis of ATI for hepatic steatosis yielded AUC values of 0.967, 0.965, and 0.953 for detecting any steatosis ($S>0$), mild or greater steatosis ($S>1$), and moderate or greater steatosis ($S>2$), respectively. The corresponding cut-off values were 0.67, 0.74, and 0.85 dB/cm/MHz. The correlation between the two operators, calculated using a two-way mixed-effects intraclass correlation coefficient, was 0.91 (95% CI 0.89–0.93), indicating a strong correlation. The inter-operator correlation was assessed using the intraclass correlation coefficient (ICC), which was calculated to be 0.91 (95% CI 0.89–0.94;). Discussion: This study highlights attenuation imaging as a reliable and promising method for detecting and staging fatty liver disease. We found a strong correlation between attenuation coefficient values and MRI-proton density fat fraction. ROC analysis showed high diagnostic accuracy for differentiating between steatosis grades. The strong agreement between observers and consistent results over repeated tests are highlighting the method's reliability and potential for effectively monitoring hepatic steatosis. Conclusion: Attenuation imaging shows potential as a reliable tool for the quantitative assessment of hepatic steatosis.

Ultrasound Attenuation Imaging



An oblique ultrasound image obtained from the right intercostal approach shows increased liver echogenicity with an AC value of 0.80 dB/cm/MHz.

MRI-PDFF acquisition



A MRI-PDFF acquisition shows increased liver steatosis.

Ultrasound Attenuation Values

	Total patients	Mean	Median	Minimum	Maximum
1. Operator	257	0.70	0.69	0.43	1.1
2. Operator	257	0.69	0.68	0.46	1.05
Test-Retest Group	49	0.75	0.73	.049	0.98

Table of measurements for each operator and the test-retest group

Keywords: fatty liver disease, quantification of liver fat, ultrasound attenuation imaging, proton density fat fraction MRI

NORMATIVE CHOROIDAL PLEXUS APPARENT DIFFUSION COEFFICIENT VALUES IN THE PEDIATRIC POPULATION

Nurullah Dağ², Abdi Gürhan¹, Sevgi Demiröz Taşolar², Mehmet Öztürk¹

¹Selcuk University, Faculty of Medicine, Department of Radiology, Division of Pediatric Radiology

²Inonu University, Faculty of Medicine, Department of Radiology

Abstract: Background and aim: The choroid plexus (CP) is crucial for cerebrospinal fluid (CSF) production and central nervous system (CNS) function. This study aimed to determine normal apparent diffusion coefficient (ADC) values of the CP on diffusion-weighted magnetic resonance imaging (DW-MRI) in the pediatric population and investigate potential variations by age and gender. Materials and methods: This retrospective study included 600 pediatric patients (0-18 years) who underwent brain DW-MRI between January 2020 and July 2024. Patients with intracranial pathologies, surgical history, or systemic diseases were excluded. The population was divided into six age groups. ADC measurements were obtained using a 2-3 mm diameter circular region of interest (ROI). Result: The mean age was 60.1 ± 64.7 (1-214) months, with 296 females and 304 males. The mean CP ADC was $1694 \pm 321.8 \times 10^{-6}$ mm²/sec (701-2422). Overall CP ADC values did not differ significantly by gender ($p > 0.05$), except in the 36-72 month group where males had significantly higher values ($p < 0.01$). A strong negative correlation was observed between ADC values and age ($r: -0.686$, $p < 0.001$). ADC values were significantly different in the 5th and 6th age groups compared to others ($p < 0.001$). Mean ADC values for patients under and over 6 years were $1829 \pm 211 \times 10^{-6}$ mm²/sec and $1391 \pm 321 \times 10^{-6}$ mm²/sec, respectively, showing a significant difference ($p < 0.001$). Simple linear regression analysis revealed that 47% of CP ADC values were associated with age ($R^2: 0.470$). Conclusion: This study presents normal CP ADC values in the pediatric age group. Higher CP ADC values observed in children under 6 years likely reflect incomplete cellular maturation and increased water molecule mobility. As CP cellular maturation completes, water molecule movement decreases, resulting in lower ADC values. This hypothesis requires confirmation through future studies incorporating histological data.

Figure 1

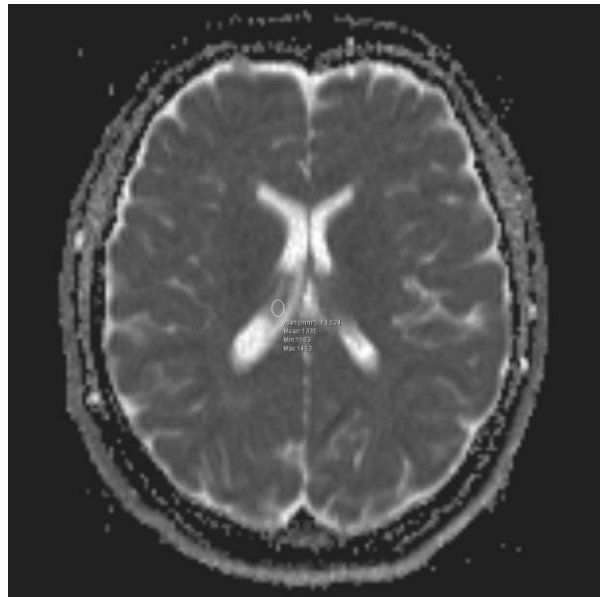


Figure 1: Signal measurement from right choroid plexus with an ellipsoid ROI of 3 mm diameter is shown.

Figure 2

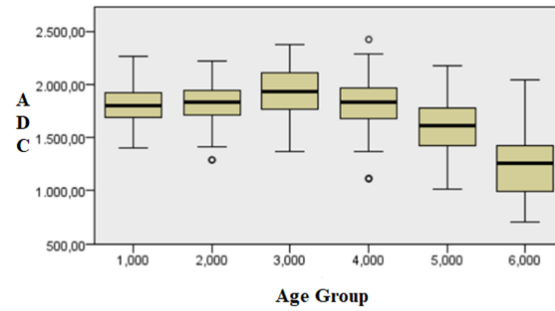


Figure 2. ADC values according to age groups.

Figure 3

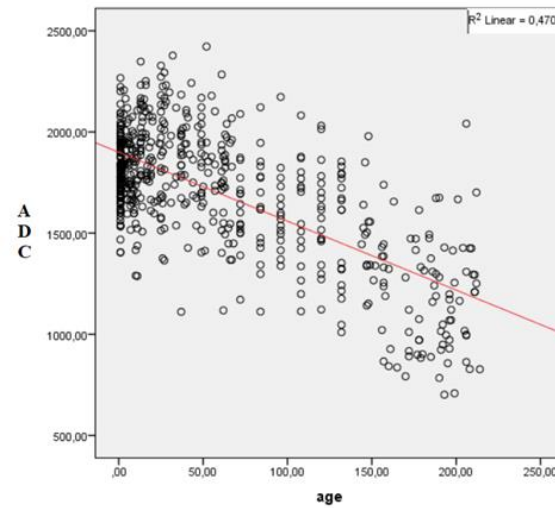


Figure 3. There was a strong negative correlation between ADC and age, and ADC values decreased as age increased. Choroid plexus ADC values were 47% related to age.

Table 1

n=600	mean±SD	min-max	median	interquartile range
Age (months)	60.1±64.7	1-214	34	6-108
ADC	1694±321.8	701-2422	1750	1518-1918

Age and ADC data of the study population

Table 2

Group	Age Range	Age	n	ADC	p
1	0-30 days	8.3±5.8 (1-29)	100	1806.0±161.2 x10 ⁻⁶ mm ² /sec (1404-2267)	p<0.001*
2	1-12 months	5.9±3.1 (1-11)	100	1814.9±179.2 x10 ⁻⁶ mm ² /sec (1288-2223)	
3	12-36 months	20.8±6.2 (13-34)	100	1917.4±226.1 x10 ⁻⁶ mm ² /sec (1365-2378)	

4	36-72 months	51.4±10.2 (37-68)	100	1807.5±239.5 x10 ⁻⁶ mm ² /sec (1111-2422)	
5	6-11 years	8.5±1.8 (6-11)	100	1588.0±248.6 x10 ⁻⁶ mm ² /sec (1010-2173)	
6	12-18 years	14.9±1.7 (12-17)	100	1232.9±286.3 x10 ⁻⁶ mm ² /sec (701-2041)	

ADC values according to age groups and comparison of ADC values between groups.

Keywords: Pediatric neuroradiology, Choroid plexus, Apparent Diffusion Coefficient

NEUROPSYCHIATRIC LUPUS OR MULTIPLE SCLEROSIS? DIFFERENTIAL DIAGNOSIS USING MYELIN CONTENT INDICES OF NORMAL APPEARING WHITE MATTER: A MYELIN WATER IMAGING STUDY.

Eleftherios Kavroulakis¹, Antonios Kagialis¹, Anna Simichanidou², Eirini Gratsia¹,
Eliza Kompoliti¹, Georgios Bertsias³, Vasileios Mastorodemos⁴, Panagiotis Simos⁵,
Dimitrios Boumbas³, Efrosini Papadaki¹

¹Department of Radiology, School of Medicine, University of Crete, University Hospital of Heraklion, Crete, Greece

²Department of Radiology, Theagenio Cancer Hospital of Thessaloniki, Thessaloniki, Greece

³Department of Rheumatology, Clinical Immunology and Allergy, School of Medicine, University of Crete, University Hospital of Heraklion, Crete, Greece

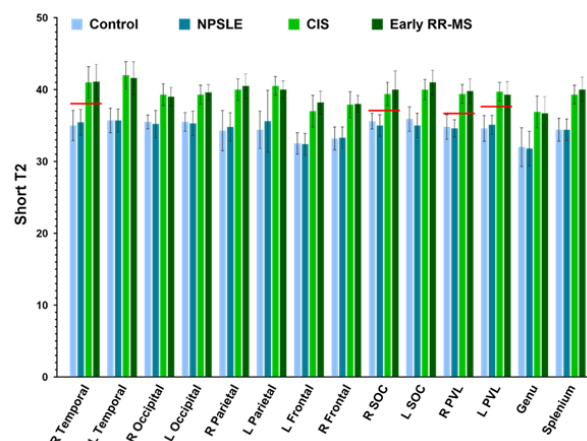
⁴Department of Neurology, School of Medicine, University of Crete, University Hospital of Heraklion, Crete, Greece

⁵Department of Psychiatry, School of Medicine, University of Crete, University Hospital of Heraklion, Crete, Greece

⁶Institute of Computer Science, Foundation of Research and Technology-Hellas, Voutes, Heraklion, Greece

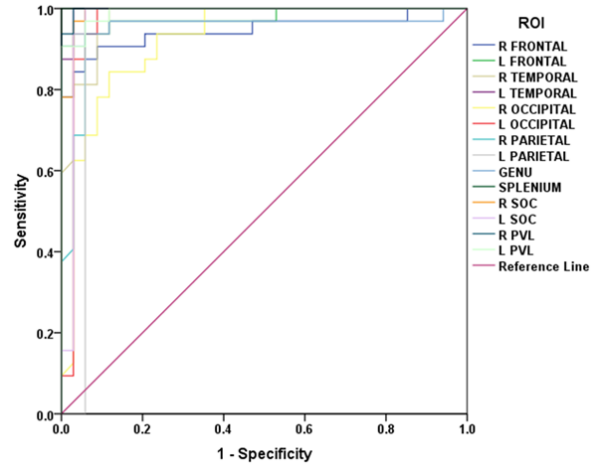
Abstract: Introduction: Neuropsychiatric Systemic Lupus Erythematosus (NPSLE) and Multiple Sclerosis (MS) are both autoimmune diseases that share inflammatory and neurodegenerative pathways of affecting central nervous system, often leading to intractable diagnostic problems. The aim of the present study was to differentiate NPSLE from clinical isolated syndrome (CIS) and early relapsing – remitting MS (RR-MS) by implementing myelin content indices of normal appearing white matter (NAWM) areas. Methods: A Myelin Water Imaging technique, specifically a 2D, Multi Echo Spin Echo (MESE), T2-weighted sequence, was performed in 24 patients with NPSLE, 32 with clinically isolated syndrome (CIS), 33 with RR-MS and in 23 healthy controls (HC). Long T2 and Short T2 values, corresponding to intra- and extra-cellular water and myelin water respectively, as well as myelin water fraction (MWF) were measured within 12 NAWM areas and the corpus callosum and group differences were examined through one-way ANCOVAs, while the discriminant capacity of T2 values and MWF between groups was assessed via ROC analyses. Results: Both NPSLE and HC groups showed significantly lower short T2 and MWF values than the CIS and RR-MS groups controlling for age, gender and total intracranial volume ($p < 0.001$) in all NAWM regions (Fig1). ROC analysis revealed very good discriminability between CIS and NPSLE patients on short T2 and MWF values with AUC values > 0.941 and > 0.936 , respectively (Fig 2), and between RR-MS patients and NPSLE with AUC > 0.963 for almost all NAWM. Cut-off short T2 of 36.96 and 36.42 in right semioval center and right periventricular NAWM discriminates CIS and RRMS from NPSLE with 100% sensitivity and 94% and 97% specificity, respectively, while a cut-off MWF of 65.26 in left temporal NAWM discriminates them with 99% sensitivity and 94% specificity. Discussion - Conclusion: Short T2 and MWF values in NAWM of NPSLE patients are significantly lower compared to CIS and RR-MS, probably reflecting the higher amount of diffuse demyelination in MS. Myelin water content, reflected by optimal cut-off short T2 and MWF values in various NAWM areas, can discriminate CIS and RR-MS from NPSLE with a sensitivity and specificity of almost 100%.

Figure 1



Average Short T2 values in each of 14 NAWM regions for healthy controls, and patients with NPSLE, CIS, and early RR-MS. Vertical bars indicate SDs and horizontal red lines mark the optimal cutoff values for discriminating between NPSLE and CIS/RR-MS patients according to ROC analyses.

Figure 2



Receiver Operating Characteristic curves of sensitivity over 1-specificity in discriminating between CIS from NPSLE patients based on NAWM Short T2 values

Keywords: CIS, MWI, NPSLE, RR-MS

EFFECT OF CHEMOTHERAPY ON HIPPOCAMPAL VOLUME: A PRELIMINARY STUDY

Kubilay Kağan Budak¹, Dilara Budak¹, Esat Kaba¹, Yusuf Çubukçu¹, Nur Hursoy¹,
Gülen Burakgazi¹, Mehmet Beyazal¹, Fatma Beyazal Çeliker¹

¹*Recep Tayyip Erdoğan University*

Abstract: Introduction: The hippocampus, a crucial structure in the medial temporal lobe, is vital for cognitive functions. Alterations in its structure and function may be central to chemotherapy-induced neurocognitive side effects. Aim: This study aimed to determine differences in hippocampal volume ratios and isolated volumes between cancer patients with chemotherapy history and a control group without chemotherapy exposure. Material and Methods: The study included 88 patients: 45 with chemotherapy history and 43 controls. Hippocampal volumes were measured using thin-section T1-weighted MRI images, segmented by an AI-based "Brain MR Atrophy Analysis" program. Hippocampal volumes and ratios to total intracranial volume were compared between groups. Findings: No significant differences were found in hippocampal volume ratios or isolated left hippocampal volume ($p>0.05$). However, isolated right hippocampal volume was significantly larger in the chemotherapy group (3.03 cm^3 vs 2.85 cm^3 , $p=0.020$). Discussion: The increased right hippocampal volume in chemotherapy patients may be due to selective effects on white matter, inducing relative volume increases in gray matter structures. This aligns with studies on differential neurotoxic effects of chemotherapy. The gender imbalance in the sample (62.2% male in chemotherapy group, 60.5% female in control) may have influenced results, highlighting the need to consider gender-based neuroanatomical differences in future research. This study provides a foundation for more comprehensive investigations. Future research should examine effects of specific malignancies and chemotherapy regimens on hippocampal morphology using larger, gender-balanced samples. Conclusion: This study establishes a methodological framework for investigating the relationship between chemotherapy and hippocampal volume, emphasizing the need for further exploration of underlying neurobiological mechanisms. Future studies should address limitations and expand on these findings to enhance understanding of chemotherapy's impact on brain structure and function.

Keywords: Hippocampus, Chemotherapy, Volume by Segmentation, Neuroradiology

COMPARATIVE ANALYSIS OF BRAIN VOLUME DIFFERENCES BETWEEN PUBERTY PRECOCIOUS AND NORMAL PUBERTY GIRLS

Hanife Gül den Dü zka l ı r¹, Gü nay Rona¹, Elif Sö bü²

¹University of Health Sciences Turkey, Kartal Dr. Lütfi Kırdar City Hospital, Clinic of Radiology, İstanbul, Turkey

²Üsküdar University Faculty of Medicine, Department of Pediatric Endocrinology, İstanbul, Turkey

Abstract: Objective: Idiopathic central precocious puberty develops as a result of premature maturation of the hypothalamic-pituitary-gonadal axis. The aim of our study was to investigate the relationship between brain maturation and puberty precocity. Material and Method: Between 2020 and 2022, patients admitted to the pediatric endocrinology department and diagnosed with puberty precocity were evaluated retrospectively. Among those who underwent brain MRI, those with appropriate imaging quality were included in the study. Height and BMI-matched healthy children were selected as the control group from among the patients who had undergone brain MRI on the same dates. The volumes of the anatomical parts of the brain were automatically measured from T1A sequences using the Volbrain program. Results: Fifteen patients with a median age of 8 (8-9) years and 22 controls with a median age of 8 (8-8) years who were height and BMI matched were included in the study. In the patient group, cerebro spinal fluid ($p<0.001$), anterior orbital gyrus ($p=0.008$), planum polare ($p=0.032$), postcentral gyrus medial segment ($p=0.005$), superior parietal lobule ($p=0.033$), occipital lobe ($p=0.004$), calcarine cortex ($p=0.023$), cuneus ($p<0.001$), occipital fusiform gyrus ($p=0.032$), inferior occipital gyrus ($p<0.001$), superior occipital gyrus ($p=0.001$), 046), occipital pole ($p=0.017$), parahippocampal gyrus ($p=0.007$), parietal operculum ($p=0.016$), inferior lateral ventricle ($p=0.007$), lateral ventricle ($p=0.012$), external SBS ($p=0.005$), cerebellar vermal lobule I-V ($p<0.001$), cerebellar vermal lobule VI-VII ($p=0.003$), cerebellar vermal lobule VIII-X ($p=0.030$) were significantly larger compared to the control group. Discussion and Conclusion: In patients with precocious puberty, the volumes of some brain parts related to visual and sensory centers were larger in the control group. The parahippocampal gyrus, which is an important part of the limbic system, some parts of the cerebellum that play a role in the control of balance and eye movements, and the volumes of cerebrospinal fluid and lateral ventricle were also found to be larger in these patients. These parts of the brain may be a factor or a consequence in the development of puberty precocity.

Table 1

Parameters(volume cm ³ , mean±SD)	Patient	Control	p value
Cerebro Spinal Fluid (CSF)	110,79±17,78	81,09±13,45	<0,001
Anterior orbital gyrus total	5,04±1,33	4,08±0,76	0,008
Planum polare total	4,45±0,85	3,94±0,55	0,032
Postcentral gyrus medial segment total	2,31±0,71	1,78±0,35	0,005
Sup, parietal lobule total	26,17±3,84	24,15±1,60	0,033
Occipital lobe total	85,10±12,83	76,46±2,22	0,004
Calcarine cortex total	7,15±1,97	6,11±0,45	0,023
Cuneus total	9,80±2,35	7,31±1,41	<0,001
Occipital fusiform gyrus total	7,97±1,70	7,00±0,94	0,032
Inf, occipital gyrus total	14,61±1,62	12,59±0,77	<0,001
Sup, occipital gyrus total	8,73±1,77	7,89±0,60	0,046
Occipital pole total	6,18±1,10	5,33±0,96	0,017
Parahippocampal gyrus total	6,26±0,99	5,59±0,42	0,007
Parietal operculum total	5,35±0,97	4,68±0,64	0,016
Inf, Lateral Ventricle	0,69±0,27	0,43±0,27	0,007
Lateral Ventricle total	12,81±4,33	9,12±4,01	0,012
External CSF	94,90±17,02	74,12±22,47	0,005
Cerebellar Vermal Lobules I-V	4,90±0,80	3,51±0,84	<0,001
Cerebellar Vermal Lobules VI-VII	2,33±0,34	1,81±0,49	0,003
Cerebellar Vermal Lobules VIII-X	2,72±0,51	2,41±0,34	0,030

Table 1: Brain volume values and comparison of patient and control groups

Figure 1

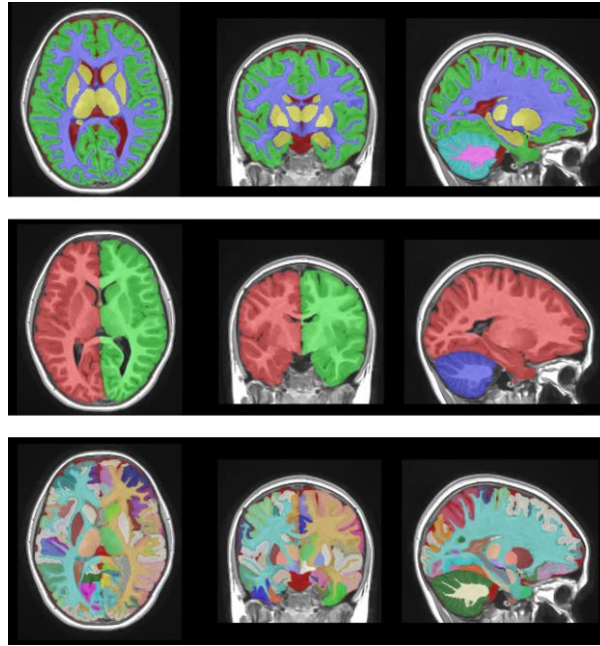


Figure 1: Measurement of brain volume values of patient and control group with Volbrain program

Keywords: Brain volume, Magnetic resonance imaging, Precocious puberty

EXCITOTOXIC WHITE MATTER INJURY ON DIFFUSION-WEIGHTED IMAGING: A REVIEW OF PEDIATRIC CAUSES

Cigdem Oztunali¹, Eylem Kırıl², Gürkan Bozan², Coşkun Yazar³, Kürşat Bora Çarman³

¹Eskisehir Osmangazi University Medical Faculty, Department of Radiology, Division of Pediatric Radiology

²Eskisehir Osmangazi University Medical Faculty, Department of Pediatrics, Division of Pediatric Critical Care

³Eskisehir Osmangazi University Medical Faculty, Department of Pediatrics, Division of Pediatric Neurology

Abstract: Aim: Excitotoxic injury of the white matter can occur due to increased release, decreased uptake, or leakage of transsynaptic excitatory amino acids. In the pediatric age group, common causes include infection-triggered encephalopathy syndromes (cytotoxic lesions of the corpus callosum (CLOCCs), mild encephalopathy with reversible splenial lesion (MERS), acute leukoencephalopathy with restricted diffusion (ALERD), febrile infection-related epilepsy syndrome (FIRES)); hypoxic-ischemic injury with or without Wallerian degeneration, trauma (accidental and non-accidental), herpes encephalitis, status epilepticus and pharmacoresistant epilepsy syndromes such as Dravet syndrome. This review aims to illustrate and describe the DWI findings in common non-metabolic causes of excitotoxic injury in children. Case Presentations DWIs and cerebral MRIs of pediatric cases with infection-triggered encephalopathies, hypoxic ischemic encephalopathies, accidental and non-accidental trauma, status epilepticus and drug-resistant epilepsy syndromes, herpes encephalitis, are presented to illustrate the mechanisms of excitotoxic white matter injury (Figures 1-3). Discussion: Excitotoxic injury occurs due to excitatory amino acids of the synapses, mainly glutamate. The injury can affect both the gray and the white matter. Acute white matter injury and the resultant edema are observed on DWIs as diffusion restriction areas. White matter injury can be caused by conditions resulting in energy failure and interrupted glutamate re-uptake, such as hypoxic ischemic ischemia. Increased release of glutamate can cause injury in conditions such as shaken baby syndrome, diffuse axonal injury, and status epilepticus. Parainfectious encephalopathy syndromes can be caused by increased release or decreased glutamate uptake. Conclusions: DW imaging shows various types of cytotoxic white matter edema due to excitotoxic injury in the pediatric age group. The edema's pattern, distribution, and reversibility can vary according to the etiology, age, and treatment.

Figure 1

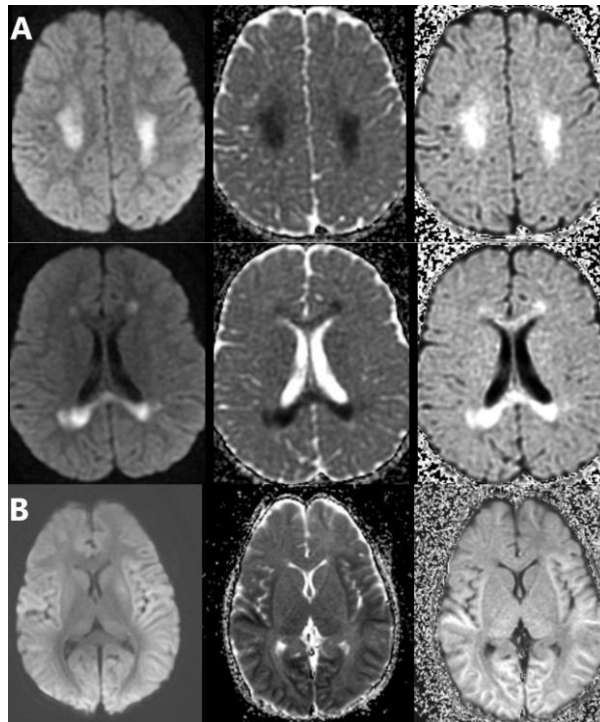


Figure 1. A. Diffusion-weighted, ADC, and exponential ADC map images (upper two rows) show diffusion restriction of the white matter in centrum semiovale, corpus callosum splenium, and genu in a patient with

MERS. The abnormalities were resolved within one week (not shown). B. Diffusion-weighted, ADC, and exponential ADC map images in a child with ALERD show restriction diffusion in the perisylvian frontotemporoparietal and posterior and paramedian occipital subcortical white matter.

Figure 2

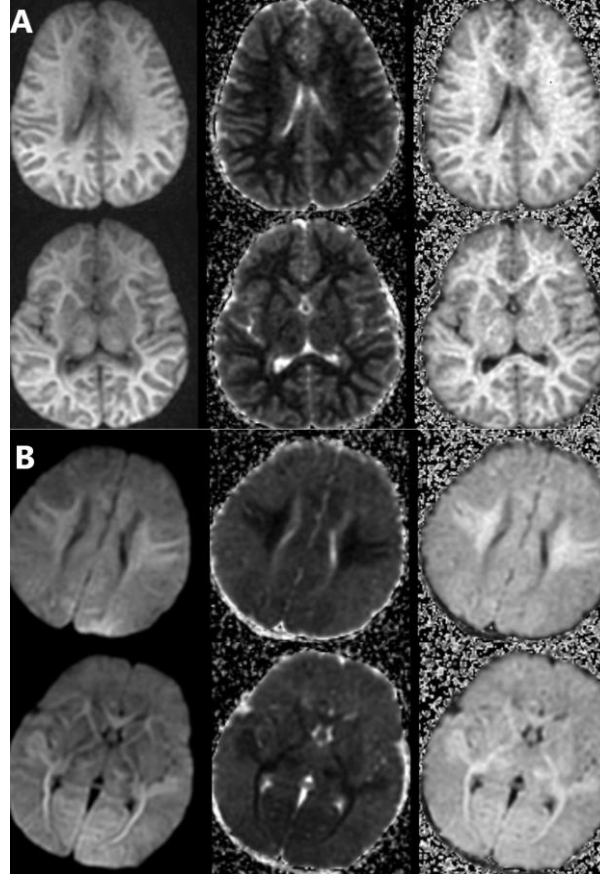


Figure 2. A. Diffusion-weighted, ADC, and exponential ADC map images of a child with cardiac arrest and severe hypoxia (upper two rows) show restricted diffusion in all cerebral white matter areas, resulting in a “bright tree” appearance. B. Diffusion-weighted, ADC, and exponential ADC map images of an infant with hypoxia due to severe non-treated pulmonary infection (lower two rows) show restriction diffusion in the peri-rolandic white matter, corona radiata, internal capsules, optic radiation, and temporal subcortical white matter.

Figure 3

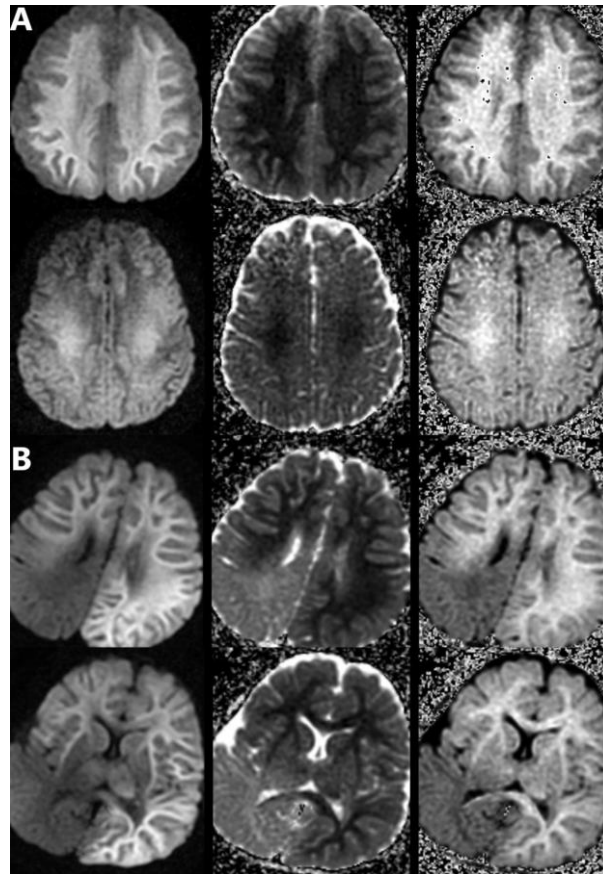


Figure 3. A. Diffusion-weighted, ADC, and exponential ADC map images of two children with a history of electric shock injury (upper two rows) show restriction diffusion in all white matter areas of the cerebrum in one (first row) and of the centrum semiovale in another (second row). B. Diffusion-weighted, ADC, and exponential ADC map images in a child with Dravet syndrome (lower two rows) show restricted diffusion in subcortical and deep white matter areas, as well as the external capsules and the corpus callosum

Keywords: cytotoxic edema, diffusion-weighted imaging, excitotoxic injury, intramyelinic edema, cerebral white matter

THE ROLE OF APPARENT DIFFUSION COEFFICIENT ASSESSMENT IN WILSON DISEASE WITH NEUROLOGICAL INVOLVEMENT

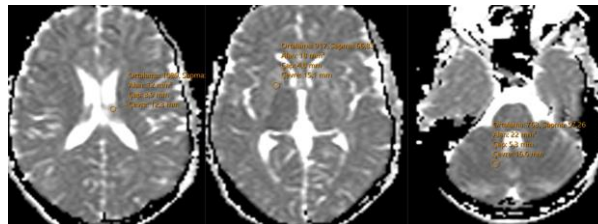
Nurullah Dağ², Sevgi Demiröz Taşolar², Abdi Gürhan¹, Mehmet Öztürk¹

¹Selcuk University, Faculty of Medicine, Department of Radiology, Division of Pediatric Radiology

²Inonu University, Faculty of Medicine, Department of Radiology

Abstract: Objective: Wilson's disease is a genetic disorder characterized by abnormal copper accumulation in the body, leading to damage in the liver, brain, and other organs. Diffusion-Weighted Magnetic Resonance Imaging (DW-MRI) is a technique that images the diffusion of water molecules within brain tissue, enabling quantitative measurement through the Apparent Diffusion Coefficient (ADC). This study aims to investigate the role of DW-MRI in assessing neurological involvement in patients with Wilson's disease. Methods: ADC measurements were taken from the basal ganglia, periventricular white matter, cortex, dentate nucleus, and choroid plexus on a workstation. Participants were divided into three groups: Wilson's disease with neurological involvement, Wilson's disease without neurological involvement, and controls. Differences between groups were statistically analyzed. Results: A total of 122 participants were evaluated, including 66 Wilson's disease patients and 56 controls. Neurological involvement was present in 17 Wilson's disease patients. No significant age or gender differences were found between groups. Significant differences in ADC values were observed in the basal ganglia, dentate nucleus, and choroid plexus, with higher values in the Wilson's disease group. No significant differences were found in periventricular white matter and cortex ADC values. Subgroup analysis of Wilson's disease patients revealed higher ADC values in the basal ganglia and periventricular white matter of those with neurological involvement compared to those without. No significant differences were found in cortex, dentate nucleus, and choroid plexus ADC values between subgroups. ANOVA testing showed significantly higher ADC measurements in the basal ganglia of patients with neurological involvement compared to other groups. ADC measurements in the periventricular deep white matter and dentate nucleus were also significantly higher in Wilson's disease patients with neurological involvement compared to controls. No significant differences were found for other variables between groups. Conclusion: DW-MRI can be valuable for diagnosing and monitoring brain involvement in Wilson's disease, particularly in patients with neurological symptoms. These findings suggest that DW-MRI and ADC measurements could serve as useful tools in the management of Wilson's disease, offering insights into neurological involvement and potentially guiding treatment decisions.

Figure 1



Signal measurements from choroid plexus, basal ganlia and dentate nucleus with an ellipsoid ROI of 4 mm diameter are shown.

Table 1

Variables	Wilson's Disease (n=66)	Control (n=56)	p-value
Age (years, mean \pm SD, range)	10.9 \pm 3.8 (4-18)	10.6 \pm 3.8 (4-17)	0.656
Gender (female/male)	27/39	24/32	0.499
Basal ganglia	824.1 \pm 177.6 $\times 10^{-6}$ mm ² /sec(635-1453)	739.0 \pm 40.6 $\times 10^{-6}$ mm ² /sec (651-847)	0.006

Periventricular white matter	838.1±80.8x10 ⁻⁶ mm ² /sec (693-1121)	817.0±62.6 x10 ⁻⁶ mm ² /sec(691-939)	0.115
Cortex	817.0±65.6 x10 ⁻⁶ mm ² /sec(705-1100)	811.4±46.8 x10 ⁻⁶ mm ² /sec(714-931)	0.594
Dentate nucleus	770.6±82.1 x10 ⁻⁶ mm ² /sec (631-1097)	729.8±44.9 x10 ⁻⁶ mm ² /sec(615-855)	0.002
Choroid plexus	1648.0±418.9 x10 ⁻⁶ mm ² /sec(838-2606)	1396.1±277.2x10 ⁻⁶ mm ² /sec(913-1987)	0.001

Table 1. Comparison of demographic data and ADC measurements between Wilson disease and control groups

Table 2

Variables	Wilson's disease without neurological involvement (n=49)	Wilson's disease with neurological involvement (n=17)	p-value
Age (years, mean ± SD, range)	10.0±3.7 (4-17)	13.3±2.8 (5-18)	0.001
Gender (female/male)	24/25	12/7	0.379
Basal ganglia	745.0±43.5x10 ⁻⁶ mm ² /sec(635-854)	1018.5±230.9x10 ⁻⁶ mm ² /sec(708-1453)	<0.001
Periventricular white matter	821.4±53.4x10 ⁻⁶ mm ² /sec (693-958)	880.5±122.6x10 ⁻⁶ mm ² /sec (728-1121)	0.026
Cortex	812.1±53.9x10 ⁻⁶ mm ² /sec (768-862)	827.9±89.1x10 ⁻⁶ mm ² /sec (724-1100)	0.497
Dentate nucleus	764.3±66.8x10 ⁻⁶ mm ² /sec (631-964)	783.8±116.2x10 ⁻⁶ mm ² /sec (643-1097)	0.222
Choroid plexus	1599.5±330.2x10 ⁻⁶ mm ² /sec (838-2527)	1646.2±445.7x10 ⁻⁶ mm ² /sec (891-2606)	0.441

Table 2. Comparison of demographic data and ADC measurements between Wilson's disease without/with neurological involvement

Table 3

Variables	Control (a)	Wilson's disease without neurological involvement (b)	Wilson's disease with neurological involvement (c)	p-value
Basal ganglia	a-c	b-c		<0.001
Periventricular white matter	a-c		-	0.034
Cortex	-	-	-	-
Dentate nucleus	a-c	-		0.021
Choroid plexus	-	-	-	-

Table 3. Comparison of the ADC measurements between the 3 groups

Keywords: Wilson's disease, Apparent diffusion coefficient, Neurological involvement

COMPARISON OF T1A POST-CONTRAST AND FLAIR IMAGING METHODS IN THE DIAGNOSIS OF NON- ENHANCING LEPTOMENINGEAL METASTASES: FLAIR HYPERINTENSITY AS AN EARLY FINDING

Fatma Zeynep Arslan¹

¹*Basaksehir City Hospital*

Abstract: Introduction: Antiangiogenic agents used in the treatment of metastatic cancer are among the reasons that reduce the enhancement of leptomeningeal metastasis (LM) in brain MRI (1). In this study, we aimed to evaluate the effectiveness of FLAIR hyperintensity in detecting leptomeningeal metastasis (LM) at early stages in non-enhancing LM. Materials and Methods: In our study, follow-up brain MRI examinations of 80 patients diagnosed with leptomeningeal metastases, who showed involvement in T1A post-contrast series and malign cells in CSF, were retrospectively evaluated. Prior to contrast enhancement, data such as FLAIR hyperintensity, ADC values, age, tumor subtypes (breast cancer, lung cancer, etc.), presence of brain and spinal metastases, tumor stage (M2, M3), tumor markers, treatments applied, and clinical findings (persistent vomiting, headache...) were collected. The presence of gyral enhancement, sulcal space enhancement, basal cisterns enhancement, and dural enhancement in brain MRI T1A post-contrast series and FLAIR images were evaluated. It was investigated whether they made a significant difference in predicting non-enhancing LM. Results: In the retrospective follow-up MRIs of patients with LM, FLAIR sequence hyperintensity has shown a significant difference in the early diagnosis of non-enhancing LM ($p<0.005$). Particularly, a notable increase in signal hyperintensity in the sulcal areas and dural enhancement was detected ($p<0.005$). Discussion: FLAIR sequences appear promising in the diagnosis of early-stage LM, which do not show findings in contrast non-enhancing T1A post-contrast series. This indicates that FLAIR hyperintensity may be a more sensitive tool for early diagnosis in non-enhancing LM.

Keywords: leptomenengial metastasis, cancer

PATTERNS OF NASAL AND PARANASAL SINUS INJURIES IN MAXILLOFACIAL TRAUMA: A RETROSPECTIVE ANALYSIS OF ETIOLOGIES AND FRACTURE LOCATIONS

Gülşen Yücel Oğuzdoğan¹

¹Başakşehir Çam ve Sakura Şehir Hastanesi

Abstract: Objective: This study aims to evaluate the trauma etiologies, fracture locations, and the distribution of age and gender in patients with maxillofacial trauma involving the nose and paranasal sinuses. Methods: A retrospective analysis was conducted on 188 cases with nasal and paranasal sinus pathology out of 357 patients with maxillofacial trauma who presented to our clinic between January 2021 and November 2022. The ages of the patients ranged from 1 to 99 years, with 57 females (16.0%) and 300 males (84.0%). The mean age of the patients was 32.2 ± 15.8 years. Statistical analysis was performed using SPSS version 26.0. Independent t-tests and chi-square tests (Pearson's and Fisher's exact tests) were used to compare categorical data between groups. A p-value of less than 0.05 was considered statistically significant. Results: The etiological distribution of the cases revealed that 59.4% were caused by assault, 10.4% by pedestrian traffic accidents, 7.6% by motor vehicle accidents, and 7.8% by falls. Nasal fractures were the most common finding, seen in 83.5% of the cases, followed by maxillary sinus fractures in 23.2%, frontal sinus fractures in 11.2%, ethmoid sinus hematomas in 15.4%, maxillary sinus hematomas in 23.0%, frontal sinus hematomas in 11.8%, and sphenoid sinus hematomas in 5.6%. Additionally, 15.1% of the patients had concurrent fractures of other facial and cranial bones, and 5.9% had intracranial hemorrhage. When comparing the pathologies within etiological groups, nasal fractures were significantly more common in assault cases (95.3%) compared to other causes. In motor vehicle accidents, the presence of maxillary sinus fractures (33.3%), maxillary sinus hematomas, and sphenoid sinus hematomas (14.8%) were significantly higher. Pedestrian traffic accidents were associated with the highest occurrence of sphenoid sinus hematomas (24.3%) ($p < 0.0001$). Furthermore, the occurrence of frontal sinus fractures was significantly lower in assault cases (4.7%) compared to other etiological groups ($p < 0.0001$). Conclusion: A significant difference was found between trauma etiologies and the distribution of pathologies in the nose and paranasal sinuses among patients with maxillofacial trauma. The results highlight the importance of understanding trauma patterns to improve diagnostic accuracy and treatment strategies for patients with nasal and paranasal sinus injuries.

distributions and comparisons regards trauma etiology

Değişkenler	Trauma Etiyolojisi								p
	ADTK (n=37)	AITK (n=27)	Aynı Seviyede en Düşme (n=29)	Darp (n=212)	Diğer (n=13)	Motor Kazası (n=13)	Yüksek Düşme (n=28)	Genel Toplam (N=357)	
	n (%)	n (%)	n (%)	n (%)	n (%)	n (%)	n (%)	n (%)	
Nazal Fraktür	25(67.6)	19(70.4)	24(82.8)*	194(91.5)	7(63.6)	10(76.9)	19(67.9)	298(83.5)	<0.0001
Maxiller Sinüs Fraktürü	8(21.6)	9(33.3)	13(44.8)	27(12.7)	7(63.6)*	8(61.5)*	11(39.3)	83(23.2)	<0.0001
Frontal Sinüs Fraktürü	4(10.8)	6(22.2)*	4(13.8)	10(4.7)**	3(27.3)*	4(30.8)*	9(32.1)*	40(11.2)	<0.0001
Etmoid Sinüs Fraktürü	3(8.1)	5(18.5)	3(10.3)	2(0.9)	4(36.4)*	2(15.4)	6(21.4)*	25(7.0)	<0.0001
Sfenoid Sinüs Fraktürü	2(5.4)	1(3.7)	0(0)	0(0)	0(0)	1(7.7)	5(17.9)*	9(2.5)	<0.0001
Maksilla Fraktür	1(2.7)	2(7.4)	0(0)	2(0.9)	1(9.1)	1(7.7)	0(0)	7(2.0)	0.069
Orbita Fraktür	6(16.2)	7(25.9)	7(24.1)	16(7.5)	3(27.3)	3(23.1)	12(42.9)*	54(15.1)	<0.0001
Mandibula Fraktür	2(5.4)	1(3.7)	0(0)	1(0.5)	2(18.2)	1(7.7)	1(3.6)	8(2.2)	0.002
Zigoma Fraktür	1(2.7)	2(7.4)	2(6.9)	5(2.4)	1(9.1)	4(30.8)*	4(14.3)*	19(5.3)	<0.0001
Temporal Kemik Fraktür	5(13.5)	5(18.5)*	0(0)	0(0)	2(18.2)*	0(0)	4(14.3)	16(4.5)	<0.0001
Frontal Kemik Fraktürü	4(10.8)*	2(7.4)	2(6.9)	0(0)	2(18.2)*	2(15.4)*	7(25.0)*	19(5.3)	<0.0001
Parietal Kemik Fraktür	3(8.1)	0(0)	1(3.4)	0(0)	0(0)	0(0)	3(10.7)	7(2.0)	0.001
Occipital Kemik Fraktür	0(0)	0(0)	0(0)	1(0.5)	0(0)	0(0)	1(3.6)	2(0.6)	0.513
Kafa Tabanı Fraktür	1(2.7)	1(3.7)	0(0)	0(0)	1(9.1)	0(0)	6(21.4)*	9(2.5)	<0.0001
Frontal Sinüs Hematom	4(10.8)	6(22.2)	4(13.8)	12(5.7)	2(18.2)	4(30.8)	10(35.7)*	42(11.8)	<0.0001
Etmoid Sinüs Hematom	7(18.9)	10(37.0)*	6(20.7)	12(5.7)	4(36.4)*	2(15.4)	14(50.0)*	55(15.4)	<0.0001
Maxiller Sinüs Hematom	7(18.9)	9(33.3)	14(48.3)*	24(11.3)	8(72.7)*	8(61.5)*	12(42.9)*	82(23.0)	<0.0001
Sfenoid Sinüs Hematom	9(24.3)*	4(14.8)*	1(3.4)	1(0.5)	0(0)	1(7.7)	4(14.3)*	20(5.6)	<0.0001
Intracranial Hemoraji	0(0)	0(0)	0(0)	1(0.5)	0(0)	0(0)	1(3.6)*	2(0.6)	<0.0001

it was very difficult to upload this table to the system, so I have attached a photo of it. if the paper is accepted, I will present the table in detail.

demographic characteristics

Continuous Variables		Min-Max	Mean±SD
Age		1-99	32,2±15,8
Categorical Variables		n	%
Gender	Female	57	16,0
	Male	300	84,0
Trauma Etiology	Pedestrian Traffic Accident (PTA)	37	10,4
	Vehicle Traffic Accident (VTA)	27	7,6
	Fall from Same Level	29	8,1
	Assault	212	59,4
	Other	11	3,1
	Motorcycle Accident	13	3,6
	Fall from Height	28	7,8

Keywords: maxillofacial trauma, radiology, maxillofacial fractures, Paranasal Sinuses

IMAGING OF CONGENITAL PYRIFORM SINUS FISTULA IN CHILDREN: A REVIEW OF SIX CASES

Cigdem Oztunali¹, Merve Yazol², Berat Acu³

¹Eskisehir Osmangazi University Medical Faculty, Department of Radiology, Division of Pediatric Radiology

²Gazi University Medical Faculty, Department of Radiology, Division of Pediatric Radiology

³Eskisehir Osmangazi University Medical Faculty, Department of Radiology, Division of Interventional Radiology

Abstract: Aim: Congenital pyriform sinus fistula (CPSF) is a rare pathology and occurs due to incomplete obliteration of the fourth pharyngeal pouch during fetal development. The fistula causes severe recurrent neck infections and suppurative thyroiditis in children, with or without abscess formation. This review aims to describe and illustrate the imaging findings of CPSF in six children. Case Presentations: Ultrasonography, magnetic resonance imaging, computed tomography, and fluoroscopy images of the neck in six children diagnosed with CPFS are presented to illustrate the multimodality imaging findings of CP (Figures 1-3). Discussion: The CPSF follows the proximal course of the embryologic fourth branchial pouch sinus and is mainly seen as a left-sided sinus or fistula tract originating from the pyriform fossa, coursing posterolateral to the cricothyroid, lateral to the thyroid lamina and the trachea. It usually ends in or around the left lobe of the thyroid gland. Esophagography with barium or non-ionic contrast agents clearly shows the sinus tract, mainly when performed after the subsidence of the infection. Air bubbles within the sinus tract can be best observed with CT and suggest the diagnosis. During acute infection, CT and MRI show asymmetrical thickening and contrast enhancement of the left pyriform fossa walls and asymmetrical thickening of the left aryepiglottic fold. US, CT, and MRI all show the sinus-related neck infection in the course of the sinus. Suppurative thyroiditis, intrathyroidal, parathyroidal, paratracheal, or paralaryngeal abscesses can be found. Phlegmonous infection of the deep neck spaces or the thyroid and parathyroid tissues may mimic solid aggressive tumors of the deep neck spaces. Conclusion: CPSF is a rare and often misdiagnosed condition in children. Knowledge of the CSSF's course and characteristic imaging findings of an infected CPSF may help diagnose it, especially in children with a history of recurrent deep neck infections and suppurative thyroiditis

Figure 1

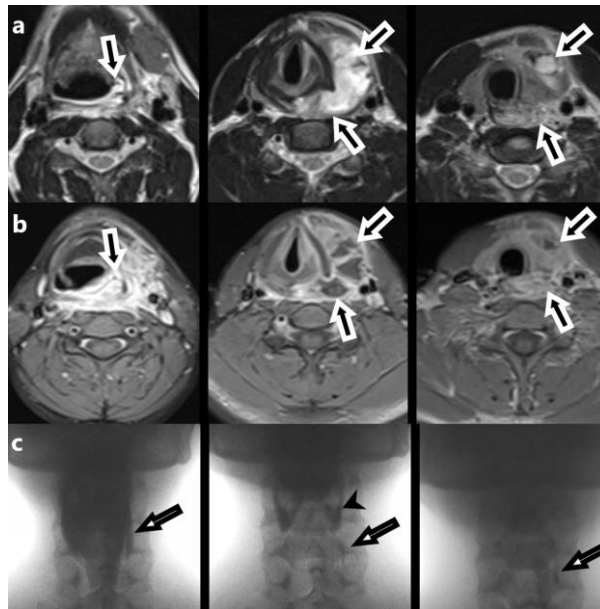


Figure 1. Axial T2-weighted (a) and axial post-contrast T1-weighted MR images of the neck in a 16-year-old boy with acute suppurative thyroiditis and a history of recurrent deep neck infections show edema, thickening, and contrast-enhancement of the left pyriform fossa walls with asymmetrical obliteration of the left pyriform fossa. A lobulated heterogeneous fluid collection with thickened-enhancing walls, extending from the left cricothyroid space, coursing lateral to the left thyroid lamina and ending anterior and posterior to the left thyroid lobe, is seen (arrows in a and b). Anteroposterior esophagography images with non-ionic contrast (c) show the congenital

pyriform sinus fistula tract (arrows in c) originating from the left pyriform sinus (arrowhead in c) and coursing inferiorly.

Figure 2

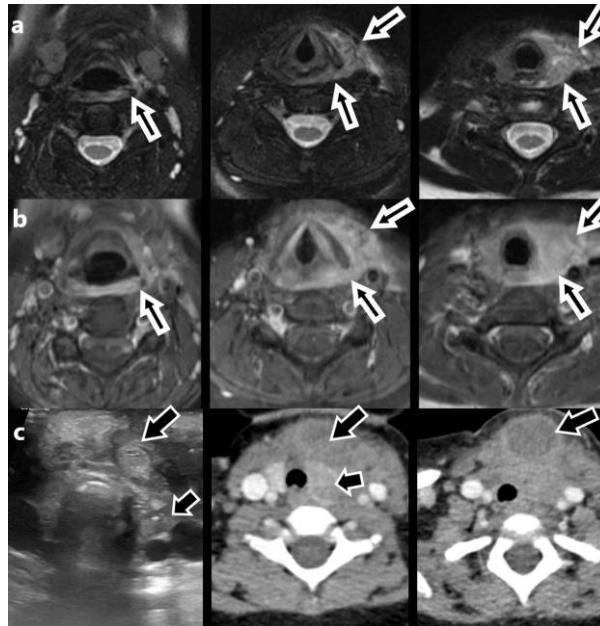


Figure 2. Axial T2-weighted (a) and axial post-contrast T1-weighted (b) MR images of the neck in a 14-year-old girl with acute suppurative thyroiditis show edema, thickening, and contrast-enhancement of the left pyriform fossa walls. A phlegmonous infection originating from the left pyriform fossa extending from the left cricothyroid space, coursing lateral to the left thyroid lamina and ending in the left thyroid lobe, is seen. The left lobe of the thyroid gland is diffusely enlarged; parathyroidal soft tissues demonstrate diffuse thickening and contrast enhancement (arrows in a and b). Transverse ultrasonography and axial CT images of the neck in a 2-year-old girl show diffuse heterogeneity of the left lobe of the thyroid gland, indicating suppurative thyroiditis (short arrows). A peripherally enhancing fluid collection originating from the left thyroid lobe and extending anteriorly to into the strap muscles (long arrows) is also seen.

Figure 3

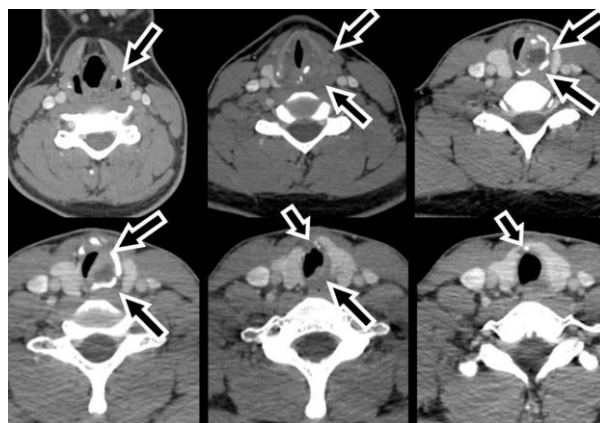


Figure 3. Axial contrast-enhanced CT images of the neck in a 16-year-old boy with a history of recurrent left-sided deep neck infections (a and b) show asymmetrical thickening of the left aryepiglottic fold with partial obliteration of the left pyriform sinus. Soft tissues posterior, medial, and lateral to the left thyroid cartilage show diffuse thickening with dystrophic calcification foci from the previous infections. A left paratracheal hypodense fluid collection is seen with peripheral dystrophic calcifications and contrast enhancement. The fluid collection extends inferiorly between the left tracheal wall and the left thyroid lobe. The thyroid isthmus also contains a small fluid

collection with a calcification focus (arrow in a and b). Axial contrast-enhanced CT images of the neck of the same child on follow-up (at one year) show asymmetrical thickening of the left aryepiglottic fold (arrow, c) and foci of air in and around the left paratracheal fluid collection, indicating communication with pharyngeal space.

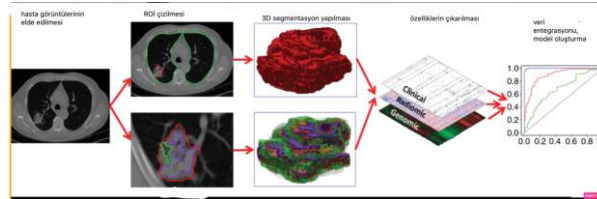
Keywords: abscess, branchial pouch anomalies, congenital pyriform sinus fistula, pyriform sinus, suppurative thyroiditis

COMPARISON OF PET/CT AND CT TEXTURE ANALYSIS IN PATIENTS WITH STAGE III-IV LUNG CANCER RECEIVING CHEMORADIOOTHERAPY: CAN WE PREDICT THE TREATMENT RESPONSE OF THE TUMOR?

Nilufar Gasimli¹, Sukru Mehmet Erturk¹, Hakan Ayyildiz¹, Vusal Mammadli¹
¹Istanbul University Istanbul Faculty of Medicine

Abstract: Introduction: Comparison of pet/ct and ct texture analysis in patients with stage iii-iv lung cancer receiving chemoradiotherapy: Can we predict the treatment response of the tumor? Aim: The aim of this study is to reveal the correlation between the tissue analysis characteristics of non-small cell lung cancer and the response of the lesion to treatment in pet/ct examination. Materials and methods: the images of 106 patients who were diagnosed with non-small cell lung cancer by biopsy in istanbul faculty of medicine between 2020-2023 and underwent thoracic CT imaging were retrospectively evaluated. For texture analysis, volumetric segmentation was performed by two radiologists on 'OLEA' software. In addition, kernels and Laplacian of Gaussian filters were applied to the images. Statistically significant differences were found in the treatment-responsive and unresponsive groups. Data were standardized. The features were selected using the wrapper-based sequential feature selection algorithm. After the optimization of the models with the double-layered cross-validation technique, validation was performed. RESULTS: The study included stage III-IV lung diagnosis, CT imaging performed and histopathologically verified; 106 patients were included (82 patients were considered as responding and 24 patients was considered as unresponsive according to response to treatment). 111 features were extracted from each image. In the CT texture analysis, 202 features out of 444 features were found to be compatible in the responding and unresponsive patient groups. After Pearson correlation, SFS selected 7 features. Accuracy rates were calculated. Sensitivity was calculated as 54% for LR, 64% for SVM, 90% for NB, and 67% for kNN. Specificity was calculated as 69% for LR, 72% for SVM, 86% for NB, and 69% for kNN. Accuracy rates of SVM and LR models created with AUC values of CT images were found to be 72 and 74%. The accuracy of the kNN and NB models was 72% and 68%.

Radiomics analiz basamakları



Radiomics analiz aşamaları

. Radiomics analiz aşamaları

Görüntü toplanması	Görüntü segmentasyonu	Özellik çıkarma	Analiz ve veritabanı oluşturma
BT ve PET-BT	Uzaktan algılanan verinin doğrulanması	Toplanan datanın özelliklerini karakterize etmek	Klinik veya araştırma PACS sistemi
Görüntü toplama	Otomatize etmek	Otomatik veri çıkarmak	Raporların ve görüntü açıklamalarının kaydedilmesi ve paylaşılması
Rekonstrüksiyon			

Veritabanına imaj depolama	Yeniden elde edilebilir hale getirmek	Bilgilendirici	Klinik, görüntüleme ve genbilimi veritabanının entegrasyonu
	Doğrulamak	Yeniden elde edilebilir hale getirmek	Bilgi analiz
		Gereksiz dataları çıkarma	

Keywords: lung cancer, texture analysis, deep learning

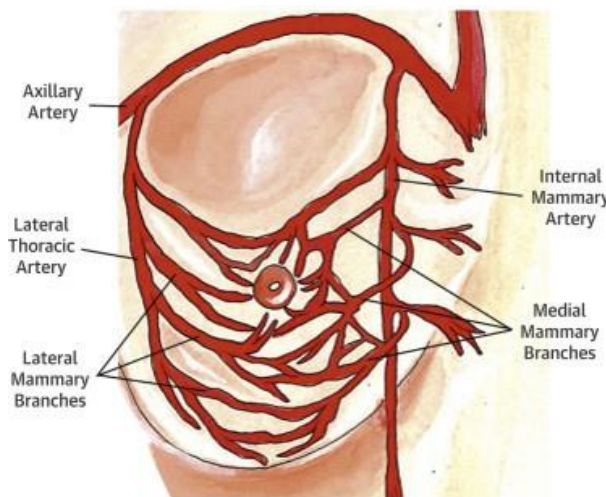
EVALUATION OF THE VARIABILITY OF AXILLARY ARTERY AND INTERNAL MAMMARY ARTERY DIAMETERS ACCORDING TO INTRAMAMMARY TUMOR LOCATION IN BREAST CANCER PATIENTS WITH MAGNETIC RESONANCE IMAGING

Gizem Özmen¹, Deniz Esin Tekcan Şanlı¹

¹Gaziantep University Faculty of Medicine, Department of Radiology

Abstract: Purpose: It was aimed to evaluate the increase rates of internal mammarian (IMA) and axillary artery (AA) vessel diameters in breast cancer patients according to the location of the tumor in the breast (inner, outer, middle) according to Magnetic Resonance Imaging (MRI). Methods: Newly diagnosed breast cancer patients (invasive carcinoma and ductal carcinoma in situ) with histopathologically proven malignancy but not yet treated who had breast MRI examinations performed were included in the study. Tumor localization was grouped as lateral-medial-central localization. IMA and AA diameters in pathological and intact breasts were measured in dynamic Maximum Intensity Projection (MIP) images and recorded. The width of vessel diameters according to tumor localization and the variability of vessel diameters on the diseased side compared to the normal side (tumor-side IMA (mm)/intact side IMA (mm), tumor-side AA (mm)/intact side AA (mm),) were statistically analyzed. Results: In all patients, IMA diameter was 3.71 ± 1.53 mm on the tumor side and 2.58 ± 0.94 mm on the intact side; AA diameter was 2.39 ± 0.88 on the tumor side and 2.10 ± 0.71 mm on the intact side and both IMA and AA diameters were significantly larger on the tumor side ($p < 0.01$). In all patients, tumor side/ intact side IMA ratio was 1.51 ± 0.57 , AA ratio was 1.18 ± 0.37 ; in patients with lateral localization, IMA ratio was 1.47 ± 0.53 , AA ratio was 1.18 ± 0.39 ; in patients with medial localization, IMA ratio was 1.58 ± 0.67 , AA ratio was 1.16 ± 0.38 ; in patients with central localization, IMA ratio was 1.52 ± 0.51 , AA ratio was 1.21 ± 0.30 and IMA increase rate was significantly higher than AA increase rate regardless of tumor localization. While IMA increase rate was the highest in medial localized tumors, AA increase rate was higher in central localized tumors. Conclusion: The results of this study showed that both IMA and AA were significantly wider on the tumor side than on the intact side in breast cancer patients and that IMA was wider than AA on the tumor side regardless of the lateral-medial-central location of the tumor. On the tumor side, the expansion rate of the IMA was significantly greater than the expansion rate of the AA regardless of tumor localization.

Figure 1



Normal vascularization of the breast

Keywords: breast cancer, internal mammarian artery, axillary artery, tumour vascularization

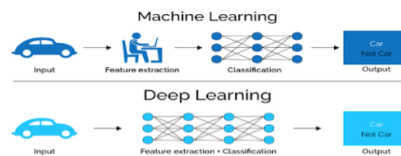
EVALUATION OF PNEUMOTHORAX PREDICTONABILITY BY DEEP LEARNING METHOD BEFORE TRANSTHORACIC FINE NEEDLE ASPIRATION BIOPSY (TTIAB) IN LUNG MASSES

Vusal Mammadli¹, Nilufar Gasimli¹, Sukru Mehmet Erturk¹, Hakan Ayyıldız¹

¹Istanbul University Istanbul Faculty Of Medicine

Abstract: AIM: For the definitive diagnosis of new lung lesions, histopathological diagnosis, that is, a tissue sample, is required. The most important method for histopathological diagnosis is percutaneous transthoracic biopsies performed under CT guidance. Although PTBs are minimally invasive methods, complications such as pneumothorax, pulmonary hemorrhage have been encountered. Our aim in this study is to evaluate the predictability of pneumothorax, the most common complication of PTB, before TTNAB with deep learning algorithms, and to plan patient management. MATERIALS AND METHODS: A total of 403 PTB procedures performed under CT guidance in our institution's Interventional Radiology Department were included in our retrospective study. In our hospital system, images of patients who underwent TTIAB between 2018 and 2023 were downloaded as a single section in DICOM format, and the data was processed with deep learning algorithms in anonymized form. Control CT images of the patients taken during the PTB planning phase before biopsy and after PTB were used. In our study, a deep learning model was created using the VGG-19 algorithm to classify DICOM images. During the analysis process, steps such as data preprocessing, model creation, training phase and performance evaluation were applied. RESULTS: When the Px status was evaluated in the patients who underwent the procedure, Px did not develop in 271 (67%) of the patients who underwent the procedure, while Px development was observed in 132 cases (33%). When 132 cases that developed Px were evaluated, 76 of these cases (58%) did not require hospitalization, but 54 cases (42%) required hospitalization. According to the results obtained as a result of the analysis process in our study, the VGG-19 model has 68.7% accuracy and 0.68 AUC values. However, the sensitivity value calculated as 52% as a result of the analysis shows that approximately half of the positive cases are predicted correctly. As a result of the application of the model, 73% of negative cases were classified correctly. This can be attributed to the fact that the chosen method has more effective success on negative cases. Finally, the F1 score used to measure the balance between sensitivity and sensitivity values was calculated as 41%.

ARTIFICIAL INTELLIGENCE ALGORITHM



CHIBA NEEDLES



Keywords: Pneumothorax, Lung Mass, Lung Cancer, Deep Learning

COMPUTED TOMOGRAPHIC PULMONARY ANGIOGRAPHY PARAMETERS IN THE ASSESSMENT OF THE RIGHT VENTRICULAR DYSFUNCTION: PROGNOSTIC ROLE IN ACUTE PULMONARY EMBOLISM

Zeycan Kubra Cevval¹, Masıde Arı², İrfan Durmuş³

¹Kastamonu Training and Research Hospital

²Ankara Sanatoryum Training and Research Hospital

³Ankara Etlik City Hospital

Abstract: Computed Tomography Pulmonary Angiography (CTPA) is widely regarded as the gold standard for diagnosing acute pulmonary embolism (PE). There is a early mortality risk (within 30 days) classification based on PESI score, haemodynamic instability, RV dysfunction and cardiac troponin levels in PE patients. This risk classification is used to determine patient prognosis and management. Since the severity of PE and high early mortality risks are associated with right ventricular dysfunction (RVD), in this study it has been hypothesized that quantitative and qualitative CTPA parameters (which indirectly suggest RVD) can predict the prognosis of the disease. A total of 119 patients were included in the study with PE at Dışkapı Training and Research Hospital between 2020 and 2022. Pulmonary embolism severity index (PESI) scores and early mortality risk groups were determined by a pulmonologist according to clinical and laboratory findings. Other parameters related to RVD were measured in CTPA. The parameters evaluated by an 8-year experienced radiologist in CTPA were as follows: Diameters of the right ventricle (RV), left ventricle (LV), pulmonary trunk (PA), pulmonary arteries, ascendant aorta (Ao) and coronary sinus (in mm), the ratio of RV/LV and PA/Ao, the presence of contrast reflux indicating regurgitant flow in the inferior vena cava (VCI) and the morphology of the interventricular septum (IVS). There were 65 female and 54 male patients. The age values ranged from a minimum of 19 to a maximum of 96, with a median value of 68. A significant difference was detected in RV/LV>1 ratios, reflux in VCI and IVS morphology in the midline/left in high-risk early mortality groups and PESI high risk groups ($p<0.0001$). Also a significant difference was detected in terms of numerical variables such as increased PA diameter, Ao diameter and RV diameter. Unlike the literature, no significant difference was detected in coronary sinus diameters and PA/Ao ratios among the risk groups. As a result, in this study, we found that CTPA parameters can predict RVD and can be used as an alternative to ecocardiography to determine of prognosis and early mortality risk groups.

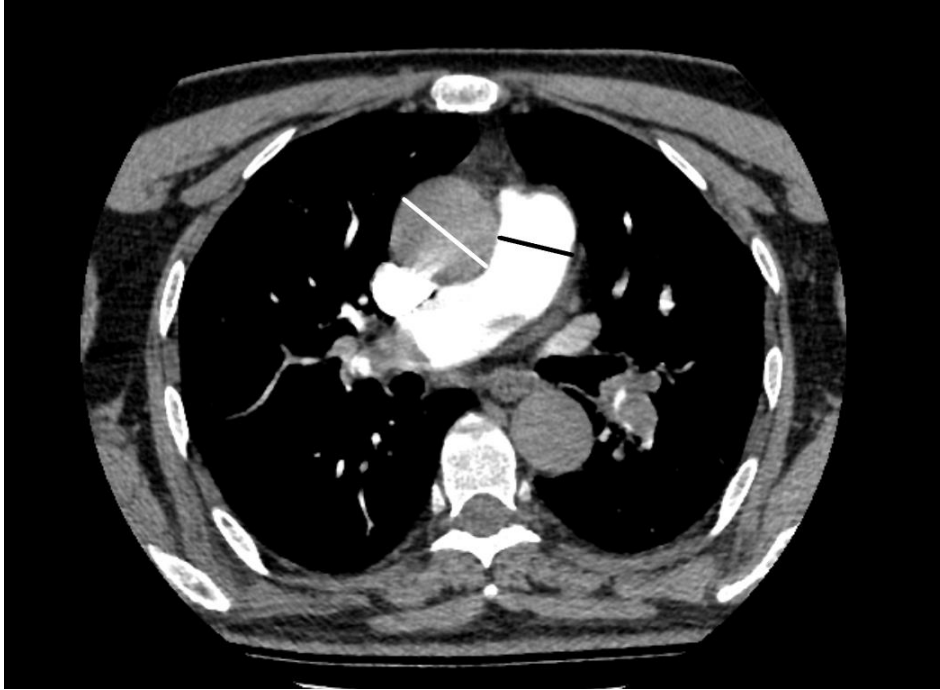


Figure 1: Pulmonary trunk and ascendan aorta diameter measurement is seen.

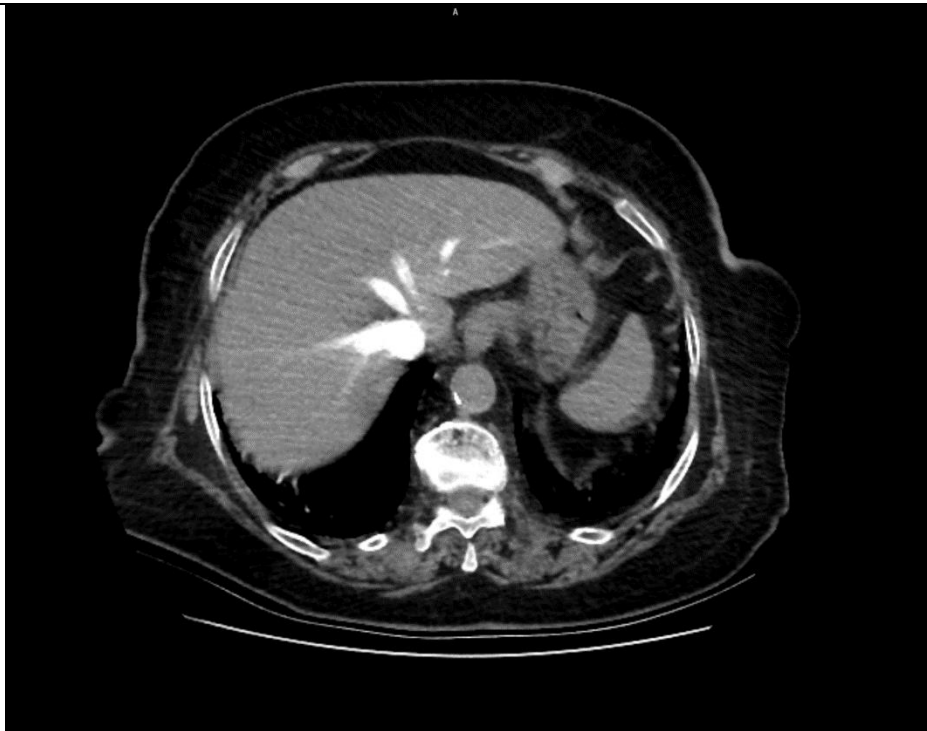


Figure 2: Contrast agent is seen in inferior vena cava and hepatic veins in association with reflux due to right ventricular dysfunction.

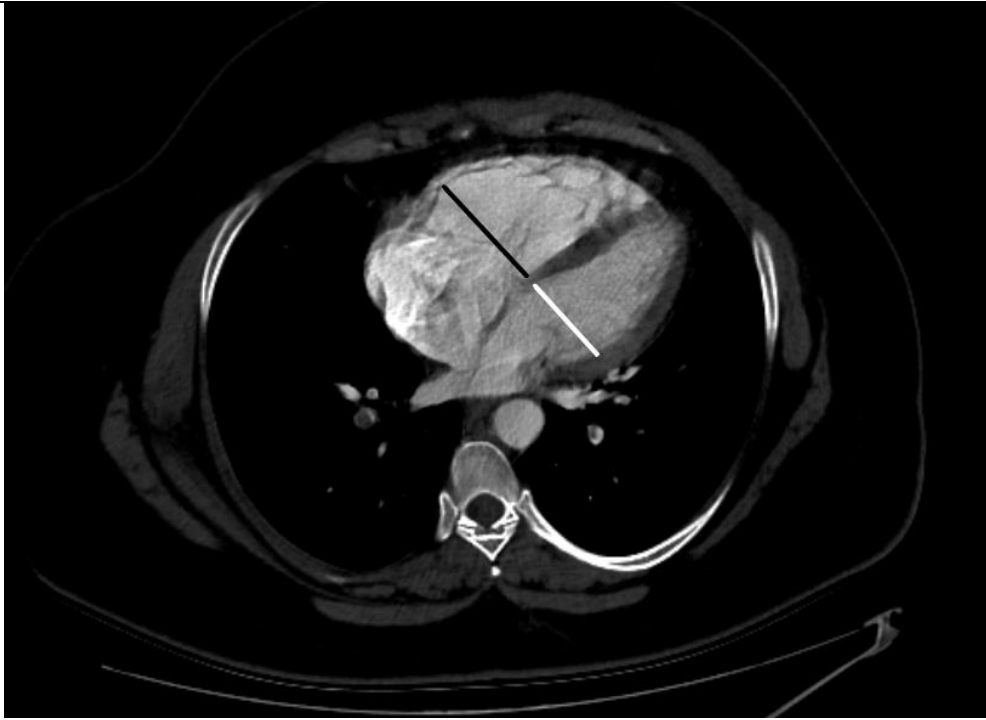


Figure 3: Left and right ventricle diameter measurement below the atrioventricular valve can be seen in the axial image.

Keywords : Computed Tomography Angiography, Pulmonary Artery, Pulmonary Embolism Severity, Right Ventricular Dysfunction

COMPARISON OF A DEEP LEARNING RECONSTRUCTION METHOD WITH OTHER RECONSTRUCTION METHODS IN CORONARY CT ANGIOGRAPHY

Zeynep Nur Akyol Sarı¹, Eda Cingoz², Memduh Dursun³

¹Beth Israel Deaconess Medical Center

²Bagcilar Training and Research Hospital

³Istanbul University Faculty of Medicine

Abstract: Introduction and aim: Deep learning reconstruction (DLR) has been used to improve imaging quality of computed tomography (CT) images via denoising. The purpose of the study was to compare DLR with other reconstruction methods for image quality, sharpness of vessel wall, and the ease of coronary artery evaluation on coronary computed tomography angiography (CCTA). Material and method: Four reconstruction techniques, filtered back projection (FBP), hybrid iterative reconstruction (AIDR), model-based iterative reconstruction (MBIR-FIRST), and DLR-AICE, were evaluated for their impact on image quality and delineation of vessel wall and lumen in coronary artery disease assessments (Fig 1). Signal to noise ratio (SNR) and contrast to noise ratio (CNR), along with soft tissue resolution via SNR of the interventricular septa, and the edge rise distance (ERD) and the edge rise slope (ERS) in the principal coronary arteries (LMCA, LAD, LCX, RCA), were measured at identical locations across all reconstructions (Fig 2,3). Findings: In this comparative analysis, the AICE protocol consistently demonstrated superior performance in several imaging parameters. AICE also achieved statistically significantly higher SNR and CNR in the RCA and LMCA territories compared to the MBIR-FIRST, AIDR and FBP reconstructions ($p<0.01$). Furthermore, ERD values were substantially lower with AICE in the RCA, LMCA, LAD, and LCX arteries ($p\leq0.001$), while ERS values were significantly elevated ($p\leq0.003$). Conclusion: DLR demonstrated the shortest ERD and steepest ERS, indicating superior edge definition and minimal transition zones compared to MBIR, AIDR, and FBP ($p<0.01$). DLR was associated with a significant reduction in blurring due to vessel diameter and pulsation artifacts. It enhanced the ability to distinguish between plaque and normal vessel wall in coronary arteries.

Figure1

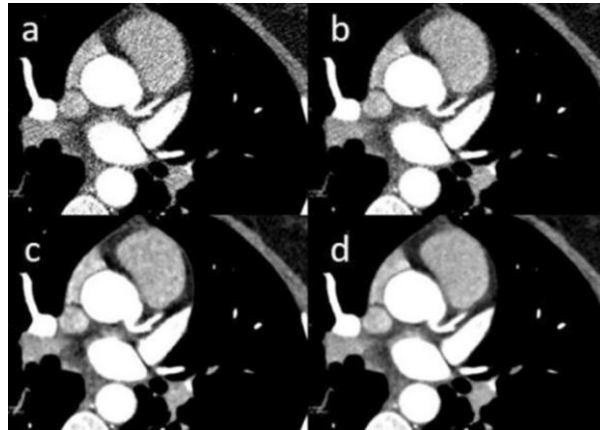


Fig 1. Raw images obtained with Coronary Computed Tomography Angiography were reconstructed using the following methods: FBP (a), AIDR (b), FIRST (c), and AICE (d).

Figure2

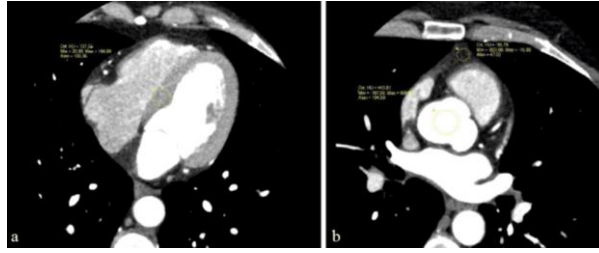


Fig 2. a. Attenuation (HU) and Noise (SD) values were assessed in a Coronary Computed Tomography Angiography image using a circular ROI on the interventricular septum. b. HU and SD values were similarly measured in the ascending aortic lumen and anterior mediastinum using a circular ROI.

Figure3

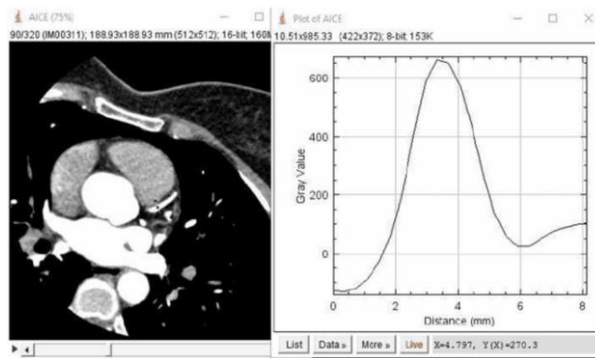


Fig 3. Lines were drawn perpendicular to the vessel wall in Coronary Computed Tomography Angiography images to measure vessel wall sharpness, and the attenuation (HU)/mm graph was generated using the 'Image J' software.

Keywords: Coronary computed tomography angiography, Reconstruction, Deep Learning

IS THERE A CORRELATION BETWEEN CORONARY ARTERY CALCIUM SCORE AND EPICARDIAL/PARACARDIAL ADIPOSE TISSUE QUANTIFICATION

Osman Konukoğlu¹, Murat Kaya¹
¹Gaziantep City Hospital

Abstract: Background and Purpose: Recently, researchers have measured epicardial and paracardial adipose tissue (EAT and PAT) and coronary artery calcium scores to determine the risk of coronary heart disease. We aimed to research the correlation between EAT and PAT CSA values and increased coronary artery calcium scores. Materials and Methods: The research included 117 individuals who underwent coronary CT angiography between November 2023 and July 2024. CT was performed using a 1024-slice dual-source scanner (Somatom Force, Siemens Healthineers). Two experienced radiologists used the Syngo.via software to measure manually the adipose tissue cross-sectional area (CSA) adjacent to the heart, specifically in the apical 4-chamber plane (Figure 1). The two radiologists reached a mutual agreement on the measurement. The software automatically calculates the value and percentile of the coronary artery calcium score. Statistical analysis: The analyses were performed using the SPSS 23.0 (SPSS Inc., IL, United States) software. The Kruskal-Wallis one-way ANOVA was used to compare continuous variables. Pearson's and Spearman's correlation tests were used to examine the relationship between continuous variables. Categorical variables and frequencies were compared using the χ^2 test. Results: The research involved 117 individuals, including 67 (57.3%) males and 50 (42.7%) females. The mean age of all patients was 49.1 ± 11.5 years. The mean age was higher in the group with high calcium scores compared to the group with low calcium scores ($P < 0.001$). Furthermore, the patients in the group with high calcium scores had a greater PAT CSA value than those with low calcium scores ($P = 0.045$) (table 1). Table 2 displays the comparison of variables based on percentile values. There was a significant increase in age in the group with high persantine values ($P < 0.001$). Similarly, the PAT CSA value was significantly higher in the group with a high percentile value ($P = 0.037$). Furthermore, when the percentile value increased, the CACS value was shown to be higher ($P < 0.001$). There was a positive correlation between age and CACS ($r = 0.440$) and between age and EAT ($r = 0.426$) ($P < 0.001$). Conclusion: As individuals get older, their calcium scores tend to rise, resulting in a significant increase in EAT and PAT CSA values.

Measurement of EAT and PAT CSA

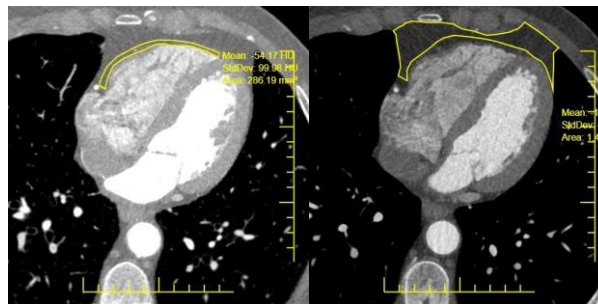


Table 1

	0	1-10	11-100	101-400	401-1000	Patients	P
	(n=98)	(n=2)	(n=7)	(n=4)	(n=6)	(n=117)	
Gender (Male)	54(%55.1)	1 (%50)	6 (%85.7)	2 (%50)	4 (%66.7)	67 (%57.3)	0.640
Age	46.1 \pm 9.1	54	64.8 \pm 11.1	60.7 \pm 8.4	67.4 \pm 14.1	49.1 \pm 11.5	<0.001
EAT	5.4 \pm 1.9	4.9 \pm 2.4	7.7 \pm 3.7	7.4 \pm 2.7	7.1 \pm 2.6	5.7 \pm 2.3	0.08
PAT	5.9 \pm 6.7	3.1 \pm 3.5	10.5 \pm 8.1	8.1 \pm 3.6	17.6 \pm 20.1	6.7 \pm 7.9	0.045

Patient characteristics categorized by coronary artery calcium scoring distribution.

Table 2

	<i>0</i>	<i>0-25</i>	<i>26-50</i>	<i>51-75</i>	<i>76-90</i>	<i>>90</i>	<i>P</i>
	<i>(n=98)</i>	<i>(n=1)</i>	<i>(n=5)</i>	<i>(n=5)</i>	<i>(n=4)</i>	<i>(n=4)</i>	
Gender (Male)	54(%55.1)	0 (0)	5 (%100)	3 (%60)	3 (%75)	2 (%50)	0.319
Age	46.1±9.1	82	64.1±8.2	58.0±8.6	67.0±13.1	64.2±13.4	<0.001
EAT	5.4±1.9	6.68	8.8±4.1	6.1±2.1	7.7±3.6	6.2±1.1	0.06
PAT	5.9±6.7	5.55	12.8±8.3	6.3±4.3	9.5±4.4	17.2±24.7	0.037
CACS	0	3.1	27.9±19.5	90.3±60.1	523.7±323.1	938.1±528.5	<0.001

Comparison of patient characteristics based on percentile values

Keywords: CACS, coronary CT angiography, epicardial adipose tissue, paracardial adipose tissue

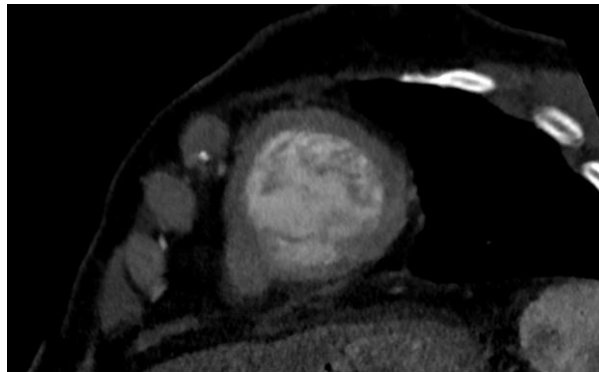
EVALUATION OF THE RELATIONSHIP BETWEEN COINCIDENTALLY DETECTED NON-COMPACTION CARDIOMYOPATHY ON CORONARY CT ANGIOGRAPHY AND THE LEVEL OF CORONARY ARTERY DISEASE AND THE PATIENT'S SYMPTOMS; A RETROSPECTIVE STUDY

Serhat Akış¹, Nurullah Çakır¹, Mustafa Mahmut Barış¹, Ayşe Çolak¹

¹Dokuz Eylul University

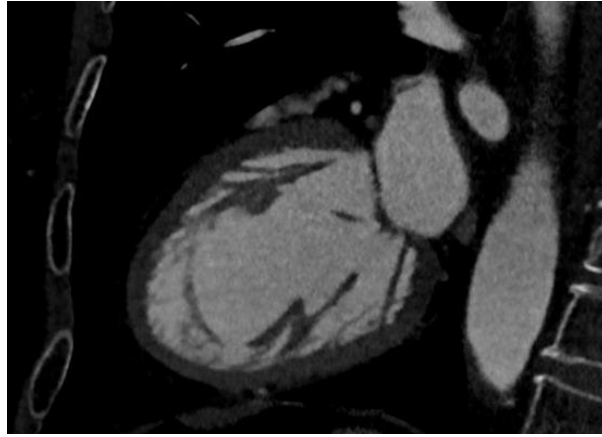
Abstract: **INTRODUCTION** Left ventricular non-compaction describes the presence of excessive trabeculation of the left ventricle. The most common clinical presentations at the time of the first diagnosis are heart failure, thromboembolic events, and different rhythm disturbances. In our daily practice with the patients referred to our department for CAD investigation with coronary CT, we have detected left ventricular non-compaction without accompanying significant coronary artery stenosis. In this study, we aimed to investigate if non-compaction may mimic initial CAD symptoms. **METHODS** Between January 2021 and September 2024, coronary CTAs obtained in our department with suspicion of CAD were scanned and patients with coincidentally detected left ventricular non-compaction were collected. For the control group, patients who were referred with suspected CAD and underwent coronary CTA were selected randomly for a period of 3 months starting from January 2024, matched in terms of age, gender, and comorbidity, but not detected as non-compaction. Our patient group included 43 patients with non-compaction. The selected patient and control groups were evaluated in terms of CAD severity using the CAD-RADS 2.0 classification. Symptoms are noted as chest pain, atypical pain, palpitations, exertional dyspnea. Additionally, the noncompacted myocardium/compacted myocardium ratio was evaluated in the patient group. **FINDINGS** The increase in trabeculation observed in NC-CMP can be measured with CT. For this purpose, Melendez-Ramirez et al. accepted that a non-compact/compact myocardium ratio of 2.3 and above in at least 2 segments in a 17-segment heart model is diagnostic for NC-CMP. The highest NC/C ratio was noted in the non-compaction group and its average was 2,88. In our NC group, no significant coronary artery stenosis was detected in %90.7 (CAD-RADS 0,1,2). In our control group, significant CAD stenosis is seen at the rate of %25.5 (CAD-RADS, 3,4,5). A statistically significant higher level of coronary artery disease was found in the control group between these two groups. **CONCLUSION** Although the non-compaction and control groups had similar presenting symptoms, age, gender and comorbidity factors, no significant CAD was detected in the NC group. This suggests that NC may present with symptoms mimicking CAD in the early period, before the typical late-term findings appear, as stated in our hypothesis.

Elevated NC/C ratio



Elevated non-compacted myocardium at segment 13

Elevated NC/C ratio



Elevated NC/C ratio in a patient with angina. CAD-RADS 0 (coronaries not shown)

Keywords: non-compaction cardiomyopathy, trabeculation, chest pain

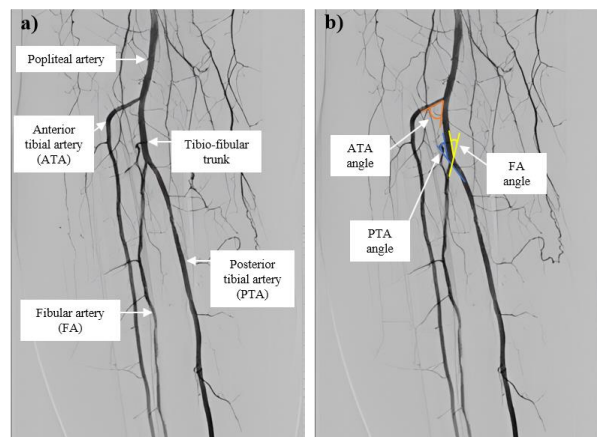
RELATIONSHIP BETWEEN THE ANGLE OF POPLITEAL ARTERY TRIFURCATION BRANCHES AND ATHEROSCLEROSIS BURDEN IN CHRONIC PERIPHERAL ARTERIAL DISEASE

Ahmet Tanyeri¹, Ali Alkaşı¹

¹Aydın Adnan Menderes University, Faculty of Medicine, Department of Radiology, Aydın, Türkiye

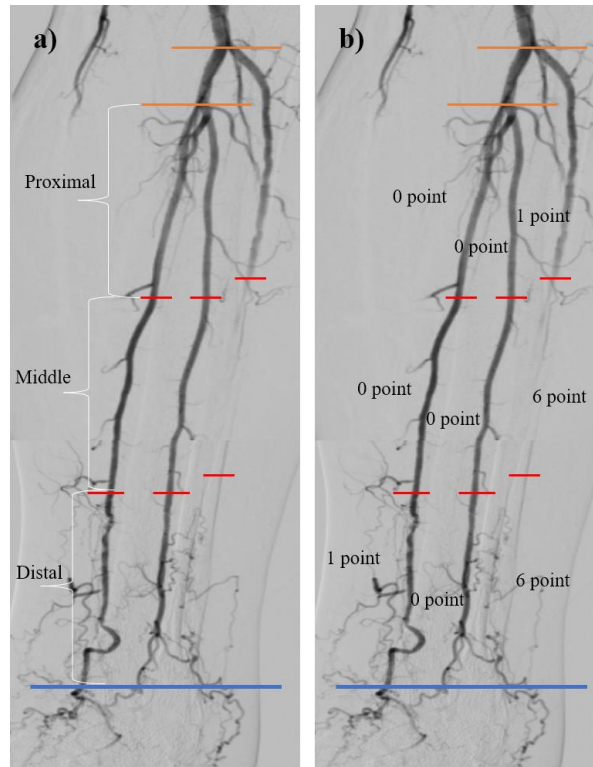
Abstract: Aim: Many different classical etiological factors have been identified for the development of atherosclerosis. However, the hypothesis that vessel geometry may also be related to atherosclerosis has only been investigated in a few coronary artery studies. The aim of this study was to investigate the relationship between the angles of the popliteal artery trifurcation branches and atherosclerosis burden in patients with peripheral arterial disease (PAD). Material-Methods: Digital subtraction angiography (DSA) images of patients who underwent angioplasty for lower extremity PAD between April 2021 and 2023 were retrospectively analysed. Non-type 1a popliteal artery branching, cases of critical femoropopliteal stenosis or occlusion, history of femoropopliteal bypass surgery, and DSA images with motion artefacts were excluded. Angles of the anterior tibial artery (ATA), posterior tibial artery (PTA), and fibular artery (FA) were measured (Figure 1). Atherosclerosis burden was scored from 0 to 18 based on luminal narrowing and occlusion in each artery (Figure 2). Spearman correlation analysis was used to examine the relationship between trifurcation angles and atherosclerosis burden. Results: A total of 68 patients were included, with a mean age of 65 years. Angioplasty was performed on the right side in 56% of patients and on the left side in 44%. The trifurcation angles were $58^\circ \pm 11^\circ$ for ATA, $23^\circ \pm 8^\circ$ for PTA, and $15^\circ \pm 8^\circ$ for FA. Atherosclerotic lesions were located on ATA in 56 patients (82%), on PTA in 50 patients (73%), and on FA in 27 patients (40%). Atherosclerosis burden was calculated as 11 (5–15) points for the ATA, 9 (3–16) points for the PTA, and 3 (0–11) points for the FA (Table 1). The ATA angle showed a weak positive correlation with atherosclerosis burden ($r_s = 0.144$, $p = 0.29$). In contrast, PTA and FA angles exhibited moderate ($r_s = 0.398$, $p = 0.001$) and strong ($r_s = 0.599$, $p < 0.001$) positive correlations, respectively. Conclusion: This study highlights the significant association between the angulation of popliteal artery trifurcations and atherosclerosis burden, suggesting that vessel geometry should be considered in the management of PAD.

Figure 1. A 58-year-old woman with a right diabetic foot wound.



a) The DSA image shows a type 1a trifurcation branching pattern in the popliteal artery. b) An angle measurement of the popliteal artery trifurcation branches is shown. The angle of the anterior tibial artery (ATA) is orange; the angle of the posterior tibial artery (PTA) is blue; and the angle of the fibular artery (FA) is yellow.

Figure 2. A 72-year-old male patient with an ischaemic wound on the left foot.



a) The division of each trifurcation artery into proximal, middle, and distal segments is shown. Orange lines show the origin of ATA, PTA, and FA; blue lines show the intermalleolar line; and red lines show the division of the arteries into three equal segments. b) To calculate the atherosclerotic burden of the trifurcation arteries, the scores given to each segment are shown. In total, ATA received 13 points, PTA 1 point, and FA 0 points.

Table 1. Presence and burden of atherosclerotic lesions in the trifurcation arteries

n: 68	
Angioplasty (right-left)	38 (56%) - 30 (44%)
Trifurcation arteries angle degree	
Anterior tibial artery	58°±11°
Posterior tibial artery	23°±8°
Fibular artery	15±8°
Localisation of atherosclerotic lesions	
Anterior tibial artery	56 (82%)
Posterior tibial artery	50 (73%)
Fibular artery	27 (40%)
Burden of atherosclerosis	
Anterior tibial artery	11 (5-15) points

Posterior tibial artery	9 (3-16) points
Fibular artery	3 (0-11) points

Keywords: atherosclerosis, peripheral arterial disease, angioplasty, trifurcation artery, digital subtraction angiography

EFFICACY OF US-GUIDED PERCUTANEOUS FINE NEEDLE ASPIRATION BIOPSY IN PATIENTS WITH PAROTID GLAND MASSES

Cigdem Oztunali¹, Berat Acu¹, Serhat Demir¹

¹Eskisehir Osmangazi University Medical Faculty, Department of Radiology

Abstract: Aim: To evaluate the efficacy and the diagnostic yield of percutaneous US-guided fine needle aspiration biopsy (FNAB) for parotid gland masses. Methods: This retrospective study included 130 patients with parotid gland mass lesions who underwent US-guided percutaneous FNAB in a single institution between 2014 and 2024. Biopsies were performed by an experienced interventional radiologist using 22G needles, a high-frequency linear transducer, a freehand technique, and an out-of-plane approach. The obtained specimen was injected into 50% alcohol - 50% formalin solution. Cytopathological evaluation was performed using the cytoblock technique. Post-procedural control US examination was performed. The age and gender of the patients, the location and pre-biopsy US features of the lesions, FNAB results, post-biopsy operation, and imaging follow-up status of the lesions were recorded. Results: 139 biopsies were performed in 135 lesions and 130 patients (mean age 57.5, 68 females and 62 males. Five patients had bilateral lesions, and two biopsies were performed on a single lesion of four patients. On cytopathologic evaluations, 117 of 139 lesions (84.1%) were diagnosed and categorized with certainty as malignant or benign. 40 of 67 benign lesions (59.7%) and 16 of 23 lesions (69.5%) were operated on. The accuracy of FNAB in diagnosing benign and malignant cytopathology groups was 100%. 16 of 139 biopsies (11.5%) were classified as non-diagnostic. Of these, 6 (37.5%) were operated on, and 4 (25%) were diagnosed histopathologically as malignant. 6 of 139 biopsies (4.3%) were categorized as suspicious for malignancy. Of these, 3 (50%) were operated on, and 2 (33.3%) were diagnosed histopathologically as malignant. One lesion within the suspicious malignancy FNAB category (16.6%) was operated on and found malignancy negative on histopathology (Tables 1-3). No biopsy-related complications occurred. Discussion: FNB is accurate, sensitive, and specific, with the reported sensitivity and specificity rates between 60% and 92% and 87.7% to 100%. The sensitivity and specificity rates of the present study in FNAB diagnosis of parotid gland masses were in accordance with the literature. Conclusion: FNAB of parotid gland tumors is a useful diagnostic procedure in the workup of parotid gland tumors. Ultrasound guidance may increase the accuracy of FNAB.

Table 1. FNAB and postoperative histopathology results in terms of the number and percentages of biopsies, patients, and lesions.

	Number of biopsies	Number of patients	Number of lesions, bx	Number of lesions, definitive
Warthin tumor	42	38 ^a	42	43
Non-neoplastic	26	24 ^b	24	25
Pleomorphic adenoma	23	23	23	23
Non-diagnostic	16	15 ^c	14 ^d	9
Malignant salivary gland tumor	10	10	10	12
Metastatic tumor	8	8	8	10
Suspicious for malignancy	6	6	6	3

Lymphoid neoplasia	5	5	5	6
Pleomorphic adenoma or basal cell adenoma	2	2	2	0
Salivary gland tumor, NS	1	1	1	0
Basal Cell Adenoma				4
Total	139	132	135	135

a, Bilateral Warthin tm in four patients. b. Two biopsies of a single lesion in 2 patients were non-diagnostic, and one biopsy of a single lesion in 2 patients was non-neoplastic. c, Two biopsies of a single lesion in 1 patient were non-diagnostic. d, One lesion in one patient was biopsied twice (first biopsy was non-diagnostic, 2nd biopsy was mucoepidermoid ca), bx, biopsy, NS, not specified.

Table 2. Table 2. FNAB results in terms of the cytopathology category.

Cytopathology	No / (%)
Benign	94 (67.6)
Warthin Tumor	42 (30.2)
Non-neoplastic	26 (18.7)
Pleomorphic Adenoma	23 (16.5)
Pleomorphic a./ Basal cell adenoma	2 (1.4)
Benign Salivary Gland Tumor, NS	1 (0.7)
Malignant	23 (16.5)
Malignant Salivary Gland Tumor	10 (7.1)
Metastatic Salivary Gland Tumor	8 (5.7)
Lymphoid neoplasia	5 (3.5)
Non-diagnostic	16 (11.5)
Suspicious for Malignancy	6 (4.3)
Total	139 (100)

Table 3. FNAB cytopathology, definitive histopathology, and follow-up results

Warthin tumor (42)	Metastatic tumor (8)
• Operated (15)	• Operated (3)
• Not operated (27)	Gastric carcinoma metastasis (1)
Non-neoplastic (26)	Squamous cell carcinoma metastasis (1)
• Operated (7)	Malignant melanoma of skin metastasis (1)
Tuberculous lymphadenitis (3)	• Not operated (5)
Cholesteatoma (1)	Larynx carcinoma metastasis (1)
Lymphoid tissue (2)	Hypopharynx carcinoma metastasis (1)

IGG-4-related disease (1)	Squamous cell carcinoma of skin metastasis (1)
• Not operated (19)	Malignant melanoma of skin metastasis (1)
Lymphoid tissue (14)	Adenocarcinoma of lung metastasis (1)
Non-neoplastic cyst (4)	Suspicious for malignancy (6)
Suppurative lymphadenitis (1)	• Operated (3)
Pleomorphic adenoma (23)	Metastatic adenocarcinoma
• Operated (15)	Metastatic small cell lung carcinoma
• Not operated (8)	Malignancy-negative lymphoid hyperplasia
Non-diagnostic (16)	• Not operated (3)
• Operated (6)	Regressed on follow-up (2)
Mucoepidermoid carcinoma (1)	Not followed-up (1)
Ductal adenocarcinoma (1)	Lymphoid neoplasia (5)
Marginal zone lymphoma (1)	• Operated (4)
Basal cell adenoma (1)	Follicular lymphoma (2)
Warthin tumor (1)	Marginal zone lymphoma (1)
Synovial chondromatosis (1)	Low-grade B cell lymphoma (1)
• Not operated (10)	• Not operated (1)
Regressed or stable on follow-up (4)	Plasma Cell Neoplasia (1)
Not followed-up (6)	

Keywords: biopsy, cytopathology, fine-needle aspiration biopsy, parotid gland, ultrasonography

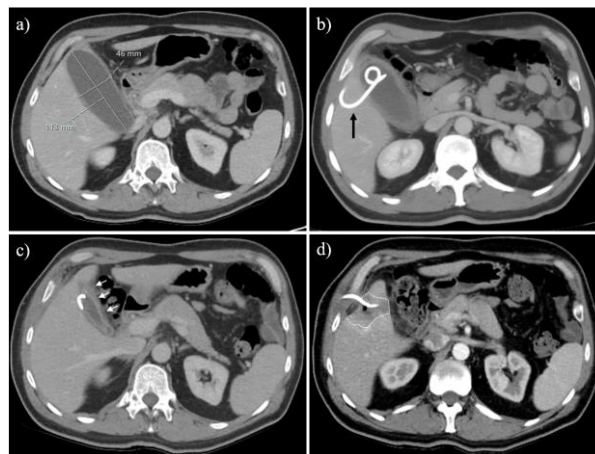
PERCUTANEOUS CHOLECYSTOSTOMY AND ITS IMPACT ON SUBSEQUENT SURGICAL INTERVENTIONS IN ACUTE CHOLECYSTITIS

Ahmet Tanyeri¹, Emir Hüseyin Nevai¹

¹Aydın Adnan Menderes University Faculty of Medicine, Department of Radiology, Aydın, Turkey

Abstract: Aim: The primary aim of percutaneous cholecystostomy (PC) is to provide a temporary solution for patients who are unable to undergo early laparoscopic cholecystectomy. This study aims to evaluate the impact of PC on subsequent surgical procedures. Material-Methods: We evaluated the surgical outcomes of 80 patients (mean age 53±14 years; 36 males, 44 females) who underwent ultrasound-guided transhepatic percutaneous cholecystostomy between 2022 and 2023. The severity of acute cholecystitis was categorized according to the Tokyo Guidelines (2018): 18 patients (22%) were classified as grade 1, 47 patients (59%) as grade 2, and 15 patients (19%) as grade 3, (Table 1). All patients underwent cholecystectomy 4-6 weeks after the PC procedure. The patients were categorized based on whether the cholecystectomy was performed laparoscopically or required conversion to open surgery. Patients in whom laparoscopic surgery was not attempted were not included in the study. Results: Of the 80 patients, cholecystectomy was initiated laparoscopically in all but was converted to open surgery in 59 patients (74%). Specifically, among the grade 1 patients, 10 (56%) required conversion to open surgery (Figure 1). For grade 2, 34 patients (72%) needed open surgery, and all grade 3 patients were converted to open procedures (Table 1). Open surgery was required in 39 (66%) patients due to extensive fibrotic changes detected around the gallbladder during laparoscopic surgery, in 8 (14%) patients due to anatomical changes after PC and in 12 (20%) patients due to residual infection and other reasons (Table 2). Conclusion: Percutaneous cholecystostomy is a critical, life-saving intervention for patients with acute cholecystitis who cannot undergo immediate laparoscopic cholecystectomy. However, careful patient selection and minimizing the interval between PC and surgery are crucial to maintaining the viability of laparoscopic procedures. Delays can lead to increased fibrotic changes, significantly reducing the chances of successfully completing the surgery laparoscopically. Therefore, timely surgical intervention post-PC is imperative to enhance the likelihood of laparoscopic success and minimize complications associated with open surgery.

Figure 1. A 53-year-old male patient with acute calculous cholecystitis. CT images are shown of the patient who had a laparoscopic start and then had an open cholecystectomy.



a) Shown is a CT image of the patient in whom acute calculous cholecystitis was diagnosed after US confirmation. According to the Tokyo guideline (2018), the severity of acute cholecystitis was classified as grade 1. b) The transhepatic percutaneous cholecystostomy drainage catheter (8F pig-tail catheter) placed under local anaesthesia with US guidance is shown by the black arrow. The CT scan was performed 2 days after the procedure due to complaints of pain and increased infection parameters. c) Control CT scan 4 weeks after percutaneous cholecystostomy. Heterogeneity associated with fibrosis at the fat interface adjacent to the semi-contracted gallbladder wall is shown by white arrows. d) Another section of the same scan as in image C shows an area of local parenchymal infection in the trace of the drainage catheter in liver segment 5 (dotted line).

Table 1. Severity grading of acute cholecystitis in accordance with the Tokyo guidelines (2018) and surgical procedure

Severity of acute cholecystitis	Percutaneous cholecystostomy	Open surgery	Laparoscopic surgery
Grade 1-Mild	18 (22%)	10 (56%)	8 (44%)
Grade 2-Moderate	47 (59%)	34 (72%)	13 (28%)
Grade 3-Severe	15 (19%)	15 (100%)	-
Total	80 (100%)	59 (74%)	21 (26%)

Table 2. Reasons for patients with acute cholecystitis to convert from laparoscopic to open surgery

Open surgery reasons	n: 59
Fibrotic changes and adhesions	39 (66%)
Anatomic changes	8 (14%)
Residual infection or abscess	7 (12%)
Other conditions (technical difficulties, previous abdominal surgery, obesity)	5 (8%)

Keywords: acute cholecystitis, percutaneous cholecystostomy, laparoscopic cholecystectomy, open cholecystectomy

THE ROLE OF KAISER SCORING SYSTEM IN BREAST MRI FOR RISK STRATIFICATION OF INTRADUCTAL PAPILLOMA

Gülbanu Güner¹, Ayşe Şilan Kapuçi¹, Fatma Kulalı¹

¹University of Health Sciences Umraniye Training and Research Hospital, Department of Radiology

Abstract: Objective: The differentiation of benign Intraductal papilloma (IDP) from IDP with high risk for malignancy is important for patient management. Therefore, we aimed to investigate the role of the Kaiser scoring system for risk stratification of IDP in magnetic resonance imaging (MRI). Methods and Materials: The Institutional Review Board approved this retrospective study, and informed consent was waived. A total of 42 patients with 44 histopathological proven IDP who had undergone dynamic contrast enhanced breast MRI were included. The mean age of patients was 46 years (range: 23-71 years). MRI features were evaluated by two radiologists. Kaiser score (root sign, dynamic enhancement time curve, circumscribed/irregular margins, internal enhancement pattern, edema around lesion) was recorded. A score between 1 and 11 is assigned. Scores below 5 are considered benign whereas higher scores require histological examination. All patients had histopathological results. Patients were classified into three groups according to histopathological results: low-risk, moderate-risk and high-risk groups. Low-risk group consisted of patients with benign IDP whereas moderate-group included patients with proliferative or florid ductal component containing IDP. IDP with atypia or ductal invasive carcinoma component formed high-risk group. The relationship between Kaiser score and histopathological groups was statistically analyzed by Kruskal Wallis test. Inter-reader agreement was investigated by Pearson correlation coefficient. Results: A total of 44 lesions were enrolled in our study. Of 44, there were 24, 11, and 9 lesions in low-risk, moderate-risk, and high-risk group, respectively. There was no statistically difference between three groups about age of patients and size of tumor ($p>0.05$). Kaiser scores were found significant between three groups ($p<0.05$). Higher Kaiser scores were obtained at high-risk group. There was strong positive correlation between two radiologists ($r=0.94$, $p<0.05$). Conclusion: The risk prediction in patients with IDP is possible with estimation of Kaiser score on MRI. We recommended to point out Kaiser score in daily MRI report for IDP to avoid unnecessary invasive procedures.

Keywords: breast, intraductal papilloma, kaiser score, magnetic resonance imaging, risk stratification

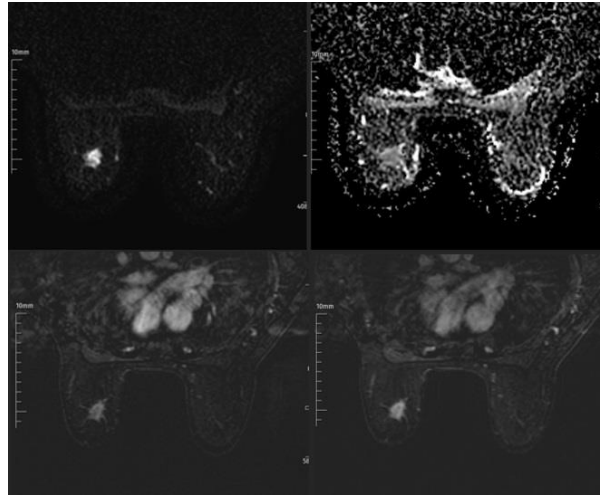
RELATIONSHIP BETWEEN ADC VALUES AND HISTOPATHOLOGIC PROGNOSTIC MARKERS OF BREAST CARCINOMA

Ayşegül Taşdöğen¹

¹Ümraniye Eğitim ve Araştırma Hastanesi

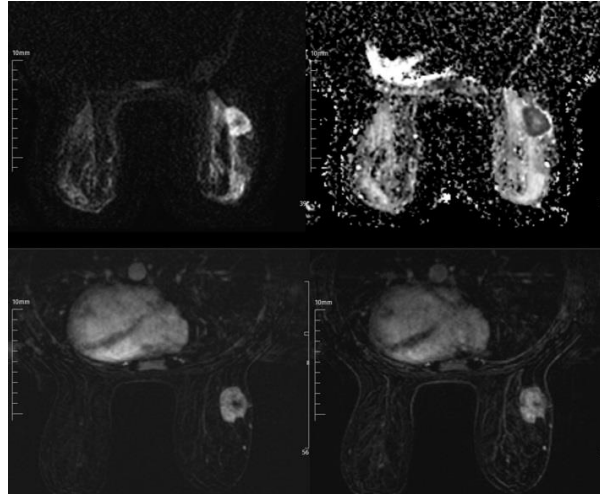
Abstract: **OBJECTIVE:** In breast cancer, diffusion-weighted imaging (DWI) can be used to assess tumor cellularity and predict response to treatment. The apparent diffusion coefficient (ADC) is a quantitative measure derived from DWI that reflects the degree of water diffusion restriction in a tissue. Lower ADC values are associated with higher cellularity and more aggressive tumors. In our study, we aimed to demonstrate the relationship between histopathological prognostic markers and ADC values. We analyzed the relationship between ADC values and Ki-67 index, estrogen receptor, progesterone receptor, and c-erb-B2 (Her2/neu) values in pathology results of 40 patients. **MATERIALS AND METHODS:** In this retrospective study, radiological and histopathological findings of patients diagnosed with breast carcinoma by tru-cut biopsy in our clinic between January 2022 and May 2024 were evaluated. Among the cases, those with a maximum interval of 2 months between the biopsy procedure and breast MRI examination were selected. The ADC values of the lesions detected in the MRI examination were calculated by identifying contrast-enhancing solid areas in dynamic series and using a circular ROI (region of interest) from the area with the lowest signal intensity on ADC mapping. The agreement between ADC value and Ki-67 proliferation index, estrogen receptor (ER), progesterone receptor (PR), and c-erbB-2 score was assessed using the Kruskal-Wallis H test. **FINDINGS:** In the analysis performed with groupings, a significant relationship was found between ADC values and Ki-67 proliferation index (p: 0.036). No significant relationship was found between ADC values and ER, PR, and c-erbB-2 scores. **CONCLUSION:** In this study on patients with breast cancer, a significant correlation was found between ADC values, indicating tumor diffusion restriction, and Ki-67 index, reflecting tumor proliferation rate. This finding suggests that the DWI sequence in Breast MRI could be a useful non-invasive tool for predicting the biological behavior of the tumor. More research is needed to clarify the relationship between ADC values and specific prognostic markers and to determine how ADC values can be best used in clinical practice.

Image 1



DWI, ADC, and dynamic contrast-enhanced MRI imaging were performed on a 60-year-old female patient with a lesion in the upper inner quadrant of the left breast. The average ADC value of 1029.7 was measured with a circular ROI from the area with the most diffusion restriction in the lesion. Pathology results reported a Ki-67 index of 40%, ER positivity of 35%, PR positivity of 1%, and positive c-erb b2 (score 3).

Image 2



DWI, ADC, and dynamic contrast-enhanced MRI imaging were performed on a 32-year-old female patient with a lesion in the upper outer quadrant of the right breast. The average ADC value of 539.7 was measured with a circular ROI from the area with the most diffusion restriction in the lesion. Pathology results reported a Ki-67 index of 80%, ER positivity of 80%, PR positivity of 80%, and positive cerb b2 (score 3).

Table 1

	H statistics	P value
ADC value – Ki 67	6.66803	0.0356497
ADC value – Cerb B2 score	2.8279	0.243181
ADC value – PR	1.9317	0.380659
ADC value – ER	1.54452	0.461968

The Kruskal-Wallis H test results indicate a statistically significant relationship between ki 67 and adc values ($p < 0.05$). No statistically significant relationship was found between the other variables and adc values ($p > 0.05$).

Keywords: ki-67 antigen, breast carcinoma, Diffusion MRI

THE EFFECTIVENESS OF ULTRASOUND-GUIDED PERCUTANEOUS tPA INJECTION IN THROMBOSED ARTERIOVENOUS FISTULA

Ahmet Taha Kayaoğlu¹, Mehmet Beyazal¹

¹Rize Research and Training Hospital

Abstract: Introduction Chronic kidney failure requires reliable vascular access for hemodialysis, with arteriovenous (AV) fistulas—both native and grafts—preferred over catheters due to lower infection risk and longer-term effectiveness. However, challenges such as thrombosis and maturation issues can complicate their successful use, underscoring the need for careful management to optimize outcomes in these patients. Aim To evaluate the effectiveness of ultrasound-guided tPA injection in patients with thrombosis developing in the efferent vein of arteriovenous fistulas Materials and Methods Between 2019 and 2024, 15 patients with total thrombosis in the efferent vein of arteriovenous fistulas with total thrombosis and no aneurysms larger than 3 cm were included. Patients with thromboses lasting longer than 2 weeks were not included. Under ultrasound guidance, tPA injection was administered starting from the distal segment of the thrombosed fistula to the proximal segment using a 27G needle. Achieving effective clearance for hemodialysis and palpable thrill were considered successful outcomes. Results Average thrombosed segment length was 12.8 ± 7 cm, age was 61.6 ± 10.8 years, fistula age was 28.8 ± 13.7 months, and tPA dose was 6.6 ± 2.3 mg. In 7 patients (%46.6), there was minor bleeding at the needle insertion sites, which stopped with compression. No additional interventional treatment and erythrocyte replacement was required. Mechanical thrombectomy was performed in 2 patients (%13.3) due to residual chronic thrombus. PTA (percutaneous transluminal angioplasty) was performed in all patients. after tPA. 2 patients (%13.3) required additional sessions within 1 month. Effective flow was achieved in all patients after interventional procedures. Conclusion Ultrasound-guided tPA injection is an effective and minimally invasive treatment method and has lower complication; especially for acute thromboses.

Keywords: Tissue Plasminogen Activator, Hemodialysis fistulas, Thrombosis, Percutaneous

EFFICACY OF ULTRASOUND-GUIDED MICROWAVE ABLATION IN THE TREATMENT OF BREAST FIBROADENOMAS: A FOLLOW-UP STUDY

Mehmet Cingoz¹, Emel Esmerer¹, Eda Cingoz², Suleyman Sonmez³

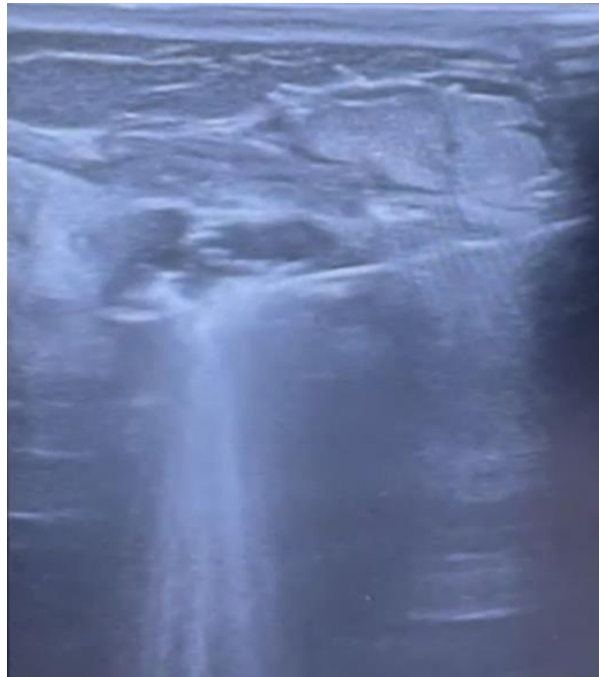
¹Basaksehir Cam and Sakura City Hospital

²Bagcilar Training and Research Hospital

³Kanuni Sultan Suleiman Training and Research Hospital

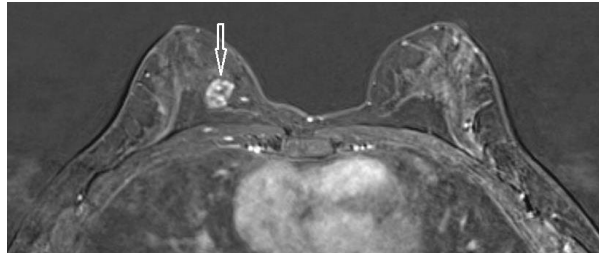
Abstract: Introduction and aim: The aim of the study was to ascertain the efficacy of ultrasound-guided microwave ablation (MWA) in the management of breast fibroadenomas. Material and method: The study included 37 females with histopathologically confirmed breast fibroadenomas. Vascular scores, symptoms using visual analogue scale and tumor volumes measured via ultrasound were recorded pre-procedure and post-procedure at 1, 3, 6, and 12 months. The vascular score was graded according to the following scale: grade 0 = no vascularity, grade 1 = only perinodular vascularity, grade 2 = <50% intra-nodular vascularity, and grade 3 = >50% intra-nodular vascularity. In a supine position, the patients underwent hydrodissection around the lesion under local anesthesia and sterile conditions. MWA was applied with 20 W output and 3 mm active edge for tumors ≤2 cm, and 30 W output and 5 mm active edge for tumors >2 cm in diameter using the withdrawal technique (Fig 1). The differences in tumor volume changes before and after the MWA procedure and across the follow-up period were analyzed with ANOVA, while paired-samples t-test was used to compare pre- and post-procedure changes in symptom and vascular score. Findings: The initial mean tumor volume of $4.38 \pm 4.74 \text{ cm}^3$ (0.37-23.60) decreased to $2.22 \pm 2.69 \text{ cm}^3$ (0.10-14.00) at 1 month ($p<0.05$), $1.79 \pm 2.22 \text{ cm}^3$ (0.05-11.40) at 3 months ($p<0.05$), $1.39 \pm 1.81 \text{ cm}^3$ (0.04-9.20) at 6 months ($p<0.05$), and $1.10 \pm 1.58 \text{ cm}^3$ (0.04-8.10) at 12 months ($p<0.05$) post-MWA (Table 1). Symptom scores improved markedly from a pre-procedure average of 6.32 ± 1.84 (4-10) to a 12-months post-ablation average of 2.54 ± 0.69 (1-4) with a 95% CI of 3.26-4.31. Pre-procedure vascular scores were classified as grade 1 in 5 (13.5%), grade 2 in 23 (62.2%), and grade 3 in 9 (24.3%) patients. Post-procedure evaluations showed a significant shift, with 22 patients (59.5%) achieving grade 0 and the remaining 15 (40.5%) improving to grade 1 with a 95% CI of 1.47-1.94 (Fig 2, 3 and Table 2). Conclusion: Post-procedural assessment of ultrasound-guided MWA of breast fibroadenomas demonstrated significant tumor volume loss and improved symptom and vascular scores, affirming the effectiveness of the treatment.

Figure1



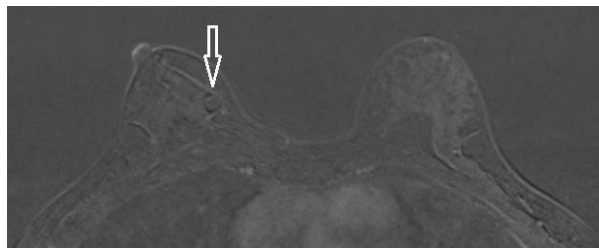
Multiple echogenic microbubbles were recorded around the antenna within the fibroadenoma during the ultrasound-guided microwave ablation.

Figure2



Pre-procedural contrast-enhanced breast MRI revealed a histopathologically verified vividly contrast-enhancing fibroadenoma in the deep plane of the inner quadrant of the right breast (white arrow).

Figure3



Contrast-enhanced breast MRI taken at the 12th month follow-up post-procedure in the same patient as Fig 2, revealed significant regression in both the vascularization and size of the lesion (white arrow).

Table1

	Min	Max	Mean±standard deviation	P value
Baseline	0.37	23.60	4.38 ± 4.74	
1 months	0.10	14.00	2.22 ± 2.69	0.011 *
3 months	0.05	11.40	1.79 ± 2.22	0.001*
6 months	0.04	9.20	1.39 ± 1.81	0.000*
12 months	0.04	8.10	1.10 ± 1.58	0.000*

Changes in fibroadenoma volume (cm3) following MWA

Table2

Score	n(%) Pre-procedure	n(%) Post-procedure
Grade 0		22 (59.5%)
Grade 1	5 (13.5%)	15 (40.5%)

Grade 2	23 (62.2%)	
Grade 3	9 (24.3%)	

Vascular scores before and after MWA.

Keywords: Fibroadenoma, Microwave ablation

DIGITAL BREAST TOMOSYNTHESIS-GUIDED BIOPSY: INITIAL EXPERIENCE

Umur Anıl Pehlivan¹, Hülya Özdemir¹, Bermal Hasbay², Filiz Aka-Bolat²

¹Başkent University Adana Dr. Turgut Noyan Application and Research Center Department of Radiology

²Başkent University Adana Dr. Turgut Noyan Application and Research Center Department of Pathology

Abstract: Introduction: Digital breast tomosynthesis (DBT)-guided biopsy is increasingly recognized as the preferred method for targeting abnormalities that are predominantly visualized on mammography, such as microcalcifications, architectural distortions, asymmetries, and masses without corresponding sonographic findings. The aim of this study was to present our initial experience with DBT-guided biopsy. Materials and Methods: This retrospective study was conducted at a single institution. Between July 2023 and June 2024, DBT-guided biopsies were performed on 56 lesions in 43 patients at our hospital's breast center. We reviewed the pathology results of these lesions and documented any complications encountered. Results: Among the biopsied lesions, 29 were located in the left breast and 27 in the right breast. Microcalcifications were the most prevalent abnormality detected on mammography. A 14-gauge tru-cut biopsy was performed on 52 lesions. Either a 7 or a 10-gauge vacuum-assisted biopsy was performed on the remaining four lesions. Proliferative breast lesions with atypia were identified in 5.3% (n=3) of cases, while papillary neoplasia was diagnosed in 1.8% (n=1). Ductal carcinoma in situ (DCIS), lobular carcinoma in situ (LCIS), and/or invasive tumors were present in 10.7% (n=6) of the lesions. The remaining lesions were diagnosed as proliferative and/or non-proliferative lesions without atypia. Discrepancies between imaging findings and histopathologic results were categorized as discordant, leading to additional interventions such as surgical biopsy. Of the lesions, 23.2% (n=13) were referred for surgical excision following mammography-guided wire localization. In the surgical specimens, two patients were found to have DCIS (previously identified proliferative lesion with atypia), and one patient had an invasive tumor associated with DCIS (previously identified as a proliferative lesion with atypia). The final pathological diagnoses of the remaining ten lesions did not upgrade. The vast of patients experienced clinically insignificant hematoma or superficial bruising. The complication rates were as follows: vasovagal reactions occurred in 18.6% (n=8) of patients, and large hematomas were observed in 2.3% (n=1). Conclusion: DBT-guided biopsy is a minimally invasive and safe procedure with a low incidence of non-serious complications. Accurate correlation between imaging findings and histopathologic results remains crucial and constitutes an essential component of the biopsy process.

Keywords: Digital Breast Tomosynthesis, Breast Neoplasms, Biopsy.

ULTRASOUND-GUIDED THROMBIN INJECTION FOR THE TREATMENT OF ARTERIAL PSEUDOANEURYSM

Aslı Aras¹, Gizem Nur Çolak Aslan¹, Eren İsmailoğlu¹, Mehmet Hakan Pıçak¹

¹*Izmir Bakircay University Çiğli Regional Education Hospital*

Abstract: Introduction: Pseudoaneurysm is formed when the sac is not surrounded by the triple layers of arterial structures (intima, media, adventitia) and disrupted. Predisposing factors for pseudoaneurysm development include anticoagulant therapy, use of a wide vascular sheath during catheterization, inadequate post-procedural compression, superficial or deep femoral artery puncture, obesity, hypertension, arterial calcifications, thrombocytopenia, and platelet dysfunction. Pseudoaneurysm treatment options; USG-guided compression, direct percutaneous embolization with embolic agents, endovascular treatment methods (transcatheter embolization, stent-graft application). Method: In our retrospective study, we have investigated direct percutaneous embolization with thrombin in treating pseudoaneurysms. After the embolization area and USG probe were prepared under standard sterile conditions, local anesthetic was applied to the procedure area. Embolization was performed under USG guidance with 22 G needles. Low-volume, slow injections (average 1000 u/ml thrombin) were performed by entering the cavity from the upper part of the aneurysm. In 42 sessions, thrombin injection pseudoaneurysm volume, thrombin volume, complete occlusion, and findings related to recurrence were evaluated retrospectively. Results: Percutaneous thrombin injection was administered to 39 patients (22 males, 17 females) with pseudoaneurysms in two brachial and 37 femoral arteries (14 common femoral arteries, 22 superficial femoral arteries, 1 deep femoral) following 25 coronary, 12 peripheral angiography, two dialysis fistula interventions. The mean age of the patients was 62.61 ± 14.07 and the mean of aneurysm volume was $14,41 \pm 18,69$ mm³. Thrombin injection between 0.5 and 7cc was performed in 39 pseudoaneurysms. All patients were re-examined with RDUS 1 day later. Complete occlusion occurred in 36 patients. During the follow-up, recurrence occurred in 3 of the patients. Repeated injections were given to 3 patients who developed recurrence. A second recurrence two patients were referred to surgery after second recurrence occurred. The success rate after the procedure was over 94,8% and no major complications were observed. Conclusion: In the treatment of iatrogenic pseudoaneurysms, thrombin injection treatment with ultrasonography is a fast, comfortable and safe method compared to pseudoaneurysm compression and surgical treatment options. Keywords: Pseudoaneurysm, thrombin, ultrasonography

Keywords: Pseudoaneurysm, thrombin, ultrasonography

EFFICACY AND SAFETY OF ENDOVASCULAR EMBOLIZATION WITH N-2-BUTYL-CYANOACRYLATE IN PATIENTS WITH MASSIVE HEMOPTYSIS: RESULTS OF A SINGLE-CENTER EXPERIENCE

Merve Solak¹, Mehmet Beyazal¹

¹*Recep Tayyip Erdogan University, Department of Radiology, Rize, Türkiye*

Abstract: Hemoptysis is defined as the coughing up of blood from the respiratory tract. Hemoptysis is a life-threatening respiratory emergency and may indicate a serious underlying medical condition. Therefore, massive hemoptysis requires urgent evaluation and intervention. Although chest radiography can diagnose hemoptysis, it can miss many pathologies. In 90% of cases, the source of massive hemoptysis is the bronchial circulation. Bronchial artery embolization (BAE) is now recognized as the most effective first-line treatment for hemoptysis. The aim of this retrospective evaluation was to assess the short-term efficacy of n-butyl-2-cyanoacrylate (NBCA) adhesive embolization in the treatment of acute hemoptysis with UAE and to demonstrate the safety of this embolic material. This study was designed as a single-center and retrospective study. Among 50 patients who underwent endovascular treatment for hemoptysis at the Interventional Radiology Clinic of Recep Tayyip Erdoğan University Faculty of Medicine Training and Research Hospital between January 2020 and July 2024, those who used NBCA adhesive embolization were included. Thirty-five patients were enrolled within the specified time frames. The procedures were performed by the interventional radiologist in the angiography suite under local anesthesia only. The images were evaluated, and the artery thought to be the source of hemoptysis and targeted for embolization was superselectively catheterized with a microcatheter. Glu-lipiodol mixture was used as embolization material. Occlusion of the relevant vascular structure was ensured without reflux. Post-procedural complications, technical success, clinical success in the first 24 hours and the first 1 month were recorded. The study included 35 patients with a mean age of 63.5 years. The most common etiologic diseases were tuberculosis, bronchiectasis and lung cancer. Endovascular treatment was successful in all patients. The clinical success rate within the first month was 98.7%. The most common findings on angiography were dilated bronchial artery, hypervascularity and arteriovenous shunt. There were no complications causing mortality and morbidity. Endovascular therapies are the preferred treatment modality for hemoptysis. Our study shows that NBCA embolization is an effective treatment modality for early intervention in patients with hemoptysis. The absence of major complications, including ischemic damage to the airways and lung parenchyma, demonstrates the safety of NBCA embolization.

Keywords: Hemoptysis, bronchial artery embolization, N-2-Butyl-Cyanoacrylate, computed tomography angiography

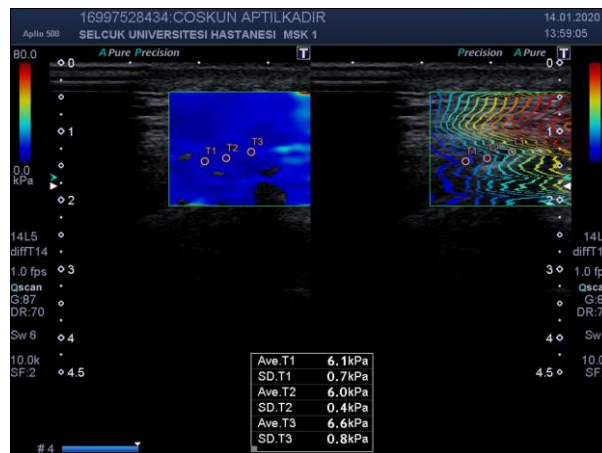
COMPARISON OF TEMPOROMANDIBULAR JOINT DISC IN CHRONIC RENAL FAILURE PATIENTS AND HEALTHY ADULTS WITH SHEAR WAVE ELASTOGRAPHY

Nusret Seher¹, Mehmet Öztürk¹, Abdi Gürhan¹, Alaaddin Nayman¹, Halil Özer¹,
Gülperi Çelik²

¹Selcuk University, Faculty of Medicine, Department of Radiology
²Selcuk University, Faculty of Medicine, Department of Nephrology

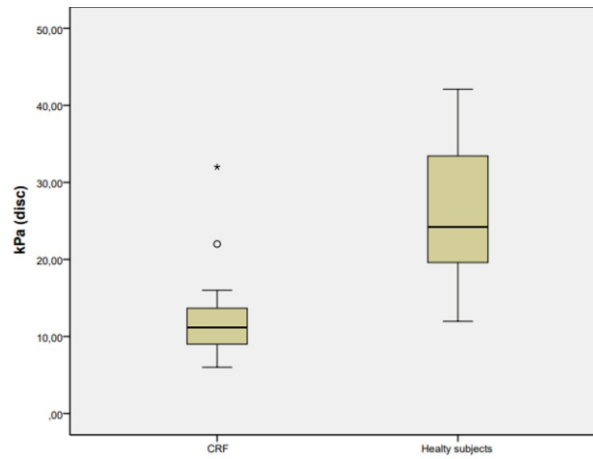
Abstract: Introduction: Chronic Kidney Disease (CRF) is a common condition that causes illness and death in society (1). The articular disc of the temporomandibular joint (TMJ) can be affected by degenerative and inflammatory processes, leading to TMJ disorders (2). Shear Wave Elastography (SWE) provides quantitative results about tissue elasticity. Temporomandibular disc elastography can aid in diagnosing disc conditions caused by systemic diseases and evaluating treatment response in patients (3,4). This study aimed to examine how CRF affects the temporomandibular disc in patients with chronic renal failure compared to healthy volunteers. Materials- Methods: This cross-sectional study, conducted between March-December 2022 at our university hospital, included 30 patients with CRF and 30 adults without CRF or other chronic diseases. The study utilized SWE to obtain kPa (kilopascal), m/s (meter/second) values, which were then compared. The SWE measurements were taken from the temporomandibular disc of the patient group, with the average of ROI taken from 3 different parts of the patients' bilateral temporomandibular disc, ensuring a comprehensive and reliable assessment that you can trust (Figure 1). Results: The average ages of the patient group and healthy volunteers were similar ($p > 0.05$). The average kPa, m/s values of SWE measurements made from the temporomandibular disc of the patient group were lower than those of the healthy group (Figure 2,3, Table 1). Conclusion: Our findings, consistent with previous studies, indicate that multisystem inflammation caused by CRF is an important trigger for musculoskeletal and temporomandibular disc damage in patients. The decrease in kPa and m/s values measured by SWE in the patients' temporomandibular discs compared to the healthy group of similar age also supports this. More importantly, our study demonstrates that SWE has the potential to be a valuable tool in the evaluation of muscles in patients with CRF, providing you with the latest advancements in CRF research. References 1. Ruiz-Ortega M, et al. Targeting the progression of chronic kidney disease. Nat Rev Nephrol. 2020;16(5):269–288. 2. Habibi HA, et al. Quantitative temporomandibular disc and masseter muscle assessment with shear wave elastography. Oral Radiol. 2022 Jan;38(1):49-563. Arijji Y, et al. Shearwave sonoelastography for assessing masseter muscle hardness in comparison with strain sonoelastography: study with phantoms and healthy volunteers. Dentomaxillofac Radiol. 2016;45(2):20150251. 4. Niitsu M, et al. Muscle hardness measurement using ultrasound elastography: a feasibility study. Acta Radiol. 2011;52:99–105.

Figure 1



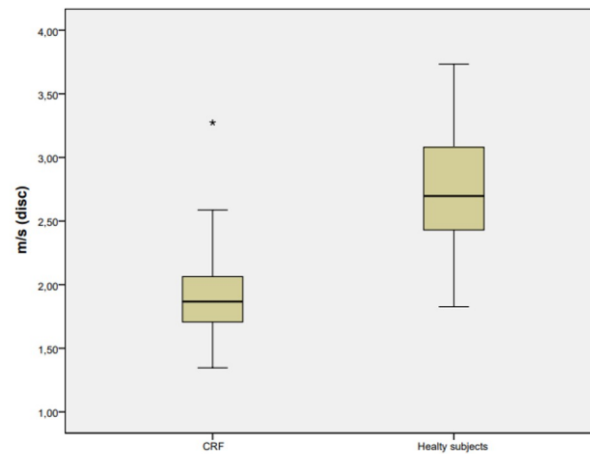
SWE measurements were made from the anterior, middle and posterior of the disc.

Figure 2



There were significant differences between the kPa measurements of the disc of patients with CRF and healthy adults.

Figure 3



There were significant differences between the m/s measurements of the disc of patients with CRF and healthy adults.

Table 1

AUC: Area under the curve, 95% CI: 95% confidence interval.

	AUC (95% CI)	p-value	Cut- off	Sensitivity	Specificity
kPa (disc anterior)	0.976 (0.944- 1)	<0.001	>20.05	93.3	96.6
kPa (disc middle)	0.923 (0.852- 0.994)	<0.001	>16.15	86.7	89.7
kPa (disc posterior)	0.783 (0.663- 0.903)	<0.001	>17.05	66.7	89.7

m/s (disc anterior)	0.952 (0.899-1)	<0.001	>2.46	90.0	96.6
m/s (disc middle)	0.874 (0.779-0.968)	<0.001	>2.24	86.7	86.2
m/s (disc posterior)	0.702 (0.567-0.838)	0.008	>2.51	50.0	89.7
kPa (disc)	0.951 (0.891-1)	<0.001	>16.07	96.7	93.1
m/s (disc)	0.908 (0.831-0.985)	<0.001	>2.36	80.0	93.1

ROC analysis results of 2D SWE parameters for differentiation CRF from healthy subjects.

Keywords: Chronic Kidney Disease, Inflammation, Shear Wave Elastography, Temporomandibular Disc

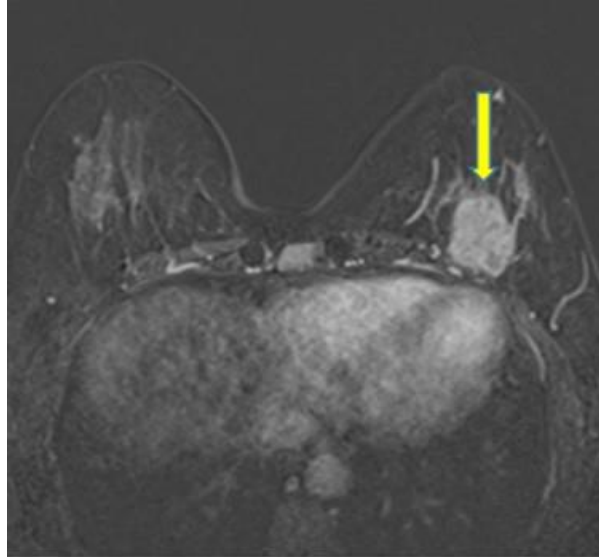
THE RADIOLOGICAL-PATHOLOGICAL CORRELATION IN BREAST CANCER CASES WITH NEOADJUVANT CHEMOTHERAPY

Gulten SEZGIN¹, Merve KURT KOCAK¹

¹Izmir Katip Celebi University Atatürk Training and Research Hospital, Radiology

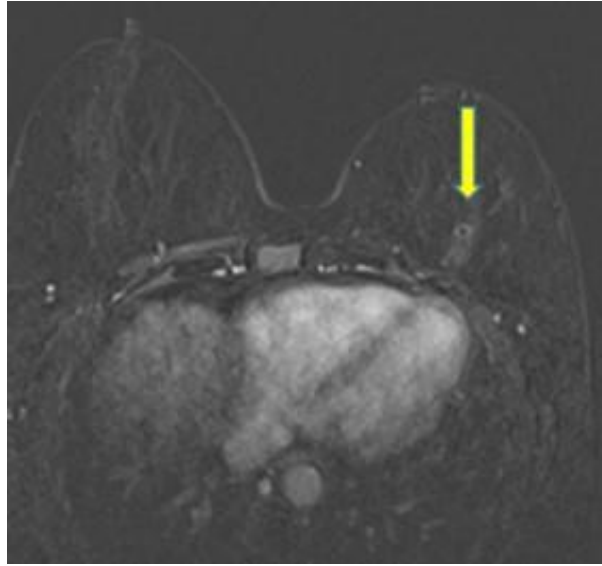
Abstract: Objective: In this study, we discussed the radiological-pathological correlation of the breast cancer cases in which received neoadjuvant chemotherapy (NAC), procedures started and ended in our center. Materials and Methods: Local ethics committee approval was obtained (2021/374). Of the 108 cases diagnosed with breast cancer, for whom a diagnosis and NAC decision were made between January and December 2020, 81 cases whose treatment stages were completed in our center were included in the study. Cases who underwent NAC or surgery at an external center were excluded from the study. Pearson correlation test was used in statistical analysis. Results: While the average age was 52 ± 1 mm (31-74), the average long axis of the lesions was 28 ± 2 mm (10 – 61). While 72 of the malignant lesions were invasive ductal (88. 8 %), 6 were invasive lobular (7. 4 %), and there was one invasive papillary, metaplastic, and mucinous (3. 7 %). 16 of the cases (19. 7%) were triple negative, 26 (32. 1%) were HER 2 positive, and the others (n = 39, 29.2%) were luminal type breast cancer. Pathological complete response (pCR) was achieved in 54 patients (66. 6%). Only two of these cases were luminal type. While the radiological complete response was identified in 29 patients (35. 8 %), those that coincided with pCR were 21 cases (38. 8 %). There was no statistically significant correlation between pCR and radiological complete response ($p= 0.153$). Discussion and conclusion: Neoadjuvant chemotherapy is becoming the standard of care for locally advanced and triple negative, and HER 2 positive breast cancer. Radiological response is important in determining the effectiveness of the treatment and in determining the surgical treatment to be chosen (1, 2). In our study, while most cases were luminal cancers, the opposite was true in cases where pCR was taken. Consistent with other studies, no correlation was observed between radiological and pathological complete response in cases where NAC was applied. This result may be affected by factors such as the molecular subtype of the tumor, and the shape of the tumor response, but also depending on factors that are still unknown (3).

Figure 1



48-year-old triple negative breast cancer patient (yellow arrow).

Figure 2



Complete radiological response is observed after NAC (yellow arrow). A tumor bed is observed at the arrow tip.

Keywords: breast cancer, neoadjuvant chemotherapy, radiological-pathological correlation

DETECTION OF URGENT PATHOLOGY IN PEDIATRIC EMERGENCY ULTRASOUND REPORTS USING LARGE LANGUAGE MODELS

Nur Hursoy¹, Hafsa Kolluk¹, Esat Kaba¹, Ahmet Taha Kayaoglu¹, Huseyin Er¹, Yusuf
Cubukcu¹, Dilara Yilmaz Budak¹

¹Rize Research and Training Hospita

l

Abstract: AimThis study aims to quickly assess pediatric emergency ultrasound reports using LLM models to expedite notifying the relevant department of urgent cases, ultimately improving clinical outcomes. Material and MethodThe dataset consists of ultrasound reports requested from the pediatric emergency department in 2023 for a total of 196 patients, comprising 101 males (51.53%) and 95 females (48.47%), aged between 0-18 years (mean age 9.53 ± 5.14). A specialist radiologist evaluated these reports for the presence or absence of urgent pathology. Initially, in March 2024, the reports were analyzed for the presence or absence of urgent pathology using the zero-shot technique with Chat-GPT 3.5 and 4. In June 2024, the same reports were assessed using both zero-shot and few-shot techniques with different accounts on Chat-GPT 3.5 and 4. In the zero-shot technique, ChatGPT was instructed to "act as a specialist pediatric radiologist with 30 years of experience" to identify urgent pathology in reports. In the few-shot technique, the LLM was first trained with four example reports evaluated by a specialist, then given the same command to assess for urgent pathology. ResultsAppendicitis, testicular and ovarian torsion, ovarian cyst rupture, incarcerated inguinal hernia, intussusception, epididymitis, and infected cyst were classified as urgent pathologies, with a total of 56 patients identified as having urgent pathology. The highest success rate for recognizing these pathologies from the reports was 93.88%, achieved by the ChatGPT-4 zero-shot system in March. ConclusionThe results show that large language model can detect urgent cases with high accuracy. The integration of specialized large language models into hospital systems can be used as a supportive tool in emergency departments' diagnostic processes. This will accelerate clinical decision-making processes, thereby optimizing patient management

Keywords: large language model, pediatric ultrasound, urgent pediatric pathology

DETECTION OF BRAIN ANEURYSMS ON T2W IMAGES BY USING ARTIFICIAL INTELLIGENCE

Hamza Eren Güzel¹, Leander Maerkisch², Christian Wiedemeyer², Bianca
Teoderescu², Leonard Gölberg², Ali Murat Koç³

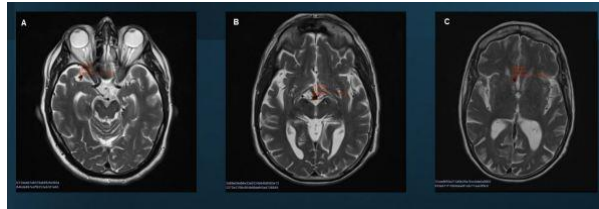
¹izmir Şehir Hastanesi

²floy GmbH

³izmir Katip Çelebi Üniversitesi Atatürk Eğitim Ve Araştırma Hastanesi

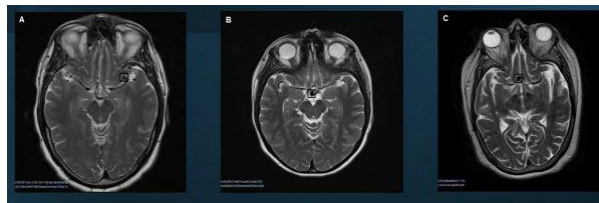
Abstract: Purpose: Brain aneurysm is a pathology that occurs in approximately 3% of the population and can sometimes be life-threatening. The diagnosis of aneurysms is generally made by Magnetic Resonance Angiography (MRA), which takes longer and is performed much less frequently than routine brain MRI. Many aneurysms larger than 4 mm in size can also be seen on T2W images in routine brain MRI, but it is difficult to scan vascular structures in brain MRI during daily practice. With this project, we aimed to investigate the aneurysm detection success of the machine learning model that we created using axial T2W images in routine MRI. Methods and Materials: By using MRA reports and images, total 467 cases diagnosed with brain aneurysm that is 4 mm or larger and that have a conventional axial T2W images are used. Their T2W images are extracted, aneurysms are detected and annotated on T2W images. Image processing has been done. Region of interest (locations in brain MRI that aneurysm can be seen) has been defined by using an MNI template. T2W images and the annotation masks are used for machine learning process. 320 cases have been used in training and 147 cases have been used for testing. Results: The sensitivity of the product was %94 and the specificity was %61. The most common false positive location was vessel curving especially in ICA location. The second most common false positive location was top of basilar artery. Conclusions Brain aneurysms larger than 4 mm can be successfully detected on routine axial T2W brain MRI by using artificial intelligence, if the algorithm is trained appropriately. The high false positive rate might cause unnecessary MR Angiograms. Clinical Relevance/Application: Aneurysms can be life-threatening, and with early detection, treatment is possible before they cause irreversible consequences. Detecting aneurysms with routine brain MRI by using artificial intelligence can contribute to many patients and healthcare systems.

Aneurysm Annotations by Radiologists



Aneurysms were annotated on T2W axial brain MR images. The outer contours of the saccular aneurysms of the right middle cerebral artery (A), the apex of the basilar artery (B), and the anterior communicating artery (C) were drawn.

Aneurysm Detections by AI



Predictions made by the artificial intelligence algorithm on T2W axial brain MR images: left middle cerebral artery (A), basilar artery apex (B), and anterior communicating artery (C) aneurysm detections were realized in the form of bounding boxes.

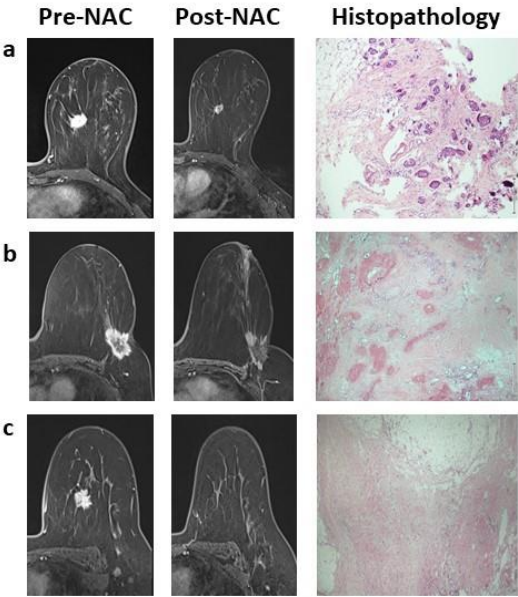
Keywords: brain MRI, aneurysm, artificial intelligence, angiography, detection

CORRELATION OF HISTOPATHOLOGICAL AND RADIOLOGICAL RESPONSE PATTERNS AND THEIR PROGNOSTIC IMPLICATIONS IN BREAST CANCER AFTER NEOADJUVANT CHEMOTHERAPY

Ahmet Bozer¹, Cengiz Yilmaz¹, Hülya Çetin Tunçez¹, Demet Kocatepe Çavdar¹,
Zehra Hilal Adıbelli¹
¹*Izmir City Hospital*

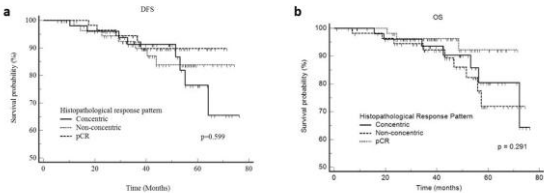
Abstract: Background: Neoadjuvant chemotherapy (NAC) is widely recognized as the standard treatment for breast cancer (BC) due to its ability to shrink tumors, facilitate breast-conserving surgeries, and provide prognostic information. Tumor response to NAC can be categorized into concentric shrinkage (CS), non-concentric shrinkage (non-CS), and complete response patterns. These patterns may have implications for surgical planning and survival outcomes. This study aims to evaluate the correlation between histopathological and radiological assessments of these tumor response patterns following NAC in BC patients and to determine their impact on overall survival (OS) and disease-free survival (DFS). Methods: This retrospective study analyzed 168 patients with BC who received NAC between 2018 and 2022. Post-treatment tumor response was evaluated radiologically using magnetic resonance imaging (MRI) and histopathologically after surgery. Radiological response patterns were categorized into CS, non-CS, and radiological complete response (rCR). Histopathologically, patients were classified into CS, non-CS, and pathological complete response (pCR). The concordance between radiological and histopathological classifications was assessed using the kappa statistic. Survival outcomes, including OS and DFS, were analyzed using Kaplan-Meier methods. Results: Moderate agreement was observed between radiological and histopathological assessments of tumor response patterns (κ : 0.439, $p < 0.001$). Tumor molecular subtype analysis revealed that triple-negative, HER2-enriched, and Luminal B-HER2(+) subtypes had higher rates of pCR, while Luminal A tumors predominantly exhibited non-CS. No significant correlation was found between histopathological response patterns (CS, non-CS, pCR) and OS (p : 0.291) or DFS (p : 0.599). Radiological response patterns (CS, non-CS, rCR) also did not significantly correlate with OS (p : 0.515) or DFS (p : 0.899). However, patients achieving pCR showed a trend toward better survival outcomes. Conclusion: We observed moderate concordance between histopathological and radiological response patterns in BC patients following NAC, but discrepancies highlight the limitations of relying solely on radiological evaluation in assessing shrinkage patterns. These patterns did not significantly correlate with prognosis. Although higher pCR rates were linked to better outcomes, response patterns alone may not predict survival, emphasizing the need for further research in larger cohorts.

Figure 1: Patient Examples of Radiological and Histopathological Response Patterns



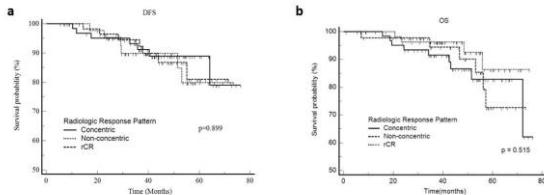
This figure presents examples using Pre-NAC (Neoadjuvant Chemotherapy) and Post-NAC MRI (Magnetic Resonance Imaging) alongside histopathological microscopic images. (a) shows both radiological and histopathological concentric shrinkage (CS). (b) displays a non-CS pattern in both assessments. (c) illustrates a case with radiological complete response (rCR) and pathological complete response (pCR). (a: x100, b–c: x40, all stained with Hematoxylin and Eosin)

Figure 2: Kaplan-Meier Survival Curves for Histopathological Response Patterns in Predicting (a) Disease-Free Survival (DFS) and (b) Overall Survival (OS).



The curves compare survival probabilities among concentric shrinkage, non-concentric shrinkage, and pathologic complete response (pCR) groups.

Figure 3: Kaplan-Meier Survival Curves for Radiologic Response Patterns in Predicting (a) Disease-Free Survival (DFS) and (b) Overall Survival (OS).



The curves compare survival probabilities among concentric shrinkage, non-concentric shrinkage, and radiologic complete response (rCR) groups.

Table 1: Concordance analysis between histopathological and radiologic response patterns

			Histopathological Response Pattern			Total
			CS	Non-CS	pCR	
Radiologic Response Pattern	CS	Count	34	19	11	64
		% Row	53%	30%	17%	100%
		% Col.	64%	33%	19%	38%
		% Tot	20%	11%	7%	38%
	Non-CS	Count	13	29	4	46
		% Row	28%	63%	9%	100%
		% Col.	25%	50%	7%	27%
		% Tot	8%	17%	2%	27%
	rCR	Count	6	10	42	58
		% Row	10%	17%	72%	100%
		% Col.	11%	17%	74%	35%
		% Tot	4%	6%	25%	35%
	Total	Count	53	58	57	168
		% Row	31.5%	35%	34%	100%
		% Col.	100%	100%	100%	100%
		% Tot	31%	35%	34%	100%

Kappa (κ) = 0.439, indicating moderate agreement ($p < 0.001$).

CS: Concentric Shrinkage, Non-CS: Non-Concentric Shrinkage, pCR: Pathologic Complete Response, rCR: Radiologic Complete Response

Table 2: Association Between Tumor Subtypes and Radiologic Response Patterns

Molecular Sub-Type	Radiologic Response Pattern						Total		P*
	CS		Non-CS		rCR				
	N	%	N	%	N	%	N	%	
Luminal A	7	11%	8	17%	1	2%	16	10%	<0.001
LB-HER2(-)	36	56%	26	57%	17	29%	79	47%	
LB-HER2(+)	7	11%	7	15%	20	34%	34	20%	
HER2 Enriched	4	6%	0	0%	11	19%	15	9%	
Triple Negative	10	16%	5	11%	9	16%	24	14%	
Total	64	100%	46	100%	58	100%	168	100%	

* Pearson Chi-Square Test

CS: Concentric Shrinkage, Non-CS: Non-Concentric Shrinkage, rCR: Radiologic Complete Response, LB-HER2(-): Luminal B HER2-Negative, LB-HER2(+): Luminal B HER2-Positive.

Keywords: Breast Cancer, Neoadjuvant Chemotherapy, Tumor Shrinkage Patterns, Survival Outcomes, Radiologic Response

CLASSIFICATION OF BRAIN CT REPORTS BY EMERGENCY LEVEL USING ARTIFICIAL INTELLIGENCE

Hamza Eren Güzel¹, Göktuğ Aşçı³, Oytun Demirbilek², Tuğçe Doğa Özdemir¹, Pelin Berfin Erekli¹

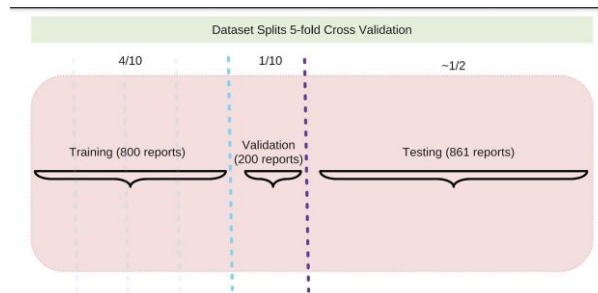
¹*İzmir Şehir Hastanesi*

²*Münih Teknik Üniversitesi*

³*İe Üniversitesi*

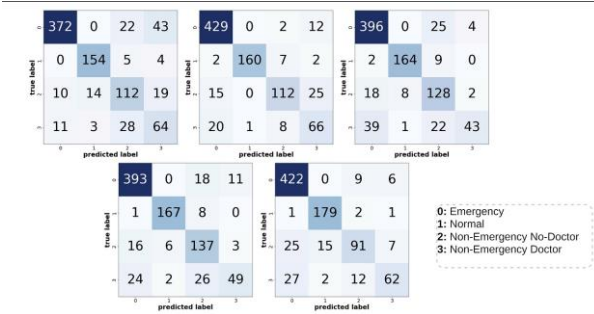
Abstract: Purpose: With the rapidly developing technology, the number of radiology examinations has increased over the years, and it has become difficult for the primary physician to evaluate the scan reports rapidly and effectively. Delays or errors in the evaluation of radiology reports can lead to irreversible consequences for patients. Our aim with this research is to establish an AI system that scans and classifies radiology reports and to measure the success of this system. Methods and Materials: Randomly selected 1861 Non-Contrast Brain CT reports were anonymized and annotated for emergency level by two radiologists and reviewed by one senior radiologist. Classifications were as follows: Class 1 - Emergency: Results that require the patient to apply to the emergency department immediately (intracranial bleeding, stroke, shift, skull fracture, cerebral venous sinus thrombosis etc.). Class 2 - Not Emergency But Needs Timely Attention: Reports in which the patient does not need to apply to the emergency room, but requires outpatient clinic service in a health institution as soon as possible (intracranial space-occupying lesion, change of lesions during follow up, metabolic diseases etc.). Class 3 - Not Clinically Significant: Reports in which the patient does not need an outpatient clinical service as soon as possible, the primary physician can read the report anytime (arachnoid cyst, age related changes, calcifications, variations etc.). Class 4 - Normal: Completely normal findings. After the annotation, all the data was split in two; the first 1000 reports were divided, with 800 used for training and 200 used for validation. Distil BERT model was used for training. The resulting algorithm was tested on the remaining 861 annotated reports. Results: It was observed that the algorithm produced has a sensitivity of 91% and a specificity of 90% in the measurements made on the test data. The F1 score was measured as 0.89 for the best fold. The algorithm most successfully distinguished Emergency results. Conclusions: These data demonstrate that, it is possible to classify CT reports with a very high accuracy using AI. A similar classification system can be applied to other imaging methods, with a higher number of cases and predetermined decisions about which pathology belongs to which class.

Training, validation and test set



800 reports were used for training and 200 were used for validation. Testing is done on 861 reports that the algorithm has never seen before.

Success of 5 different models



All models most successfully distinguished Emergency results. The second model was the most successful one in terms of F1 score.

Keywords: artificial intelligence, brain CT, report, classification

AUTOMATED CLASSIFICATION OF THE PHASECASE SCALE IN MRI USING DEEP LEARNING METHODS

Zülküf AKDEMİR¹, Ramazan YILDIZ¹, Adem YOKUŞ¹, Murat CANAYAZ², Harun ARSLAN¹, Saim TÜRKOĞLU¹

¹Yüzüncü Yıl Üniversitesi Tıp Fakültesi, Department of Radiology, VAN

²Yüzüncü Yıl Üniversitesi, Faculty of Engineering, Computer Engineering Department, VAN

Abstract: Objective: The aim of this study was to classify the Fazekas scale, which indicates the burden of periventricular white matter hyperintensities (WMH), especially those caused by chronic small vessel disease, using deep learning techniques on MRI. Material and Methods: A total of 1266 patients (590 males and 676 females, aged 18-96 years) who underwent brain MRI at Van Yüzüncü Yıl University Dursun Odabaşı Medical Center Radiology Clinic between December 2023 and April 2024 and whose images were normal and BCH was detected in axial fat-suppressed FLAIR WI sequences were retrospectively reviewed. Images were classified into 4 classes according to Fazekas scale. For classification, we performed feature extraction on EfficientNet, one of the deep learning models, and then classified with SVM, KNN and XGBoostClassifier classifiers with CV and LOOCV crossover techniques and compared their performances. Results: Feature extraction was performed on EfficientNet. Among the extracted features, 100 features were selected with PCA and the results were obtained by running 3 classification algorithms initially. The best result was obtained from the XGBoostClassifier classifier with the features extracted from the EfficientNet B1 model with a high rate of approximately 95%. In addition, performance tests were also performed with 8 classification algorithms using CV and LOOCV crossover techniques on the extracted features. In these performance tests, an accuracy rate of 95% was achieved on the features obtained from the Efficient B1 model. Conclusion: Evaluating deep learning architectures for faster and easier detection of WMHs that can cause serious health problems can significantly reduce the workload of radiology physicians by providing ease of diagnosis.

Keywords: Phasecase Scale, Mri, Deep Learning

US-GUIDED PERCUTANEOUS TRANSABDOMINAL TRU-CUT BIOPSY IN PATIENTS WITH OVARIAN TUMORS

Berat Acu¹, Cigdem Oztunali¹, Serhat Demir¹

¹Eskisehir Osmangazi University Medical Faculty, Department of Radiology,

Abstract: Aim: This study evaluated the safety, adequacy, and diagnostic yield of percutaneous US-guided transabdominal tru-cut biopsy for ovarian tumors. The association between the diagnostic yield of the biopsy with the pre-procedural computed tomography (CT) findings and the tumor markers was analyzed. Materials and Methods: This retrospective study included 46 consecutive patients who had ovarian masses on CT and underwent US-guided percutaneous transabdominal tru-cut biopsy in a single institution between 2015 and 2024. Biopsies were performed by an experienced interventional radiologist using 18G and 16G fully automatic biopsy needles and a freehand technique. Pre-biopsy CT findings, tumor markers, and final pathological diagnosis were recorded. The technical and diagnostic success rates of the biopsies and the association between the diagnostic yield of the biopsies and the pre-biopsy findings were evaluated. Results: The mean age of the patients was 61.9 years (35-87 years). A single biopsy was diagnostic in 41 of 46 patients. Three patients had two biopsies, and two patients had three biopsies, resulting in a total of 53 biopsies. The technical and diagnostic success rates were 100% and 95.6%. Of the 46 patients, 31 had tumors of ovarian origin, 10 had metastatic tumors to the ovary, 4 had benign pathology, and 1 had metastatic leiomyosarcoma of unknown origin. Abdominal implants, omental cake, and abdominal fluid were present in 76%, 67%, and 76% of the patients. 80.4 % of the patients had bilateral tumors of the ovaries on pre-biopsy imaging. Findings are presented in Tables 1-3. Discussion: In patients with suspected ovarian malignancy, a histological diagnosis is frequently required for treatment planning. US-guided percutaneous transabdominal biopsy is a safe, quick, and efficient procedure with high diagnostic rates. Conclusion: This study demonstrates that US-guided percutaneous biopsy of ovarian tumors is safe and accurate, resulting in a tissue-specific histological diagnosis in 95.6 % of patients with a 100% technical success rate.

Table 1.

	Ovarian Origin (31)	Metastatic Tumor (10)	Benign Pathology * (4)	Tumor of unknown origin (1)
	Serous Carcinoma (23)	Gastric Carcinoma (3)	Tuba-ovarian abscess (1)	Leiomyosarcoma (1)
	Mucinous Carcinoma (2)	Colon Carcinoma (2)	Fibroadipose tissue (1)	
	Malignant Spindle Cell Tumor (1)	Lung Adenocarcinoma (1)	Fibroadipose tissue*(1)	
	Endometrioid Carcinoma (2)	GIST (1)	Histiocytes and Erythrocytes (1)	
	Sex Cord Stromal Tumor (2)	Parotid Acinic Cell Carcinoma (1)		
	Squamous Cell Carcinoma (1)	Pancreas Adenocarcinoma (1)		

		Breast Carcinoma (1)		
	Ovarian Origin (31)	Metastatic Tumor (10)	Benign Pathology* (4)	Tumor of Unknown Origin (1)
Implants (35) (76%)	26	8	1*	0
Omental Cake (31) (67%)	25	5	1*	0
Fluid (35) (76%)	25	8	2*	0
SMJ nodule (26) (60%)	21	5	0	0
Bilateral (37) (80.4 %)	28	7	2*	0
Unilateral (9) (19.6 %)	3	3	2	1

Table 1: Pathology results of the diagnosed tumors and the pre-biopsy CT findings. *, radiologically and clinically malignant but negative for malignancy pathologically. SMJ, Sister Mary Joseph nodule.

Table 2

		Age	Tumor Marker	Pathology
2 Biopsies (n=3)				
Benign (1)	Negative/ Negative	42	Negative	Histiocytes, Erythrocytes / Histiocytes, Erythrocytes
Benign (1)	Negative/ Negative	39	Negative	Fibroadipose Tissue / Fibroadipose Tissue
Malignant (1)	Negative/ Positive	67	Positive	Necrosis / Ovarian Serous Carcinoma
3 Biopsies (n=2)				
Malignant (1)	Negative/ Negative	67	Positive	Necrosis / Necrosis /

	Negative/ Positive			Ovarian Endometrioid Carc.
Benign* (1)	Negative/ Negative/ Negative	67	Positive	Necrosis / Fibroadipose tissue / Necrosis
1 Biopsy (n=41)				
Malignant (40)	Positive	62.9 ^b	Positive	Ovarian (29) Metastatic (10) Leiomyosarcoma of unknown origin (1)
Benign (1)	Negative	35	Positive ^a	Tuba-ovarian abscess

Table 2. Number of biopsies with patient age, tumor marker status and final pathology. n; number of patients, *; radiologically and clinically malignant but negative for malignancy pathologically, a; CA 125 (24-fold). b; mean age. Diagnostic biopsies: 44/46 (95.6 %), Non-diagnostic biopsies: 2/46 (4.4 %)

Table 3

		CA 125				CA - 15.3		
	n	Mean	Median	Min-Max	n	Mean	Median	Min-Max
Serous Carcinoma 23	23/23	116.6	47	3 - 589	13/23	12.4	12	3-24
Mucinous Carcinoma 2	1/2	15	15	15	1/2	1.5	1.5	1.5
Malignant Spindle Cell Tumor 1	0/1	0	0	0	1/1	3.9	3.9	3.9
Endometrioid Carcinoma 2	2/2	198.5	198.5	111 - 286	2/2	4.5	4.5	3 - 6
Sex Cord Stromal Tumor 2	1/2	2	2	2	1/2	1.2	1.2	1.2

Squamous Cell Carcinoma 1	1/1	4	4	4	1/1	1.4	1.4	1.4
Total 31	28/31	93.95	38.5	2 - 589	19/31	10.43	7.5	1.2 - 24
		CA 19.9				CEA		
	n	Mean	Median	Min-Max	n	Mean	Median	Min-Max
Serous Carcinoma 23	3/23	17	7	3 - 41	0/23	0	0	0
Mucinous Carcinoma 2	1/2	6	6	6	1/2	1	1	1
Malignant Spindle Cell Tumor 1	0/1	0	0	0	0/1	0	0	0
Endometrioid Carcinoma 2	1/2	235	235	235	1/2	1.4	1.4	1.4
Sex Cord Stromal Tumor 2	0/2	0	0	0	0/2	0	0	0
Squamous Cell Carcinoma 1	1/1	3	3	3	0/1	0	0	0
Total 31	6/31	60.66	24	3 - 235	2/31	1.4	1.4	1.4

Pre-biopsy tumor markers and final diagnosis in masses of ovarian origin.

Keywords: ovarian tumor, percutaneous transabdominal biopsy, US-guided biopsy

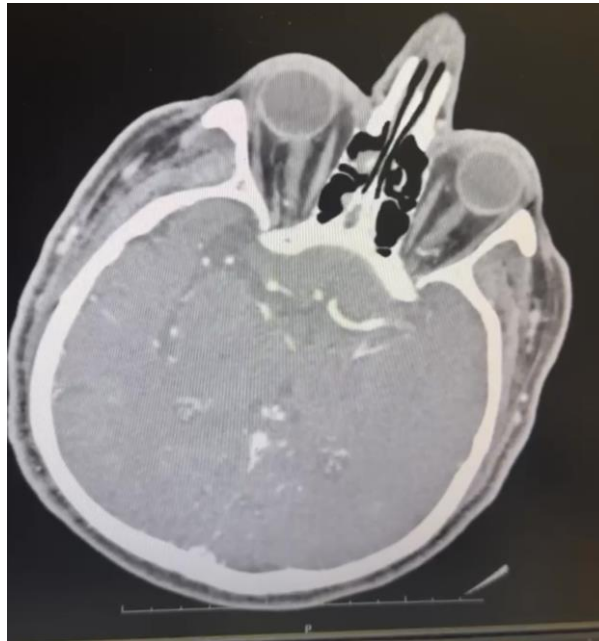
IS IT FEASIBLE TO ESTABLISH A STROKE UNIT IN THE REMOTEST CORNER OF TÜRKİYE? A CASE SERIES FROM HAKKARİ

Eyup Kızıl¹

¹*İzmir Tepecik Eğitim Ve Araştırma Hastanesi*

Abstract: Is It Feasible to Establish a Stroke Unit in the Remotest Corner of Türkiye? A Case Series from HakkariBackground: Acute ischemic stroke (AIS) is one of the most common causes of severe disability and death worldwide. Timely intervention is critical, as delayed treatment and inter-hospital transfers are linked to poor outcomes. The nearest stroke center is in Van, 3 hours away under optimal weather conditions.Objective: We aimed to share our experience in establishing a thrombectomy-capable stroke unit in Hakkari.Methods: A multidisciplinary committee, including an interventional radiologist, neurologist, and neurosurgeon, was formed. Specialized training was provided to nurses and technicians. Permissions were obtained from the Ministry of Health, and necessary mechanical thrombectomy (MT) equipment was procured. Local hospitals were informed about the initiative. Patients with large vessel occlusion (LVO) confirmed by CT and CTA, without hemorrhage, were selected for MT. We evaluated times from last known well (LKW) to first hospital contact, transfer time to the stroke unit, door-to-needle time, and MT procedure times. Angiographic outcomes were assessed using the Thrombolysis in Cerebral Infarction (TICI) score, and clinical outcomes with the modified Rankin Scale (mRS).Results: Seven consecutive patients (four male, three female) with an age range of 29 to 81 years presented with LVO and were found eligible for MT. The time from LKW to needle ranged from 6 to 7 hours, primarily delayed by interhospital transfers (mean 3 hours). MT was performed in five patients, with TICI 3 recanalization in two and partial recanalization in two. One patient underwent carotid stenting with successful recanalization. Clinical outcomes were generally poor, with one patient achieving mRS 1 (who later died from recurrent stroke) and five patients with mRS 6 (death).Conclusion: Hakkari State Hospital has demonstrated the capacity to perform MT with acceptable door-to-needle and procedure times, achieving full recanalization in three patients and partial recanalization in two. Even in remote regions like Hakkari, Türkiye has the infrastructure to establish stroke centers. However, optimizing stroke outcomes requires minimizing interhospital transfer times and raising public awareness to reduce the time from LKW to MT, which seems to be the primary challenge

CTA, DSA



Pre-procedure CTA and DSA Images, and Post-thrombectomy DSA Images of a Patient with Left MCA M1 Occlusion

CTA, DSA



Pre-procedure CTA and DSA Images, and Post-thrombectomy DSA Images of a Patient with Left MCA M1 Occlusion

DSA



Pre-procedure CTA and DSA Images, and Post-thrombectomy DSA Images of a Patient with Left MCA M1 Occlusion

Keywords: Neuroradiology, Interventional Neuroradiology, Interventional Radiology

EVALUATING SPECIMEN ADEQUACY IN THYROID FNAB: A COMPARISON OF TRANSFER TECHNIQUES

Mehmet Karagülle¹, Fatma Zeynep Arslan¹

¹*Basakşehir City Hospital*

Abstract: Aim: In this study, we compared the differences between the conventional smear methods of tapping the green part of the syringe against the slide and rapidly pressing the syringe to spray the contents onto the slide to evaluate specimen adequacy during FNAB. We also investigated whether there are any significant differences in the diagnoses between pathological subgroups. Methods: A total of 119 patients underwent FNAB, and their samples were categorized using the Bethesda System. The study analyzed the efficiency of the two transfer techniques in terms of specimen adequacy and diagnostic outcomes, considering factors such as positive cell count and pathological subgroup diagnoses. Results: Among the 119 patients included, 103 were diagnosed with adenomatoid nodules. Comparing the two techniques, there was no significant difference in the overall rate of insufficient pathological results. The average number of positive cells detected using the tapping the green part of the syringe against the slide technique was 2.22 (min: 0, max: 3+, SD: 0.87). For the rapidly pressing the syringe to spray the contents onto the slide technique, the average number of positive cells was 1.33 (min: 0, max: 3+, SD: 1.21). Thus, tapping method resulted in slightly higher positive cell quantities compared to the rapidly pressing the syringe to spray the contents onto the slide technique. Conclusion: This study investigated the differences between two FNAB transfer techniques regarding specimen adequacy and diagnostic outcomes. While both the tapping and rapid spraying methods resulted in a similar rate of nondiagnostic outcomes, tapping the green part of the syringe yielded a slightly higher average of positive cell detection. However, the rapid spraying technique might be preferable due to its simplicity and safety. The findings suggest that neither method shows definitive superiority, indicating the necessity for further research to establish standardized procedures. Moreover, addressing other variables that can affect diagnostic accuracy, such as nodule characteristics and needle gauge, is critical for a comprehensive evaluation. Although our study offers valuable insights, its limitations highlight the need for larger-scale studies to confirm these results and contribute to refining FNAB techniques in clinical practice

Keywords: tapping, throid

DIAGNOSTIC UTILITY OF QUANTITATIVE AND SEMI-QUANTITATIVE PARAMETERS FROM MULTIPARAMETRIC MRI IN PROSTATE CANCER DETECTION: A RETROSPECTIVE STUDY

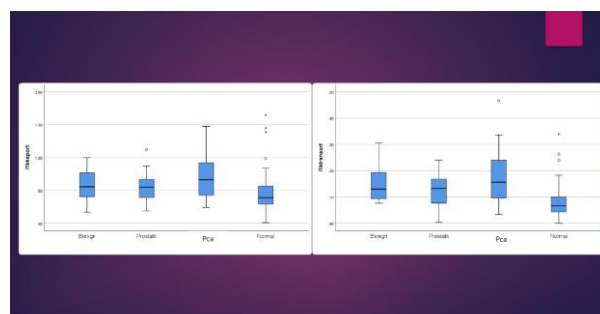
Gülşen Yücel Oğuzdoğan¹
¹Başakşehir Çam ve Sakura Şehir Hastanesi

Abstract: Objective: This retrospective study aims to evaluate the effectiveness of quantitative and semi-quantitative parameters from multiparametric MRI (mpMRI) in differentiating prostate cancer (PCa) from benign prostatic lesions. The study also assesses the diagnostic accuracy of these parameters in relation to cancer grade (ISUP score) and examines intraobserver variability in interpreting mpMRI findings using PI-RADS v2.1, alongside histopathological correlation in patients undergoing transrectal ultrasound-guided biopsy (TRUS-Bx). Materials and Methods: A total of 252 patients, with 318 lesions detected on mpMRI, who underwent TRUS-guided cognitive fusion biopsy between June 2018 and December 2023, were retrospectively reviewed. Imaging was performed using a 1.5T Siemens Magnetom Aera MRI system, and the mpMRI images were interpreted by a radiologist following PI-RADS v2.1 guidelines. Parameters such as age, PSA levels, PSA density, prostate volume, PI-RADS v2.1 scores, and pharmacokinetic measures (K_{trans}, K_{ep}, V_e, iAUC, Chi2, W-in, W-out, TTP, AT, PEI, iAUC*) were recorded for normal peripheral zones and lesions. Lesions with a Gleason score of 3 + 3 or higher were classified as malignant, while PI-RADS 4 and 5 were considered indicative of malignancy. Results: The average age of patients was 65.5 years, with a mean serum PSA of 13.68 ng/mL, prostate volume of 64.4 cc, and PSA density of 0.27. PI-RADS scores were distributed as follows: 5% for PI-RADS 1, 4% for PI-RADS 2, 54% for PI-RADS 3, 25% for PI-RADS 4, and 18% for PI-RADS 5. Of the malignant lesions, 65% were located in the peripheral zone, 14% in the transitional zone, and 21% extended beyond these areas. PSA density and prostate volume significantly differentiated benign from malignant conditions. K_{trans} and K_{ep} values were highest in PCa, while Chi2 values also elevated in malignant cases. Conclusion: mpMRI and the PI-RADS v2.1 scoring system demonstrate high effectiveness in diagnosing and managing prostate cancer, particularly in determining the need for biopsy and predicting tumor aggressiveness. Future developments in PI-RADS are expected to improve observer agreement and refine criteria for PI-RADS 3 lesions.

findings1

Variables	Normal	Benign prostatic tissue	Prostatic Ca	P value
K _{trans}	Median (IQR) 0.05 (0.03-0.1) Median (25p-75p) 0.04 (0.03-0.102)	Median (IQR) 0.11 (0.07-0.17) Median (25p-75p) 0.09 (0.07-0.203)	Median (IQR) 0.17 (0.107-0.241) Median (25p-75p) 0.14 (0.087-0.241)	<0.001
K _{ep}	Median (IQR) 0.49 (0.28-0.7) Median (25p-75p) 0.39 (0.27-0.527)	Median (IQR) 0.87 (0.57-1.27) Median (25p-75p) 0.59 (0.347-0.822)	Median (IQR) 0.71 (0.45-1.0) Median (25p-75p) 0.44 (0.23-0.72)	<0.001
V _e	Median (IQR) 0.21 (0.11-0.248) Median (25p-75p) 0.18 (0.11-0.248)	Median (IQR) 0.27 (0.19-0.322) Median (25p-75p) 0.22 (0.14-0.307)	Median (IQR) 0.29 (0.19-0.307) Median (25p-75p) 0.14 (0.10-0.207)	0.870
AUC	Median (IQR) 0.09 (0.04-0.1) Median (25p-75p) 0.07 (0.04-0.102)	Median (IQR) 0.14 (0.10-0.203) Median (25p-75p) 0.08 (0.07-0.107)	Median (IQR) 0.14 (0.10-0.207) Median (25p-75p) 0.09 (0.04-0.1)	<0.001
Chi2	Median (IQR) 0.00 (0.00-0.007) Median (25p-75p) 0.04 (0.00-0.053)	Median (IQR) 0.14 (0.10-0.203) Median (25p-75p) 0.08 (0.07-0.107)	Median (IQR) 0.14 (0.10-0.207) Median (25p-75p) 0.09 (0.04-0.1)	0.123
W _{in}	Median (IQR) 0.14 (0.10-0.173) Median (25p-75p) 0.11 (0.04-0.173)	Median (IQR) 0.24 (0.10-0.330) Median (25p-75p) 0.20 (0.12-0.340)	Median (IQR) 0.24 (0.10-0.330) Median (25p-75p) 0.20 (0.12-0.340)	<0.001
W _{out}	Median (IQR) 0.007 (0.00-0.018) Median (25p-75p) 0.00 (0.00-0.0147)	Median (IQR) 0.00 (0.00-0.022) Median (25p-75p) 0.00 (0.00-0.022)	Median (IQR) 0.00 (0.00-0.022) Median (25p-75p) 0.00 (0.00-0.022)	0.797
TTP	Median (IQR) 1.07 (0.54-1.58) Median (25p-75p) 1.14 (0.79-1.58)	Median (IQR) 0.01 (0.00-0.023) Median (25p-75p) 0.00 (0.00-0.023)	Median (IQR) 0.00 (0.00-0.023) Median (25p-75p) 0.00 (0.00-0.023)	0.027
AT	Median (IQR) 0.33 (0.31-0.37) Median (25p-75p) 0.29 (0.20-0.415)	Median (IQR) 0.54 (0.40-0.68) Median (25p-75p) 0.58 (0.437-0.638)	Median (IQR) 0.47 (0.35-0.58) Median (25p-75p) 0.58 (0.437-0.638)	0.001
PEI	Median (IQR) 0.19 (0.08-0.28) Median (25p-75p) 0.14 (0.10-0.24)	Median (IQR) 0.47 (0.35-0.62) Median (25p-75p) 0.27 (0.20-0.352)	Median (IQR) 0.24 (0.15-0.34) Median (25p-75p) 0.24 (0.15-0.34)	<0.001
iAUC	Median (IQR) 0.08 (0.04-0.113) Median (25p-75p) 0.07 (0.04-0.113)	Median (IQR) 0.14 (0.10-0.203) Median (25p-75p) 0.08 (0.07-0.107)	Median (IQR) 0.14 (0.10-0.207) Median (25p-75p) 0.09 (0.04-0.1)	0.005

findings2



findings

Results or Findings

- The mean values of V_e was the lowest in the normal PZ, but the highest in the benign prostatic tissue.
- Chi^2 value was the highest in the cancer group and was measured quite close to each other in the other groups.

Variables	Normal	Benign prostatic tissue	Prostatic Ca	p value
K_{trans}	Mean±SD Median(25p-75p)	0.062(0.042-0.100) 0.068(0.043-0.100)	0.111(0.071-0.203) 0.13(0.091-0.203)	0.171(0.107-0.241) 0.148(0.087-0.241)
				<0.001
K_{ep}	Mean±SD Median(25p-75p)	0.46(0.28-0.84) 0.392(0.293-0.673)	0.59(0.27-0.203) 0.55(0.347-0.828)	0.715(0.33-0.928) 0.663(0.428-0.928)
				<0.001
V_e	Mean±SD Median(25p-75p)	0.214(0.165-0.183) 0.183(0.119-0.240)	0.271(0.089-0.323) 0.273(0.193-0.323)	0.228(0.104-0.307) 0.224(0.163-0.307)
				<0.001
AUC	Mean±SD Median(25p-75p)	0.59(0.56-0.54) 0.073(0.040-0.102)	0.16(0.09-0.230) 0.140(0.100-0.230)	0.148(0.09-0.307) 0.140(0.100-0.307)
				<0.001
Chi^2	Mean±SD Median(25p-75p)	0.08(0.037-0.040) 0.040(0.030-0.083)	0.081(0.037-0.040) 0.083(0.033-0.040)	0.040(0.033-0.093) 0.040(0.033-0.093)
				<0.001
W_2	Mean±SD Median(25p-75p)	0.145(0.121-0.117) 0.117(0.063-0.173)	0.247(0.107-0.330) 0.247(0.107-0.330)	0.224(0.125-0.360) 0.224(0.125-0.360)
				<0.001
W_3	Mean±SD Median(25p-75p)	0.007(0.000-0.017) 0.003(0.000-0.017)	0.007(0.000-0.017) 0.007(0.000-0.017)	0.007(0.000-0.017) 0.007(0.000-0.017)
				<0.001
Time to peak	Mean±SD Median(25p-75p)	1.287(0.642-1.143) 1.143(0.790-1.588)	0.301(0.32-0.023) 0.301(0.32-0.023)	0.99(0.44-1.28) 0.99(0.44-1.28)
				<0.001
AT	Mean±SD Median(25p-75p)	0.332(0.313-0.290) 0.290(0.20-0.418)	0.56(0.291-0.436) 0.56(0.437-0.436)	0.441(0.288-0.700) 0.441(0.288-0.700)
				<0.001
PB	Mean±SD Median(25p-75p)	0.192(0.098-0.146) 0.146(0.100-0.243)	0.49(0.452-0.382) 0.49(0.327-0.382)	0.34(0.193-0.347) 0.34(0.193-0.347)
				<0.001
AUC	Mean±SD Median(25p-75p)	0.08(0.047-0.110) 0.070(0.043-0.110)	0.18(0.08-0.201) 0.18(0.078-0.201)	0.14(0.081-0.201) 0.14(0.081-0.201)
				<0.001

Keywords: PIRADSV2.1, MpMRI, prostate cancer

THE UTILITY OF QUANTITATIVE ADC AND T2 VALUES, ENHANCEMENT PATTERN, AND LESION SHAPE CHARACTERISTICS IN DIFFERENTIATING TRUE POSITIVE FROM FALSE POSITIVE LESIONS ON MULTIPARAMETRIC PROSTATE MRI

Selahattin Durmaz¹, Sinan Seyrek², Kaan Ozbozduman³, İbrahim Halil Akkis², Merve Gulbiz Dagoglu Kartal²

¹Department of Radiology, Gaziosmanpasa Training and Research Hospital, University of Health Science, Istanbul, Türkiye

²Department of Radiology, Istanbul Faculty of Medicine, Istanbul University, Istanbul, Türkiye

³Physics Department, Bogazici University, Istanbul, Türkiye

Abstract: Background: Multiparametric MRI (mpMRI) is considered the most reliable imaging modality for detecting prostate cancer (PCa). However, its specificity and positive predictive value remain relatively low, as benign conditions such as prostatitis, hemorrhage, and benign hyperplasia can mimic PCa on mpMRI, leading to unnecessary biopsies Purpose: To investigate the utility of quantitative ADC and T2 values, the presence of early enhancement (EE), and lesion shape characteristics in differentiating true positive from false positive lesions on multiparametric MRI. Material and Methods: The pathology reports of 136 patients with PI-RADS 3, 4, or 5 peripheral zone (PZ) lesions detected on mpMRI and sampled by cognitive fusion biopsy between January 2019 and January 2024 were retrospectively reviewed. Based on pathology results, patients were classified into two groups: true positives ($GS \geq (3+3)$, $n=101$) and false positives (negative, $n=35$). MpMRI characteristics, including quantitative ADC and T2 values, shape features (round-oval, wedge, or non-circumscribed heterogeneous), and EE, were compared between the two groups. Demographic variables, including age, PSA, and PSA density (PSAD) at the time of mpMRI, were also included in the analysis. A subgroup analysis comparing the csPCa group ($GS \geq 3+4$, $n=79$) to the false positive group was performed. Statistical significance was defined as $p < 0.05$. Results: The mean age, median PSA, PSAD, and lesion size for the true positive ($n=101$), csPCa ($n=79$), and false positive ($n=35$) groups are presented in Table 1. Univariate analysis revealed statistically significant differences between the true positive and false positive groups in terms of age, ADC value, PSAD, lesion size, EE, and T2 signal intensity (Table 2). Additionally, a round-oval shape characteristic was significantly associated with true positivity. In multivariate analysis, only ADC value ($p=0.042$) and age ($p=0.024$) remained significant, while all other variables lost statistical significance (Table 2). Similarly, in the subgroup analysis comparing the csPCa and false positive groups, univariate analysis showed significant differences for age, ADC value, PSA, PSAD, lesion size, EE, and T2 signal intensity, with the round-oval shape significantly associated with clinical significance. In multivariate analysis, only ADC value ($p=0.025$) and age ($p=0.034$) remained significant (Table 3). Conclusion: Quantitative ADC values, along with age were effective in differentiating true positive from false positive lesions on multiparametric prostate MRI.

Table 1.

Features	True positive group	Clinically significant PCa group	False positive group
Number of Patients	101	79	35
Mean age (\pm SD)	65.8 years (\pm 7.8 years)	65.5 years (\pm 7.8 years)	59.3 years (\pm 7.2 years)
Median PSA value (range)	6.5 ng/mL (1-157.6 ng/mL)	7.55 ng/mL (1.2-157.6 ng/mL)	4.4 ng/mL (1.14-24 ng/mL)

Median PSAD value (range)	0.19 ng/mL/mL (0.03- 3.8 ng/mL/mL)	0.21 ng/mL/mL (0.03- 3.8 ng/mL/mL)	0.09 ng/mL/mL (0.03- 0.6 ng/mL/mL)
Median lesion size (range)	12 mm (5-60 mm)	13 mm (5-60 mm)	11 mm (4-28 mm)

Demographic and clinical characteristics of true positive, clinically significant prostate cancer (csPCa), and false positive patient groups

Table 2

Variable	Univariate Analysis	Multivariate Analysis
ADC value	<0.001	0.042
Age	<0.001	0.024
Presence of early enhancement	0.002	0.71
PIRADS score	<0.001	0.84
PSA	0.051	0.11
PSA Density	0.008	0.06
Shape 1 (round-oval)	<0.001	0.74
Shape 2 (wedge)	0.9	0.9
Shape 3 (non-circumscribed heterogeneous)	0.07	0.49
Size	0.03	0.77
T2 Signal Value	<0.001	0.13

Results of univariate and multivariate analyses for diferantiating true positive from false positive lesions on mpMRI

Table 3

Variable	Univariate Analysis	Multivariate Analysis
ADC value	<0.001	0.025
Age	<0.001	0.034
Presence of early enhancement	<0.001	0.44

PIRADS score	<0.001	0.39
PSA	0.027	0.09
PSA Density	0.002	0.06
Shape 1 (round-oval)	<0.001	0.9
Shape 2 (wedge)	0.9	0.9
Shape 3 (non-circumscribed heterogeneous)	0.02	0.62
Size	0.007	0.3
T2 Signal Value	<0.001	0.33

Results of univariate and multivariate analyses for diferantiating csPCa from false positive lesions on mpMRI

Keywords: Prostate Cancer, Magnetic resonance imaging, PIRADS, ADC value, Diffusion-weighted imaging

MAGNETIC RESONANCE IMAGING FINDINGS OF NEONATAL OVARIAN TORSION

Umur Anıl Pehlivan¹, Cankat Erdoğan², Şenay Demir-Kekeç¹

¹Başkent University Adana Dr. Turgut Noyan Application and Research Center Department of Radiology

²Başkent University Adana Dr. Turgut Noyan Application and Research Center Department of Pediatric Surgery

Abstract: Introduction: Fetal ovaries are prone to cyst development due to exposure to the maternal hormonal environment during pregnancy. Advances in imaging technologies have facilitated the frequent detection of ovarian cysts during the prenatal period. Torsions arising from these cysts can present diagnostic challenges, with differential diagnoses including ovarian neoplasms and intestinal obstructions. Therefore, the imaging findings of ovarian cysts are of considerable clinical significance. The objective of this study was to retrospectively review the magnetic resonance imaging (MRI) findings of neonatal ovarian torsion cases diagnosed at our hospital. Materials and Methods: This retrospective study was conducted at a single center. Between January 2010 and January 2024, 12 female patients diagnosed with neonatal ovarian torsion were included. Clinical data, including patients' age at the time of surgery, prenatal diagnosis status, and MRI findings such as fluid-debris level, presence of hemorrhagic or proteinaceous content, septation, presence of free fluid, contrast enhancement status, and diffusion restriction, were analyzed retrospectively. Results: The clinical and radiological characteristics of patients diagnosed with neonatal ovarian torsion are presented in Table 1. The mean age of the patients at the time of surgery was 33.33 days (age range: 4-156 days). Torsion was detected in the right ovaries of all patients except one. Prenatal diagnosis was available in nine patients, while not in three patients. The most frequently observed MRI findings were a fluid-debris level (100%), presence of hemorrhagic or proteinaceous fluid (100%), septation (83.33%), and pelvic free fluid (66.67%) (Figure 1a-d). Peripheral contrast enhancement was observed in 33.33% of cases, while components demonstrating diffusion restriction were observed in 25% (Figure 1e-f). Conclusion: The predominant MRI findings in neonatal ovarian torsion cases included fluid-debris level, T1 hyperintensity indicating internal hemorrhagic or proteinaceous fluid, septation, and pelvic free fluid. These imaging findings are crucial for predicting and diagnosing neonatal ovarian torsion, highlighting the pivotal role of MRI in clinical decision-making for this condition.

Figure 1

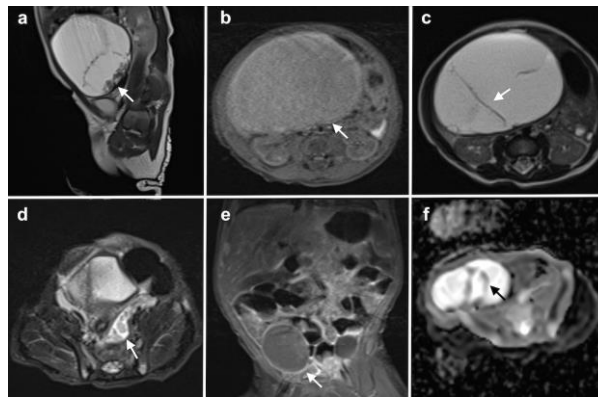


Figure 1. The fluid-debris level is shown on the coronal T2-weighted image (arrow in a). The hemorrhagic or proteinaceous fluid is revealed on the pre-contrast axial fat-suppressed T1-weighted image (arrow in b). Septation is seen on the axial T2-weighted image (arrow in c). Pelvic free fluid is demonstrated on the axial fat-suppressed T2-weighted image (arrow in d). Peripheral contrast enhancement is noted on the post-contrast axial fat-suppressed T1-weighted image (arrow in e). Diffusion restriction is revealed on the apparent diffusion coefficient map (arrow in f).

Table 1

	Age (Days)	Prenatal diagnosis	Cyst size (mm)	Fluid- debris level	Hemorrhagic or	Septation	Pelvic free fluid	Contrast enhancement status	Diffusion restriction
--	---------------	-----------------------	-------------------	---------------------------	-------------------	-----------	-------------------------	-----------------------------------	--------------------------

					proteinaceous content				
Patient 1	4	-	46×44×38	+	+	+	-	-	+
Patient 2	6	+	77×60×56	+	+	+	+	-	-
Patient 3	7	+	62×67×46	+	+	+	-	Peripheral	-
Patient 4	7	+	73×64×45	+	+	+	+	-	-
Patient 5	9	+	37×40×30	+	+	-	+	Peripheral	-
Patient 6	9	+	55×50×45	+	+	+	+	-	+
Patient 7	13	+	48×55×32	+	+	+	+	-	-
Patient 8	20	-	38×36×30	+	+	+	-	Peripheral	-
Patient 9	41	+	57×47×34	+	+	+	-	-	+
Patient 10	48	+	36×42×35	+	+	+	+	Peripheral	-
Patient 11	80	-	29×28×23	+	+	+	+	-	-
Patient 12	156	+	25×24×22	+	+	-	+	-	-

Table 1. Characteristics of patients diagnosed with neonatal ovarian torsion

Keywords: magnetic resonance imaging, ovarian torsion, newborn

PREOPERATIVE PREDICTION OF SEROUS AND MUCINOUS BORDERLINE OVARIAN TUMORS ACCORDING TO MRI FEATURES

Tuğçe Hancıoğlu¹, Aslı Irmak Akdoğan², Muzaffer Sancı³, Esra Canan Kelten Talu⁴,
Hilal Şahin⁵

¹Department of Radiology, Manisa Turgutlu State Hospital, Manisa, Turkey

²Department of Radiology, Atatürk Training and Research Hospital, Katip Celebi University, Izmir, Turkey

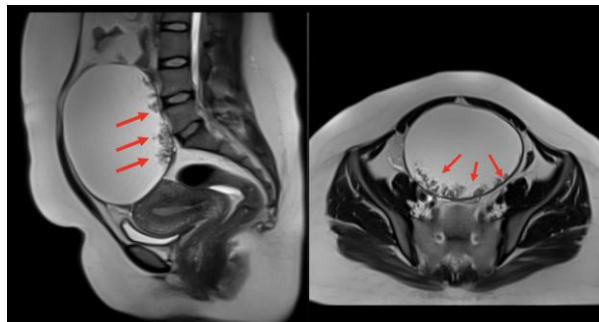
³Department of Obstetrics and Gynecology, Izmir City Hospital, Izmir, Turkey

⁴Department of Pathology, Tepecik Training and Research Hospital, Izmir, Turkey

⁵Department of Radiology, Izmir City Hospital, Izmir, Turkey

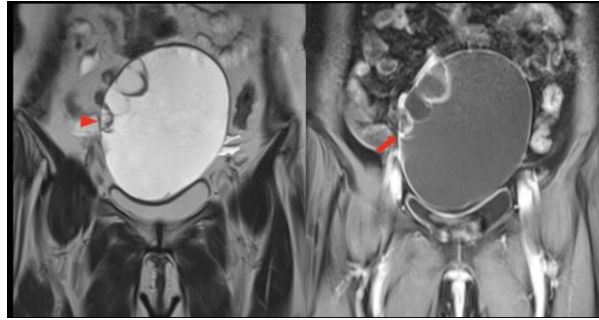
Abstract: Introduction: Borderline ovarian tumors (BOT) are intermediate group of neoplasms between benign and malignant ovarian tumours. Patients with BOT tend to be younger than their malignant counterparts. On histopathological examination, there are two main subtypes: serous (SBOT) and mucinous (MBOT). To specify the treatment to be applied, it is important and necessary to differentiate these subtypes. When the general approach to BOT is considered, the first preferred treatment method is usually fertility-preserving surgery. However, it is essential to distinguish mucinous borderline ovarian tumors from other subgroups because of the necessity of appendectomy. The aim of this study was to investigate characteristic imaging findings of serous and mucinous BOT. Materials-Methods: Institutional review board approval was taken for this study. Patients who had a preoperative MRI examination and diagnosed as BOT pathologically between 2016 and 2021 were retrospectively reviewed. After exclusion of 17 patients with rare subtypes of BOT, 88 patients with pathological diagnosis of SBOT or MBOT were included. Images were reviewed by two radiologists. O-RADS MRI lexicon was used to describe the determined imaging features. Descriptive statistics were done. In addition, Fisher's exact test, specificity, sensitivity and accuracy were calculated. A p-value of less than 0.05 was considered to indicate a statistically significant difference. Results: There were 61 (69.3 %) SBOT and 27 (30.6%) MBOT in the study cohort. A descriptive analysis of each MRI feature is shown in Table 1. 'Sea anemone sign' was found in 43 (48.8%) lesions of which 40 (93.02%) were SBOT (Figure1). Specificity of 'sea anemone sign' for preoperative diagnosis of SBOT was 88.89%. 'Honeycomb sign' was noted in 15 (17.6%) of the lesions, and all the lesions were pathologically proven to be MBOT (Figure2). Specificity of the 'honeycomb sign' for the diagnosis of MBOT was 100%. There were significant differences in terms of presence of papillary projections, sea anemone sign, multilocularity, honeycomb sign between SBOT and MBOT ($p < 0.05$). Conclusion: MRI can be used to identify main subtypes of borderline ovarian tumours. Papillary projections and 'sea anemone sign' seem to be distinctive features for SBOT whereas Multilocularity and honeycomb sign are predictive of MBOT.

Figure1



33-year-old woman presented with abdominal distention. Sagittal and axial T2-weighted images show well-demarcated large cystic lesion with hypointense papillary projections. Note the protrusion of these projections from the posterior wall of the lesion.

Figure2



58-year-old woman presented with abdominal pain. Axial T2-weighted image shows a large multilocular cystic tumor with honeycomb sign (arrowhead). Contrast- enhanced T1-weighted image reveals enhanced thin septa.

Table-1

MRI features	Histological subtypes of borderline ovarian tumors	
	Serous (n=61, 69.3%)	Mucinous (n=27, 30.6%)
Content of the mass		
*Cystic w/o solid component	3	2
*Cystic with solid component	55	25
*Predominantly solid	3	0
Cystic component		
*Homogeneity	4	1
*Heterogenous	54	26
Unilocular	52	15
Multilocularity	6	12
Papillary projection		
-present	45	5
-absent	16	22
Sea anemone sign		
-present	40	3
-absent	48	24
Stained glass appearance		
-present		
-absent	11	20
	47	7

Fluid-fluid level		
-present	2	0
-absent	56	27
Honeycomb sign		
-present	0	15
-absent	58	12
Mural nodule		
-present	13	5
-absent	48	22
Preserved ovarian stroma		
-present	34	6
-absent	27	21
Ascites		
-present	20	15
-absent	41	12
Peritoneal implant		
-present	2	0
-absent	59	27

MRI features of serous and mucinous borderline ovarian tumors

Keywords: borderline, oncology, magnetic resonance imaging

A COMPREHENSIVE REVIEW OF POST-TREATMENT IMAGING IN GYNECOLOGIC MALIGNANCIES: CASE-BASED TIPS AND TRICKS FOR DETECTING POTENTIAL COMPLICATIONS AND AVOIDING PITFALLS

Yesim Yekta YURUK¹, Mehmet SIMSAR², Erdem KISA⁴, Muzaffer SANCI⁵, Hilal SAHIN³

¹University of Health Sciences, Izmir Tepecik Education and Research Hospital, Department of Radiology

²Izmir City Hospital, Department of Radiology

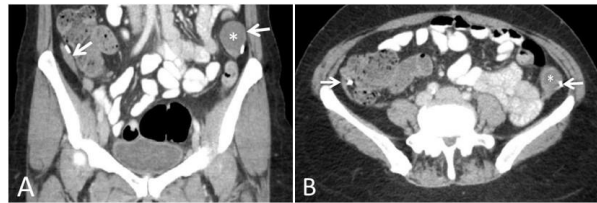
³University of Health Sciences, Izmir Faculty of Medicine, Department of Radiology

⁴Medicana International Izmir Hospital, Clinic of Urology

⁵University of Health Sciences, Izmir Faculty of Medicine, Department of Gynecologic Oncology Surgery

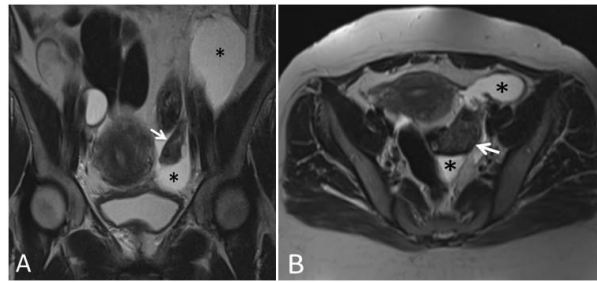
Abstract: Gynecological malignancies are among the most important malignancies affecting women after breast cancer. There are many different treatment strategies available depending on type, stage, and grade of malignancies. However, surgery and chemotherapy are the main treatment methods. Surgery remains the most effective treatment for most gynecological diseases. The most frequently performed surgical technique in gynecological malignancies is total abdominal hysterectomy. Chemotherapy and radiation therapy can be used as treatment options for the management of gynecologic malignancies in addition to surgery. Post-treatment complications may appear in days to months or even years. The common complications of gynecological malignancies are hemorrhage, hematoma, infection, abscess, bowel perforation, bowel obstruction, bowel fistula, vesicovaginal fistula, rectovaginal fistula, enterocutaneous fistula, bladder perforation, ureteral injury, omental infarction, lymphocele, peritoneal inclusion cyst, abdominopelvic granuloma, radiation cystitis, distal ureteral strictures, chronic radiation injury to the colon and rectum. There is a wide range of diagnostic imaging modalities for the assessment of complications. Computer tomography (CT), ultrasonography, magnetic resonance imaging (MRI), intravenous urography, fistulography, CT urography, retrograde pyelography, and cystography are diagnostic imaging modalities for these complications. In addition to post-treatment complications, possible pitfalls should also be kept in mind. The most well-known example of this pitfall is the ovarian transposition method used to remove the ovaries from the radiotherapy field during the operation. Lack of knowledge about the patient's surgical history and/or this surgical technique may lead to misidentification of transposed ovaries as recurrence or implant. Therefore, knowing the treatment methods used in gynecological malignancies, post-treatment complications, and possible pitfalls is vital for correcting diagnosis and determining the treatment method.

Fig.8



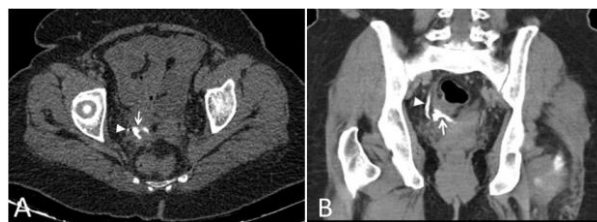
A 32-year-old woman with total abdominal hysterectomy. The coronal (A) and axial (B) contrast-enhanced CT images show the ovaries (arrows) are marked with metallic clips and moved laterally within the pelvis. This method is used to move functional ovaries out of the radiotherapy area. There is also a follicle cyst in the left ovary (asterisk).

Fig.7



A 69-year-old woman with myomectomy and polypectomy operation 11 years ago, with a diagnosis of low-grade endometrial carcinoma. Coronal (A) and axial (B) T2W images show a peritoneal inclusion cyst which is demonstrated as a cystic area (asterisks) lying in the left adnexal fossa. The left ovary (arrow) seems to be floating in this cystic area. This classic appearance is defined as a “spider in the web”.

Fig.3



A 60-year-old woman with a total abdominal hysterectomy and bilateral salpingo-oophorectomy. Axial (A) and coronal (B) delayed phase (10 min) CT images show ureterovaginal fistula (arrow) shown as contrast extravasation from the right ureter (arrowhead).

The common complications with diagnostic imaging modalities and surgery technique

Table 1. The common complications with diagnostic imaging modalities and surgery technique		
Complications	Imaging Method	
Hemorrhage and hematoma	CT	
Infection and abscess	US, CT	
Bowel perforation	CT, gastrografen small bowel follow-through or enema examination	
Bowel obstruction	CT, gastrografen small bowel follow-through or enema examination	
Fistula	Bowel fistula: CT, gastrografen small bowel follow-through, or enema examination	
	Vesicovaginal fistula: MRI, cystography	
	Rectovaginal fistula: MRI, gastrografen enema examination	
	Enterocutaneous fistula: Fistulography, CT with oral contrast material and multiplanar reformation, MRI	

Urinary tract complication	Bladder perforation: CT, cystography, CT cystography	High risk
	Ureteral injury: IVU, CT urography, retrograde pyelography	Low risk
Omental infarction	CT	High risk: TAH,
Lymphocele	US, CT	Hi,
Peritoneal inclusion cyst	US, CT	Low
Abdomino-pelvic granuloma	US, CT	Low
CT: Computer tomography, US: Ultrasonography, MRI: Magnetic resonance imaging, IVU: Intravenous urography		
TAH: Total abdominal hysterectomy, TLH: Total laparoscopic hysterectomy, VH: Vaginal hysterectomy, LAVH: Laparoscopically assisted vaginal hysterectomy, C/S: Cesarean section		

Keywords: Oncologic imaging, Surgical Oncology, Chemoradiotherapy, Theranostics, Education

POSTER PRESENTATIONS

Authors	Presenter Author	Abstract Title
Zeynep Nur Akyol Sarı, Eda Cingoz, Memduh Dursun	Eda Cingoz	Comparison of a Deep Learning Reconstruction Method With Other Reconstruction Methods In Coronary CT Angiography
Eda Cingoz, Rana Gunoz Comert, Mehmet Cingoz, Zuhul Bayramoglu	Eda Cingoz	Radiological Differences Between Neuroblastoma and Wilms Tumor
Cigdem Oztunali, Zeynep Canan Özdemir, Özcan Bör	Cigdem Oztunali	Bronchiolitis Obliterans Secondary to Graft Versus Host Disease in a Child with Acute Myeloid Leukemia
Cigdem Oztunali, Berat Acu, Zeynep Canan Ozdemir	Cigdem Oztunali	Polyostotic Fibrous Dysplasia Isolated to the Thoracolumbosacral Spine in a Child
Milena Spirovski, Silvija Lucic, Mladen Popov, Stefan Stojanoski, Aleksandar Ragaji, Kristina Polak, Milos Lucic	Milena Spirovski	Negative multiparametric prostate MRI in biopsy-naïve men - dynamic of the prostate volume and prostate-specific antigen density during follow-up
Cigdem Oztunali, Aslı Kavaz Tufan, Nuran Çetin, Coskun Yazar, Selcan Demir	Cigdem Oztunali	Pediatric Neuro Behçet Disease Presenting with Longitudinally Extensive Myelitis: The Bagel Sign on MRI
Cigdem Oztunali, Mehmet Surhan Arda, Hüseyin İlhan	Cigdem Oztunali	Torsion in a Bipartite Spleen: Imaging Findings in a Child
Cigdem Oztunali, Eylem Kırıl, Gürkan Bozan, Coşkun Yazar, Kürşat Bora Çarman	Cigdem Oztunali	Excitotoxic White Matter Injury on Diffusion-Weighted Imaging: A Review of Pediatric Causes
Cigdem Oztunali, Zeynep Canan Özdemir, Ersin Töret, Mehmet Surhan Arda	Cigdem Oztunali	Imaging Findings of Primary Peritoneal Rhabdomyosarcomatosis in a Child
Cigdem Oztunali, Merve Yazol, Berat Acu	Cigdem Oztunali	Imaging of congenital pyriform sinus fistula in children: A review of six cases
Cigdem Oztunali, Zeynep Canan Özdemir, Coşkun Yazar	Cigdem Oztunali	Magnetic resonance imaging of chemotherapy treatment-related intracranial complications in children with hematologic malignancies
Mehmet Cingoz, Emel Esmerer, Eda Cingoz, Suleyman Sonmez	Eda Cingoz	Efficacy of Ultrasound-Guided Microwave Ablation in the Treatment of Breast Fibroadenomas: A Follow-Up Study
Gulten SEZGIN, Merve KURT KOCAK	Merve KURT KOCAK	THE RADIOLOGICAL-PATHOLOGICAL CORRELATION IN BREAST CANCER CASES WITH NEOADJUVANT CHEMOTHERAPY
Berat Acu, Cigdem Oztunali, Serhat Demir	Berat Acu	US-guided Percutaneous Transabdominal Tru-cut Biopsy in Patients with Ovarian Tumors
Jasmina Kovacevic	Jasmina Kovacevic	BRAIN ARTERIOVENOUS MALFORMATIONS

Mehmet Seker, Mehmet Sait Dogan, Hayrettin Temel, Osman Kahraman, Fatma Zeynep Güngören, Mehmet Koçak, Cengiz Erol	Osman Kahraman	Normal Liver Stiffness Values Measured with MR Elastography and 2-D Shear Wave Elastography in Children (9-17 ages)
Sevde Nur Emir, Safiye Sanem Dereli Bulut	Sevde Nur Emir	Evaluating the Potential of Abbreviated MRI Protocols for Liver Metastasis Detection: A Study in Colorectal Cancer Patients
Kubilay Kağan Budak, Dilara Budak, Esat Kaba, Yusuf Çubukçu, Nur Hursoy, Gülen Burakgazi, Mehmet Beyazal, Fatma Beyazal Çeliker	Kubilay Kağan Budak	Effect Of Chemotherapy On Hippocampal Volume: A Preliminary Study
Merve Solak, Mehmet Beyazal	Merve Solak	Efficacy And Safety Of Endovascular Embolization With N-2-Butyl-Cyanoacrylate In Patients With Massive Hemoptysis: Results Of A Single-Center Experience
Serhat Akış, Mustafa Mahmut BARIS, Ayse COLAK	Serhat Akış	IgG4 related coronary artery periarteritis in a patient with coronary artery anomaly : a case report
Cigdem Oztunali, Berat Acu, Zühtü Özbek, Evrim Yılmaz	Cigdem Oztunali	Primary Synovial Sarcoma of the Cranial Vault
Gülbanu Güner, Ayşe Şilan Kapuci, Fatma Kulalı	Ayşe Şilan Kapuci	The Role Of Kaiser Scoring System In Breast MRI For Risk Stratification Of Intraductal Papilloma
Ahmet Taha Kayaoğlu, Mehmet Beyazal	Ahmet Taha Kayaoğlu	The Effectiveness of Ultrasound-Guided Percutaneous tPA Injection in Thrombosed Arteriovenous Fistula
Cigdem Oztunali, Selcan Demir	Cigdem Oztunali	Imaging Findings of Chronic Recurrent Multifocal Osteomyelitis and Its Mimics in Children
Ceren Aydın, Nurdan Çay	Ceren Aydın	Correlation of skeletal muscle index with T-score to determine the bone mineral density
Jasmina Kovacevic	Jasmina Kovacevic	Pulmonary arteriovenous malformations
Seda Sogukpınar Karaagac, Nevzat Yesilmen	Seda Sogukpınar Karaagac	Evaluation Of The Efficacy Of Deep Transverse Friction Massage In Lateral Epicondylitis Using Superb Microvascular Imaging On Common Extensor Tendon Vascularisation
Nilufar Gasimli, Sukru Mehmet Erturk, Hakan Ayyildiz, Vusal Mammadli	Nilufar Gasimli	COMPARISON OF PET/CT AND CT TEXTURE ANALYSIS IN PATIENTS WITH STAGE III-IV LUNG CANCER RECEIVING CHEMORADIOTHERAPY: CAN WE PREDICT THE TREATMENT RESPONSE OF THE TUMOR?

VUSAL MAMMADLI, NILUFAR GASIMLI, SUKRU MEHMET ERTURK, HAKAN AYYILDIZ	NILUFAR GASIMLI	EVALUATION OF PNEUMOTHORAX PREDICTIONABILITY BY DEEP LEARNING METHOD BEFORE TRANSTHORACIC FINE NEEDLE ASPIRATION BIOPSY (TTIAB) IN LUNG MASSES
Milena Spirovski, Mila Kovacevic, Iva Popov, Aleksandra Milovancev, Silvija Lucic, Andrea Peter, Branislava Ilincic, Milos Lucic	Milena Spirovski	Could cardiac magnetic resonance imaging help in the assessment of the underlying cause of the significantly improved congestive heart failure?
Umur Anıl Pehlivan, Cankat Erdoğan, Şenay Demir-Kekeç	Umur Anıl Pehlivan	Magnetic Resonance Imaging Findings of Neonatal Ovarian Torsion
Cigdem Oztunali, Berat Acu, Serhat Demir	Berat Acu	Efficacy of US-guided Percutaneous Fine Needle Aspiration Biopsy in Patients with Parotid Gland Masses
Ayşegül Taşdöğen	Ayşegül Taşdöğen	Relationship Between ADC Values And Histopathologic Prognostic Markers of Breast Carcinoma
İrfan Durmuş, Yeliz Aktürk, Ebru Çılbır	İrfan Durmuş	Investigation Of The Effect Of Body Composition Measurements Defined By Computed Tomography Before Treatment On Disease Prognosis In Patients With Metastatic Colon Cancer And Comparison With Other Clinicopathological Prognostic Parameters
HAMZA EREN GÜZEL, GÖKTUĞ AŞÇI, OYTUN DEMİRBİLEK, TUĞÇE DOĞA ÖZDEMİR, PELİN BERFİN EREKLİ	HAMZA EREN GÜZEL	CLASSIFICATION OF BRAIN CT REPORTS BY EMERGENCY LEVEL USING ARTIFICIAL INTELLIGENCE
Seyit Erol, Halil Özer, İsmail Dilek, Abdi Gürhan, Mehmet Öztürk	Abdi Gürhan	Evaluation of Lateral Pterygoid Muscle Signal and Mandibular Condyle Morphology with Anterior Disc Dislocation of the Temporomandibular Joint in Adolescents.
Seyit Erol, Halil Özer, Abdi Gürhan, Mustafa Koplay, Mehmet Öztürk	Abdi Gürhan	Assessment of Lateral Pterygoid Muscle Signal and Mandibular Condyle Morphology with Anterior Disc Dislocation of the Temporomandibular Joint on 3T MRI
Ahmet Tanyeri, Emir Hüseyin Nevai	Emir Hüseyin Nevai	Percutaneous Cholecystostomy and Its Impact on Subsequent Surgical Interventions in Acute Cholecystitis
Celal Caner Ercan, Edanur Karapınar, Asli Ciftcibasi Ormeci, Mesut Bulakci	Celal Caner Ercan	Quantitative Evaluation of Liver Steatosis Using Ultrasound Attenuation Imaging: A Comparison with MRI
Cigdem Oztunali, Mehmet Surhan Arda, Hüseyin İlhan	Cigdem Oztunali	Double Bubbles Beyond the Neonatal Period: Imaging Findings of Duodenal Obstruction in Children

Sezer Nil YILMAZER ZORLU, Ruhi Erdem ERGÜDEN, Diğdem KURU ÖZ, Ayşe ERDEN	Sezer Nil YILMAZER ZORLU	COMPARATIVE DIAGNOSTIC PERFORMANCE OF TWO ABBREVIATED MRI PROTOCOLS FOR HEPATOCELLULAR CARCINOMA
Olgun Şahin, Hilal Şahin	Hilal Şahin	Collision tumors of the ovary: "Two in one"
Milan Pantelic, Tamara Vucinic, Milica Stanucevic, Milos Dujovic, Masa Pantelic	Milan Pantelic	Interventional radiology management of splenic abscess due to Salmonella enteritidis following abdominal trauma – case report
HAMZA EREN GÜZEL, LEANDER MAERKISCH, CHRISTIAN WIEDEMEYER, BIANCA TEODERESCU, LEONARD GILBERG, ALİ MURAT KOÇ	HAMZA EREN GÜZEL	DETECTION OF BRAIN ANEURYSMS ON T2W IMAGES BY USING ARTIFICIAL INTELLIGENCE
Şefika Bengi Cilasın, Hasan Erdogan, Ali Koç	Şefika Bengi Cilasın	A CASE OF PULMONARY ALVEOLAR MICROLYTICOSIS
Ahmet Tanyeri, Ali Alkaşı	Ali Alkaşı	Relationship between the angle of popliteal artery trifurcation branches and atherosclerosis burden in chronic peripheral arterial disease
Elçin Aydın, Hülya Çetin Tuncez, Özden Karadeniz, Gül Çolakoğlu, Hüseyin Esin, Cem Karaali, Emel Ebru Pala, Şükrü Şahin	Elçin Aydın	THE IMPACT OF BODY FAT DISTRIBUTION AND SARCOPENIA ON NAC REACTION AND RECURRENCE IN LABC PATIENTS DEPENDING ON MOLECULAR SUBTYPES
CHRISTOS KORRES, ANASTASIA DOUKOPOULOU, FOTINI MERMIGKA, CHARIKLEIA TRIANTOPOULOU	CHARIKLEIA TRIANTOPOULOU	From Headaches to Obstructive Ileus: Following the dots
Sule Ozer, Bilge Gultac	Bilge Gultac	Subclavian Artery Dissection: The Visible Tip of the Aortic Iceberg!
Mesut Furkan Yazar, Elif Kır Yazar, Kadir Çorbacı	Mesut Furkan Yazar	Gossypiboma: a diagnosis to be remembered
Gulseher Saylan, Seda Sogukpınar Karaagac	Seda Sogukpınar Karaagac	A rare sesamoid bone of the foot; os vesalianum
Nusret Seher, Mehmet Öztürk, Abdi Gürhan, Alaaddin Nayman, Halil Özer, Gülperi Çelik	Abdi Gürhan	Comparison of Temporomandibular Joint Disc in Chronic Renal Failure Patients and Healthy Adults with Shear Wave Elastography
Mesut Furkan Yazar, Elif Kır Yazar, Özcan Emre, Kadir Çorbacı, Mehmet Emin Gönüllü	Mesut Furkan Yazar	Gastropancreatic Fistula: A Rare Complication of Recurrent Pancreatitis.
Onur Başdemirci, Merve Başdemirci, Safiye Gürel	Onur Başdemirci	Mayer-Rokitansky-Küster-Hauser Syndrome with Supernumerary Ovary: Very Rare Congenital Co-occurrence
Mesut Furkan Yazar, Elif Kır Yazar, Dilay Demirayak, Ezgi Emre	Mesut Furkan Yazar	Overlooked Small Bowel Mass: Gastrointestinal Stromal Tumor

Elif Kır Yazar, Mesut Furkan Yazar, Kadir Çorbacı, Mehmet Emin Gönüllü	Mesut Furkan Yazar	Dangerous Complication of Acute Cholecystitis: Gallbladder Perforation
Osman Konukoğlu, Murat Kaya	Osman Konukoğlu	Is There A Correlation Between Coronary Artery Calcium Score And Epicardial/Paracardial Adipose Tissue Quantification
Ruhi Erdem Ergüden, Sezer Nil Yılmaz Zorlu, Diğdem Kuru Öz, Ayşe Erden	Sezer Nil Yılmaz Zorlu	Uterine Smooth Muscle Tumors Of Uncertain Malignant Potential (STUMP): A Report Of Two Cases
Gulden Karatag, Ahmet Topal	Ahmet Topal	What if it is not just wall thickening?
Sule Ozer, Ahmet Topal	Ahmet Topal	Delayed Diagnosis of Subclavian Artery Pseudoaneurysm Following Suicide Attempt in Major Depression: The Critical Role of Detailed Ultrasound Imaging
Gulden Karatag, Saner Esmer	Saner Esmer	Intraperitoneal Pregnancy: A Ticking Time Bomb in the Abdomen - A Critical Diagnostic Challenge
Merve Başdemirci, Onur Başdemirci	Merve Başdemirci	An Uncommon Cause of Abdominal Pain: Huge Gastric Bezoar
ZEYCAN KUBRA CEVVAL, MASIDE ARI, İrfan Durmuş	İrfan Durmuş	Computed tomographic pulmonary angiography in the assessment of severity of acute pulmonary embolism and right ventricular dysfunction
Nihal Deniz Menten, Serhat Akis, Sinem GEZER	Nihal Deniz Menten	Lung Involvement in Rheumatoid Arthritis: Radiological Approach
Tuğçe Hancioğlu, Aslı Irmak Akdoğan, Muzaffer Sancı, Esra Canan Kelten Talu, Hilal Şahin	Tuğçe Hancioğlu	Preoperative prediction of serous and mucinous borderline ovarian tumors according to MRI features
Jasmina Kovacevic	Jasmina Kovacevic	Gastric Diverticulum
Mesut Furkan Yazar, Şevket Kahraman, Hüseyin Aydemir, Mehmet Gündüz, Mecit Kantarcı, Sonay Aydın	Mesut Furkan Yazar	Correlation Between CT Liver Density (HU values) and Laboratory Values in Hepatosteatos
Ayşe Ozkan, Seda Sogukpinar Karaagac, Gulseher Saylan	Seda Sogukpinar Karaagac	Primary pathology or secondary? Disseminated Intravascular Coagulopathy with Differential Diagnosis
Anna Simichanidou, Nikolaos Bouras, Vasiliki Alexiadou, Melpomeni Kosmidou, Ekaterini Xinou, Eleni Karoglou	Anna Simichanidou	Hepatic Gas Gangrene: Two Cases Of A Rare Post - Operative Complication
Anna Simichanidou, Nikolaos Bouras, Ekaterini Xinou, Anna Paschali, Eleni Karoglou	Anna Simichanidou	Pancreatic Neuroendocrine Tumors: A Stepwise Approach To Differential Diagnosis.
Anna Simichanidou, Nikolaos Bouras, Ekaterini Xinou, Eleni Karoglou	Anna Simichanidou	Pancreatic Ductal Adenocarcinoma And Mimics: Tips To Avoid Misdiagnosis In Computed Tomography

Eleftherios Kavroulakis, Antonios Kagialis, Anna Simichanidou, Eirini Gratsia, Eliza Kompoliti, Georgios Bertsias, Vasileios Mastorodemos, Panagiotis Simos, Dimitrios Boumbas, Efrosini Papadaki	Anna Simichanidou	Neuropsychiatric Lupus Or Multiple Sclerosis? Differential Diagnosis Using Myelin Content Indices Of Normal Appearing White Matter: A Myelin Water Imaging Study.
Merve Başdemirci, Onur Başdemirci	Merve Başdemirci	Acute Aortic Syndrome: General Radiological Overview with Cases
Celal Caner Ercan, Sait Kayalı, Edanur Karapınar, Zeynep Nur Akyol Sarı, İbrahim Demir, Bülent Acunaş	Celal Caner Ercan	Proximal Stent Holder Fracture: A Rare Complication of Endurant II® Aortic Stent-Graft
Yeliz Aktürk, Rasime Pelin Kavak	Yeliz Aktürk	Left atrial band; a rare congenital anomaly
Nur Hursoy, Hafsa Kolluk, Esat Kaba, Ahmet Taha Kayaoglu, Huseyin Er, Yusuf Cubukcu, Dilara Yilmaz Budak	Hafsa Kolluk	Detection of Urgent Pathology in Pediatric Emergency Ultrasound Reports Using Large Language Models
Fatih Ateş	Fatih Ateş	Imaging Findings and Complications in Anterior Cruciate Ligament Reconstruction
İbrahim Çağrı Tural	İbrahim Çağrı Tural	Extensor digitorum brevis manus muscle; a rare variant
Merve Başdemirci, Onur Başdemirci	Merve Başdemirci	Inferior Vena Cava Duplication – A Case Report
Safiye Gürel, Mete Sezer, Merve Başdemirci, Onur Başdemirci, Samet Töken	Merve Başdemirci	MRI DIAGNOSIS OF OVARIAN MASSES: MAKE THIS PUZZLE EASY
Ahmet Bozer, Cengiz Yilmaz, Hülya Çetin Tunçöz, Demet Kocatepe Çavdar, Zehra Hilal Adıbelli	Ahmet Bozer	Correlation of Histopathological and Radiological Response Patterns and Their Prognostic Implications in Breast Cancer After Neoadjuvant Chemotherapy
Onur Başdemirci, Merve Başdemirci	Onur Başdemirci	A Rare Cause of Ileus in Adults: Intussusception-Case Report
Umur Anıl Pehlivan, Hülya Özdemir, Bermal Hasbay, Filiz Aka-Bolat	Umur Anıl Pehlivan	Digital Breast Tomosynthesis-Guided Biopsy: Initial Experience
Fatma Zeynep Arslan, Sinan Erdemi	Fatma Zeynep Arslan	A High Acromion-Greater Tuberosity Impingement Index Increases the Risk of Labral Tear
Mehmet Karagülle, Fatma Zeynep Arslan	Fatma Zeynep Arslan	Evaluating Specimen Adequacy in Thyroid FNAB: A Comparison of Transfer Techniques
Serhat Akış, Fatma Ceren Sarıoğlu, Handan Güleriyüz	Serhat Akış	Meckel diverticulum pathologies in pediatric patients; case-based approach
İbrahim Çağrı Tural	İbrahim Çağrı Tural	Accessory extensor carpi radialis longus tendon

Serhat Akış, Nurullah Çakır, Mustafa Mahmut Barış, Ayşe Çolak	Serhat Akış	Evaluation of the relationship between coincidentally detected non-compaction cardiomyopathy on coronary CT angiography and the level of coronary artery disease and the patient's symptoms ; a retrospective study
İbrahim Çağrı Tural	İbrahim Çağrı Tural	The accessory extensor carpi radialis intermedius tendon
İbrahim Çağrı Tural	İbrahim Çağrı Tural	Radiological Features of Placental Mesenchymal Dysplasia
İbrahim Çağrı Tural	İbrahim Çağrı Tural	The accessory extensor carpi radialis longus and brevis coincidence
İbrahim Çağrı Tural	İbrahim Çağrı Tural	Absence of Extensor Carpi Radialis Longus Tendon
Oner Ozbey, Fatma zeynep Arslan	Fatma Zeynep Arslan	Acromion–great tuberculous impingement index may predict the susceptibility to rotator cuff tears and sports injury in children.
İbrahim Çağrı Tural	İbrahim Çağrı Tural	Radiological Features of Borderline Serous Ovarian Tumor
İbrahim Çağrı Tural	İbrahim Çağrı Tural	intracranial lesions of tuberous sclerosis
Elçin Aydın, Raşit Eren Büyüktoka, Hilal Şahin	Elçin Aydın	Imaging findings of granulosa cell tumor: ovarian mass and endometrial hyperplasia
Aykut Teymur	Aykut Teymur	Tetralogy of Fallot (ToF) and Major Aortopulmonary collateral Arteries (MAPCAs)
Şule Özer, Saner Esmer	Saner Esmer	A Curious Twist: The Discovery of Extensive Calcinosis Universalis Revealed in a Case of Rectus Sheath Hematoma
Dursun Can KARAKUŞ, Hasan ERDOĞAN, Ömer Baran YAMAN, Elif Aybala YILDIRIM, Esad Cihan LÜY	Hasan ERDOĞAN	Situs inversus and autosomal dominant polycystic kidney disease in an adult patient
Nurullah Dağ, Abdi Gürhan, Sevgi Demiröz Taşolar, Mehmet Öztürk	Abdi Gürhan	Normative Choroidal Plexus Apparent Diffusion Coefficient Values in the Pediatric Population
İsmail Furkan ŞİMŞEK, Hasan ERDOĞAN	İsmail Furkan ŞİMŞEK	The impact of defect size on hernia sac contents and the development of ileus in abdominal wall hernias
Mehmet Demir, Nicon Nita	Nicon Nita	"Radiological and Clinical Evaluation of Enchondromas: A Retrospective Study of 112 Cases"
Esin Cibiroglu, Fatma Kulali	Esin Cibiroglu	Gd-EOB-DTPA-enhanced MRI with T1 mapping versus fibrosis-4 index for staging liver fibrosis
Narmin Hüseyinli, Ezgi Güler, Laman Hüseyinzade	Narmin Hüseyinli	Inferior mesenteric vein thrombophlebitis secondary to acute diverticulitis

Yesim Yekta YURUK, Mehmet SIMSAR, Erdem KISA, Muzaffer SANCI, Hilal SAHIN	Yesim Yekta YURUK	A comprehensive review of post-treatment imaging in gynecologic malignancies: case-based tips and tricks for detecting potential complications and avoiding pitfalls
Vedat Yaman, Selin Ardali Duzgun, Tuncay Hazirolan	Vedat Yaman	Isolated Liver Herniation to Posterior Mediastinum Through Gastroesophageal Hiatus
Selahattin Durmaz, Sinan Seyrek, Kaan Ozbozduman, İbrahim Halil Akkis, Merve Gulbiz Dagoglu Kartal	Selahattin Durmaz	The Utility of Quantitative ADC and T2 Values, Enhancement Pattern, and Lesion Shape Characteristics in Differentiating True Positive from False Positive Lesions on Multiparametric Prostate MRI
Catarina TRINDADE, Labrini ADAMOPOULOU, Afroditi KAROUTA, Foteini MERMIGKA, Anastasia TSAKIRI, Dimitrios FAGKREZOS, Charikleia TRIANTOPOULOU	Charikleia TRIANTOPOULOU	The importance of Dorsal (supine) decubitus X-ray in Pneumoperitoneum
İbrahim Çağrı Tural	İbrahim Çağrı Tural	Herlyn-Werner-Wunderlich syndrome
Foteini MERMIGKA, Labrini ADAMOPOULOU, Vasileios CHATONIDIS, Catarina TRINDADE, Chrysi CHATZIKONSTANTINOU, Petros MANIATIS, Charikleia TRIANTOPOULOU	Charikleia TRIANTOPOULOU	AI IN RADIOLOGY: A ROBUST ASSISTANT OR A MISLEADING TOOL? PRIMARY RESULTS
Anastasios GIAPRAKIS, Afroditi KAROUTA, Anastasia PAPA, Konstantinos VITZILAIOS, Dimitrios ARGYROPOULOS, Georgios ANASTOPOULOS, Charikleia TRIANTOPOULOU	Charikleia TRIANTOPOULOU	A case of suspected foreign body swallowing: the use of X-ray and Ultrasound as screening methods
İbrahim Çağrı Tural	İbrahim Çağrı Tural	Rice bodies in the wrist
Nurullah Dağ, Sevgi Demiröz Taşolar, Abdi Gürhan, Mehmet Öztürk	Abdi Gürhan	The role of apparent diffusion coefficient assessment in Wilson disease with neurological involvement
Dilşah Oral, Ahmet Burak Kale, Gülgün Yılmaz Ovalı	Ahmet Burak Kale	Solitary Fibrous Tumor in the Central Nervous System: Two Cases
Ahmet Burak Kale, Ozan Acar, Dilşah Oral, Gülgün Yılmaz Ovalı	Ahmet Burak Kale	Ischemic Stroke as a Rare Complication of a Bee Sting: A Case Report
Halil İbrahim Şara, Nusret Seher, Abdi Gürhan, Fatih Ateş, Mustafa Azmi Eyiol	Abdi Gürhan	A Rare Coronary Artery Anomaly: Congenital Absence of the LCX

Halil İbrahim Şara, Nusret Seher, Fatih Ateş, Abdi Gürhan, Mustafa Azmi Eyiöl	Abdi Gürhan	Dominant LCX Originating from the Right Sinus of Valsalva
Yeliz Akturk, Rasime Pelin Kavak	Yeliz Akturk	A rare case: Unroofed coronary sinus ASD and persistent left superior vena cava
Halil İbrahim Şara, Nusret Seher, Abdi Gürhan, Fatih Ateş, Mustafa Azmi Eyiöl	Abdi Gürhan	A rare coronary artery anomaly: Left main coronary artery originating from right sinus valsalva
Halil İbrahim Şara, Nusret Seher, Abdi Gürhan, Fatih Ateş, Öznur Güvenç Uzunay	Abdi Gürhan	A rare case: Pulmonary Cement Embolism
Nisa Serin, Abdi Gürhan, Mehmet Öztürk	Abdi Gürhan	Neonatal Osteomyelitis: Plain Radiography And Ultrasound Findings
Fatma Zeynep Arslan	Fatma Zeynep Arslan	Comparison of T1A Post-Contrast and FLAIR Imaging Methods in the Diagnosis of Non-Enhancing Leptomeningeal Metastases: FLAIR Hyperintensity as an Early Finding
Damla Arslan, Seda Sogukpınar Karaagac	Seda Sogukpınar Karaagac	A Rare Case; Trigeminal Nerve Root Involvement Of Sinonasal Mucormycosis In An Immunocompromised Patient
Ahmet Nedim Kahraman, Kamber Göksu, Ahmet Vural, Uğur Berk Akdağ	Ahmet Nedim Kahraman	LUMBAR MRI FINDINGS IN CHILDREN AND ADOLESCENTS PRESENTING WITH NON-SPECIFIC LOW BACK PAIN
İbrahim Çağrı Tural	İbrahim Çağrı Tural	Fibrous talocalcaneal coalition on MRI
Zülküf AKDEMİR, Ramazan YILDIZ, Adem YOKUŞ, Murat CANAYAZ, Harun ARSLAN, Saim TÜRKOĞLU	Zülküf AKDEMİR	Automated Classification Of The Phasexase Scale In Mri Using Deep Learning Methods
Olgun Şahin, Hilal Şahin	Hilal Şahin	Ileocolic and colocolic intussusception in adults: CT features and pathological correlation
Gülşen Yücel Oğuzdoğan	Gülşen Yücel Oğuzdoğan	Diagnostic Utility of Quantitative and Semi-Quantitative Parameters from Multiparametric MRI in Prostate Cancer Detection: A Retrospective Study
Abdi Gürhan, Nusret Seher, Mustafa Koplay	Abdi Gürhan	A Rare Anomaly: Partial Pericardial Agenesis Imaging Findings
Melike Zeynep AYBAK, Süleyman Men	Melike Zeynep AYBAK	Orbital Tumors
Gülşen Yücel Oğuzdoğan	Gülşen Yücel Oğuzdoğan	Patterns of Nasal and Paranasal Sinus Injuries in Maxillofacial Trauma: A Retrospective Analysis of Etiologies and Fracture Locations

Gizem Özmen, Deniz Esin Tekcan Şanlı	Deniz Esin Tekcan Şanlı	Evaluation of the Variability of Axillary Artery and Internal Mammary Artery Diameters According to Intramammary Tumor Location in Breast Cancer Patients with Magnetic Resonance Imaging
Zeynep Banu Aydın	Zeynep Banu Aydın	The mammographic and MRI appearances of ultrasonographic visible malignant breast microcalcifications
Fatih ATES, Mehmet Sedat DURMAZ	Fatih ATES	Radiological Imaging Characteristics of Teratomas Detected During the Prenatal Period
Laman Huseynzade	Laman Huseynzade	TART (Testicular adrenal rest tumors)
Kübra Bozkurt, Hüseyin Bozkurt, Hanife Özdemir, Abdullah Soydan Mahmutoglu	Kübra Bozkurt	Lipoma arborescens of the knee on MRI : A rare case report
EYUP KIZIL	EYUP KIZIL	Is It Feasible to Establish a Stroke Unit in the Remotest Corner of Türkiye? A Case Series from Hakkari
Mete Sezer, Merve Başdemirci, Onur Başdemirci, Safiye Gürel, Samet Töken	Onur Başdemirci	MRI OF OVARIAN CYSTADENOMAS
Hanife Gülden Düzkalır, Günay Rona, Elif Söbü	Hanife Gülden Düzkalır	Comparative Analysis of Brain Volume Differences Between Puberty Precocious and Normal Puberty Girls
Abdi Gürhan, Nusret Seher	Abdi Gürhan	Adenoma Malignum of Uterin Cervix:Magnetic Resonance Imaging Findings
Gulseher Saylan, Seda Sogukpinar Karaagac	Seda Sogukpinar Karaagac	Rare Accessory Bone Of The Foot; Os Calcaneus Secundaris
Aslı Aras, Gizem Nur Çolak, Eren İsmailoğlu, Mehmet Hakan Bıçak	Aslı Aras	Ultrasound-Guided Thrombin Injection for the Treatment of Arterial Pseudoaneurysm
Atakan Kurt, Deniz Esin Tekcan Şanlı	Deniz Esin Tekcan Şanlı	Rare Involvement of Sarcoidosis: Intramammarian and Bilateral Axillary Multiple Lymphadenopathies
Yasemin Kucukciloglu, Deniz Aydın	Yasemin Küçükçiloğlu	MRI-based Comparative Assessment of Cam and Pincer Type Hip Morphology Between Semi-Professional Soccer Players and Non-Athlete Controls
Deniz Esin Tekcan Şanlı	Deniz Esin Tekcan Şanlı	A Rare and Interesting Case Report: Invasive breast carcinoma with spontaneous regression after labour
Dragana Nikolić, Fahad Al Abdughani	Dragana Nikolić	Left circumflex aorta -case report

Fatih ATES, Mehmet Sedat DURMAZ, Mustafa KOPLAY	Fatih ATES	A RETROSPECTIVE ANALYSIS OF CASES AND RADIOLOGICAL EVALUATION OF PATHOLOGICAL FINDINGS BASED ON 13 YEARS OF EXPERIENCE IN FETAL MRI AT A TERTIARY CARE CENTER.
Dilara Budak, Kubilay Kağan Budak, Esat Kaba, Hande Melike Bülbül, Gülen Burakgazi	Dilara Budak	A Rare Urogenital Anomaly: Zinner Syndrome
Aytekin Erol, Zülküf Akdemir, Saim Türkoğlu, Ensar Türko, Bulut Tuğal, Muhammed Bilal Akıncı, Mesut Özgökçe	Aytekin Erol	A RARE CASE: HEPATIC EPITHELIOID HEMANGIOENDOTHELIOMA WITH LUNG METASTASIS

RADIOLOGICAL DIFFERENCES BETWEEN NEUROBLASTOMA AND WILMS TUMOR

Eda Cingoz¹, Rana Gunoz Comert², Mehmet Cingoz³, Zuhay Bayramoglu²

¹Bagcilar Training and Research Hospital

²Istanbul University Faculty of Medicine

³Basaksehir Cam and Sakura City Hospital

Abstract: Introduction and aim: Both neuroblastoma and Wilms tumor are among the most common intra-abdominal malignancies in childhood, with treatments differing significantly. Therefore, proper distinction between these tumors is imperative. The aim of the present study was to identify radiological differences between neuroblastoma and Wilms tumor. Material and method: Contrast enhanced computed tomography (CT) images of 20 patients diagnosed with neuroblastoma (median age 15 months; interquartile range 48 months) and 22 patients diagnosed with Wilms tumor (median age 31 months; interquartile range 35 months) who applied to our hospital between 2020 and 2023 were evaluated. Using Pearson Chi-Square analysis, lesions were categorized according to unilaterality or bilaterality, presence of multilobulation and macroscopically visible vessels, calcification and necrosis, and vascular encasement. Findings: There was no significant difference in the median age (p: 0.11) and gender distribution (p: 0.46) between the two tumor types. Evaluation of macroscopically detectable intra-lesional vessel feature by 2 different board-certified radiologists with 7 and 12 years of radiology experience respectively revealed a consensus of significantly higher visibility of intralesional vessels in Wilms tumor (p< 0.001). Although multilobulation (p:0.22) and calcification (p:0.5) were more commonly seen in neuroblastoma, the difference was not statistically significant. Unilaterality (p:0.012) and vascular encasement (p<0.001) were significantly more frequently seen in neuroblastoma. Conclusion: Lobulation, unilaterality or bilaterality, and vascular surroundings of the tumors may vary depending on the tumor stage. However, intra-tumor selectable vascular evaluation, which was found to be significantly higher in Wilms tumor, was revealed as an important discrimination criterion for tumor histology. The retrospective design and relatively small patient cohort may be counted as limitations of the study.

Figure1

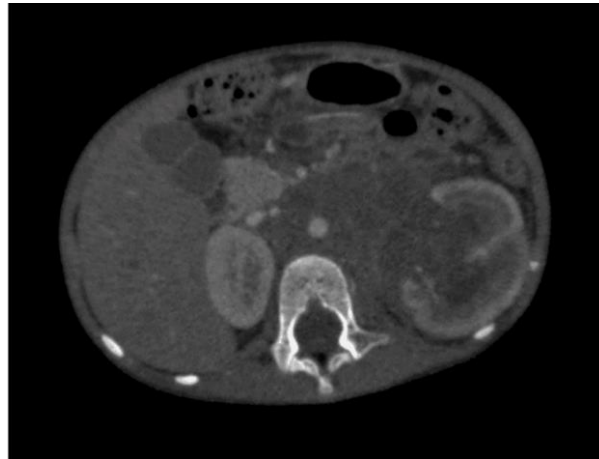


Fig1. Axial CT image of a 57-month-old female with neuroblastoma, showing the tumor encircling the aorta 360 degrees.

Figure2



Fig2. Axial CT slice of a 31-month-old male with a diagnosis of neuroblastoma demonstrating multilobulation within the mass. Macroscopic examination reveals visible vessels (black arrows) and encasement of the abdominal aorta.

Figure3



Fig3. Axial CT scan of a 29-month-old male diagnosed with bilateral Wilms tumor. The image shows bilateral renal masses with visible calcifications, indicated by white arrows.

Keywords: Neuroblastoma, Wilms Tumor, Computed tomography

BRONCHIOLITIS OBLITERANS SECONDARY TO GRAFT VERSUS HOST DISEASE IN A CHILD WITH ACUTE MYELOID LEUKEMIA

Cigdem Oztunali¹, Zeynep Canan Özdemir², Özcan Bör²

¹Eskisehir Osmangazi University Medical Faculty, Department of Radiology, Division of Pediatric Radiology

²Eskisehir Osmangazi University Medical Faculty, Department of Pediatrics, Division of Pediatric Hematology and Oncology

Abstract: Aim: To present radiography and computed tomography (CT) findings of a case of bronchiolitis obliterans (BO) secondary to graft versus host disease (GVHD) in a child with acute myeloid leukemia (AML). Case Presentation: A 12-year-old boy with AML treated with chemotherapy received hematopoietic stem cell transplantation (HSCT). One year later, he was diagnosed with GVHD with skin and muscle involvement and had dyspnea on admission. A radiograph of the chest showed mild hyperinflation with flattening of both hemidiaphragms. Mild bronchial thickenings were observed. CT of the thorax showed mild bronchiectases, bronchial wall thickening, peribronchial reticulonodular markings (Fig.1). An expiratory high-resolution CT showed patchy mosaic attenuation pattern (Fig 2). Bronchiolitis obliterans due to GVHD was diagnosed, and the patient received corticosteroids and photopheresis. Clinical response was achieved. A post-treatment CT showed regression of the bronchial wall thickening and peribronchial infiltrates (Fig 3). Discussion: Pulmonary GVHD is one of the thoracic complications of hematopoietic stem cell transplantation. It may be divided into acute and chronic pulmonary GVHD. Chronic GVHD most commonly manifests with bronchiolitis obliterans (BO). BO is characterized by concentric stenosis of the bronchial lumen due to inflammation and fibrosis of the terminal bronchioles, leading to airway obstruction and air trapping. Plain radiographs of the chest can be normal in the presence of BO. If abnormal, non-specific findings may include hyperinflation, attenuation of pulmonary vascular markings, and abnormal reticular markings. On CT, bronchiectasis, small airway thickening, and peribronchial reticulonodular markings can be observed. On expiratory high-resolution CT scans, air trapping and oligemia of the affected lung areas result in a mosaic attenuation pattern characterized by the presence of sharply demarcated hypo- and hyperattenuating lung areas. The mosaic attenuation pattern can be found in various pulmonary diseases, including occlusive vascular or infiltrative parenchymal diseases. In BO, the low-attenuation lung areas result from air trapping and oligemia. Conclusion: BO secondary to GVHD can occur in patients who have undergone HSCT. The condition presents clinically with dyspnea, dry cough, and reduced expiratory volume. Inspiratory CT may show bronchial wall thickening, bronchiectasis, and peribronchial reticulonodular infiltrates. An expiratory high-resolution CT better demonstrates the air trapping and the resultant mosaic attenuation pattern.

Figure 1



A normal chest radiograph before the development of pulmonary symptoms (A). A radiograph obtained at the pulmonary symptoms' onset (B) shows flattening of the diaphragms due to air trapping (long arrows, B) with occasional mild peribronchial wall thickenings (short arrow, B). Inspiratory CT images of the thorax (a-d) show mild tubular bronchiectases, bronchial wall thickenings, and peribronchial reticulonodular infiltrates (arrows).

Figure 2

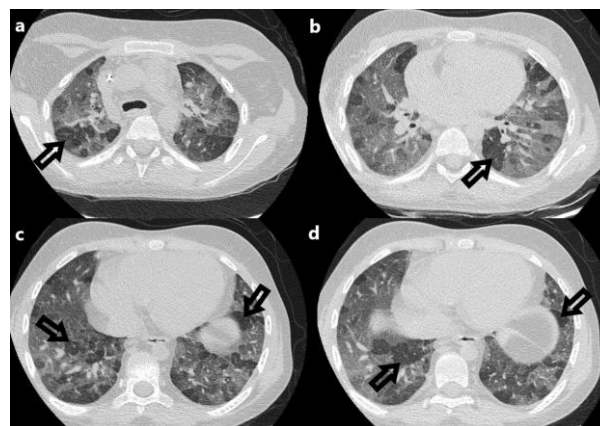
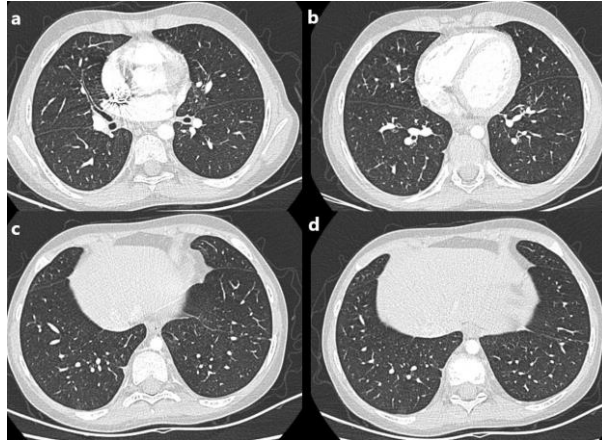


Figure 3. Expiratory HRCT images show the affected lung fields as sharply demarcated hypoattenuating oligemic areas (arrows). A combination of affected and less affected–nonaffected areas results in the mosaic attenuation pattern.

Figure 3



Post-treatment inspiratory CT images show regression of bronchial wall thickenings and peribronchial infiltrates, with normal attenuation of the lung parenchyma.

Keywords: acute myeloid leukemia, bronchiolitis obliterans, computed tomography, graft versus host disease, high resolution expiratory computed tomography

POLYOSTOTIC FIBROUS DYSPLASIA ISOLATED TO THE THORACOLUMBOSACRAL SPINE IN A CHILD

Cigdem Oztunali¹, Berat Acu², Zeynep Canan Ozdemir³

¹Eskisehir Osmangazi University Faculty of Medicine, Department of Radiology, Division of Pediatric Radiology

²Eskisehir Osmangazi University, Faculty of Medicine, Department of Radiology, Division of Interventional Radiology

³Eskisehir Osmangazi University, Faculty of Medicine, Department of Pediatrics, Division of Pediatric Hematology and Oncology

Abstract: Aim: To present magnetic resonance imaging (MRI) and computed tomography (CT) findings of polyostotic fibrous dysplasia of the spine isolated to the thoracolumbosacral vertebrae. Case: A 13-year-old boy with a history of recent minor trauma was imaged due to back pain. A lateral lumbosacral radiograph of the spine showed a collapsed L2 vertebra. A pathological fracture was suspected, and an MRI was obtained. MRI confirmed the pathological signal of the collapsed L2 corpus and revealed additional solid expansile bone lesions of the sacral vertebrae with well-defined sclerotic margins, variable T2W signal intensity, and T1W hypointensity (Fig.1). MRI of the thoracic spine demonstrated multiple vertebral lesions with similar MR signal characteristics and contrast enhancement. Most lesions were of ground glass density on CT, and some had cystic-lytic appearing hypodense components (Fig 2 and Fig 3). An ultrasound-guided biopsy of the S1 vertebra revealed a fibro-osseous lesion consistent with fibrous dysplasia. Discussion: FD is a benign fibro-osseous bone lesion characterized by the replacement of the medullary bone in one (monostotic form) or multiple (polyostotic form) bones. Polyostotic form occurs less frequently than monostotic and usually involves the femur, tibia, pelvis, foot, skull, and facial bones. Polysostotic form isolated to the spine is rarer. On radiographs and CT, FD lesions are well-defined, intramedullary-located expansile lesions, and they can be radiolucent, sclerotic, or mixed. Endosteal scalloping may be present. No perilesional medullary edema, periosteal reaction, or extraskelatal soft tissue components are expected. The signal intensity of the lesions on MRI may vary depending on the fibrous and cystic components; fibrous sclerotic components show T2 hypointensity, while cystic components are usually T2 hyperintense. Conclusion: Polyostotic fibrous dysplasia may be isolated to the spine. Cystic and fibrous changes may result in a combination of lytic and sclerotic changes in imaging studies. Cystic changes may cause vertebra plana.

Figure 1

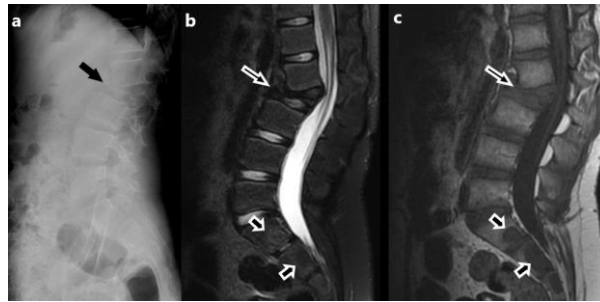


Figure 1. The lateral radiograph of the lumbosacral vertebrae (a) shows the collapsed L2 vertebra, resulting in vertebra plana appearance (black arrow). Sagittal T2 weighted (b) and sagittal T1 weighted MR images show the collapsed L2 vertebra, with a slightly increased signal on T2 and a decreased signal on the T1 weighted image (long white arrows). Sacral vertebrae also show lesions of similar signal intensity with well-defined margins and no peripheral medullary edema.

Figure 2

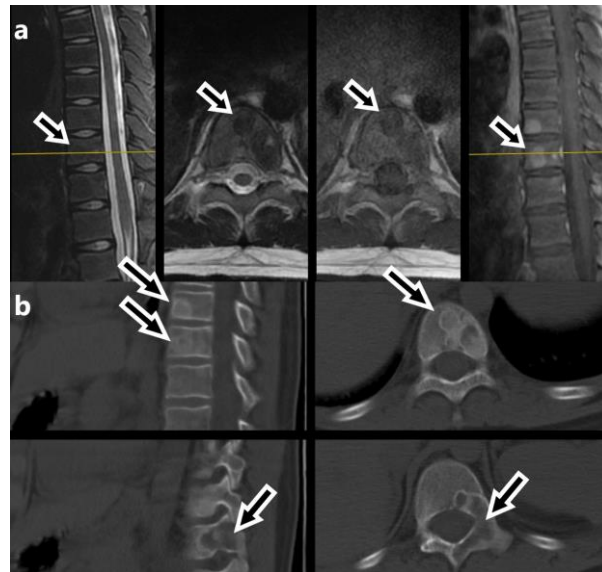
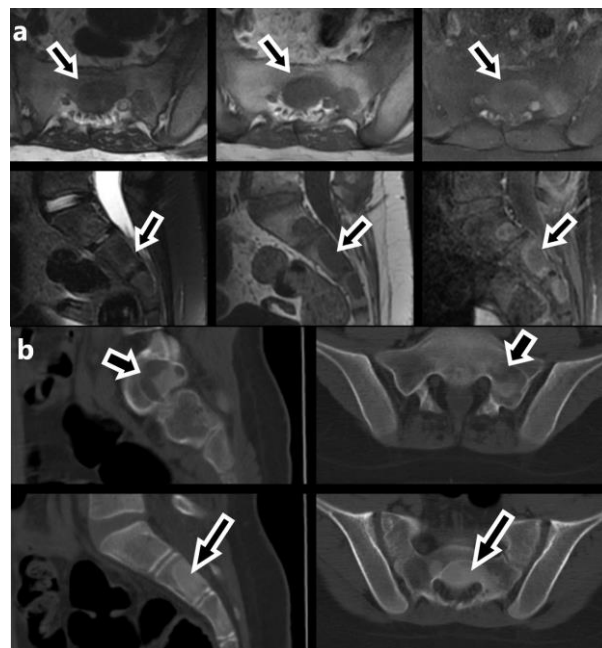


Figure 2. Sagittal and axial MR images of the thoracic vertebrae (a) show the lesions as hypointense on T2, hypointense on T1, and hyperintense on post-contrast T1W images (arrows, a). Sagittal and axial CT images (b) show well-defined expansile lesions with dominantly sclerotic and lytic cystic density changes. Most lesions have thin sclerotic margins (arrows, b).

Figure 3



Axial and sagittal MR images of the sacral vertebrae (a) show T1 hypointense, expansile, well-defined lesions that enhance heterogeneously; the signal intensity of the lesions on T2 weighted images vary from prominent hypointensity to slight hyperintensity (arrows, a). Sagittal and axial CT images of the sacral vertebrae show lesions with ground glass density, some of which have cystic hypodense components (arrows, b).

Keywords: computed tomography, fibrous dysplasia, magnetic resonance imaging, spine, vertebrae

NEGATIVE MULTIPARAMETRIC PROSTATE MRI IN BIOPSY-NAÏVE MEN - DYNAMIC OF THE PROSTATE VOLUME AND PROSTATE-SPECIFIC ANTIGEN DENSITY DURING FOLLOW-UP

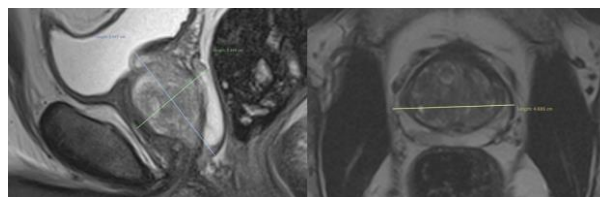
Milena Spirovski¹, Silvija Lucic¹, Mladen Popov¹, Stefan Stojanoski¹, Aleksandar Ragaji², Kristina Polak², Milos Lucic¹

¹Faculty of Medicine, University in Novi Sad

²Oncology Institute of Vojvodina

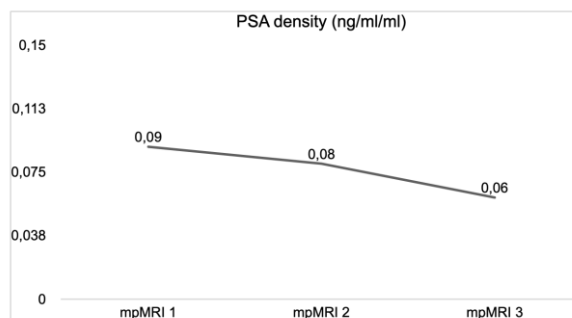
Abstract: Introduction: Negative multiparametric magnetic resonance imaging (mpMRI) of the prostate could obviate biopsy in correlation to clinical risk parameters. Prostate-specific antigen density (PSAD) was found to be the strongest predictor in risk calculators. Moreover, recent studies showed prostate volume (PV) as a significant risk factor for prostate cancer and clinically significant prostate cancer. The aim: The aim of this study was to assess the dynamic of prostate-specific antigen density and prostate volume change in biopsy-naïve men with negative mpMRI and clinical suspicion of prostate cancer, who were followed clinically and with mpMRI and never underwent a biopsy. Material and methods: Prospective study included biopsy-naïve men with elevated serum PSA levels, negative digital rectal exam and negative mpMRI (PI-RADS 1 or PI-RADS 2 category), who were followed clinically and with mpMRI (minimum urological follow-up time of two years, minimum two negative follow-up mpMRI scans in six and twelve months). Multiparametric MRI using a 3T MRI scanner was performed in concordance with PI-RADS recommendations. PSAD was calculated for each MRI as PSA value divided by prostate volume, using the PSA value prior to MRI and the PV that was calculated using ellipsoid formulation with manual measurement of the prostate dimensions at MRI images (figure 1). Results: During the mean follow-up period of nine years 118 men underwent three mpMRI scans, while 16 men (14%) had additional mpMRIs according to the clinical indication (between four and six). Significant decrease in PSAD was observed during the study, from mean value of 0,09 ng/ml/ml to 0,06 ng/ml/ml ($p=0.000$) (figure 2). Mean PV changed from 73,4 ml to 80,5 ml, which showed to be significant increase ($p=0.000$) (figure 3). Conclusion: Significant decrease in PSAD and increase in PV in men with clinical suspicion of prostate cancer and negative mpMRI during follow-up favours monitoring over imminent prostate biopsy. Clinical and radiological follow-up without prostate biopsy could be feasible in biopsy-naïve men with negative mpMRI if the dynamic of the risk factors is favourable.

Figure 1. Measurement of the prostate for volume calculation



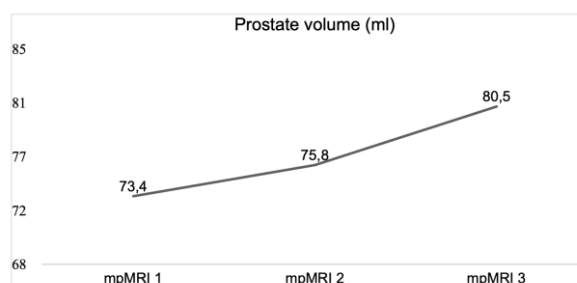
Prostate volume was calculated using the formula $PV(ml) = AP(cm) \times LL(cm) \times CC(cm) \times 0.52$

Figure 2. PSA density values change over time



mpMRI 1 - mean PSA density calculated at first mpMRI; mpMRI 2 and mpMRI 3 - mean PSA density calculated at second and third mpMRI, for men with more than three mpMRI scans, this is the value at second to last and the last one

Figure 3. Prostate volume change over time



mpMRI 1 - mean prostate volume calculated at first mpMRI; mpMRI 2 and mpMRI 3 - mean prostate volume calculated at second and third mpMRI, for men with more than three mpMRI scans, this is the value at second to last and the last one

Keywords: multiparametric prostate MRI, prostate-specific antigen density, prostate volume

PEDIATRIC NEURO BEHÇET DISEASE PRESENTING WITH LONGITUDINALLY EXTENSIVE MYELITIS: THE BAGEL SIGN ON MRI

Cigdem Oztunali¹, Aslı Kavaz Tufan², Nuran Çetin², Coskun Yazar³, Selcan Demir⁴

¹Eskisehir Osmangazi University Medical Faculty, Department of Radiology, Division of Pediatric Radiology

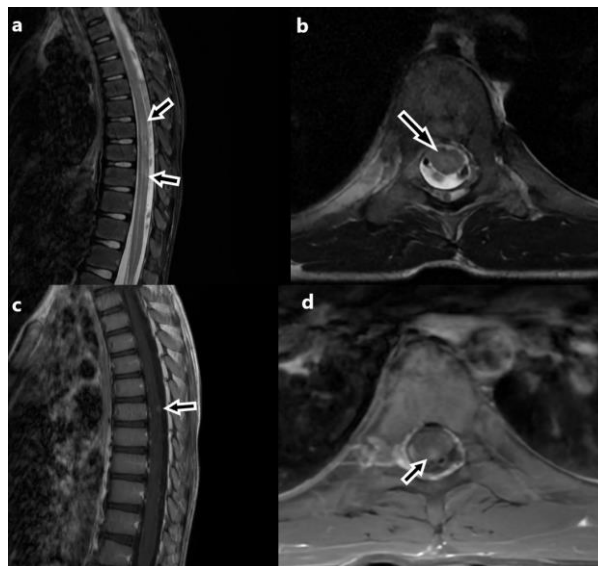
²Eskisehir Osmangazi University Medical Faculty, Department of Pediatrics, Division of Pediatric Nephrology

³Eskisehir Osmangazi University Medical Faculty, Department of Pediatrics, Division of Pediatric Neurology

⁴Eskisehir Osmangazi University Medical Faculty, Department of Pediatrics, Division of Pediatric Rheumatology

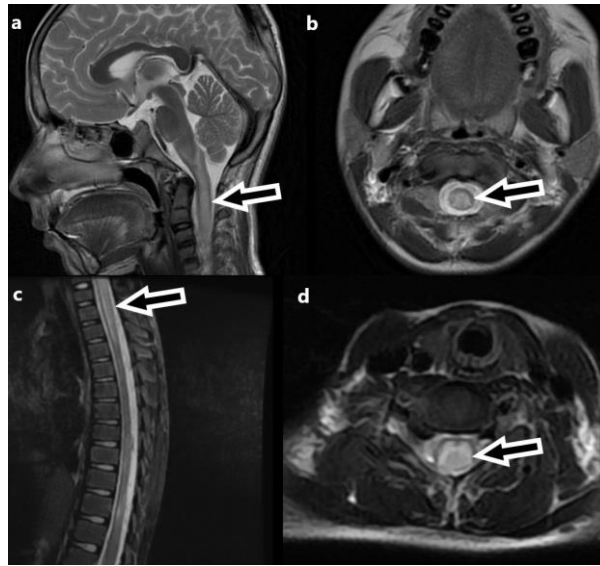
Abstract: Aim: To describe the MRI findings in a pediatric case of neuro Behçet disease presenting with spinal involvement. Case Presentation: A 13-year-old boy was admitted due to difficulty in walking and urinary retention. He had a history of oral aphthous ulcers. MRI of the thoracic spinal cord showed longitudinally extensive myelitis with central gray matter involvement and the Bagel Sign. Post-contrast images showed small nodular enhancement foci (Fig 1). Corticosteroid treatment was initiated. A few weeks later, he had confusion and paresis of bilateral upper and lower extremities. MRI of the spine showed longitudinally extensive myelitis of the cervical spinal cord with additional brain stem involvement (Fig 2). T2-weighted images demonstrated the Bagel Sign as a central hyperintense spinal cord lesion with a hypointense cord (Fig.3). A diagnosis of neuro Behçet disease with recurrent spinal cord involvement was suspected and then confirmed clinically. Discussion: Parenchymal neuro Behçet Disease dominantly involves the telencephalic-diencephalic junction and the brain stem. Cerebral and spinal cord involvement are less common. Spinal cord involvement in neuro Behçet disease mainly occurs in single or multiple centrally or eccentrically located lesions, with or without contrast enhancement. Longitudinally extensive myelitis can also be seen in neuro Behçet disease. On MRIs of the spinal cord, Bagel Sign describes a centrally located expansile T2W hyperintense lesion with a T2W hypointense core. This sign is thought to represent venous engorgement and/or acute blood products occurring in the location of the longitudinal intrinsic venous anastomosis of the spinal cord. The sign is reported to be highly specific for neuro Behçet disease-associated myelitis. Conclusion: Neuro Behçet disease can present with predominant and recurrent spinal cord involvement. Spinal cord involvement can be seen on MRI as longitudinally extensive myelitis, demonstrating the Bagel Sign as T2 hyperintense lesions with a T2 hypointense core.

Figure 1



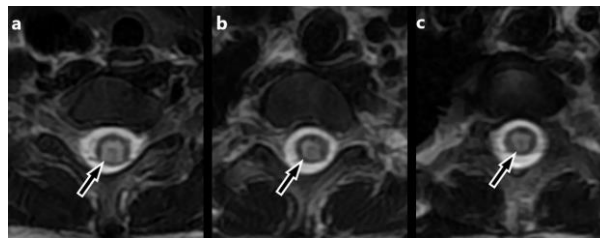
A sagittal T2-weighted image of the thoracic spinal cord (a) shows longitudinally extensive myelitis, which causes hyperintensity and mild expansion of the cord (arrows, a). Axial T2-weighted image of the thoracic spinal cord (b) shows the Bagel Sign as the hyperintense signal change of the central gray matter with a hypointense core (arrow, b). Post-contrast sagittal (c) and axial (d) images of the thoracic spinal cord show one of the nodular enhancement foci (arrows c and d).

Figure 2



Sagittal (a) and axial (b) T2-weighted images of the upper cervical spinal cord show diffuse edema and expansion in the cord (arrows a and b), extending to the ventral and dorsal medulla oblongata. Sagittal (c) and axial (d) T2-weighted images of the cervical and upper thoracic spinal cord show diffuse edema and expansion in the cord (arrows c and d).

Figure 3



Axial T2-weighted images of the cervical and upper thoracic spinal cord (a-c) show centrally located hyperintensity of the cord causing expansion. A T2-hypointense core is observed in the center of the hyperintense lesions (arrows a-c).

Keywords: Bagel sign, Behçet disease, magnetic resonance imaging, myelitis, neuro Behçet

TORSION IN A BIPARTITE SPLEEN: IMAGING FINDINGS IN A CHILD

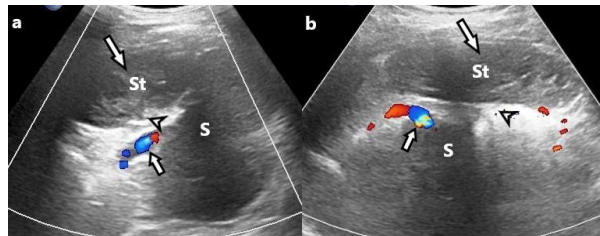
Cigdem Oztunali¹, Mehmet Surhan Arda², Hüseyin İlhan²

¹Eskisehir Osmangazi University Medical Faculty, Department of Radiology, Division of Pediatric Radiology

²Eskisehir Osmangazi University, Department of Pediatric Surgery

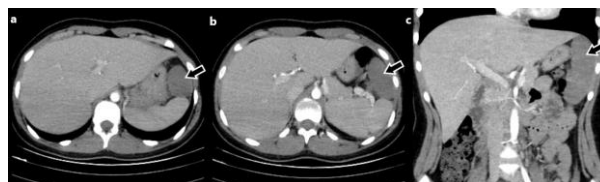
Abstract: Aim: To present ultrasonography (US), computed tomography (CT), and magnetic resonance imaging (MRI) findings of splenic torsion in a child with bipartite spleen. Case presentation: A 12-year-old girl presented with acute severe epigastric pain and vomiting. An abdominal US showed an 8x9 cm solid-appearing mass located anterior to the spleen. The mass had well-defined contours and a shape similar to the spleen. The echogenicity of the mass was lower when compared to the spleen; its echotexture was heterogeneous, and it had no internal or hilar vascularization on Doppler US (Fig. 1). A CT with intravenous contrast confirmed the mass to be the second lobule of a bipartite spleen. It had no parenchymal contrast enhancement. An MRI of the upper abdomen showed the anterior lobule of the bipartite spleen to be heterogeneously low signal intensity on T2WI; the anterior lobule had peripheral capsular and subcapsular contrast enhancement on post-contrast T1WI. A laparoscopic exploration showed the anterior lobule of the bipartite spleen to be twisted 360 degrees. Detorsion and subsequent excision of the anterior splenic lobule were performed. Pathologic examination confirmed hemorrhagic infarction of the spleen. Discussion: Torsion of one lobule of a bipartite spleen is rare. Ultrasonography shows the torsioned spleen to be of low echogenicity and heterogeneous echotexture. No color coding can be found on Doppler US if the vascular pedicle is twisted more than 360 degrees. On MRI, low T2 signal intensity of the torsioned spleen represents hemorrhagic changes within the torsioned spleen. The torsioned spleen can show linear capsular/subcapsular contrast enhancement on post-contrast MR images. The capsule itself appears hypointense on T2W images. Conclusion: Torsion of a splenic lobule may mimic a solid or a cystic mass in imaging studies. The location, contour, and shape features of the torsioned lobule are usually similar to the spleen's. On MRI, T2 hypointensity and non-enhancement of the parenchyma, except the peripheral parts, may help in the diagnosis.

Figure 1



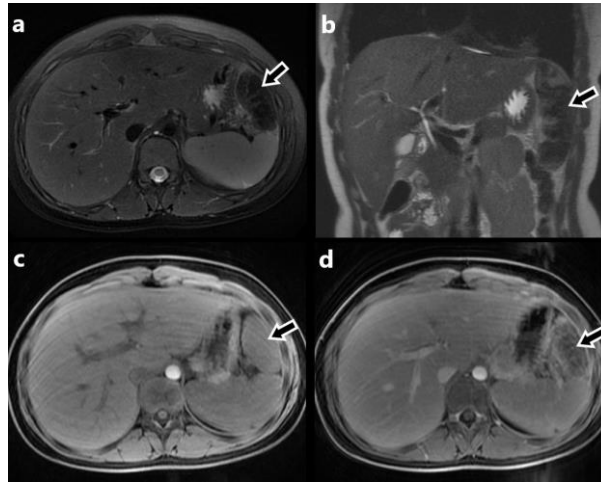
Anterior oblique transverse (a) and longitudinal (b) ultrasonography images show the torsioned anterior splenic lobule (St, long arrow) to be heterogeneous and of lower echogenicity compared to the posterior splenic lobule (S). Hilar vascularization of the posterior splenic lobule (S) is preserved, while no vascularization is observed at the hilus of the anterior lobule (arrowhead).

Figure 2



Axial (a and b) and coronal (c) contrast-enhanced CT images show the anteriorly located torsioned splenic lobule to be homogeneously low density compared to the normal posterior splenic lobule (arrows).

Figure 3



Axial (a) and coronal (b) T2-weighted images show the torsioned anterior splenic lobule to be heterogeneously low signal intensity (arrows). Pre-contrast axial T1-weighted (c) and post-contrast axial T1-weighted (d) images show the torsioned anterior splenic lobule with only peripheral capsular enhancement (arrows).

Keywords: acute abdomen, accessory spleen, bipartite spleen, spleen, splenic torsion

IMAGING FINDINGS OF PRIMARY PERITONEAL RHABDOMYOSARCOMATOSIS IN A CHILD

Cigdem Oztunali¹, Zeynep Canan Özdemir², Ersin Töret², Mehmet Surhan Arda³

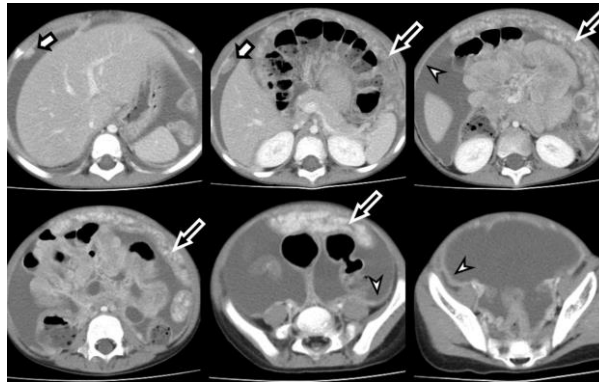
¹Eskisehir Osmangazi Medical Faculty, Department of Radiology, Division of Pediatric Radiology

²Eskisehir Osmangazi University, Department of Pediatrics, Division of Pediatric Hematology and Oncology

³Eskisehir Osmangazi University Medical Faculty, Department of Pediatric Surgery

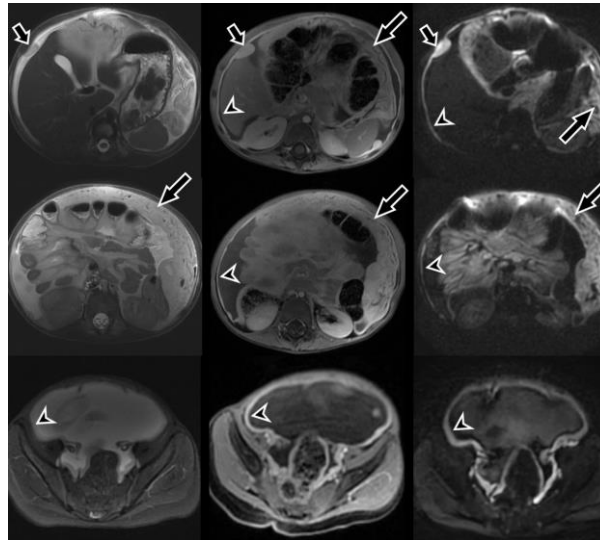
Abstract: Aim: To describe the computed tomography (CT) and magnetic resonance imaging (MRI) findings of the very rare primary peritoneal rhabdomyosarcomatosis (PPR) in a child and to present an overview of the more common pathologies that can involve the pediatric abdomen diffusely and with multifocal soft tissue masses. Case Presentation: A 3-year-old girl was admitted to the hospital due to newly noticed abdominal distention following an upper respiratory tract infection. Ultrasonography of the abdomen showed ascites, mass-like thickening of the greater omentum, and soft tissue masses over the right subdiaphragmatic area and the pelvic peritoneum. A contrast-enhanced CT of the abdomen showed ascites, diffuse mass-like thickening of the omentum, diffuse peritoneal thickening, and a few homogeneously enhancing soft tissue masses attached to the peritoneal surfaces. MRI of the abdomen better demonstrated the diffuse thickening of the peritoneum, omentum, and soft tissue masses with intense contrast enhancement and diffusion restriction. No primary tumor was observed in the solid visceral organs. A whole-body PET-CT showed no uptake except in the abdomen. A tru-cut biopsy from the omentum showed alveolar-type rhabdomyosarcoma. Discussion: PPR is an exceedingly rare malignant neoplasm in children. Ascites, omental-peritoneal thickening with lymphadenopathies in a child may be found in more common abdominal tuberculosis. Of the malignant pathologies, Burkitt lymphoma, desmoplastic small round-cell tumor (DSRCT), peritoneal malignant mesothelioma, and peritoneal carcinomatosis are the more common pathologies. Abdominal tuberculosis in the wet form usually shows necrotic lymphadenopathies rather than peritoneal soft tissue deposits. DSRCT occurs more commonly in adolescents, and a primary peritoneal tumoral mass is generally observed in the paravesical pelvic region. Burkitt lymphoma of the intestinal system may cause peritoneal, mesenteric, and omental soft tissue deposits; the soft tissue masses are the main imaging findings. Conclusion: Primary peritoneal rhabdomyosarcomatosis is a rare malignant neoplasm in children. It presents imaging findings of ascites, omental and peritoneal thickening, and mass-like soft tissue masses on the peritoneal and omental surfaces. The differential diagnosis includes both benign infectious pathologies, mainly tuberculosis, and the more common malignant neoplasms of the pediatric abdomen.

Figure 1



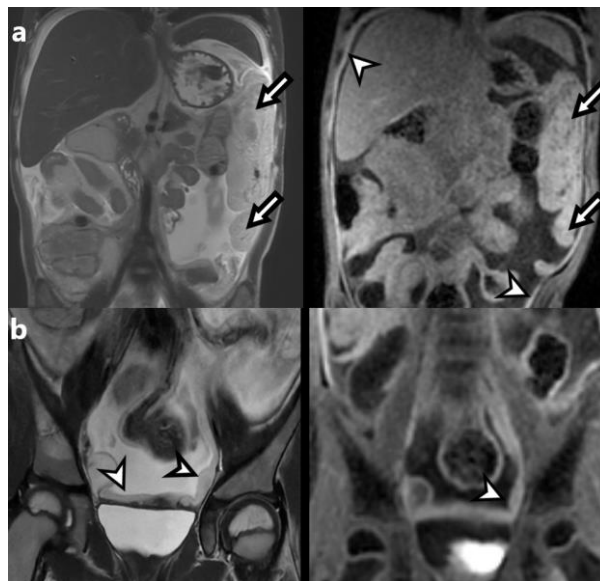
Axial contrast-enhanced CT images on admission show ascites, mass-like omental thickening (long arrows), peritoneal soft tissue deposits (short arrows), and diffuse peritoneal thickening and contrast enhancement (arrowheads).

Figure 2



Axial T2-weighted (left column), post-contrast T1-weighted (middle column), and diffusion-weighted (right column) MR images show T2 hyperintense contrast-enhancing and diffusion-restricting soft tissue deposit attached to the peritoneal surface in the subhepatic area (short arrows). The greater omentum (long arrows) is diffusely thickened and shows intense contrast enhancement and diffusion restriction. The peritoneum is diffusely thickened and restricts diffusion (arrowheads).

Figure 3



Coronal T2-weighted (left column) and post-contrast T1-weighted (right column) MR images show diffusely thickened and contrast-enhancing greater omentum (arrows). The peritoneal surfaces are diffusely thickened and contrast-enhancing (arrowheads).

Keywords: omental cake, pediatric abdomen, peritoneum, rhabdomyosarcoma, primary peritoneal tumor

MAGNETIC RESONANCE IMAGING OF CHEMOTHERAPY TREATMENT-RELATED INTRACRANIAL COMPLICATIONS IN CHILDREN WITH HEMATOLOGIC MALIGNANCIES

Cigdem Oztunali¹, Zeynep Canan Özdemir², Coşkun Yazar³

¹Eskisehir Osmangazi University Medical Faculty, Department of Radiology, Division of Pediatric Radiology

²Eskisehir Osmangazi University Medical Faculty, Department of Padiatrics, Division of Pediatric Hematology and Oncology

³Eskisehir Osmangazi University Medical Faculty, Department of Pediatrics, Division of Pediatric Neurology

Abstract: Aim: Systemic and intrathecal chemotherapy may induce several treatment-related intracranial complications in children with hematologic malignancies. These include toxic leukoencephalopathy, posterior reversible encephalopathy syndrome (PRES), cranial infections due to immunosuppression (viral and fungal), and microvasculopathic changes. This review aims to describe and illustrate the common cranial complications encountered in cerebral MRI of children receiving chemotherapy for hematologic malignancy. Case Presentations: Cerebral MRIs of pediatric cases in which intracranial complications were developed during chemotherapy are presented to describe and illustrate the characteristic findings. Cases include intracranial hypotension due to cerebrospinal fluid leak after lumbar puncture, dural sinus venous thrombosis, PRES, vasculopathy-related microhemorrhages, reversible leukoencephalopathy due to methotrexate toxicity, and cranial infections caused by opportunistic pathogens. Discussion: PRES developing during hematologic malignancies in children may have the typical MRI features with bilateral vasogenic edema in the parietoccipital cortical and subcortical regions, but it can also demonstrate basal ganglia and brainstem involvement. Of the opportunistic viral infections, HSV encephalitis mostly starts in the medial and anterior temporal lobes. However, it can progress rapidly to involve both cerebral hemispheres and result in laminar necrosis. Methotrexate toxicity involves the deep and periventricular white matter areas symmetrically; acute changes may restrict diffusion, and the condition is usually reversible. Dural sinus venous thrombosis may occur due to drug toxicity or in the presence of coagulopathies and may cause hemorrhagic strokes if not treated. Vasculopathy of the small vessels in long-term treatment may cause microhemorrhages without clinical abnormalities; those are best observed in susceptibility images. Lumbar puncture for diagnostic or therapeutic purposes may cause intracranial hypotension, observed as engorgement of the dural venous sinuses, enlargement of the pituitary gland, and dural thickening on MRI. Conclusion: Prompt recognition and correct interpretation of cerebral magnetic resonance imaging (MRI) findings in chemotherapy treatment-related changes are essential in patient management. Knowledge of the characteristic and atypical presentations of these conditions on MRI may help in early diagnosis and treatment of complications.

Figure 1

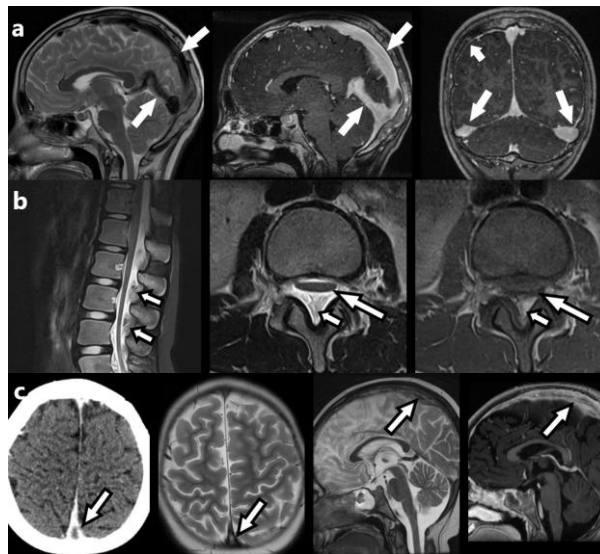


Figure 1. MR images of the cerebrum (a) and lumbar spine (b) in a 10-year-old girl with a diagnosis of acute myeloid leukemia, obtained after a lumbar puncture for initiation of intrathecal treatment show distention of dural venous sinuses (long arrows, a) with mild and diffuse dural thickening and contrast-enhancement (short arrow, a). The posterior epidural fat of the lumbar spine is engorged (short arrows, b); the thecal sac is narrowed anteroposteriorly and contains almost no CSF space, and the cauda equina nerves are clumped together (long arrows, b), consistent with CSF leak and resultant intracranial hypotension. Contrast-enhanced CT and MR images of the cerebrum in a 10-year-old boy with acute lymphoblastic leukemia show the subacute thrombosis of the superior sagittal sinus as a filling defect on CT. The thrombus is of heterogeneous signal intensity on T2-weighted images; the post-contrast mid-sagittal T1W image shows the thrombus as non-enhancing hypointensity in the sinus, with peripheral wall enhancement.

Figure 2

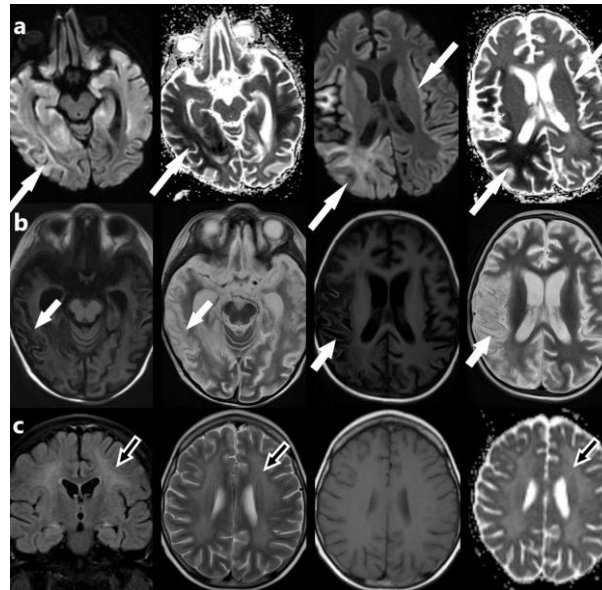


Figure 2. Diffusion-weighted ADC map images (a) of a 4-year-old boy receiving radiotherapy and chemotherapy for parapharyngeal rhabdomyosarcoma show diffusion restriction in the temporal lobes, hypothalamus, amygdala, insular cortex, and parietal cortex (arrows, a). CSF PCR showed herpes virus infection. Follow-up cerebral MR images of the same boy after two months (b) show laminar necrosis of the cerebral cortex and volume loss in the cortex and the subcortical areas (arrows, b). Cerebral MR images of a 10-year-old boy with acute lymphoblastic lymphoma and encephalopathy (c) show symmetrically increased signal intensity in the centrum semiovale and periventricular deep white matter areas on T2W and FLAIR images due to methotrexate related toxic leukoencephalopathy. The U fibers are preserved. T1W images show the normal signal intensity of the deep white matter areas. ADC map shows the increased signal of the affected white matter, indicating no diffusion restriction (arrows, c).

Figure 3

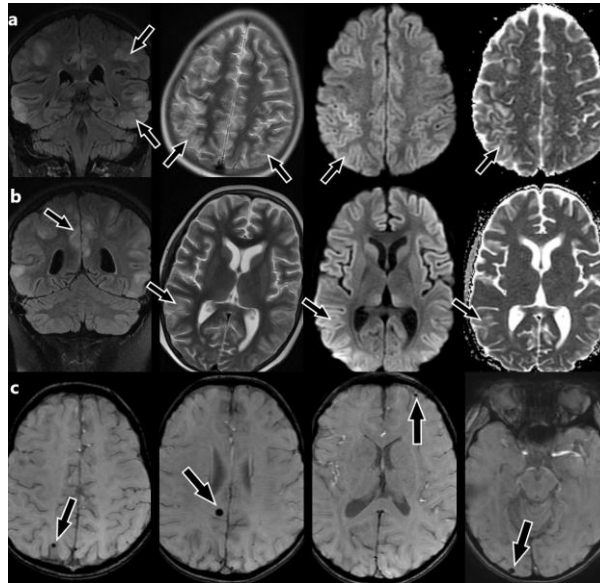


Figure 3. MR images of the cerebrum of an 11-year-old boy with Burkitt lymphoma and PRES (a and b) show mild edema and increased signal in the temporal, parietal, occipital, and frontal cortex and the subcortical white matter. ADC map image shows increased signal and no diffusion restriction (arrows in a and b). Susceptibility images of an 8-year-old boy (c) with acute myeloid leukemia show a few subcortical hemorrhage foci after chemotherapy (arrows, c).

Keywords: cerebral, chemotherapy, complication, magnetic resonance imaging, pediatric hematologic malignancy

BRAIN ARTERIOVENOUS MALFORMATIONS

Jasmina Kovacevic¹

¹Health Centre Valjevo, General Hospital

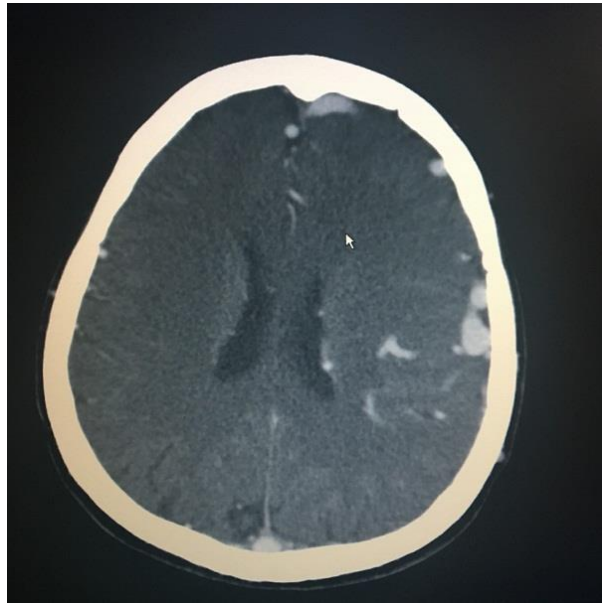
Abstract: A brain arteriovenous malformation (AVM) is a type of intracranial high-flow vascular malformation that creates irregular connections between dilated arteries and veins in the brain. It can vary in size from very small to very large, and consists of enlarged feeding arteries, a nidus of vessels closely associated with the brain parenchyma through which arteriovenous shunting occurs and draining veins. It is considered as a congenital anomaly, but the symptoms usually appear in adulthood between the ages of 20 and 40 and are rare. There are the three ways how AVM can damage the brain: 1. The blood steal phenomenon with brain parenchyma hypoperfusion, 2. Arteries and veins in an AVM can rupture, causing bleeding in the brain, 3. An AVM can compress or displace parts of the brain. Symptoms are rare and can be epileptic seizures, headaches, muscle weakness, instability, confusion etc. Usually they are incidental finding on CT or MR. On the native CT examination, the dilated blood vessels usually are impossible to detect, but we can see slightly hyperdense nidus compared to the brain parenchyma, with frequent calcification. If the surrounding hypodensity is present, it indicates ischemia or sequel of hemorrhage. On the MR examination, a tortuous flow void can be observed in blood vessels, mainly veins, as well as hemosiderin deposits. On post-contrast CT and MR tomograms, the AVM malformation, its arterial and venous blood vessels, are clearly shown. The final diagnosis is made by digital subtraction angiography (DSA). Here are three cases of AVM one patient with epileptic seizures and small AVM in right temporal lobe and hippocampal region and two with headaches, from which one have gigantic AVM of left frontal, temporal and parietal lobe, and other one have AVM of corpus callosum. Although AVM is usually incidental finding, contrast administration during examination is necessary, because on native images especially on CT it can be missed.

right temporal AVM



post contrast image shows enhancement of vascular structures, mostly vein of AVM

gigant AVM



post contrast CT shows gigantic AVM of left frontal, temporal, partially parietal region

AVM of corpus callosum



MR angiography

Keywords: Brain AVM

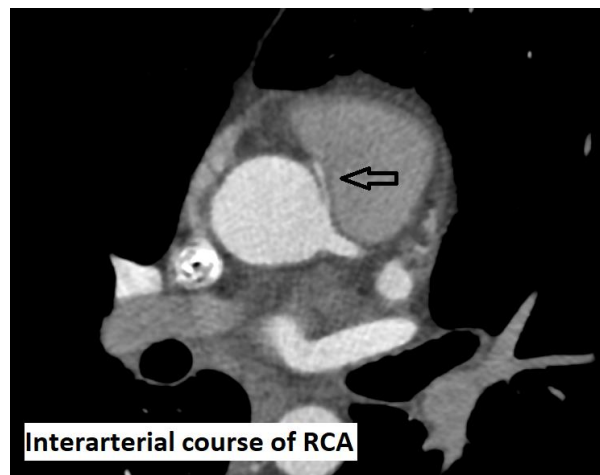
IGG4 RELATED CORONARY ARTERY PERIARTERITIS IN A PATIENT WITH CORONARY ARTERY ANOMALY: A CASE REPORT

Serhat Akış¹, Mustafa Mahmut BARIS¹, Ayse COLAK¹

¹Dokuz Eylul University

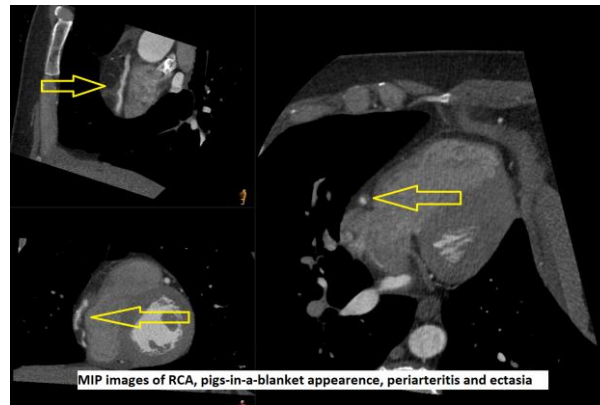
Abstract: Introduction Immunoglobulin G4-related disease (IgG4-RD) is a systemic immune-mediated disease which can affect almost all organs of the body. Awareness is important because the disorder is treatable. Coronary artery involvement is a rare condition in IgG4-RD. Coronary artery anomalies (CAAs) are disorders that can vary widely in their presentation, ranging from benign variants with no clinical significance to potentially life-threatening conditions. Interarterial course anomaly is known as the most hemodynamically serious coronary artery anomaly. Case Report A 38-year-old male patient without any disease was admitted to the cardiology outpatient clinic with chest pain that had persisted for 2 months. ECG showed normal sinus rhythm. Cardiac biomarkers were normal. To further evaluate the chest pain, coronary CT angiography (CCTA) was performed. CCTA revealed diffuse and continuous periarterial soft tissue thickening surrounding the coronary arteries, particularly RCA and LA. There was significant luminal stenosis in distal LAD and acute marginalis branch of RCA. There were also ectatic segments involving both arteries. RCA was running between ascending aorta and the pulmonary trunk showing interarterial course. Invasive coronary angiography (ICA) didn't show any adventitial changes. It only revealed luminal coronary ectatic changes. IgG4 level increased by 216 mg/dL. Sedimentation, WBC count and neutrophil ratio were also increased. With appropriate laboratory values accompanying typical radiological findings, coronary artery involvement due to IgG4-related disease was initially considered in the patient. The coronary anomaly was accompanied by unrelated IgG4 disease. Discussion Coronary artery involvement is a rare condition of IgG4-RD. Diffuse and continuous periarterial soft tissue thickening surrounding the coronary arteries is called "pigs-in-a-blanket" appearance on CCTA and it is typical for this disease. Also partial aneurysmal dilatation of the affected coronary segments may be observed. ICA may show coronary aneurysms but is limited in detecting the typical adventitial changes. Interarterial course coronary artery anomaly is considered malignant due to its association with an increased risk of sudden cardiac death. In the interarterial course, the coronary artery is located between aorta and pulmonary artery. Conclusion The combination of these two conditions in this patient increases the risk of life-threatening complications. Prompt recognition and appropriate management are crucial this complex patient.

INTERARTERIAL COURSE OF RCA



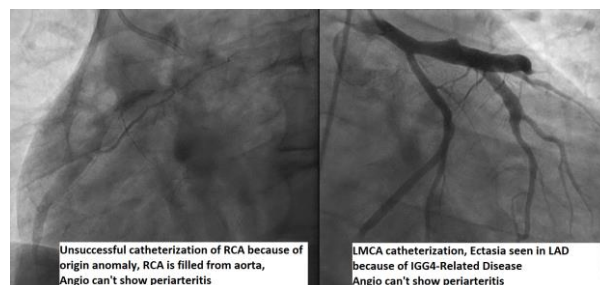
In the interarterial course, the coronary artery is located between aorta and pulmonary artery. It is a malignant type of coronary artery anomalies.

IGG4 RELATED DISEASE INVOLVEMENT OF CORONARY ARTERY



CCTA revealed diffuse and continuous periarterial soft tissue thickening surrounding the coronary arteries.(here in RCA) There was significant luminal stenosis and also ectatic segments involving the arteries.

INVASIVE ANGIOGRAPHY



Angiography can't show periarthritis because the lumen is filled inside. Also origin anomalies are difficult to catheterise. CT is very valuable in this patient to show both anomaly and periarthritis. This case shows the power of CCTA in cardiac work-up.

Keywords: IGG4 related disease, coronary artery anomaly, coronary artery disease, periarthritis, interarterial course

PRIMARY SYNOVIAL SARCOMA OF THE CRANIAL VAULT

Cigdem Oztunali¹, Berat Acu¹, Zühtü Özbek², Evrim Yılmaz³

¹Eskisehir Osmangazi University Medical Faculty, Department of Radiology

²Eskisehir Osmangazi University Medical Faculty, Department of Neurosurgery

³Eskisehir Osmangazi University Medical Faculty, Department of Pathology

Abstract: Aim: Synovial sarcomas are malignant soft tissue tumors typically occurring in the extremities of adolescents and young adults and are related to tendons, tendon sheaths, joint cavities, and bursae. In the head and neck region, they are most common in the hypopharynx and the paranasal sinuses. Synovial sarcoma of the calvarial vault is an exceedingly rare pathology. We aim to describe the imaging findings of a primary synovial sarcoma arising from the parietal bone. Case Presentation: A seventy-five-year-old male presented with a slow-growing mass on the right parietal area for two months. A skull radiograph showed cortical erosion and lytic regions of the parietal diploe space at the level of the soft tissue mass. A contrast-enhanced computed tomography showed a 3,5x2 cm homogeneously enhancing transdiploic soft tissue mass extending into the epidural and subgaleal spaces with permeative destruction of the parietal bone without causing bone expansion. Magnetic resonance imaging revealed the mass to be isointense to the muscles on T1W and moderately hyperintense on T2W images. It enhanced and restricted diffusion homogeneously. A positron emission tomography showed no tracer uptake except for the calvarial lesion. An ultrasound-guided biopsy of the extracalvarial component of the mass was consistent with a spindle cell malignant mesenchymal tumor. A craniectomy with excision of the mass resulted in a pathological diagnosis of synovial sarcoma. Discussion: Synovial sarcomas can arise from any portion of the body containing pluripotent mesenchymal cells near and can be seen remote from articular surfaces or juxta-articular membranes. In the head and neck region, synovial sarcomas are extremely rare, and they are believed to originate from the sarcomatous change of the galea aponeurosis. Radiological differential diagnoses of transdiploic calvarial tumors mainly include hemangiopericytoma, lymphoma, metastasis, and plasmacytoma. Of these, calvarial lymphoma shows a permeative growth with transdiploic spread through the Haversian canals, with little or no bone destruction and a disproportionate soft tissue component. Conclusion: Synovial sarcoma can occur primarily in the cranial vault. The main imaging findings in the presented case were a transdiploic growth through the Haversian canals toward both sides of the calvarium, with a more significant extracalvarial component.

Figure 1

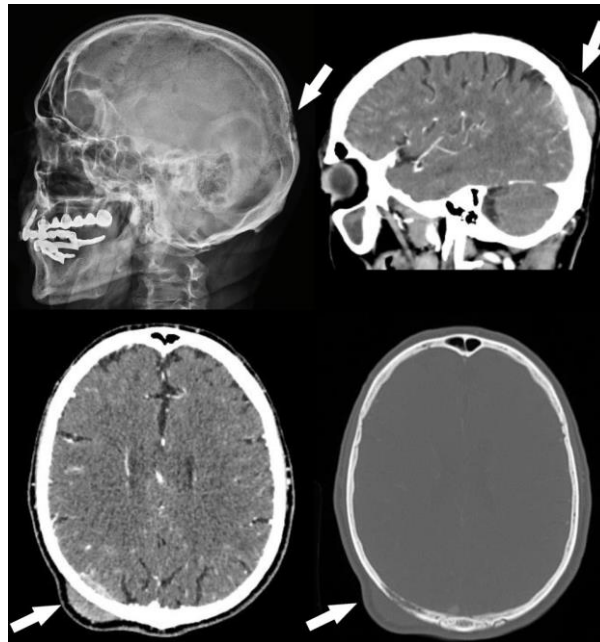


Figure 1. A lateral radiograph of the skull shows the permeative destruction of the posterior parietal bone without prominent expansion of the diploe space. Contrast-enhanced CT images show a homogeneously enhancing transdiploic soft tissue mass with more significant extracalvarial and smaller epidural intracalvarial components. The mass caused permeative destruction in the parietal bone without any expansion of the bone (arrows).

Figure 2

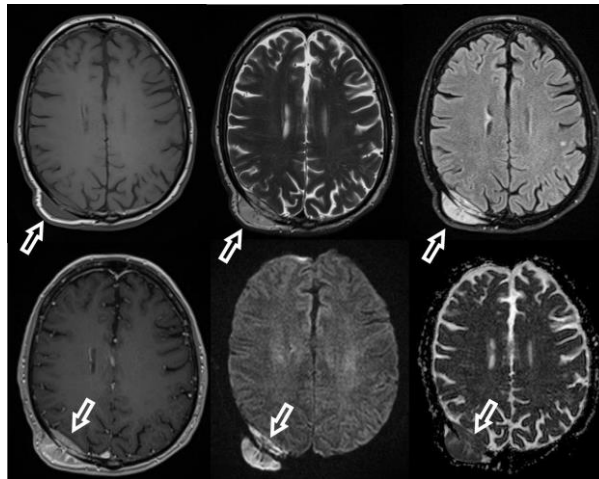


Figure 2. Axial MR images show the mass to be isointense with muscles on the T1W image. The T2W image shows moderate hyperintensity, while the FLAIR image shows prominent hyperintensity of the mass. The mass enhances homogeneously and strongly restricts diffusion. Note the transdiploic spread of the mass through the channels along the emissary veins without causing any bone expansion (arrows).

Keywords: cranial vault, lytic calvarial lesion, sarcoma, skull lesions, synovial sarcoma

IMAGING FINDINGS OF CHRONIC RECURRENT MULTIFOCAL OSTEOMYELITIS AND ITS MIMICS IN CHILDREN

Cigdem Oztunali¹, Selcan Demir²

¹Eskisehir Osmangazi University Medical Faculty, Department of Radiology, Division of Pediatric Radiology

²Eskisehir Osmangazi University Medical Faculty, Department of Pediatrics, Division of Pediatric Rheumatology

Abstract: Aim: Chronic recurrent multifocal osteomyelitis (CRMO) is an autoinflammatory disorder most commonly diagnosed in children. CRMO shares imaging features with a variety of more common disorders. This review aims to illustrate the characteristic findings of CRMO on different imaging modalities and to present the differentiating features of CRMO from its imaging mimics. Case Presentations: Radiographs, computed tomography (CT), and magnetic resonance (MR) images of pediatric cases with the involvement of different skeletal parts will be presented to illustrate and describe CRMO's classical imaging findings (Figures 1-3). Discussion: CRMO mainly involves metaphyses of the long bones of the lower extremities, pelvis, and spine. Less frequent involvement sites are the sternum, ribs, upper extremities, and medial clavicle. Radiographs can be normal in early CRMO. Early lesions may be seen as small lytic lesions or increased opacity. Lesions usually heal with sclerosis. MRI shows the active lesions as marrow edema with contrast enhancement. Reactive joint fluid, single periosteal reaction, and soft tissue edema can be present. Bacterial and tuberculous osteomyelitis, scurvy, stress fractures, biphosphonate, and chemotherapy radiotherapy treatment-related changes can mimic imaging findings of CRMO. Leukemia, lymphoma, and Ewing sarcoma are among the malignant diseases that may mimic CRMO (Table 1). Conclusions: CRMO in children can demonstrate a variety of findings on different imaging modalities. Knowledge of its characteristic and atypical imaging features and the differentiating features from its mimics can aid in a timely diagnosis and avoid unnecessary invasive diagnostic procedures.

Figure 1



Coronal PD FS, axial PD FS, and sagittal T1W MR images (A) of a ten-year-old boy with CRMO show distal metaphyseal edema of the left femur (arrows, A) with accompanying soft tissue edema and solid periosteal reaction. MR images of the same child a year later (B) show medullary edema of the distal metaphysis and diaphysis of the right femur (long arrows, B) with solid periosteal reaction (arrowheads, B) and soft tissue edema (short arrows, B). CT images of the right femur (C) show increased medullary density of the right distal femoral

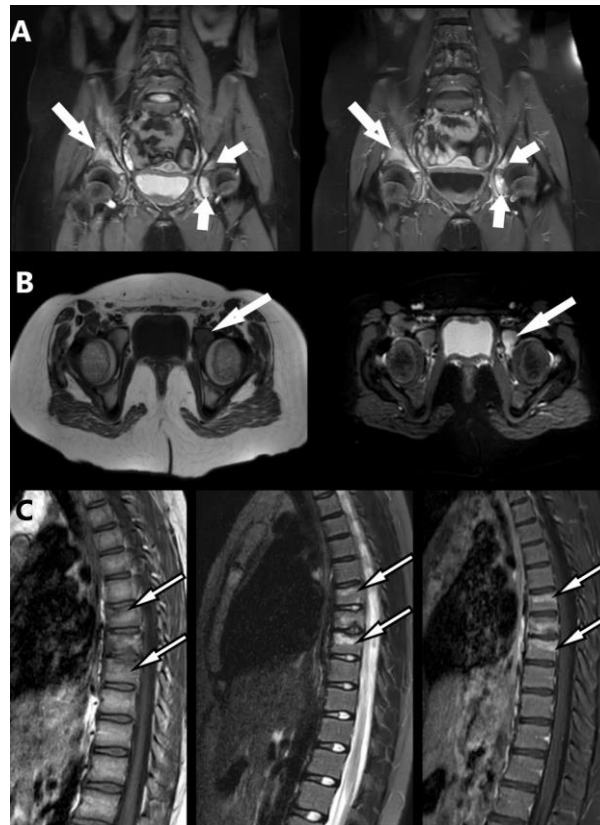
metaphysis (long arrows, C). Note the anterior solid periosteal reaction (arrowheads, C) with increased thickness and edema of the anterior cortex (short arrows, C).

Figure 2



An anterior-posterior radiograph of the right and left crural bones in an 11-year-old girl with CRMO (A, left) shows subtly increased opacity of the left tibial medullary bone (short arrow). A radiograph obtained three months later (A, right) shows prominently increased opacity of the left tibial medullary bone (short arrow) with solid periosteal reaction medially (arrowhead). Note the newly developed sclerotic areas within the medullary cavity (long arrow). Coronal PD FS and post-contrast T-weighted FS MR images of the same girl on the second admission (B) show medullary edema in the proximal metaphyseal and diaphyseal regions of the left tibia (short arrows, B) with non-enhancing hypointense sclerotic areas (long arrows, B).

Figure 3



Coronal PD FS and post-contrast T1-weighted MR images of a 10-year-old girl with CRMO (A) show medullary edema of the right and left pelvic bones around the Y cartilage of the acetabulum (long and short arrows, A). Axial T1-weighted and FS T2-weighted, MR images of the pelvis of a boy with CRMO (B), show edema and slight expansion of the left anterior acetabulum (long arrows, B). Sagittal T1-weighted, FS T2-weighted, and post-contrast FS T1-weighted images of a 12-year-old girl with CRMO (C) show end plate irregularities with mild loss of vertebral heights in 3 consecutive dorsal vertebrae. Note the bone marrow edema and the contrast enhancement near the vertebral end plates (long arrows, C).

Table 1

	CRMO	Bacterial Osteomyelitis
Soft tissue inflammation	Less prominent	Prominent
Abscess, deep vein thrombosis	Rare	Frequent
Intervertebral disk involvement	Not involved	Frequently involved
	CRMO	Tuberculous Osteomyelitis
Intervertebral disc	Not involved	May not be involved
Paraspinal, epidural abscess	Not a feature	Frequent
Anterior subligamentous spread	Not a feature	Frequent
	CRMO	Scurvy

Initial radiographs	May be normal	May be normal
Perimetaphyseal involvement	Frequent	Frequent
Symmetrical	Rarely	Frequently
Periosteal fluid collections	Not a feature	May be present
	CRMO	Leukemia Lymphoma
Radiolucent metaphyseal bands	Not a feature	Frequent
Sclerosis around the lytic lesions	May be present	Not a feature if not treated
Mottled appearance	Not a feature	Frequent
	CRMO	Langerhans Cell Histiocytosis
Punched out lytic lesions	Not a feature	Frequent
Lesions with peripheral sclerosis	May be present	Not a feature if not treated
	CRMO	Primary malignant bone tumor
Periosteal reaction	Single layered	Aggressive
Cortical break	Not a feature	May be present
Solid soft tissue component	Not a feature	May be present

Discriminating imaging features of CRMO and CRMO Mimics

Keywords: bone marrow, CRMO, non-bacterial osteomyelitis, osteomyelitis, pediatric

PULMONARY ARTERIOVENOUS MALFORMATIONS

Jasmina Kovacevic¹

¹*Health Centre Valjevo, General hospital*

Abstract: Pulmonary arteriovenous malformations (PAVM) are rare conditions characterized with abnormal connections between pulmonary arteries and pulmonary veins causing pathological intrapulmonary right to left shunt. They have slightly female predilection. Etiology: They can be congenital or sporadic. Congenital PAVMs are due to defect in the terminal capillary loops which causes vascular dilatation forming thin wall sacs. Sporadic cases are uncommon and are associated with: hereditary hemorrhagic telangiectasia, hepatic cirrhosis, prior chest surgery, trauma, schistosomiasis, actinomycosis, mitral stenosis, Fanconi syndrome etc. Usually they are solitary lesions but in one third patients they can be multiple. Symptoms are rare and they can be due to intrapulmonary right – left shunting like dyspnea, hypoxemia, exercise intolerance, chest pain or embolic events due to paradoxical emboli. Diagnosis is made: Transthoracic Contrast Echocardiography, Bubble study US; Computed tomography with contrast study; Angiography. Treatment is PAVM embolization, and like alternative surgical excision and in the most complicated and difficult cases lung transplantation. This case is about patient with prolonged cough, without any other symptoms like temperature, chest pain, dyspnea etc. She was referred by a pulmonologist for a chest CT scan with contrast administration. CT shown bilateral multiple pulmonary AVM with no other pathological changes .

Pulmonary arteriovenous malformations



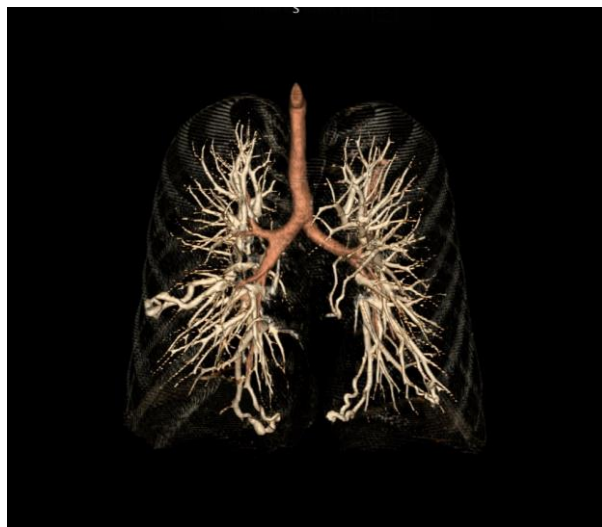
CT-Pulmonary arteriovenous malformations of middle lobe

Pulmonary arteriovenous malformations



CT-Pulmonary arteriovenous malformations in posterior basal segment of left lower lobe

Pulmonary arteriovenous malformations



CT-Pulmonary arteriovenous malformations

Keywords: Pulmonary arteriovenous malformations

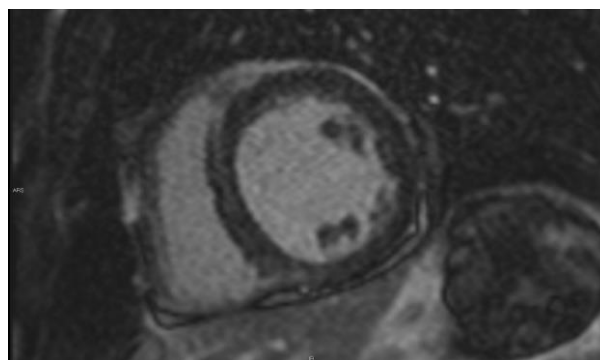
COULD CARDIAC MAGNETIC RESONANCE IMAGING HELP IN THE ASSESSMENT OF THE UNDERLYING CAUSE OF THE SIGNIFICANTLY IMPROVED CONGESTIVE HEART FAILURE?

Milena Spirovski¹, Mila Kovacevic¹, Iva Popov¹, Aleksandra Milovancev¹, Silvija Lucic¹, Andrea Peter¹, Branislava Ilincic¹, Milos Lucic¹

¹Faculty of Medicine, University in Novi Sad

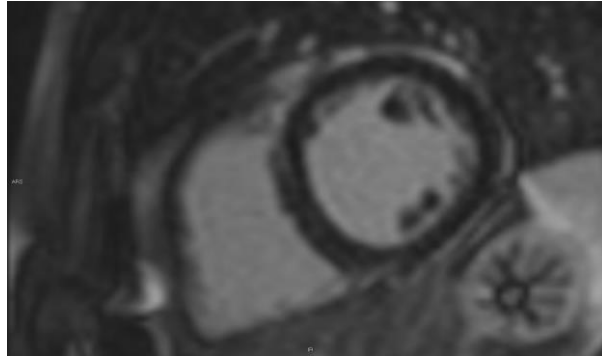
Abstract: Cardiac magnetic resonance imaging (CMR) is considered to be a valuable tool to help clinical assessment of the underlying aetiology of heart failure as well as the prognosis of the disease. We present a case of the 51-year-old male patient with clinical signs of congestive heart failure, dilated cardiomyopathy with diffuse left ventricular (LV) hypokinesia and severely reduced ejection fraction (EF) of 18% at transthoracic echocardiography (TTE), and tachycardia without ST-segment changes on electrocardiography. The patient had no history of cardiac disease, however, two months prior to the onset of the symptoms he fully recovered from the moderately severe SARS-CoV-2 pneumonia. Admission laboratory tests showed elevated high sensitivity cardiac troponin I and N-terminal pro b-type natriuretic peptide (NT-proBNP), negative real-time polymerase chain reaction (RT-PCR) for SARS-CoV-2, as well as negative serology for cardiotropic viruses and negative immune assay results. CT coronarography did not confirm the presence of significant coronary artery stenosis. Cardiac MRI was consistent with dilated LV, globally severely hypokinetic myocardium and decreased EF of 19%. No signs of edema, perfusion defect or early gadolinium enhancement was noted, while there was a septal mid-wall area of late gadolinium enhancement (LGE), typically found in dilated cardiomyopathy (DCM). Following the treatment for heart failure, the patient improved clinically, together with the improvement of the cardiac function, with the increase of EF to 30% and 47%, measured with TTE during the three- and eight-month visit respectively. Significantly improved LV myocardial contractility and systolic function with ejection fraction of 52% was noted on one year follow-up CMR. The volumes were still above the normal range, although end-systolic volumes decreased almost 50%. There was persistent, but mildly reduced area of LGE in the septal mid-wall location. Although septal mid-wall LGE is usually present in DCM, and is well known indicator of less favourable prognosis, the significant improvement of cardiac function in the patient with the history of SARS-CoV-2 infection might as well be delayed manifestation of post-covid myocarditis. Evolution of the disease and the clinical data in this case outperformed CMR tissue characterization abilities and highlights the need for a comprehensive approach.

CMR during the onset of the disease



Short axis view shows dilated left ventricle with septal mid-wall area of LGE

One year follow-up CMR



Short axis view shows decrease of the left ventricle dilatation with persistent, although reduced area of septal mid-wall LGE

Keywords: cardiac magnetic resonance imaging, dilated cardiomyopathy, myocarditis, SARS-CoV-2

DOUBLE BUBBLES BEYOND THE NEONATAL PERIOD: IMAGING FINDINGS OF DUODENAL OBSTRUCTION IN CHILDREN

Cigdem Oztunali¹, Mehmet Surhan Arda², Hüseyin İlhan²

¹Eskisehir Osmangazi University Medical Faculty, Department of Radiology, Division of Pediatric Radiology

²Eskisehir Osmangazi University Medical Faculty, Department of Pediatric Surgery
bu

Abstract: Aim: The classical double bubble sign on radiographs describes the presence of two air-filled bubbles with no distal air, typically due to neonatal duodenal atresia. Partial duodenal obstruction in older children can occur due to duodenal webs, annular pancreas, superior mesenteric artery syndrome, Ladd bands, preduodenal portal vein, and mid-gut malrotation with or without volvulus. This review aims to describe and illustrate the imaging findings in common causes of pediatric duodenal obstruction beyond the neonatal period. Case Presentations: Imaging findings will be presented in pediatric cases with duodenal obstruction due to intrinsic and extrinsic causes. Upright radiographs demonstrating the double bubble sign and their corresponding fluoroscopic and computed tomography images will be presented to illustrate the findings. Discussion: Duodenal obstruction beyond the neonatal period in children can be caused by duodenal webs, duodenal fibrosis after foreign body ingestion, mid-gut volvulus with or without intestinal malrotation, fibrotic changes after foreign body ingestion, superior mesenteric artery compression syndrome, annular pancreas, duodenal perforation, pancreatitis, and preduodenal portal vein. Upright radiographs of the abdomen show a distended stomach and proximal duodenum with air-fluid levels. Upper gastrointestinal series contrast series with non-ionic contrast agents may demonstrate the level of obstruction, can aid in differentiating intrinsic from extrinsic causes, and demonstrate the position of the cecum. Low-dose CT better shows the etiology by also illustrating the mesenteric vascular structures. Conclusion: Air fluid levels in the stomach and the first portion of the duodenum on upright abdominal radiographs in children may be caused by various pathologies. If the child is not critically ill, fluoroscopy and low-dose CT with IV and oral contrast aid in pre-surgical diagnosis. A thorough evaluation of clinical and imaging findings is always required.

Figure 1

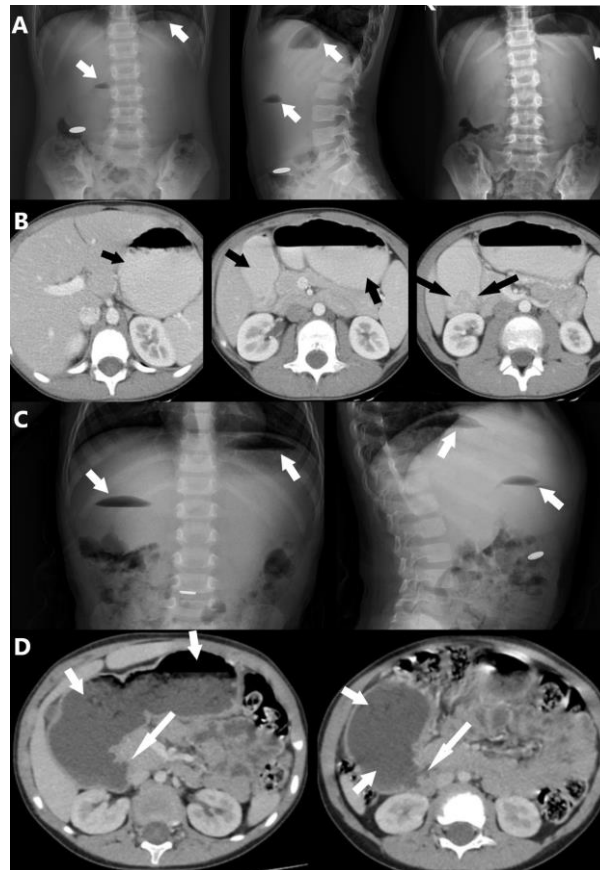


Figure 1. Upright radiographs of a ten-year-old boy who had a history of ingested disk battery for five days show a distended stomach with an air-fluid level at the fundus and a small air-fluid level at the first part of the duodenum (arrows, A, left and middle images). An upright radiograph obtained one month after removing the disk battery due to ongoing vomiting shows a distended stomach (A, arrow, right image). CT images with oral and IV contrast show a distended stomach and proximal duodenum with air-fluid levels (short arrows). The soft tissue density in the lumen of the lower end of the first part of the duodenum was found to be an obstructing fibrotic tissue caused by the ingested disk battery. Upright radiographs of a four-year-old boy who had a history of ingested disk battery for three days showed a distended stomach with an air-fluid level at the fundus and another air-fluid level at the first part of the distended duodenum (arrows, C). CT images with IV contrast obtained after the removal of the battery show a distended stomach and proximal duodenum (short arrows, D). No internal soft tissue density was observed, and a partial annular pancreas was suspected (long arrow, D). Surgery revealed an obstructing internal soft tissue density at the lower end of the first part of the duodenum.

Figure 2

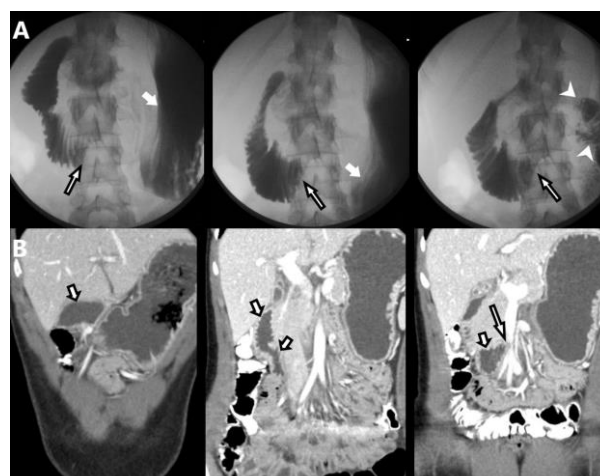


Figure 2. Fluoroscopic images with oral contrast in a fifteen-year-old girl with a history of early satiety, vomiting, and weight loss show a ptotic stomach (short arrows, A). The first and second parts of the duodenum are moderately distended, with interruption of contrast passing at the third part of the duodenum (long arrows, A). The following series shows the late passage of the contrast into the normally located jejunal segments (arrowhead, A). Coronal CT images with IV contrast show moderate distention of the stomach and the proximal duodenum (short arrows, B), with compression of the third part of the duodenum between the aorta and the superior mesenteric artery (long arrow, B).

Figure 3

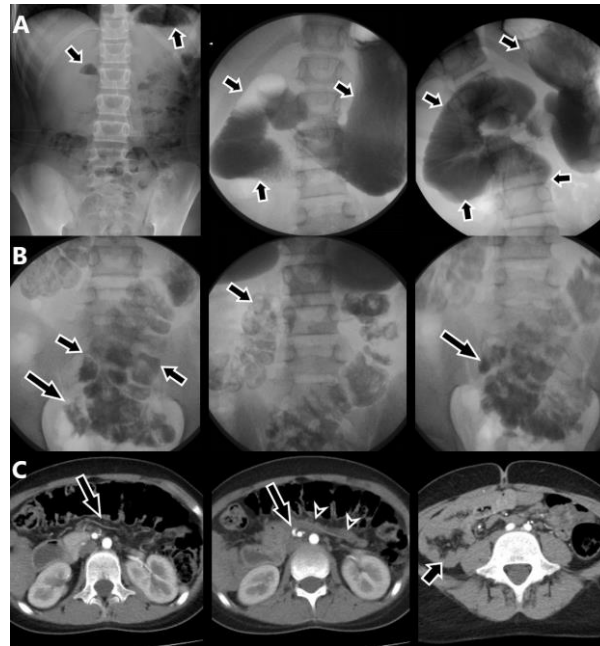


Figure 3. An upright abdominal radiograph (A, left image) of a thirteen-year-old girl with a history of vomiting and weight loss shows a fluid-distended stomach and air-fluid levels at the stomach fundus and the first part of the duodenum (short arrows, A, left image). Fluoroscopic images show the distention of the stomach and the first three parts of the duodenum with interruption of contrast passing distally (arrows, A, middle, and right images). Late fluoroscopic series (B) shows an abnormal configuration of the colonic segments with double vertical segments in the left abdomen (short arrows, B) and the abnormal position of the ileocecal junction in the pelvis (long arrow, B), consistent with mid-gut malrotation. Axial CT images with IV contrast (C) show the rotation of the superior mesenteric artery along its own axis (long arrows, C), an engorged and swirled mesenteric vein (arrowheads, C) representing mesenteric volvulus. Note the absence of the ascending colon and the terminal ileum in their normal anatomical location in the right lower quadrant (short arrow, C).

Keywords: duodenal obstruction, fluoroscopy, upper gastrointestinal series, pediatric duodenal obstruction, double bubble

COLLISION TUMORS OF THE OVARY: “TWO IN ONE”

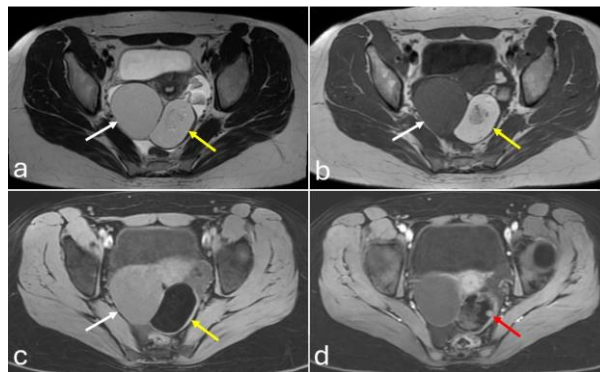
Olgun Şahin¹, Hilal Şahin²

¹Izmir City Hospital, Department of Radiology

²University of Health Sciences, Izmir Faculty of Medicine, Department of Radiology

Abstract: Educational Objectives: •to learn about the definitions of collision tumor, composite and combination tumor•to review the typical collision patterns of ovarian collision tumors•to identify pathological types of ovarian collision tumors•to review imaging features of ovarian collision tumors. Material-Methods/Results: A rare condition known as a “collision tumor” occurs when tumors of different histologic origins coexist in the same organ and have connected margins, but without discernible tissue mixing. According to previous studies, ovarian collision tumors are mixtures of different combinations of epithelial tumors, germ cell tumors, and sex-cord stromal tumors. The most common composition is the presence of epithelial tumors and germ cell tumors together. In the largest series of ovarian collision tumors in the literature, mature teratomas and mucinous epithelial neoplasms were reported to be the most common. The specific imaging features of ovarian collision tumors depend on the composition and the imaging findings of each collision tumor component. The typical morphological collision patterns include “back-to-back” with a clear margin or “nested tumor” in which one lie inside the other. The larger tumor usually represents the epithelial tumor and the smaller tumor component indicate a germ cell or sex-cord stromal tumor. A missed diagnosis of ovarian collision tumor can have unintended consequences on patient management, particularly if the pathological assessment is insufficient and a malignant component is overlooked. In this educational poster, we aim to review the MR imaging spectrum of ovarian collision tumors with emphasis on pearls and pitfalls in the diagnosis. Conclusion: The awareness of ovarian collision tumors and knowledge of imaging features by the radiologists is essential to provide a prompt diagnosis and appropriate management of the patients.

Figure 1



Right ovarian collision tumor with mucinous cystadenoma and immature teratoma. Axial T2 (a), T1 (b) and fat-suppressed T1 (c) images show two cystic lesions in the right ovary. The lateral one (white arrows) has intense content with T1 and T2 intermediate signal intensity regarding mucinous cystadenoma. The medial one (yellow arrows) has fat signal with chemical shift artefacts on T2WI. Post-contrast axial T1 (d) shows a small enhancing mural nodule (red arrow) which was proved to be immature teratoma.

Keywords: ovary, collision tumor, diagnostic imaging

INTERVENTIONAL RADIOLOGY MANAGEMENT OF SPLENIC ABSCESS DUE TO SALMONELLA ENTERITIDIS FOLLOWING ABDOMINAL TRAUMA – CASE REPORT

Milan Pantelic¹, Tamara Vucinic¹, Milica Stanucevic¹, Milos Dujovic¹, Masa Pantelic²

¹Zvezdara University Medical Center, Department of Radiology, Belgrade, Serbia

²Zvezdara University Medical Center, Department of Gastroenterology and Hepatology, Belgrade, Serbia

Abstract: Introduction: Splenic abscess is a very rare extra-intestinal complication of Salmonella infection in the post-antibiotic era with incidence between 0.14% and 2%. It usually follows bacteremia due to varied etiologies such as trauma, infective endocarditis, intravenous drug abuse, immunodeficiency status (AIDS, diabetes mellitus). We report a case of splenic abscess due to Salmonella enteritidis after abdominal trauma successfully treated with percutaneous drainage and antibiotic therapy. Case report: An 82-year-old woman presented with a history of upper abdominal pain, fever and nausea for two weeks following abdominal trauma. Laboratory investigations revealed a raised total leukocyte count, anemia and elevated C-reactive protein (111 mg/dl). Abdominal ultrasound revealed enlarged spleen with a hypoechoic cystic structure. Computed tomography scan of the abdomen showed hypodense lesion measuring 110x80mm (CCxLL) with minimal peripheral contrast enhancement, diagnosed as a splenic abscess. The patient underwent an ultrasound and X-ray guided percutaneous needle aspiration with free-hand technique using an 18 Gauge needle to collect a sample of pus for microbiological analyses. In next step 8.5F multisidehole pigtail catheter was placed in collection by performing Seldinger technique. Patient was in pronation under analgesedation and with local anesthesia on site of puncture. In next 24h 300ml of purulent fluid was drained and about 100ml each day in next 3-4 days and then catheter was extracted. Salmonella enteritidis was isolated after three days of culture, sensitive to ampicillin, ciprofloxacin and cephalosporins of third generation, so ceftriaxone was administered. After a month patient was discharged. During 6-months follow-up there were no recurrent symptoms and control CT scan showed normal size spleen with thin low-density zones under the capsula - sequels of inflammation. Discussion: Splenic abscess is associated with high morbidity and mortality if not diagnosed and treated in time. Ultrasonography and CT scan are gold standard for early diagnosis, while splenectomy is the gold standard for treatment. Only a few cases of splenic abscess caused by Salmonella enteritidis have been described in the literature and they were mostly treated with splenectomy. Conclusion: This case of rare splenic abscess due to Salmonella enteritidis was treated successfully with combination of percutaneous drainage, prolonged antibiotic therapy and intensive care.

Coronal CT scan of abdomen

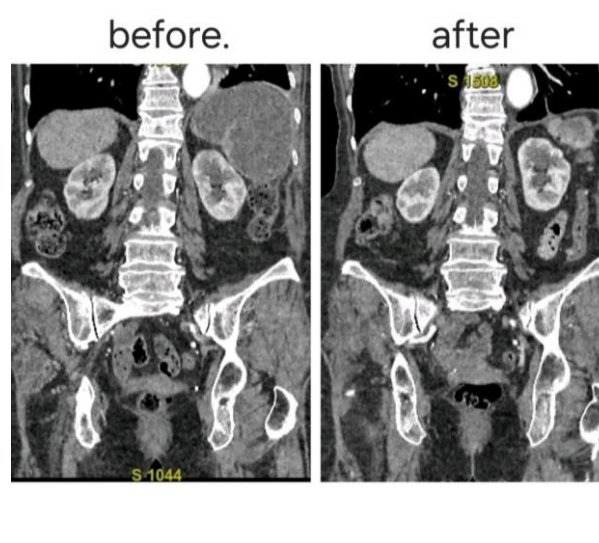
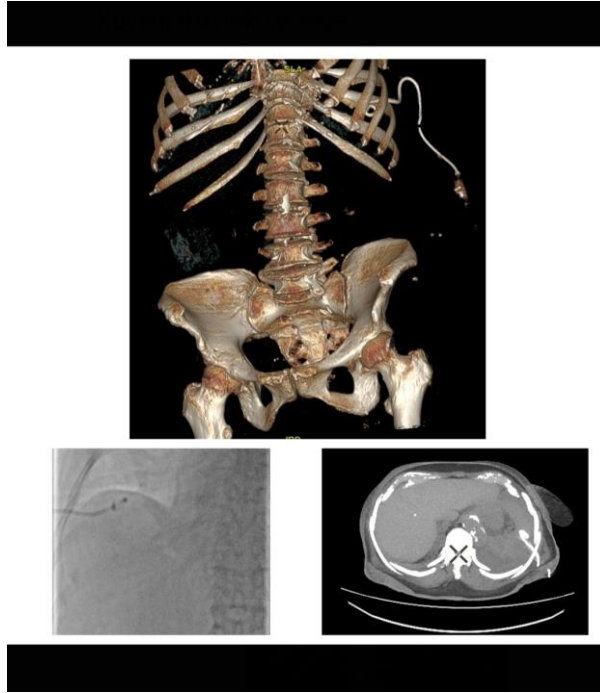


Image findings before (left) and after (right) percutaneous drainage of splenic abscess

Drainage catheter



Images show drainage catheter in collection (volume rendering, fluoroscopy, axial CT scan)

Keywords: splenic abscess, Salmonella enteritidis, percutaneous drainage

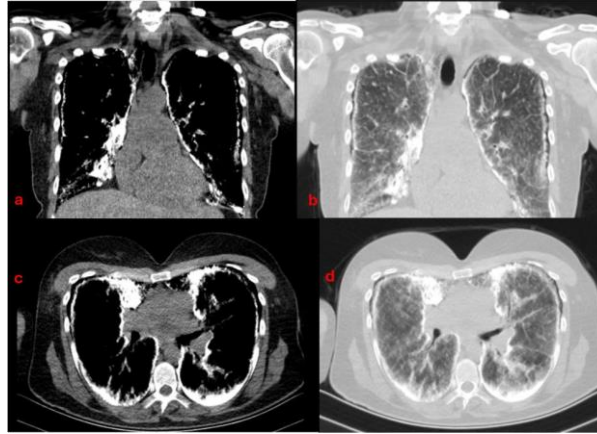
A CASE OF PULMONARY ALVEOLAR MICROLITHIOSIS

Sefika Bengi Cilasın¹, Hasan Erdogan¹, Ali Koc¹

¹Kayseri City Training And Research Hospital

Abstract: Introduction and objective: Pulmonary alveolar microlithiasis (PAM) is a rare chronic disease characterized by intraalveolar calcium and phosphate deposition in the lung parenchyma [1]. The disease may be asymptomatic or may lead to parenchymal damage resulting in pulmonary fibrosis over the years [2]. In this presentation, we aimed to share the imaging findings of our patient with PAM. Case: A 45-year-old woman was admitted to our hospital with dyspnea and underwent thoracic computed tomography (CT). Thorax CT showed diffuse calcifications in the peripheral and subpleural areas of both lungs, especially more prominent in the posterior parts of the lower lobe, and was evaluated as PAM. Discussion: Although the etiology and pathogenesis of PAM are unclear, it is thought to be an autosomal recessive disorder caused by mutations in the gene encoding a sodium phosphate co-transporter (SLC34A2 gene) [3]. Although it is usually recognized incidental, patients may also present with nonspecific symptoms such as dyspnea, cough and fatigue. Although it shows slow progression, it causes pulmonary fibrosis or heart failure. Although the definitive diagnosis is made by lung biopsy, correlation of clinical findings with radiologic images is very important. Involvement is bilateral and middle - lower zone predominates. Radiography shows calcifications forming a sandstorm appearance and a black pleural sign. While calcified interlobular septa are pathognomically seen on CT, cobblestone pattern, subpleural cysts, black pleural sign and ground glass opacities may also accompany. Since there is no definitive treatment, symptomatic treatment is given. Lung transplantation may be tried in end-stage patients. Conclusion: In conclusion, PAM is a rare chronic disease that can be asymptomatic for many years and has no effective medical treatment. The majority of cases are detected incidental, but the characteristic radiologic findings make it easy to diagnose. References: 1. Kashyap S, Mohapatra PR. Pulmonary alveolar microlithiasis. Lung India. 2013 Apr;30(2):143-7. doi: 10.4103/0970-2113.110424. PMID:23741096; PMCID: PMC3669555. 2 Åsa Lina M. Jönsson, Ulf Simonsen, Ole Hilberg, Elisabeth Bendstrup European Respiratory Review 2012 21: 249-256; DOI: 10.1183/09059180.00009411 3 Corut A, Senyigit A, Ugur SA, et al Mutations in SLC34A2 cause pulmonary alveolar microlithiasis and are possibly associated with testicular microlithiasis. Am J Hum Genet 2006; 79: 650–656.

photo 1



On non-contrast thorax CT, diffuse calcifications in the peripheral and subpleural areas of both lungs, especially more prominent in the posterior parts of the lower lobe, are seen in the mediastinal (a) and lung (b) window in coronal sections and in the mediastinal (c) and lung (d) window in axial sections.

Keywords: PAM, calcification, incidental

THE IMPACT OF BODY FAT DISTRIBUTION AND SARCOPENIA ON NAC REACTION AND RECURRENCE IN LABC PATIENTS DEPENDING ON MOLECULAR SUBTYPES

Elçin Aydın¹, Hülya Çetin Tuncez¹, Özden Karadeniz¹, Gül Çolakoğlu², Hüseyin Esin³, Cem Karaali³, Emel Ebru Pala⁴, Şükrü Şahin⁵

¹Izmir City Hospital, Department of Radiology, Izmir, Turkey

²Tepecik Training and Research Hospital, Department of Radiology, Izmir, Turkey

³Izmir City Hospital, Department of General Surgery, Izmir, Turkey

⁴Izmir City Hospital, Department of Pathology, Izmir, Turkey

⁵Elazığ City Hospital, Department of Radiology, Elazığ, Turkey

Abstract: Introduction A class of breast tumors known as locally advanced breast cancer (LABC) is defined as having metastases to axillary lymph nodes at staging but no distant organ metastases. For this group, neoadjuvant chemotherapy (NAC) is the initial line of treatment. Muscle mass and body fat distribution (BFD) are two potentially significant biomarkers. The aim This study sought to ascertain the impact of BFD on relapse and response to treatment based on molecular subtypes in LABC. Material and methods A retrospective analysis was performed on 110 LABC patients Prior to NAC, the patients' computed tomography evaluated muscle area at the level of the third lumbar vertebra, as well as their visceral fat area (VFA), subcutaneous fat area (SFA), and total fat area (TFA). The evaluation of pathological NAC response was conducted using the Residual Cancer Burden (RCB) Calculator. Based on their molecular subtypes, patients were divided into four groups and monitored for recurrence for an average of 36.27±8.67 months. Results The group with sarcopenia had greater VFA and TFA (p=0.001, p=0.024, respectively). Regarding SFA and TFA, there was no discernible difference between the RCB groups. Significantly more VFA was found in the RCB III group. The RCB and muscle area did not significantly differ from one another. Recurrence and VFA had an independent correlation (p:0.011). Subgroups based on molecular characteristics showed no discernible variations in RCB, sarcopenia, or sarcopenic obesity between the groups. Conclusion We found that higher VFA was linked to a decreased pathological cancer response (pCR) to NAC and a poorer overall survival rate. There was no evidence linking sarcopenia to pCR. Nonetheless, it was discovered that sarcopenic patients have elevated VFA, which has a secondary effect. Sarcopenia and BFD are critical factors in assessing the NACT response in LABC patients.

Figure 1

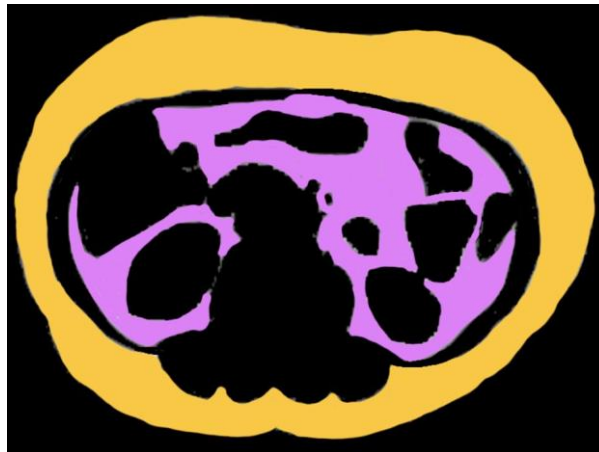


Figure 1: Measurement of subcutaneous fat volume (yellow*) and visceral fat volume (purple*),

Figure 2



Figure 2: Measurement of sarcopenia (red*). L3 vertebra was chosen both measurement

Table 2. Abdominal fat distribution of RCB groups.

Parameter	RCB0 Mean (SD)	RCB1 Mean (SD)	RCB2 Mean (SD)	RCB3 Mean (SD)	p value
Subcutaneous fat area (cm ²)	222,58 (82,21)	213,27 (78,13)	207,98 (78,86)	225,25 (81,99)	0.821
Visceral fat area (cm ²)	113,94 (48,89)	113,30 (50,46)	121,45 (53,48)	151,99 (50,11)	0.015
Total fat area (cm ²)	336,52 (121,65)	326,56 (121,32)	329,43 (121,39)	377,24 (109,83)	0.326

Table 1. Comparison of the Frequency of VFA,SFA and TFA in Groups

	Luminal A and B (n=71)	Her-2 Positive (n=18)	Triple Negative (n=21)	p-value
Visceral fat area (Mean±SD)	134,03±57,97	122,76±28,13	106,16±45,96	0.097
Subcutaneous fat area (Mean±SD)	218,65±81,385	236,63±73,59	195,25±76,89	0.262
Total fat area (Mean±SD)	352,69±123,32	359,40±92,12	301,41±117,36	0.184

Keywords: locally advanced breast cancer, sarcopenia, neoadjuvant chemotherapy, pathological cancer response

FROM HEADACHES TO OBSTRUCTIVE ILEUS: FOLLOWING THE DOTS

Christos Korres¹, Anastasia Doukoupoulou¹, Fotini Mermigka¹, Charikleia Triantopoulou¹

¹*Konstantopouleio Hospital. Athens, Greece*

Abstract: Meningioma and colorectal cancer (CRC), seemingly distinct, and usually of opposing malignancy, have nevertheless exhibited potential to synchronously affect the same person. Occasioned by a 78-year-old female patient who presents with obstructive ileus -on grounds of mucinous adenocarcinoma of the colon- and simultaneous complaints of headaches -proven to be due to a parafalcine meningioma, we explore similar genetic information that embrace both of these entities. Mutations in neurofibromatosis-2 gene (NF2) and its tumour-suppressing properties often drive meningioma development, while its poor expression is associated to high-grade CRC. Akt1 is an oncogene that downregulates NF2 in meningioma, and therefore enhances its recurrence, while it advances in higher expression with the progression of CRC. Fairing higher in the same signaling pathway as Akt1, PIK3CA, also an oncogene, may affect formation of both tumours either via the Akt1 mechanism or in cooperation with KRAS, another oncogene implicated in increased mutations specifically in mucinous CRC. Anomalous methylation of CpG loci can negatively affect expression of the respectful genes. KLF-4 is such a gene, whose tumour-suppressive characteristics are deemed insufficient in both meningioma and CRC from hypermethylating events. Independently to the epigenetical cue, KLF-4 can contribute to both neoplasms via individual genetic alterations that inhibit its antiapoptotic effects. In conclusion, we suggest common pathways of anti-apoptosis or cell-proliferative mechanisms that coalesce in the formation of both meningioma and CRC.

Keywords: meningioma, colorectal cancer, genetic alterations

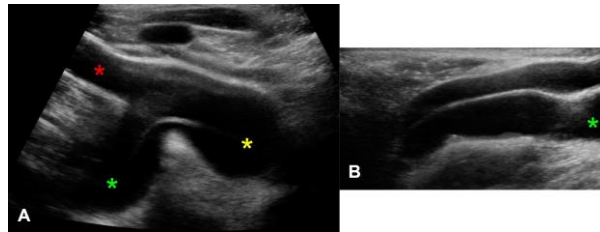
SUBCLAVIAN ARTERY DISSECTION: THE VISIBLE TIP OF THE AORTIC ICEBERG!

Sule Ozer¹, Bilge Gultac¹

¹Canakkale 18 March University Health Practice and Research Hospital, Department of Radiology

Abstract: Case: A 65-year-old male patient, who had undergone surgery for aortic dissection approximately 5 years ago, presented to the clinic with dizziness and syncope that had persisted for the past 2 weeks. The patient, referred for carotid and vertebral artery color Doppler ultrasound, was found to have a pulsatile flap (Fig.1) and a false lumen with retrograde flow (Fig.2) consistent with dissection in the right subclavian and distal innominate arteries. To clarify the extent and etiology of the dissection, a thoracic CT angiography was performed, revealing a type B aortic dissection extending to the right subclavian artery and the innominate artery (Fig.3). Discussion: Subclavian artery dissection is most commonly observed as a form of aortic dissection extending to one or both subclavian arteries [1]. Isolated subclavian artery dissection is an uncommon clinical entity that is often associated with conditions such as arterial thoracic outlet syndrome (TOS), arterial catheterization, connective tissue disorders, or blunt trauma [1,2]. Patients with subclavian artery dissection may present with nonspecific clinical symptoms including chest or back pain, arm paresthesia, and vertigo. In our case, subclavian artery dissection often presents in conjunction with aortic dissection and may manifest with non-specific symptoms. We aimed to emphasize that even in routine outpatient settings, one can encounter urgent and life-threatening pathologies, and that meticulous and detailed evaluation at this stage is crucial for diagnosing critical conditions such as aortic dissection. Don't stop searching — you might miss the next 'A-ha!' moment! References: 1. Robb CL, Bhalla S, Raptis CA. Subclavian Artery: Anatomic Review and Imaging Evaluation of Abnormalities. Radiographics. 2022 Nov-Dec;42(7):2149-2165. doi: 10.1148/rg.220064. Epub 2022 Sep 2. PMID: 36053845. 2. Jones CS, Verde F, Johnson PT, Fishman EK. Nontraumatic Subclavian Artery Abnormalities: Spectrum of MDCT Findings. AJR Am J Roentgenol. 2016 Aug;207(2):434-41. doi: 10.2214/AJR.15.15685. Epub 2016 May 17. PMID: 27187867.

Figure 1.



Gray scale ultrasonography images at the cervicothoracic junction level. Intima medial flap extending from the proximal part of the innominate artery (yellow marker) to the subclavian artery (green marker) is observed (A). Note the absence of extension to the right carotid artery (red marker) (A). Intima-medial flap in the lumen of the subclavian artery (green marker) (B).

Figure 2.

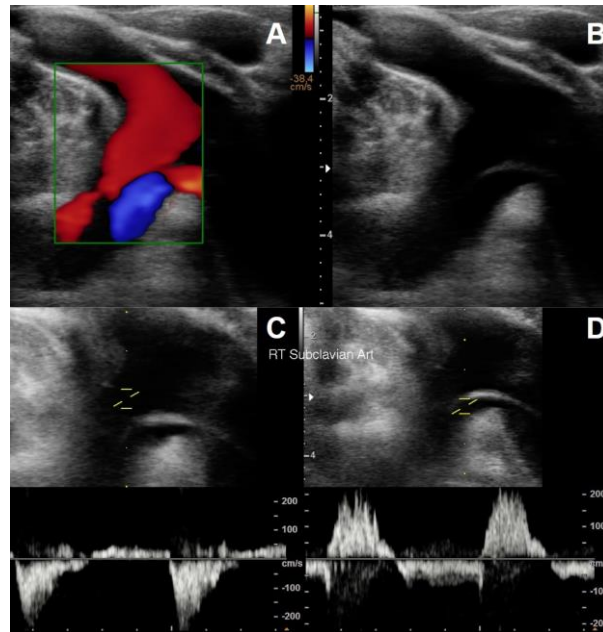


Figure 2. Color Doppler (A), gray scale (B), and spectral Doppler (C-D) ultrasonography images at the proximal segment of the right subclavian artery. The intima-medial flap extending from the innominate artery to the subclavian artery is observed (B), along with a false lumen appearance consistent with retrograde flow (A, D). Please note the antegrade flow in the true lumen (A, C).

Figure 3.

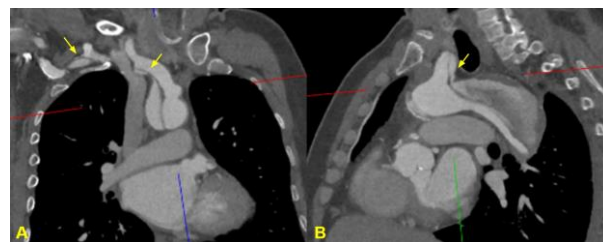


Figure 3. Coronal (A) and sagittal (B) reformatted images in thoracic angiography CT. The intima-medial flap, originating from the level of the aortic arch and extending to the innominate artery and right subclavian artery, is observed in both images (indicated by the yellow arrow).

Keywords: Subclavian artery dissection, Aortic dissection, Doppler Ultrasonography, Computer Tomography Angiography

GOSSYPIBOMA: A DIAGNOSIS TO BE REMEMBERED

Mesut Furkan Yazar¹, Elif Kır Yazar¹, Kadir Çorbacı¹

¹Bilecik Training and Research Hospital

Abstract: Introduction Gossypiboma is a rare surgical complication that results in a lesion surrounded by a foreign-body reaction from a retained surgical sponge (1). Surgical sponges or swabs that are retained in the abdomen or pelvis happen in every 100–5000 surgeries (2). A retained sponge is found after two typical reactions. The first kind, which results in an abscess and exudative inflammatory reaction, is typically detected early and surgically removed. The second kind is aseptic and develops a mass and fibrotic response to the cotton fiber (3). Case Report A 31-year-old female patient applied to the emergency department with a complaint of abdominal pain. On physical examination, there was tenderness in the right lower quadrant of the abdomen. There was a history of cesarean sections in 2015 and 2023. In imaging, firstly, abdominal radiography and ultrasonography examinations were performed. A heterogeneous hypoechoic mass lesion with a cystic component and posterior acoustic shadowing was observed on ultrasound. No vascularity was detected in the lesion on Doppler ultrasound (Figure 1). Abdominal X-ray demonstrating a curved metallic object and a well-defined spherical opacity in the right iliac fossa (Figure 2). To better evaluate the lesion character and extent, a non-contrast abdominal CT scan was performed. On CT, a well-circumscribed, oval-shaped, heterogeneous mass lesion containing linear metallic density was observed in the right lower quadrant of the abdomen (Figure 3). Gossypiboma was considered in the preliminary diagnosis due to the patient's history of cesarean section and the presence of metallic densities within the lesion on abdominal radiography and CT. The patient had surgery, and it was discovered that a piece of gauze had been retained. Conclusion Gossypibomas have non-specific imaging characteristics (4). Abdominal gossypibomas may appear polymorphic on CT scans (5). The most important finding in conventional X-rays and CT in gossypomas is the metallic wire within the soft tissue masses. It could be necessary to use a multimodality approach and correlate the diagnosis with the patient's history. (4).

Figure 1



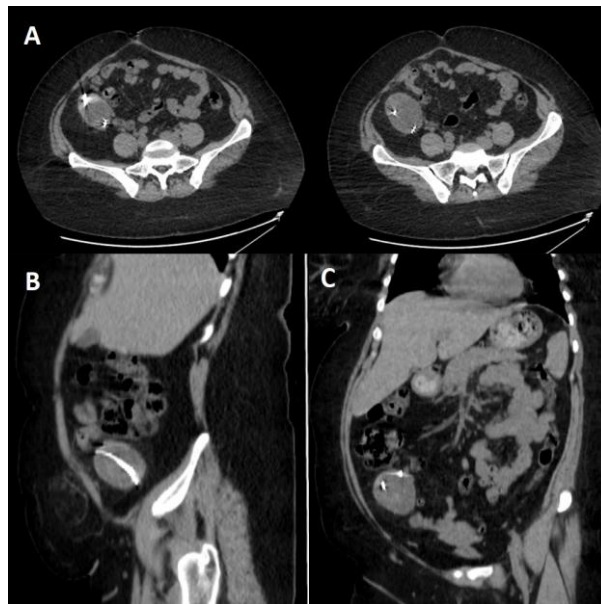
A, B: heterogeneous hypoechoic mass lesion with a cystic component and posterior acoustic shadowing on ultrasound. C: No vascularity was detected in the lesion on Doppler ultrasound

Figure 2



A curved metallic object and a well-defined spherical opacity in the right iliac fossa on abdominal X-ray

Figure 3



A: Axial B: Sagittal C: Coronal CT images, a well-circumscribed, heterogeneous mass lesion containing linear metallic density in the right lower quadrant of the abdomen

Keywords: Gossypiboma, Foreign body, intra-abdominal mass, surgical sponge

A RARE SESAMOID BONE OF THE FOOT; OS VESALIANUM

Gulseher Saylan¹, Seda Sogukpınar Karaagac¹

¹Department of Radiology, Faculty of Medicine, Firat University, Elazığ, Turkey

Abstract: A 25-year-old male patient underwent non-contrast CT scan of the right foot with a prediagnosis of morton neuroma. A sesamoid bone compatible with os vesalianum, which articulates with the cuboid and metatarsal bone, was incidentally found in the 5th metatarsal head. Our patient presented to the orthopaedic outpatient clinic with the complaint of pain in the right foot about 1 year ago. As a result of the X-rays taken, a surgical procedure was performed with the diagnosis of right foot 5th metatarsal head fracture and secondary pseudoarthrosis. During the operation, a metallic fixator extending from the bone (os vesalianum), which was indicated as pseudoarthrosis, to the body part of the 5th metatarsal was inserted (Figure 1). 1 year later, CT scan was performed and we concluded that it was not 5th metatarsal pseudoarthrosis but os vesalianum (Figure 2). Os vesalianum is a rare accessory ossicle of the foot which can be confused with other fractures of the 5th metatarsal bone head and may cause chronic foot pain. Treatment includes conservative approach and rarely surgical excision of the bone.

Figure 1



The radiographs of the patient, taken before and after the treatment; it is seen that there is a bone structure in the 5th metatarsal head and there is no difference in bone structure and shape 1 year after the surgical intervention

Figure 2



Maximum intensity projection CT scan showing the appearance of the os vesalianum sesamoid bone articulating with the cuboid and metatarsal bone at the 5th metatarsal head and surgical fixator material applied to this level.

Keywords: Os vesalianum, sesamoid, articulation

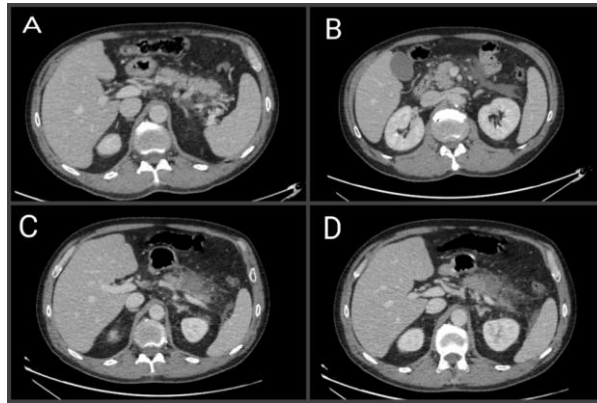
GASTROPANCREATIC FISTULA: A RARE COMPLICATION OF RECURRENT PANCREATITIS

Mesut Furkan Yazar¹, Elif Kır Yazar¹, Özcan Emre¹, Kadir Çorbacı¹, Mehmet Emin Gönüllü¹

¹Bilecik Training and Research Hospital

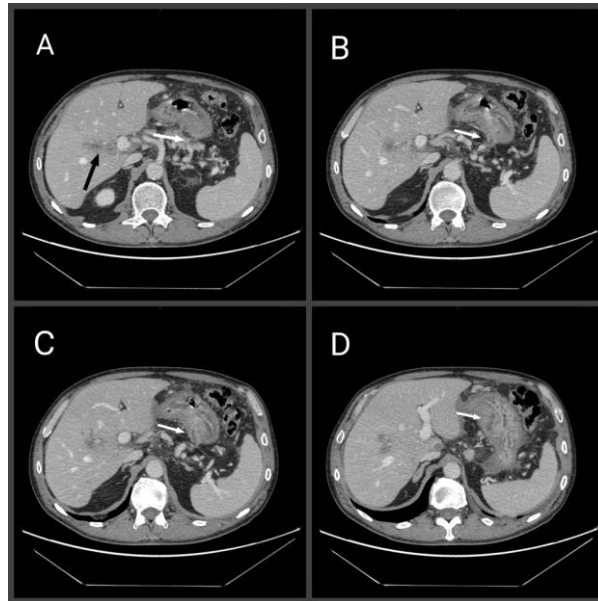
Abstract: Introduction There are numerous complications related to pancreatitis that impact both the gland and the surrounding structures (such as fluid collections, pseudocyst, abscess, pancreatic necrosis, peritonitis, cholecystitis, cholangitis, renal, splenic, or portal vein thrombosis, systemic inflammatory response syndrome, disseminated intravascular coagulopathy)(1). Gastropancreatic fistula is a rare complication of severe pancreatitis or chronic pancreatitis (2). Gastropancreatic fistula can be associated with intraductal papillary mucinous neoplasm (IPMN), peptic ulcer (3,4). Case Report A 55-year-old male patient was admitted to the emergency department due to epigastric pain. The patient has a history of chronic alcohol use and recurrent pancreatitis attacks. In July 2022 when the patient first applied, there was pain in the back, leukocytosis, and elevated amylase and lipase. Abdominal CT imaging showed typical findings of acute edematous pancreatitis (Figure 1). In February 2023, 7 months after his first pancreatitis attack, he applied to the emergency department again with similar complaints. Peripancreatic edema and fluid collections were more evident on CT imaging compared to the previous one (Figure 1). In his last application, in August 2024, the patient had epigastric pain and tenderness and an abdominal tomography was performed with the preliminary diagnosis of pancreatitis. There was a hypodense tract within thin enhancing wall between the tail of the pancreas and the lesser curvature of the stomach, compatible with pancreatico-gastric fistula (Figure 2,3). Stranding of perigastric fat and fluid collection are seen. In addition, filling defects were observed in the right portal vein and its branches, consistent with portal vein thrombosis (Figure 2,3). Conclusion The use of contrast-enhanced CT imaging is essential for the diagnosis, staging, and identification of pancreatitis related complications (5). Rarely, Recurrent pancreatitis can be complicated by fistulation between the pancreas and neighboring organs. In this instance, we present an unusual case of simultaneous fistulation to both the gastric body and the pancreas.

Figure 1



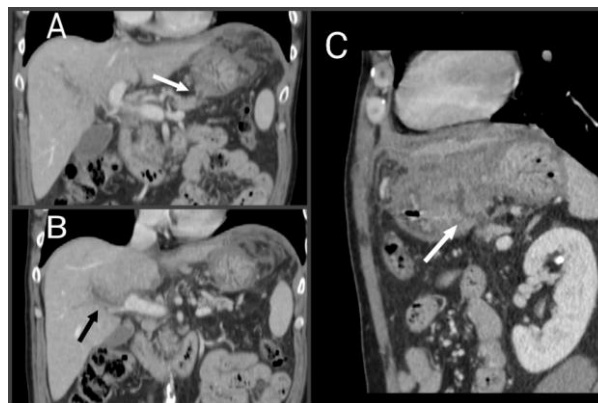
A, B: In July 2022 on Abdomen CT, pancreatic parenchymal enlargement with surrounding fat stranding and fluid collection C, D: In February 2023 on Abdomen CT, Peripancreatic edema and fluid collections were more evident compared to the previous one

Figure 2



in August 2024 on Abdomen CT A: Fistula tract between the pancreatic tail and the stomach wall (white arrow). Thrombosis in the right portal vein (black arrow). B, C: Gastropancreatic fistula tract (white arrow) D: Fistula tract advancing on the stomach wall (white arrow)

Figure 3



in August 2024 on Abdomen CT A: gastropancreatic fistula tract in coronal image B: Thrombosis in the right portal vein (black arrow) C: gastropancreatic fistula tract in sagittal image

Keywords: Pancreatitis, Gastropancreatic fistula, portal vein thrombosis, complication of pancreatitis

MAYER-ROKITANSKY-KÜSTER-HAUSER SYNDROME WITH SUPERNUMERARY OVARY: VERY RARE CONGENITAL CO-OCCURRENCE

Onur Başdemirci¹, Merve Başdemirci¹, Safiye Gürel²

¹Department of Radiology, Karabük Training and Research Hospital

²Department of Radiology, Gülhane Medical School, Gülhane Training and Research Hospital

Abstract: BACKGROUND-AIM: Supernumerary ovary is one of the rarest gynecological anomalies [1]. The presence of supernumerary ovaries together with Mayer-Rokitansky-Küster-Hauser (MRKH) syndrome is an extremely rare condition. In this article, we will present a case of supernumerary ovary with MRKH syndrome, and mention multimodal imaging findings and pathophysiology. CASE: A 17-year-old female patient presented with primary amenorrhea. In the physical examination of the patient, external genital organs, secondary sexual character development and laboratory findings were normal. In the sonographic examination, uterus and right kidney were absent. In magnetic resonance imaging, uterus, proximal part of the vagina and the right kidney were absent (Figure 1). Both ovaries were normal in size and location (Figure 2). Additionally, a suspicious appearance for the third ovary was observed at anterior neighborhood of iliac bifurcation. It contained nodular T2 hyperintense structures, which could be compatible with follicles (Figure 2, 3). In the second sonographic examination performed afterward, it was understood that it was compatible with the supernumerary ovary (Figure 3d, 3e). DISCUSSION: Supernumerary ovary was described by Wharton in 1959 [2]. There are two mechanisms for supernumerary ovary development [3]. Pearl and Plotz's theory, suggest a pause in the migration of gonocytes in the dorsal mesentery [4]. The alternative theory is Printz et al.'s transplantation theory of gonocyte participation to the gonadal ridge [5]. The supernumerary ovary might be located in pelvis, retroperitoneum, para-aortic area, colon mesentery. It's usually asymptomatic and often diagnosed incidentally [6]. MRKH syndrome is a condition in the Müllerian anomaly spectrum characterized by aplasia-agenesis of uterus and vagina in individuals with normal genotype, phenotype and hormonal status [7,8]. MRKH syndrome is second most common cause of primary amenorrhea [9]. MRKH syndrome might be seen isolated (type-A) or accompanied by non-Müllerian anomalies (type-B), such as renal, vertebral, auditory anomalies [10]. Presence of supernumerary ovary very rarely accompany type-B MRKH syndrome. CONCLUSION: As radiologists, we should remember that supernumerary ovary, a very rare oocyte migration anomaly, may be present when evaluating patients with MRKH syndrome.

Figure 1

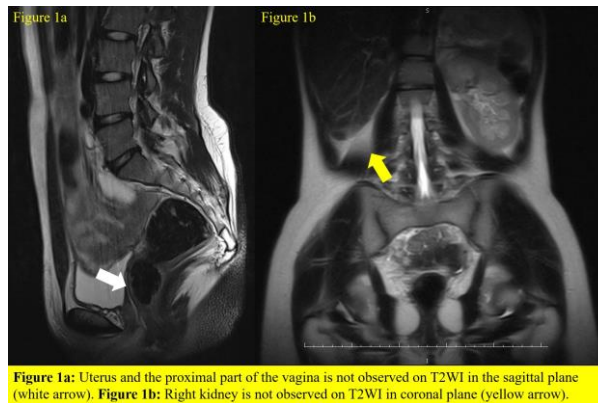


Figure 2

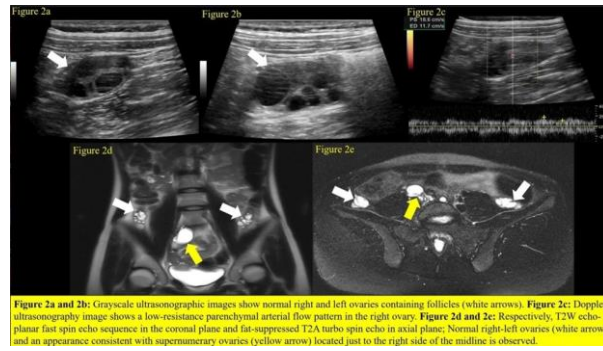
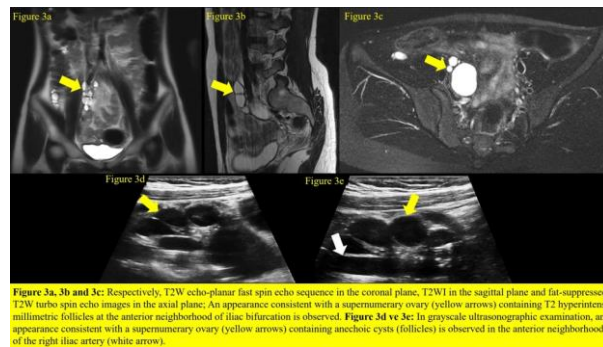


Figure 3



Keywords: Mayer-Rokitansky-Küster-Hauser Syndrome, Mullerian Anomaly, Supernumerary Ovary, MRI

OVERLOOKED SMALL BOWEL MASS: GASTROINTESTINAL STROMAL TUMOR

Mesut Furkan Yazar¹, Elif Kır Yazar¹, Dilay Demirayak¹, Ezgi Emre¹

¹Bilecik Training and Research Hospital

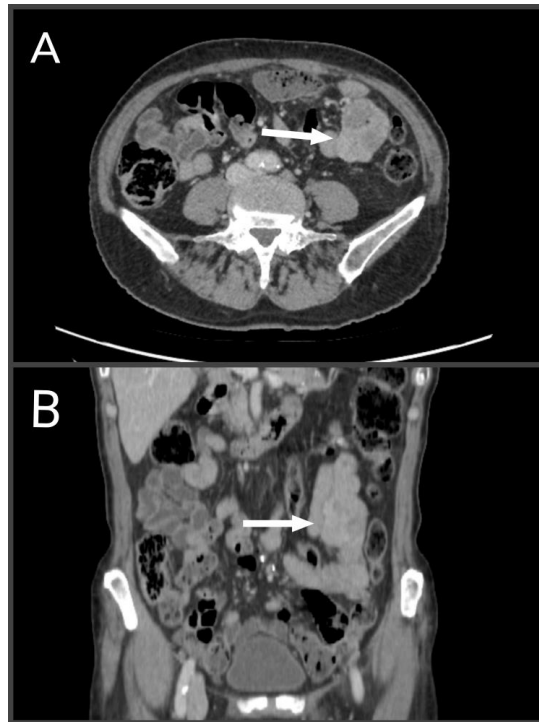
Abstract: IntroductionThe most prevalent mesenchymal neoplasm of the gastrointestinal tract are called gastrointestinal stromal tumors, or GISTs (1). Anywhere in the gastrointestinal (GI) tract can develop a gastrointestinal stromal tumor. The stomach accounts for 50% to 75% of these, the small intestine for 20%, and the colon and rectum for less often occurring sites (2,3). Here we report a case of jejunal-located GIST whose diagnosis was delayed.Case Report A 60-year-old male patient applied with complaints of recurrent melena, dizziness and fatigue. Blood tests revealed hemoglobin (hb):7,6 gr/dl, hemostasis parameters were normal. Gastroscopy and colonoscopy were performed to investigate the etiology of gastrointestinal bleeding. No pathology was detected in endoscopy to explain the gastrointestinal bleeding. Then, contrast-enhanced abdominal CT (CECT) examination was performed in July 2024. No pathology was detected in the stomach and colon in the abdominal CECT examination. An extophytic, well-circumscribed, heterogeneously enhancing mass lesion compatible with GIST was observed in the jejunal loop in the left quadrant of the abdomen. The patient had a history of repeated visits to the emergency department due to gastrointestinal bleeding. Gastroscopy and colonoscopy were performed several times to determine the etiology of GI bleeding, No pathology was found. Since a mass was detected in the jejunal loop in the last CT scan in July 2024, old CT scans were examined retrospectively. In the CT examinations dated February 2021 (Figure 1) and February 2022 (Figure 2), it was seen that there was a mass lesion in both cases. Lesion sizes were found to be smaller in previous CT examinations and progressed over time (Figure 3). The pathology result of the surgically removed mass was documented as GIST.ConclusionGIST masses in GI locations outside the small intestine can be detected by endoscopy. However, small bowel GIST masses cannot be detected by gastroscopy and colonoscopy. Radiological imaging plays a key role in the diagnosis of small bowel GIST masses. Radiologists should carefully evaluate the small bowel loops in abdominal CT examinations performed due to gastrointestinal bleeding.

Figure 1



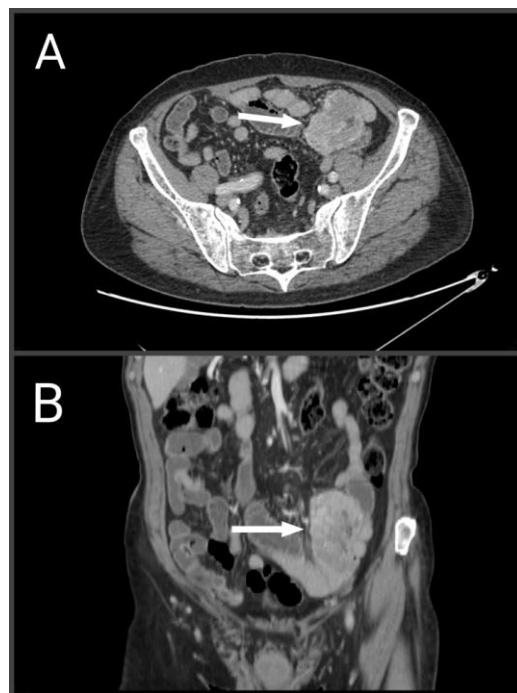
Abdominal CT in February 2021 A: Axial image B: Coronal image, An extophytic, well-circumscribed, heterogeneously enhancing mass lesion in the jejunum (White arrows).

Figure 2



Abdominal CT in February 2022 A: Axial image B: Coronal image, Jejunal mass persists with a slight increase in size (White arrows).

Figure 3



Abdominal CT in July 2024 A: Axial image B: Coronal image, Jejunal mass sizes progressed over time (White arrows).

Keywords: GIST, Gastrointestinal stromal tumors, intestinal mass, gastrointestinal bleeding

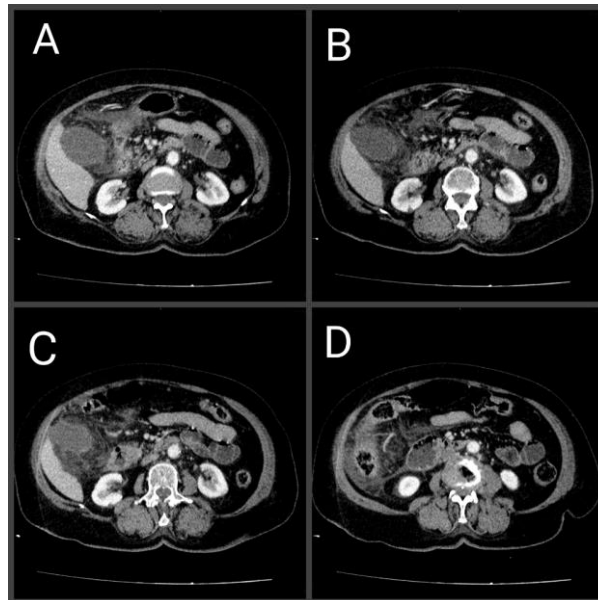
DANGEROUS COMPLICATION OF ACUTE CHOLECYSTITIS: GALLBLADDER PERFORATION

Elif Kır Yazar¹, Mesut Furkan Yazar¹, Kadir Çorbacı¹, Mehmet Emin Gönüllü¹

¹Bilecik Training and Research Hospital

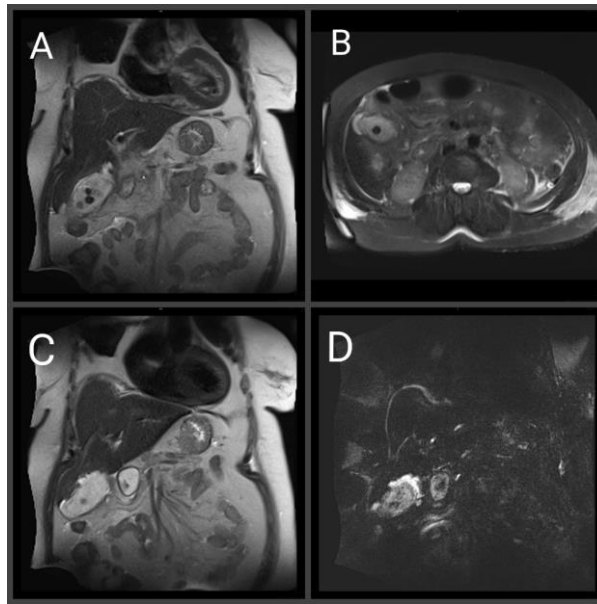
Abstract: Introduction: During or after acute cholecystitis, gallbladder perforation (GBP) is an uncommon, dangerous, and potentially fatal consequence. From a 15% rate in previous series, the incidence is now less than 1% to 2%. Prolonged cholelithiasis history, advanced age, arteriosclerosis, diabetes, immunosuppression, and steroid use are risk factors for GBP (1,2). Intraluminal hyperpression, which results from obstruction of the cystic duct and exceeds arterial pressure, is the pathogenesis that leads to mural ischemia, gangrene, and ultimately perforation (3,4). Case Report: An 80-year-old female patient was admitted to the emergency department with vomiting and abdominal pain radiating to her back for 3 days. Positive Murphy's sign at physical examination. Severe inflammatory markers (26.000/mm³ neutrophils, C-Reactive Protein 300 mg/L). An abdominal ultrasound was performed with the preliminary diagnosis of acute cholecystitis. Ultrasound (not shown) detected hydropic gallbladder with positive sonographic Murphy's sign, mural thickening, dense bile sludge and stones up to 14 mm in diameter in the gallbladder lumen, consistent with acute cholecystitis. Pericholecystic millimetric fluid collections were observed. Biliary tract and bilirubin values were normal. As the patient's general condition worsened and a septic condition developed, contrast-enhanced CT was performed to evaluate possible complications of cholecystitis. CT confirmed hydropic gallbladder with mural enhancement, mural thickening, surrounding fat inflammatory stranding and pericholecystic low-attenuation fluid collection. In a few foci on the gallbladder wall were non-enhancing/non-visualized, concerning for perforation (Figure 1). Irregularity and focal defects in the wall accompanying the findings of acute cholecystitis were observed on MRCP (Figure 2). No intrahepatic or extrahepatic biliary dilatation. Laparoscopic surgery findings confirmed acute cholecystitis with some mural necrosis, pericholecystic collection due to microperforations (Figure 3). Conclusion: Perforation of the gallbladder is a rare complication of acute cholecystitis that is associated with relatively high morbidity and mortality. Symptoms and signs of gallbladder perforation may be similar to those of acute cholecystitis. This may cause a delay in diagnosis. The possibility of perforation should be kept in mind in patients with acute cholecystitis who are in the risk group and whose clinical condition worsens.

Figure 1



on Abdomen CT, A,B, hydropic gallbladder with mural thickening, surrounding fat inflammatory stranding and pericholecystic fluid collection. C: In a few foci on the gallbladder wall were non-enhancing/non-visualized, concerning for perforation. D: Pericholecystic fluid collection and fat stranding

Figure 2



Irregularity and focal defects in the wall accompanying the findings of acute cholecystitis on MRCP

Figure 3



Acute cholecystitis with some mural necrosis and microperforations in intraoperative macroscopic view

Keywords: cholecystitis, Gallbladder perforation, acute abdomen, complication of cholecystitis, perforation

UTERINE SMOOTH MUSCLE TUMORS OF UNCERTAIN MALIGNANT POTENTIAL (STUMP): A REPORT OF TWO CASES

Ruhi Erdem Ergüden¹, Sezer Nil Yılmaz Zorlu¹, Diğdem Kuru Öz¹, Ayşe Erden¹

¹Ankara University Department of Radiology

Abstract: Introduction: Smooth-muscle tumors of uncertain malignant potential (STUMP) are uterine tumors with malignant features but lack clear classification as benign or malignant. These tumors present with symptoms similar to leiomyoma and leiomyosarcoma, including pelvic pain, abnormal bleeding, and pelvic mass. Despite favorable clinical outcomes, STUMP can recur and metastasize, necessitating postoperative follow-up. This study presents two cases illustrating the imaging features of STUMP, emphasizing the need for their identification to distinguish them from benign pathologies due to their potential for malignant behavior. Case 1: A 41-year-old woman presented with pelvic pain and menstrual irregularities. Transvaginal sonography (TVUS) revealed a large, complex uterine mass with cystic areas. While tumor markers were normal, MRI showed the mass contained cystic/necrotic regions (Figure 1), hyperintensity on T2-weighted images (T2WI), (Figure 1a-b), diffusion restriction (Figure 1d-e) in solid areas on diffusion-weighted image (DWI), and early contrast enhancement (Figure 1f). However, there was no T1WI hyperintensity suggestive of hemorrhage (Figure 1c). Histopathology confirmed multifocal necrosis with mild-to-moderate atypia, leading to a diagnosis of STUMP. Case 2: A 37-year-old woman with months of dysmenorrhea had a heterogeneous mass identified on TVUS. While tumor markers were normal, MRI revealed a mass in the uterine wall with both solid and cystic areas, hyperintensity on T2WI (Figure 2a-b), and no hemorrhagic signal on T1WI (Figure 2c). DWI showed diffusion restriction in the solid areas (Figure 2d-e), which enhanced after contrast (Figure 2f). Histopathology revealed mild atypia, necrosis, and high mitotic activity, leading to a diagnosis of STUMP. Discussion: Diagnosing STUMP remains challenging due to overlapping imaging features with leiomyosarcoma and benign cellular or degenerated leiomyomas. While MRI findings like ill-defined or irregular margins, high signal intensity on T2WI in over 50% of the lesion, and cystic-necrotic areas with marked enhancement in the solid portion can be suggestive, they aren't definitive. Thorough radiological evaluation is crucial for identifying potential STUMP characteristics in leiomyoma-like lesions that don't fit typical benign or malignant criteria.

Figure 1

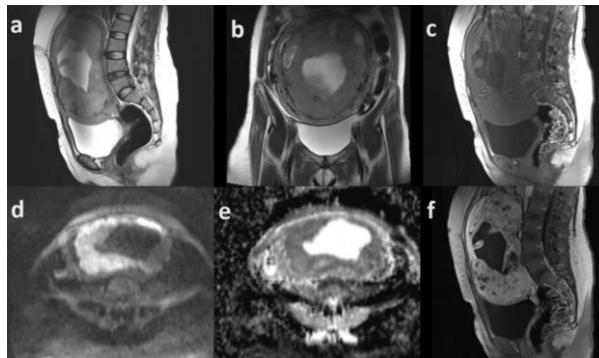


Figure 1: Uterine STUMP in a 41-year-old woman. (a) Sagittal T2 WI and (b) coronal T2 WI show an hyperintense mixed solid and cystic uterine mass, measuring 18x15x8 cm (CCxTRxAP). (c) Sagittal T1 WI showed no hyperintensity suggestive of hemorrhage. (d) Diffusion-weighted image ($b = 1000 \text{ s/mm}^2$) and (e) ADC map in the axial plane revealed diffusion restriction in solid areas. (f) Sagittal post-contrast T1-weighted MRI in the early arterial phase showed intense enhancement of the tumor's solid portions.

Figure 2

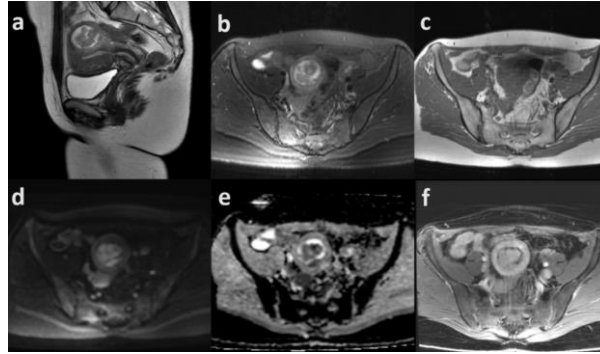


Figure 2: Uterine STUMP in a 37-year-old woman. (a) Sagittal T2WI without fat suppression and (b) axial T2WI with fat suppression show hyperintense myometrial tumor measuring 4x3.5x3.5 cm (CCxTRxAP) with cystic component. (c) Axial T1WI showed no signal of hemorrhage. (d) On high b-value diffusion-weighted images, the solid component appears markedly hyperintense and (e) diffusion restriction is detected on the ADC map in the axial plane. (f) Axial T1-weighted fat-suppressed post-contrast images demonstrate enhancement of the mass.

Keywords: smooth-muscle tumors of uncertain malignant potential, STUMP, uterine smooth-muscle neoplasms, magnetic resonance imaging

WHAT IF IT IS NOT JUST WALL THICKENING?

Gulden Karatag¹, Ahmet Topal¹

¹Canakkale 18 March University Health Practice and Research Hospital

Abstract: Gallbladder varices are a type of ectopic varices that are relatively uncommon in patients with portal hypertension [1]. Here, we present a case of gallbladder varices that was accurately diagnosed using contrast-enhanced computed tomography (CT) imaging (Fig.1) of the abdomen and confirmed by color Doppler sonography (Fig.2). A 41-year-old patient diagnosed with hepatocellular carcinoma developed portal vein thrombosis as a result of tumor progression during treatment, and incidentally, gallbladder varices were discovered. Doppler imaging has revealed the presence of gallbladder varices (Fig.2). Color Doppler sonography is a useful noninvasive technique for assessing the portal hemodynamic profile of patients with portal hypertension, as well as for detecting gallbladder varices [2]. Gallbladder varices are typically asymptomatic, however, they are associated with an increased likelihood of significant bleeding, either spontaneously or during cholecystectomy. Furthermore, it is crucial to assess patients with portal hypertension, who exhibit gallbladder varices, for potential portal vein thrombosis due to their inherent association with this condition [3]. Preoperative correct diagnosis of gallbladder varices should increase the surgeon's vigilance during biliary tract surgery in patients with portal hypertension to prevent complications [4]. In summary, gallbladder wall varices have the potential to deceive by imitating a wide range of disorders, and it is the radiologist's responsibility to differentiate gallbladder wall varices from other factors that contribute to gallbladder wall thickening. The documentation of the presence of varices is essential if patients are to undergo any surgical procedures in the abdominal region. References: 1. West MS, Garra BS, Horii SC, Hayes WS, Cooper C, Silverman PM, et al. Gallbladder varices: imaging findings in patients with portal hypertension. *Radiology*. 1991 Apr;179(1):179–82. 2. Chawla Y, Dilawari JB, Katariya S. Gallbladder varices in portal vein thrombosis. *AJR Am J Roentgenol*. 1994 Mar;162(3):643–5. 3. Gnerre J, Sun Y, Jedynek A, Gilet A. Case Report: Gallbladder Varices in a Patient with Portal Vein Thrombosis Secondary to Hepatocellular Carcinoma. *Journal of Radiology Case Reports*. 2016 May;10(5):22. 4. Mishin I. Gallbladder varices. *Rom J Gastroenterol*. 2005 Jun;14(2):165–8.

Figure 1

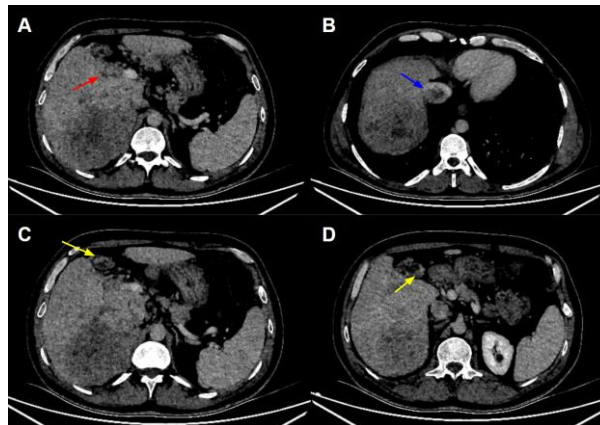
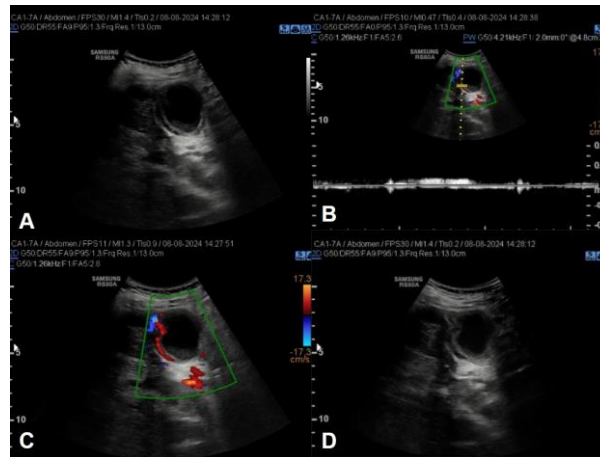


Figure 1. Contrast-enhanced abdominal CT axial images. A. Intraluminal filling defect compatible with thrombosis in the portal vein (red arrow) B. Intraluminal filling defect compatible with tumoral thrombus in the inferior vena cava (blue arrow) C-D. Thickening and serpentine enhancement in the gallbladder wall (yellow arrow).

Figure 2.



Grayscale ultrasound image demonstrates gallbladder wall thickening (A,D). Venous flow is visualized within the thickened gallbladder wall on Spectral Wave Sonography (B) with a “serpentine” pattern illustrated on Color Doppler Sonography (C).

Figure 3

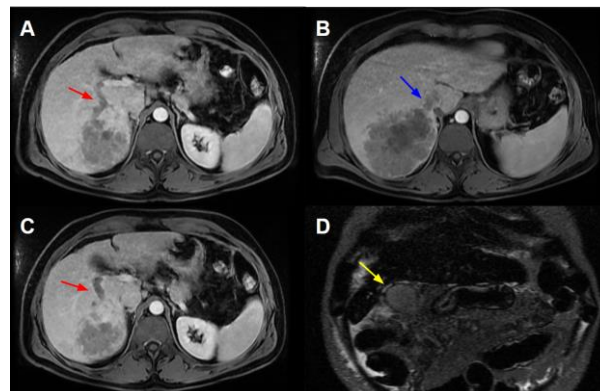


Fig.3. A-C.Intravenous contrast filling defect in the posterior branch of the right portal vein consistent with thrombosis (red arrow) and a filling defect in the inferior vena cava consistent with tumor thrombus (blue arrow). Flow-void compatible hypointense spots (yellow arrow) on the gallbladder wall in coronal T2-weighted MR images (D)

Keywords: Gallbladder varices, Portal hypertension, Portal vein thrombosis, Hepatocellular carcinoma, Color Doppler Ultrasonography

DELAYED DIAGNOSIS OF SUBCLAVIAN ARTERY PSEUDOANEURYSM FOLLOWING SUICIDE ATTEMPT IN MAJOR DEPRESSION: THE CRITICAL ROLE OF DETAILED ULTRASOUND IMAGING

Sule Ozer¹, Ahmet Topal¹

¹Canakkale 18 March University Health Practice and Research Hospital

Abstract: A 39-year-old female patient has presented to the physiotherapy department repeatedly over the past 5 years with progressively worsening pain in the right arm and shoulder. The patient, who has had persistent symptoms despite years of pharmacotherapy and physiotherapy, is referred to the cardiovascular surgery department. The cardiovascular surgery department, suspecting peripheral arterial disease, has referred the patient to the radiology department for a Doppler ultrasound of the right upper extremity. Color Doppler ultrasonography identified a 12x10 mm hypoechoic cystic structure near the right subclavian artery with a swirling flow pattern indicative of a pseudoaneurysm. CT angiography confirmed a 14 mm×12 mm×10 mm contrast-filled outpouching from the right subclavian artery, consistent with a pseudoaneurysm and without fistula formation. Subclavian artery pseudoaneurysms are a very rare condition and is most commonly caused by penetrating or blunt trauma. In particular pseudoaneurysm of the proximal right subclavian artery is a very rare condition because trauma to this area is not common [1]. Subclavian artery pseudoaneurysms are often asymptomatic and detected incidentally, but can present with symptoms like arm pain, shoulder pain, or brachial plexus compression, as seen in our patient [2]. Upon further investigation of the patient's history, it was discovered that she had been diagnosed with major depression approximately five years ago and had attempted suicide by self-hanging during that period. Given the overlap between the onset of her symptoms and the history of suicide attempt, the diagnosis was confirmed as a subclavian artery pseudoaneurysm due to blunt trauma. We aimed to emphasize the importance of a detailed clinical history and radiological evaluation in patients with long-standing undiagnosed conditions. Sometimes, radiologists need to put on their detective hats to solve the mystery hidden in the scans! References 1. Chowdhury, M. , Ahmed, S. , Haider, M. , Nine, S. , Hasan, M. and Sarker, M. (2021) Subclavian Artery Pseudoaneurysm following Stab Injury and Its Surgical Approach: A Case Report and Literature Review. World Journal of Cardiovascular Surgery, 11, 61-67. doi: 10.4236/wjcs.2021.117009. 2. Pairolero PC, Walls JT, Payne WS, Hollier LH, Fairbairn JF 2nd. Subclavian-axillary artery aneurysms. Surgery. 1981;90:757-63. [PubMed] [Google Scholar]

Figure 1

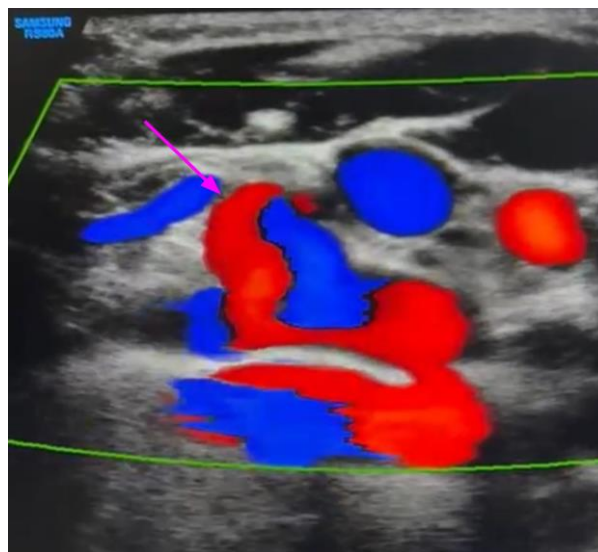


Fig 1. Color Doppler ultrasonography identified a 12x10 mm hypoechoic cystic structure near the right subclavian artery with a swirling flow pattern indicative of a pseudoaneurysm (purple arrow).

Figure 2

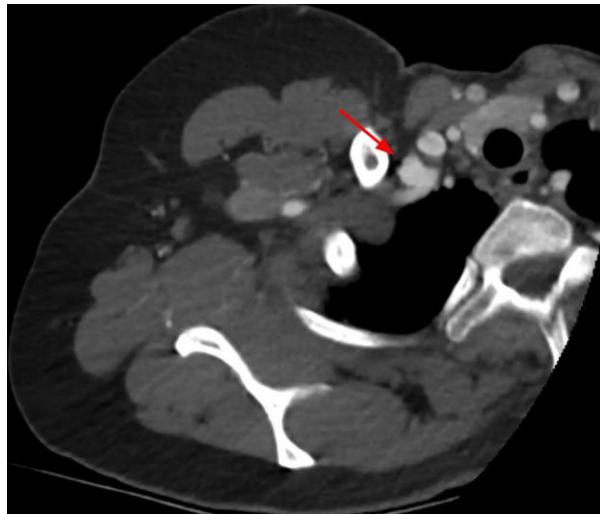


Fig 2. CT angiography confirmed a 14 mm×12 mm×10 mm contrast-filled outpouching from the right subclavian artery, consistent with a pseudoaneurysm and without fistula formation (red arrow).

Figure 3



Fig 3. CT angiography 3D reconstructive coronal image confirmed a 14 mm×12 mm×10 mm contrast-filled outpouching from the right subclavian artery, consistent with a pseudoaneurysm and without fistula formation (yellow arrow).

Keywords: Color Doppler Ultrasonography, CT Angiography, Subclavian Artery Pseudoaneurysm

INTRAPERITONEAL PREGNANCY: A TICKING TIME BOMB IN THE ABDOMEN - A CRITICAL DIAGNOSTIC CHALLENGE

Gulden Karatag¹, Saner Esmer¹

¹Çanakkale Onsekiz Mart University Hospital

Abstract: Intraperitoneal pregnancy is exceptionally rare and life-threatening form of ectopic pregnancy where fertilized ovum implants within peritoneal cavity rather than the uterus. This condition poses significant diagnostic challenges due to atypical presentation and potential for severe maternal complications. Early diagnosis through imaging is crucial for effective management and improved outcomes. 29-year-old woman, gravida 2, para 0, abortus 1, presented to the emergency department at 16 weeks and 1 day of gestation with absent fetal movements. Her medical history included a previous miscarriage. Ultrasonography confirmed the absence of fetal cardiac activity, leading to a diagnosis of missed abortion. Anemia was detected in laboratory tests, requiring her admission for treatment. Initially, a contrast-enhanced abdominal CT scan at the first facility revealed a large lesion measuring 18.5 x 16 x 18.5 cm, containing a fetus with a crown-rump length of 9.5 cm and placental tissue. The fetal bones were poorly visualized, and high-density area near the placenta suggested possible venous pooling or extravasation. Surrounding the fetus and placenta was a heterogeneously dense area up to 5.5 cm thick, raising concerns of hemorrhage. The bladder was displaced with a reduced anteroposterior diameter, and multiple air-fluid levels and a feces sign were noted in adjacent bowel loops. Subsequent surgery at an outside facility confirmed a right ovarian ectopic pregnancy. Intraperitoneal pregnancy, while rare, should be considered in cases with atypical pregnancy presentations and complex imaging findings. A systematic review by Poole A et al. on abdominal pregnancies treated before 20 weeks of gestation reported an average treatment age of 10 weeks, with common early locations being uterine pouches and serosal surfaces. Comprehensive review by Machado et al. highlighted that despite early ultrasound use, diagnosis can be missed without high suspicion and skilled imaging, and MRI can be useful when ultrasound results are inconclusive. MacDonald et al. noted the increasing use of CT in emergency settings for abdominal pain, emphasizing the need for radiologists to recognize ectopic pregnancy features on CT. This case underscores critical role of imaging in diagnosing obstetric conditions and the necessity for radiologists to collaborate closely with obstetric teams for optimal management and outcomes.

Fetal Osseous Structures



Coroner Section of Abdominal CT

Venous Pooling



Axial Seciton of Abdominal CT

Keywords: abdominal pregnancy, ectopic pregnancy, Intraperitoneal pregnancy

AN UNCOMMON CAUSE OF ABDOMINAL PAIN: HUGE GASTRIC BEZOAR

Merve Başdemirci¹, Onur Başdemirci¹

¹Department of Radiology, Karabük Training and Research Hospital

Abstract: INTRODUCTION: Bezoar is the general term for structures that form due to the accumulation of indigestible substances in the gastrointestinal tract(GI). Bezoars are classified into four main groups according to their content: trichobezoar, phytobezoar, pharmacobezoar and lactobezoar. The most common types of bezoars are trichobezoars and phytobezoars[1]. Bezoars are benign but rare conditions that can cause GI obstruction due to the mass effect and ulceration and perforation due to mucosal irritation[2]. With this case report, we aimed to provide information and raise awareness about bezoars.CASE:A 15-year-old female patient presents to the emergency department with complaints of abdominal pain, vomiting, and abdominal bloating. On physical examination, there was a palpable, painless mass at the left upper quadrant. On direct abdominal radiography mottled opacity (white arrows), conforming to the shape of the stomach and partially surrounded by gastric air was seen(Figure1). Abdominal computed tomography(CT) images showed a mass-like structure containing air bubbles consistent with bezoar, causing distension in the stomach and filling the stomach lumen(Figure2). Because trichobezoar could not be removed endoscopically, it was removed by operation(Figure3). DISCUSSION: Trichobezoars are generally seen in young women. Its etiology includes a history of stomach surgery or psychiatric diseases[1,3,4]. Bezoars can be located in any part of the gastrointestinal system, but as in our case, they are most commonly located in the stomach[4,5]. They are mostly asymptomatic in the early stages. However, as they increase in size, they can cause abdominal pain, weight loss, vomiting, and abdominal bloating[6].In these patients presenting with vague clinical findings, a good anamnesis and physical examination are guiding, but radiological findings are used in diagnosis. The first radiological method in diagnosis is direct radiography. Other radiological methods are ultrasonography and CT, with CT being the modality with the highest diagnostic power. CT has an important place both in diagnosis and in imaging possible complications[7]. They may present with clinical findings related to obstruction, but in undiagnosed, delayed or untreated cases, they may lead to adverse outcomes such as ulceration, perforation and even death[8]. Therefore, knowing and recognizing the imaging features of bezoar cases is important to prevent delay in diagnosis.

Figure 1

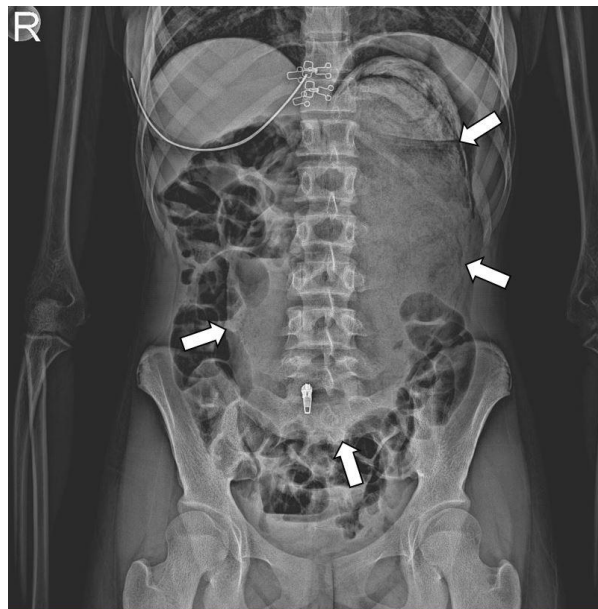


Figure 1: Direct abdominal radiography shows a mottled opacity (white arrows), conforming to the shape of the stomach and partially surrounded by gastric air. Also, this opacity was causing the displacement of intestinal loops.

Figure 2

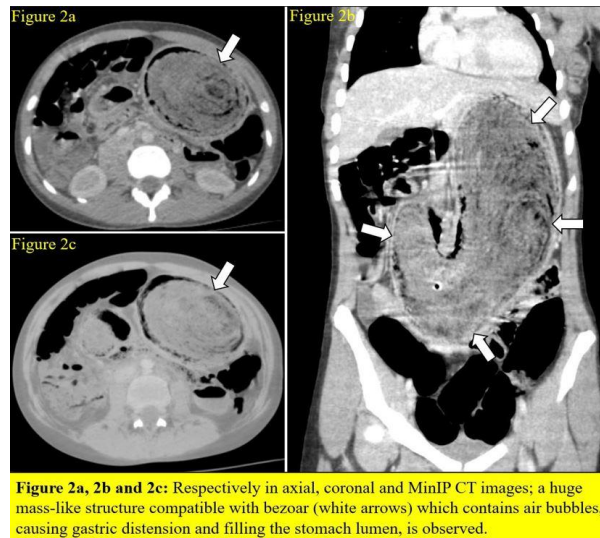


Figure 3



Keywords: Bezoar, Gastric Bezoar, Abdominal Pain, Trichobezoar

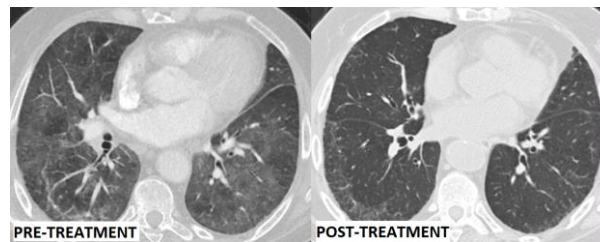
LUNG INVOLVEMENT IN RHEUMATOID ARTHRITIS: RADIOLOGICAL APPROACH

Nihal Deniz Menten¹, Serhat Akis¹, Sinem GEZER¹

¹Dokuz Eylul University

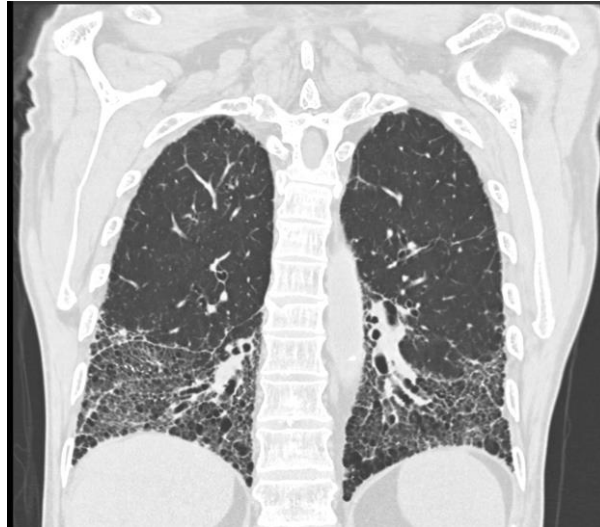
Abstract: **INTRODUCTION** Rheumatoid arthritis (RA) is a systemic autoimmune disease primarily known for its joint involvement, yet it significantly impacts pulmonary health, manifesting in various forms such as interstitial lung disease (ILD), pulmonary nodules, and follicular bronchiolitis. This abstract summarizes the pulmonary manifestations associated with RA, emphasizing their clinical relevance and underlying mechanisms. **DISCUSSION** Interstitial lung disease is one of the most serious pulmonary complications in RA, often presenting as usual interstitial pneumonia or nonspecific interstitial pneumonia. Patients may experience symptoms like dyspnea and chronic cough, which can precede or coincide with joint symptoms. The pathophysiology of ILD in RA is linked to chronic inflammation and immune dysregulation, which may be exacerbated by environmental factors and the effects of immunosuppressive therapies. Pulmonary nodules, commonly referred to as rheumatoid nodules, are another frequent manifestation, occurring in approximately 20-30% of RA patients. These nodules are typically subcutaneous but can also appear in the lungs, where they may cavitate and lead to complications such as pneumothorax. Follicular bronchiolitis, characterized by the proliferation of lymphoid follicles in the bronchioles, is less common but can occur in RA patients, contributing to airway obstruction and respiratory symptoms. **CONCLUSION** Overall, pulmonary manifestations of RA are significant contributors to morbidity and mortality, necessitating vigilant monitoring and management. Understanding these complications is crucial for improving patient outcomes and guiding therapeutic strategies in rheumatoid arthritis management.

BRONCHIOLITIS OBLITERANS



66 y/o F w RA, Shortness of breath. Pretreatment CT shows thickening of the interlobular septums in both lungs, diffuse reticular density increase predominantly peripheral, and peribronchovascular thickening, accompanied by large ground-glass densities, interface findings. Patient was evaluated compatible with Bronchiolitis Obliterans and Interstitial Lung Disease exacerbation. After the treatment, the patient's clinical condition improved and he was discharged. HRCT performed for follow-up showed regression in the appearance of diffuse ground glass density in both lungs in the previous examination. The appearance of bronchiolitis obliterans is similar.

INTERSTITIAL LUNG DISEASE - UIP



53 y/o M, RA diagnosed HRCT shows coarse reticular pattern density increases in the middle-lower zones of both lungs, predominantly in the basal segments, diffuse ground-glass density increase in these levels, some consolidation findings in the peripheral parts, and structural distortion in the parenchyma. There are diffuse cystic formations in the basal segments of the lower lobe which may be compatible with bronchiolectasis and is compatible with interstitial lung involvement (UIP) of rheumatoid arthritis

NECROBIOTIC NODULE



57 y/o M w RA Imaging revealed multiple necrobiotic nodules with fibrocatricular changes, the largest of which was observed in the right lung lower lobe superior segment.

Keywords: rheumatoid nodule, rheumatoid arthritis, lung, radiology, usual interstitial pneumonia

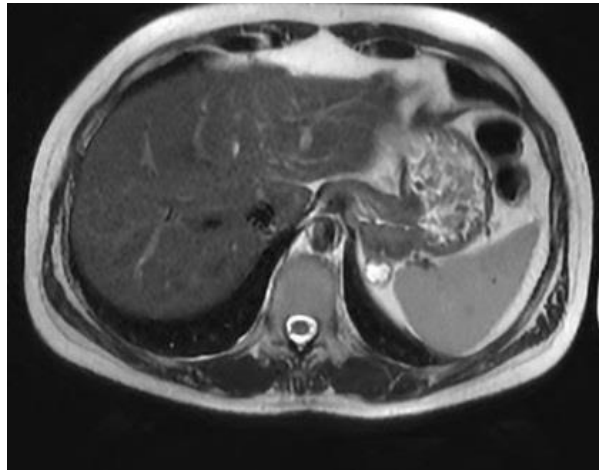
GASTRIC DIVERTICULUM

Jasmina Kovacevic¹

¹Health Center Valjevo, General Hospital Valjevo

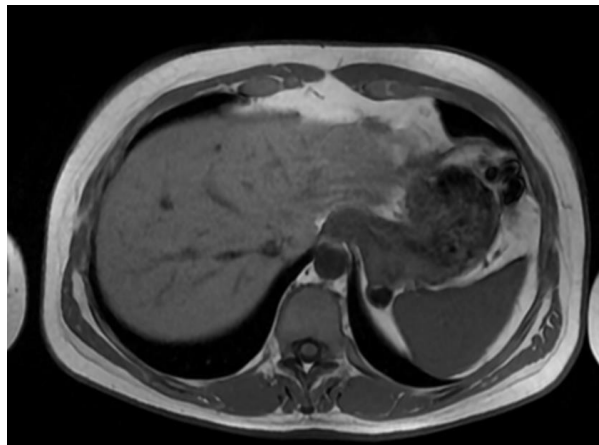
Abstract: Gastric diverticula is rare form of diverticular disease. Gastric diverticula are sac-like outpouchings that most commonly originate from the posterior surface of the gastric fundus. They are usually incidental finding with incidence less than 0, 11 % at endoscopy. The patients are asymptomatic or have stomachache or stomach bloating and discomfort immediately after meal. They may be congenital as true diverticula that have all layers of the gastric wall or acquired as false diverticula and arise virtually anywhere along the stomach. Diagnostic procedures are: endoscopy, fluoroscopy, CT or MRI. Surgical treatment is needed when they are big. This case is about young woman, 41 years old, with long history of stomach discomfort and fullness after meal. She did pelvic MRI six years ago, which shown ovarian cyst. Now, because of the above symptoms, she was performed abdominal and pelvic MRI. Pelvic MRI was the same. On abdominal MRI tomograms, a cystic lesion in contact with gastric fundus and left adrenal gland was shown. The fundus wall was hypertrophic due to spasm. The gastric diverticula was diagnosed. Confirmation of the diagnosis was made fluoroscopically, to distinguish gastric diverticulum from eventual cystic lesion of left adrenal gland which was differential diagnose.

MRI t2w axial plane



t2w axial plane image shows hyperintense lesion (due to gastric fluid) in contact with gastric fundus and left adrenal gland. Gastric wall in that region is hypertrophic due to spasm. The lesion is gastric diverticulum

MRI t1w axial plane



t1w axial plane shows hypointense lesion (due to gastric fluid) in contact with gastric fundus and left adrenal gland. Gastric wall in that region is hypertrophic due to spasm. The lesion is gastric diverticulum

fluoroscopy



Small outpouching arising from the fundus of the stomach- gastric diverticulum

Keywords: Gastric diverticulum

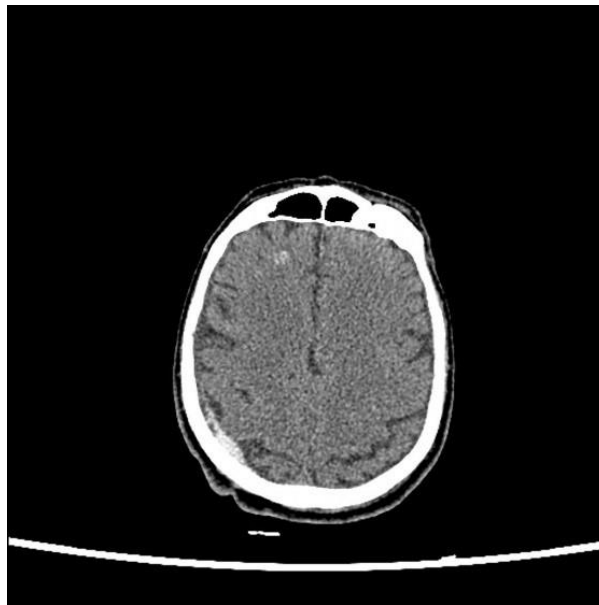
PRIMARY PATHOLOGY OR SECONDARY? DISSEMINATED INTRAVASCULAR COAGULOPATHY WITH DIFFERENTIAL DIAGNOSIS

Ayşe Ozkan¹, Seda Sogukpınar Karaagac¹, Gulseher Saylan¹

¹Department of Radiology, Faculty of Medicine, Firat University, Elazığ, Turkey

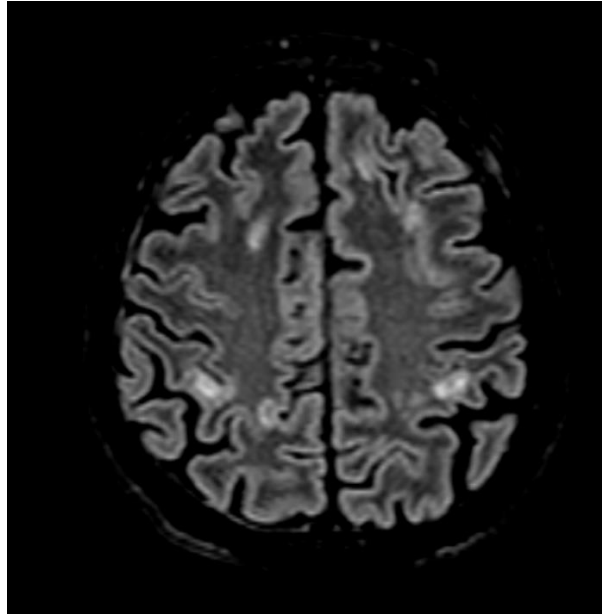
Abstract: A 64-year-old male patient was operated 5 days ago with a diagnosis of bladder cancer (CA). He could not be extubated because of haematemesis and confusion during extubation. The patient is followed up in the intensive care unit with a prediagnosis of oesophageal rupture and sepsis. Cranial computed tomography (CT) of the patient showed subdural haemorrhage and parenchymal haemorrhage areas, more prominent in the juxtacortical area (Figure 1). Cranial magnetic resonance imaging (MRI) was performed with suspicion of metastasis in the patient with a diagnosis of bladder CA. On brain MRI, multiple hyperintense foci were noted on T2, FLAIR sequences (Figure 2a). On SWI sequence, scattered juxtacortical localised hypointense haemorrhage areas are observed (Figure 2b). Diffusion restriction and no contrast enhancement after IV contrast agent are detected in the lesions. Given the patient's history of CA, metastasis was considered as a potential differential diagnosis. However, this was excluded on the basis of the absence of pathology in the preoperative images and the lack of evidence that the defined CA type causes haemorrhagic metastasis. Since the patient was in the intensive care unit, no growth was detected in blood and urine cultures. Septic embolism is excluded because white blood cell values are also normal. However, the elevated D-dimer levels, abnormal coagulation parameters, the prolongation of the intensive care period and the concomitant occurrence of subdural haemorrhage with parenchymal haemorrhage indicate the potential involvement of immunological mechanisms and associated disseminated intravascular coagulopathy (DIC). DIC is a life-threatening systemic syndrome characterised by activation of systemic intravascular coagulation, which may be triggered by various underlying diseases, leading to thrombosis and haemorrhage and multiple organ failure. Thrombosis in small and medium vessels and parenchymal haemorrhages in vital organs such as the brain may be observed in the disease.

Figure 1



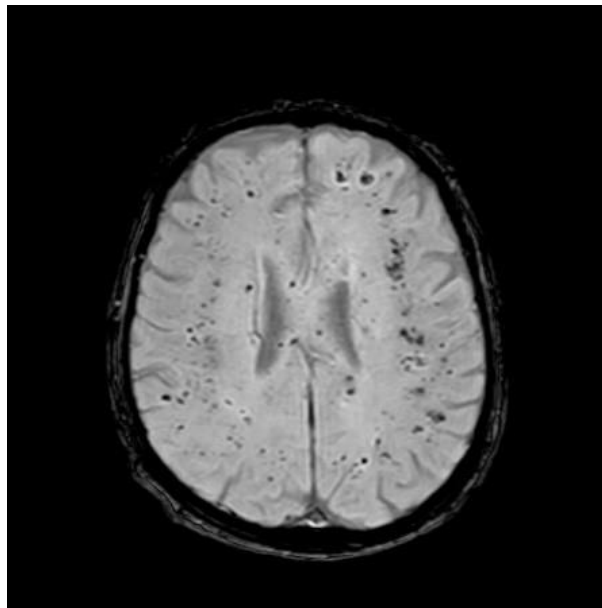
CT image of subdural and parenchymal haemorrhages

Figure 2a



FLAIR and SWI sequence of parenchymal haemorrhages

Figure 2b



FLAIR and SWI sequence of parenchymal haemorrhages

Keywords: Hemorrhage, Disseminated intravascular coagulopathy, Subdural

HEPATIC GAS GANGRENE: TWO CASES OF A RARE POST - OPERATIVE COMPLICATION

Anna Simichanidou¹, Nikolaos Bouras¹, Vasiliki Alexiadou¹, Melpomeni Kosmidou¹,
Ekaterini Xinou¹, Eleni Karoglou¹

¹Radiology Department, Theagenio Cancer Hospital, Thessaloniki, Greece

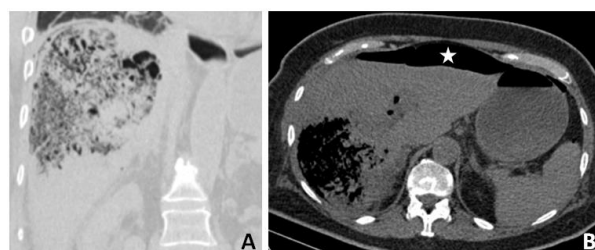
Abstract: Hepatic gas gangrene constitutes a rare entity characterized by a cascade of catastrophic conditions comprising sepsis, multi – organ failure and high mortality. It is the result of a fulminant infection of liver parenchyma by intestinal bacteria, typically anaerobic, in the setting of extensive ischemic injury. Usually, it is preceded by a surgical procedure, such as hepatic and biliary interventions or liver transplantation. Less often, it may be post – traumatic or spontaneous. Predisposing factors include immunosuppression, diabetes mellitus, neoplastic disease and infection of neighbor organs. Hepatic gas gangrene requires early diagnosis and urgent care, despite lacking specific clinical features. Typical imaging findings, such as the emphysematous pattern of hepatic damage and the compromise of both arterial and portal blood supply, render computed tomography (CT) an indispensable tool that allows prompt diagnosis. Treatment consists of surgical debridement of the necrotic liver tissue and intensive antibiotics administration. Despite the aggressive treatment, the condition is usually lethal. Hereby, we present two cases of post – operative hepatic gas gangrene. The first case, a 73 – year – old woman with pancreatic cancer, presented with high fever and clinical deterioration a month after liver metastasectomy. Abdominal CT revealed a well – defined hypoenhancing area in the periphery of the liver parenchyma, which was misdiagnosed at first as a post-operative subcapsular air-fluid collection. In a closer look, an emphysematous interstitial pattern of injury was depicted and both right portal vein and the respective branch of right hepatic artery were found to be interrupted. The placement of a drainage tube was almost futile, confirming the diagnosis (figure 1). The second case, a 60 – year – old woman with pancreatic cancer presented with abdominal pain and rapidly evolving multi – organ failure a day after radiofrequency ablation of a hepatic metastasis. The abdominal x – ray revealed free intraabdominal air and a large air collection projecting within the liver outline. CT confirmed the presence of pneumoperitoneum and revealed an interstitial air pattern within the anticipated area of ablation, as well as pneumobilia and air in the portal veins (figure 2). Both aforementioned cases were fatal.

Figure 1



A well – defined hypoenhancing area can be readily appreciated in the right liver lobe. The emphysematous pattern of damage with the presence of air within the hepatic parenchyma (A – C), as well as the abrupt interruption of both the right portal vein (A) and the respective branch of the right hepatic artery (B) constitute the imaging hallmarks of the diagnosis.

Figure 2



Air can be appreciated within the hepatic parenchyma, the biliary tree and the portal veins. Spontaneous pneumoperitoneum (star) can also be seen. No fluid collection is seen within the affected area.

Keywords: gas gangrene, interstitial air

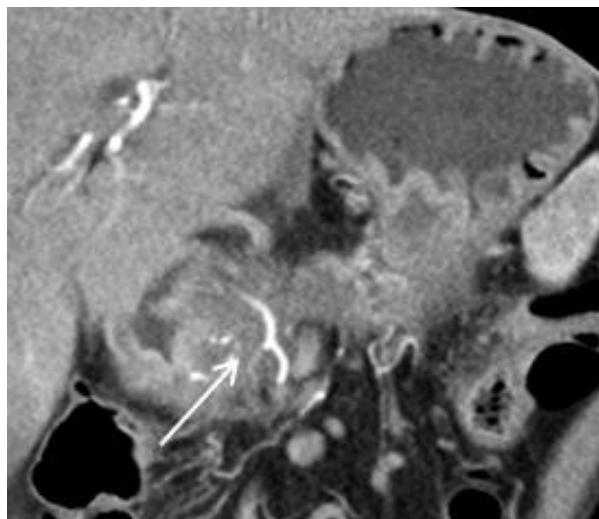
PANCREATIC DUCTAL ADENOCARCINOMA AND MIMICS: TIPS TO AVOID MISDIAGNOSIS IN COMPUTED TOMOGRAPHY

Anna Simichanidou¹, Nikolaos Bouras¹, Ekaterini Xinou¹, Eleni Karoglou¹

¹Radiology Department, Theagenio Cancer Hospital, Thessaloniki, Greece

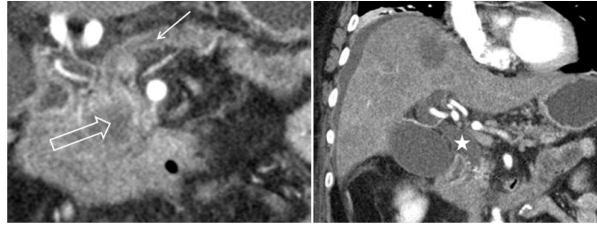
Abstract: Introduction: Pancreatic ductal adenocarcinoma (PDAC) is the most common pancreatic neoplasm, characterized by a low survival rate. PDAC is often overdiagnosed, leading to unnecessary procedures and high morbidity. Atypical imaging presentations of neoplastic and inflammatory diseases of the pancreas may mimic PDAC. Hereby, we present computed tomography (CT) key findings that can assist correct diagnosis. Results: PDAC typically appears as a hypovascular mass, usually located at the pancreatic head, causing abrupt disruption of the common bile duct and the main pancreatic duct (PD) with upstream dilation of both (“double – duct sign”). The mass encases and infiltrates vessels and other neighbouring structures and it results to atrophy of the peripheral pancreatic parenchyma. The second most common pancreatic neoplasms are neuroendocrine tumors (NETs), which are typically hypervascular and accompanied by hypervascular liver metastases, as well. They may sometimes appear as non – hypervascular lesions, however they usually have smooth margins, without infiltrating phenomena or significant duct dilation. Metastases may be misdiagnosed as PDAC when they are hypovascular, such as in cases of lung cancer, or become large enough to produce mass effect on the PD. However, they usually present as small, non – obstructive lesions with smooth margins and hypervascularity, since renal cell carcinoma still consists the most common primary site. Autoimmune pancreatitis (AIP) is a type of chronic pancreatitis that may seldom appear with a focal form not accompanied by the typical ancillary extrapancreatic manifestations and high IgG4 serum levels. Nevertheless, it is typically penetrated by the PD without causing significant dilation and it exhibits delayed enhancement with a hypoenhancing rim. Groove pancreatitis may also simulate PDAC, since it corresponds to mass – like soft tissue with irregular margins and fat stranding. Important aspects here are the preserved vessels within the mass and the widening of the space between CBD and PD, without them being obstructed. Conclusion: Many pancreatic lesions may mimic PDAC creating intractable diagnostic problems. Hence, awareness of discriminative CT features is of great importance in order to achieve diagnosis and avoid harmful procedures.

Figure 1



A soft tissue mass – like lesions is recognized in the pancreatoduodenal groove surrounding the pancreatic vessels without infiltrating them (arrow). This is a case of groove pancreatitis.

Figure 2



A hypoenhancing mass is recognized in the pancreatic head (open arrow) causing obstruction and dilation of the main pancreatic duct (arrow) and the common bile duct (star), also known as “double – duct sign”. Furthermore, excessive atrophy of the peripheral pancreatic parenchyma, as well as multiple liver metastases are apparent.

Keywords: CT, NET, pancreatitis, PDAC

ACUTE AORTIC SYNDROME: GENERAL RADIOLOGICAL OVERVIEW WITH CASES

Merve Başdemirci¹, Onur Başdemirci¹

¹Department of Radiology, Karabük Training and Research Hospital

Abstract: INTRODUCTION: Acute aortic syndrome (AAS) describes a spectrum of life-threatening emergent aortic pathologies[1]. This spectrum includes aortic dissection (AD), intramural hematoma (IMH), and penetrating atherosclerotic ulcer (PAU). AIM: We aimed to present the diagnostic features of this spectrum, which requires rapid diagnosis and treatment due to its mortality, with the cases in our clinic (Figure 1-3). DISCUSSION: Patients with AAS usually present with symptoms such as acute onset severe chest and back pain. Clinical distinction between AAS types cannot be made because the symptoms are similar. Therefore, radiological diagnostic imaging is used in the diagnosis of AAS, determination of its type and severity, and detection of accompanying complications[2,3]. CT Angiography (CTA) is the preferred imaging method in diagnosis because it's easily accessible and fast. The point that distinguishes PAU from ulcerated plaque is that it exceeds the internal elastic lamina, and radiologically it is observed as extra filling that exceeds the intimal calcification and usually causes overflow in the contour. IMH is the name given to bleeding in the media layer. IMH is radiologically observed as a crescent-shaped, high-density wall thickening in the non-contrast series and is diagnosed by the absence of contrast filling in the post-contrast series. AD occurs when blood passes through the tear in the intima layer and progresses into the media layer, creating a false lumen. AD is the most common type of AAS and it's diagnosed radiologically by visualizing the intimal flap and false lumen[4]. It's important to specify where the dissection start/endpoint, which branches originate from false lumen, its extension to aortic branches, and complications when radiologic reporting. Since it changes the treatment approach in AAS, classification is made according to the affected areas in the aorta and most commonly used method is the Stanford classification[5]. The basic anatomical point in the classification is whether the ascending aorta is involved or not. In type-A dissection with proximal involvement, the treatment method is emergency surgery, while endovascular treatment is performed in type-B dissection[6]. CONCLUSION: In conclusion, AAS is a pathology with high mortality and requires rapid diagnosis and treatment. It's important to be able to differentiate radiologically and to know the issues to be considered in reporting.

Figure 1



Figure 2

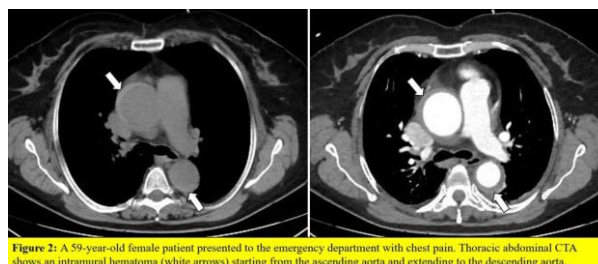


Figure 3

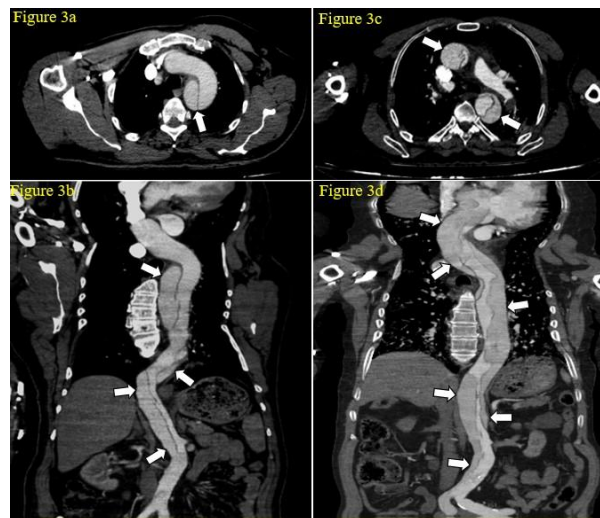


Figure 3a and 3b: A 50-year-old male patient presented to the emergency department with complaints of severe back and chest pain. Respectively in axial and curved planar reformat CT angiography images revealed a dissection (white arrows) starting from the distal of the left subclavian artery origin and extending to the iliac arteries (Stanford type B). **Figure 3c and 3d:** A 71-year-old male patient presented to the emergency department with severe chest pain. Respectively in axial and curved planar reformat CT angiography images show a dissection (white arrows) starting from the ascending aorta and extending to the iliac arteries (Stanford type A).

Keywords: Acute Aortic Syndrome, Aortic Dissection, Intramural Hematoma, Penetrating Atherosclerotic Ulcer, CT Angiography

PROXIMAL STENT HOLDER FRACTURE: A RARE COMPLICATION OF ENDURANT II® AORTIC STENT- GRAFT

Celal Caner Ercan¹, Sait Kayalı¹, Edanur Karapınar¹, Zeynep Nur Akyol Sarı¹, İbrahim Demir², Bülent Acunaş¹

¹Istanbul University, Medical Faculty of Istanbul, Department of Radiology, Istanbul, Turkey

²Kirsehir Education and Research Hospital, Department of Cardiovascular Surgery, Kirsehir, Turkey

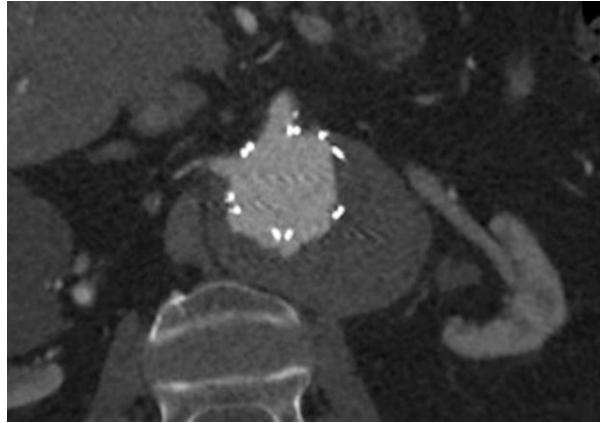
Abstract: Aims: Aortic stent-grafts are being used to treat abdominal aortic aneurysm (AAA) for three decades. According to literature stent fractures are rarely reported. Here we aim to present a case report of a rare aortic stent-graft failure and a review of the literature. Case: A 79-year-old male patient previously treated with Medtronic Endurant II® for AAA four years ago, now presents with a growing right common iliac artery (CIA) aneurysm. Although the EVAR procedure was successfully performed without CIA aneurysm, the patient has since developed a CIA aneurysm and is referred for endovascular repair. During the endovascular graft limb extension procedure for that, fracture and down migration were observed in the proximal part of the aortic stent (Figure 1). Digital subtraction angiography (DSA) images show free moving of separated parts but there was no type 1a endoleak. Medtronic stent-graft was placed to treat right iliac artery aneurysm. After extension placement, DSA images showed no endoleak at neither proximal part of AAA nor right iliac site. Since the neck of the infrarenal AAA became widened over time, there was no adequate size of aortic extension graft to cover fracture site. Open surgery, endoanchor implants, chimney eva techniques were considered as other treatment options. Due to risk factors related both the patient and procedure itself, open surgery was excluded. Endoanchor treatment requires safe attachment sites between graft and aortic wall which is not possible for our patient since there was intraluminal thrombus formation in between due to migration (Figure 2). Since there was no endoleak, conservative approach with close follow-ups was preferred. Conclusions: The proximal end of the Endurant II®, stent-graft is composed of nitinol stents (which is not covered with graft fabric) sewn to a fabric graft. Uncovered stent part also contains two anchor pins for each stent crown. To illustrate fracture site better, we also prepared a digitally edited image (Figure 3). Stent holder fractures are rare but possible complication even in new generation stent-grafts. In relation to that migration, type 1a endoleak, aneurysmal sac enlargement and rupture can be seen. Management should be planned depending on clinical symptoms, radiological findings and patient characteristics.

Fracture of the stent



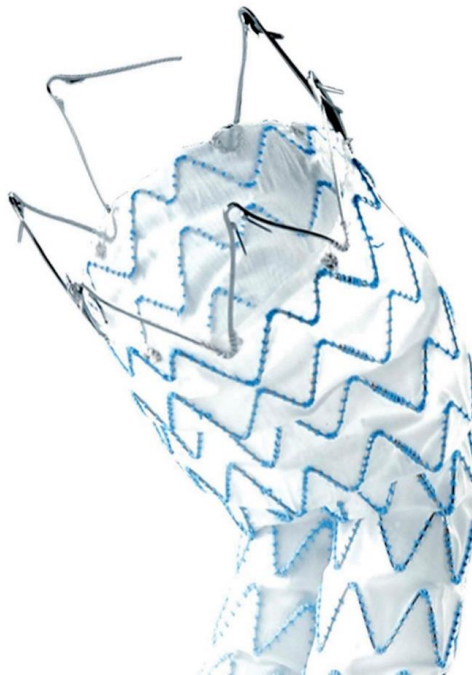
Fluoroscopy shows the fracture of the stent.

Intraluminal thrombus between graft and aortic wall



Axial CT image shows intraluminal thrombus between graft and aortic wall. Due to the presence of thrombus formation, the patient was considered unsuitable for endoanchor therapy.

Digitally edited image of the case



Digitally edited image of the case. To better illustrate and present the condition, edited visual representation has been created using digital editing programs.

Keywords: stent fracture, aortic intervention complications, stent-graft migration, EVAR

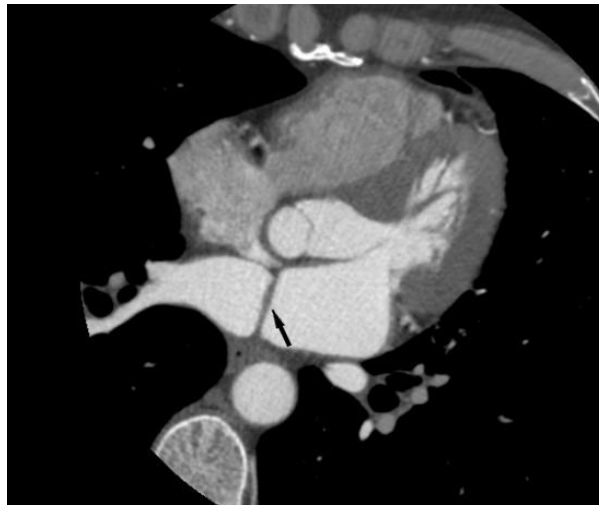
LEFT ATRIAL BAND; A RARE CONGENITAL ANOMALY

Yeliz Aktürk¹, Rasime Pelin Kavak¹

¹*Etlik City Hospital, Department of Radiology*

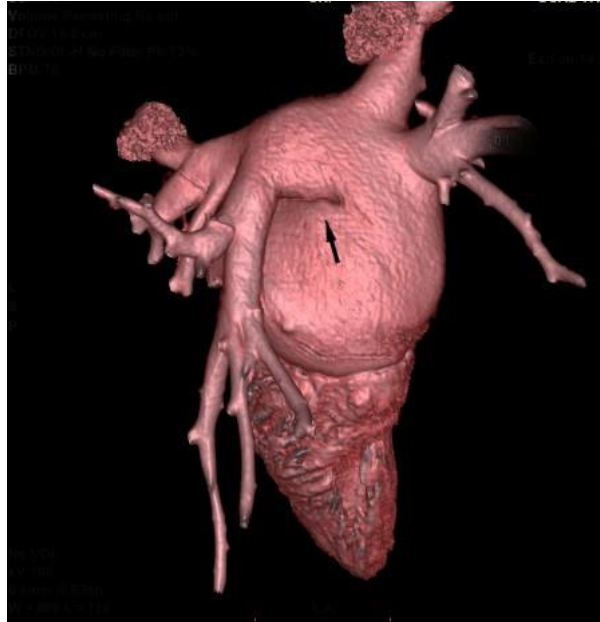
Abstract: Introduction Although its clinical significance is not yet fully understood, left atrial band may be associated with the presence of Chiari network, premature atrial complexes, patent foramen ovale, mitral valve prolapse/insufficiency and cardioembolic attacks. It is important to be aware of their presence, as misinterpretation of images can lead to inappropriate medical or surgical treatment. Coronary CT angiography (CCTA) plays an important role in defining the anatomy of the left atrium and associated abnormalities. CT localizes the course of the atrial bands anatomically and their relationship with the mitral valve can be evaluated. Case report Our case was a 38-year-old female patient who applied with the complaint of chest pain. In the CCTA performed, a linear fibrous band measuring 2.2 mm at its thickest point was detected, extending from the posterior wall of the left atrium to the middle part of the interatrial septum. No other anomaly or variation was detected. This anomaly was detected in two cases of 2000 CCTA examinations in our radiology department, and our incidence rate was 0.1%. We present one of the two cases with abnormal atrial band findings which were detected incidentally and their anatomical features and courses were well described by CCTA. Discussion Abnormal muscular bands in the left atrium were first described at the end of the 19th century. Their incidence has been reported as 2% in autopsy cases (22/1100). In 86.4% of these cases, a fibrous band was identified between the left atrial side of the fossa ovalis and other areas of the left atrial endocardium (1). They have fibrous and muscular components and are usually detected incidentally (2). References 1. Yamashita T et al. Prevalence and clinical significance of anomalous muscular band in the left atrium. *Am J Cardiovasc Pathol* 1993;4:286–932. Pizzuti A et al. Left Atrial Anomalous Muscular Band: Case Report, Literature Review, and Role of Three-Dimensional Echocardiography *J Cardiovasc Echogr* 2023 Jan-Mar; 33:51–

Figure 1



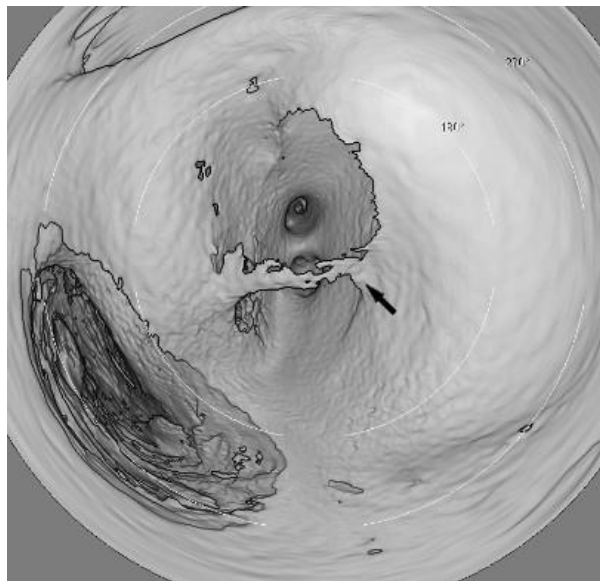
Axial CT angiography image. A linear fibrous band was detected, extending from the posterior wall of the left atrium to the middle part of the interatrial septum (black arrow)

Figure 2



3D reconstructed image of cardiac CT angiography. Linear fibrous band (black arrow) in the left atrium

Figure 3



Virtual endoscopic image obtained from cardiac CT angiography images. Fibrous structure in the left atrium (black arrow)

Keywords: atrium, fibrous band, CT angiography

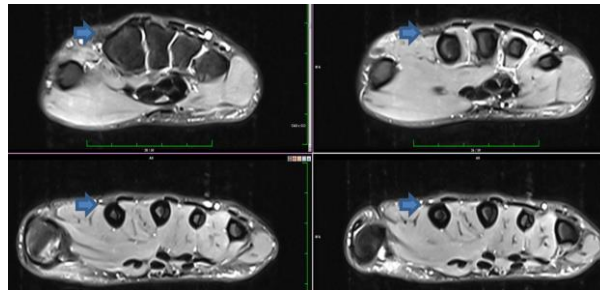
EXTENSOR DIGITORUM BREVIS MANUS MUSCLE; A RARE VARIANT

İbrahim Çağrı Tural¹

¹Necipfazıl State Hospital, K.Maras Turkey

Abstract: Introduction: The extensor digitorum brevis manus muscle (EBDM) is a short muscle located on the dorsum of the hand, occurring as an extensor muscle anomaly. It causes pain with movement and can be confused with a ganglion cyst due to the soft swelling created by the muscle body. Case: 20-year-old girl, suffering from pain in her wrist applied to ortopedics clinic. On examination, it was seen that the swelling was close to the wrist level. The patient complained of pain in the swelling area that increased with movement. On palpation, a mass with a soft consistency that felt like a cystic lesion was detected on the dorsum of the hand. She underwent an MRI due to an atypic ultrasound appearance on Ultrasound. MRI was reported as accesorry extensor digitorum brevis manus muscle inserting to 2nd digit (Figure 1) Discussion: Accessory extensor digitorum brevis manus muscle is a normal variant seen on dorsum of the hand. It is seen approximately 2-5% of the population (1) . The EDBM originates from the dorsal wrist capsule or posterior radiocarpal ligament passes through 4th dorsal wrist compartment and inserts to extensor hood of 2nd, 3rd or 4th digits. Dorsal soft mass is often confused with ganglion cyst and tenosynovitis . In addition, extensor indicis proprius muscle, which causes similar swelling and causes compression findings in the extensor retinaculum similar to EDBM muscle anomaly, and another extensor muscle anomaly, extensor digiti minimi proprius muscle, should be kept in mind in the differential diagnosis. Ultrasound is primary radiological method whereas MRI is crucial for extend and contiguity of the muscle due to its soft tissue resolution and discrimination (2) .References1-Ogura T, Inoue H, Gozo T. Anatomic and clinical studies of the extensor digitorum brevis manus muscle. J Hand Surg 1987; 12(1):100-7.2-2. Anderson M, Benedetti P, Walter J, Steinberg D. MR Appearance of the Extensor Digitorum Manus Brevis Muscle: A Pseudotumor of the Hand. AJR Am J Roentgenol. 1995;164(6):1477-9.

Figure 1



PD MRI images of accesorry extensor digitorum brevis manus muscle inserting to 2nd digit

Keywords: accessory muscle, hand, MRI

INFERIOR VENA CAVA DUPLICATION – A CASE REPORT

Merve Başdemirci¹, Onur Başdemirci¹

¹Department of Radiology, Karabük Training and Research Hospital

Abstract: INTRODUCTION-AIM: Inferior vena cava (IVC) duplication is a rare congenital vascular anomaly. Its frequency in the literature has been reported as %0.1-3.5 [1]. IVC duplication is usually asymptomatic and detected incidentally during intraoperative or diagnostic imaging. However, diagnosing this anomaly may be critical during retroperitoneal surgery and venous interventional radiologic procedures[2-3]. We aimed in this article to present a case of IVC duplication and inform about this. CASE: A 74-year-old male patient was admitted to General Surgery clinic with complaints of abdominal pain. In the axial CT image, right and left IVC are observed on both sides of the abdominal aorta (Figure 1). Coronal MIP and 3D reconstructed CT images revealed the presence of the IVC on both sides of abdominal aorta at the infrarenal level, and showed that left renal vein drains to the left IVC (Figure 2). DISCUSSION: The IVC develops as a result of a complex process that involves the formation and regression of three pairs of primitive veins (posterior cardinal, subcardinal, and supracardinal veins) embryologically between the 7th and 10th weeks of gestation. Posterior cardinal veins are initially formed and give rise to distal IVC, which is the iliac bifurcation. Subcardinal veins then form and the left subcardinal vein regresses, while the right subcardinal vein forms the supracardinal IVC. Finally, supracardinal veins are formed and left supracardinal vein regresses, while the right supracardinal vein forms the infrarenal IVC [3-6]. Various anatomical venous anomalies occur due to differences that may occur at any stage of this complex process. In the literature, some anomalies such as IVC duplication, left IVC, retroaortic left renal vein, circumaortic left renal vein, continuity of IVC with azygos have been reported as major anomalies[5]. IVC duplication occurs due to the left supracardinal vein's failure to regress[7,8]. Recognition of VCI duplication is important to prevent complications that may occur during retroperitoneal surgery and vascular interventional procedures and recurrent pulmonary embolism after IVC filter placement[9]. CONCLUSION: In conclusion, IVC duplication is a rare, mostly asymptomatic, and incidentally diagnosed vascular congenital anomaly. However, recognizing IVC duplication is crucial in treatment of recurrent thromboembolic diseases and in preventing complications that may occur during retroperitoneal surgery and interventional vascular procedures.

Figure 1

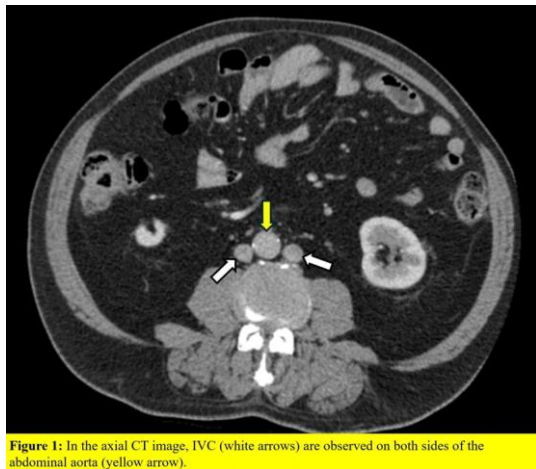


Figure 2



Keywords: Inferior Vena Cava, IVC, Duplication of IVC, Congenital Vascular Anomaly

MRI DIAGNOSIS OF OVARIAN MASSES: MAKE THIS PUZZLE EASY

Safiye Gürel², Mete Sezer³, Merve Başdemirci¹, Onur Başdemirci¹, Samet Töken²

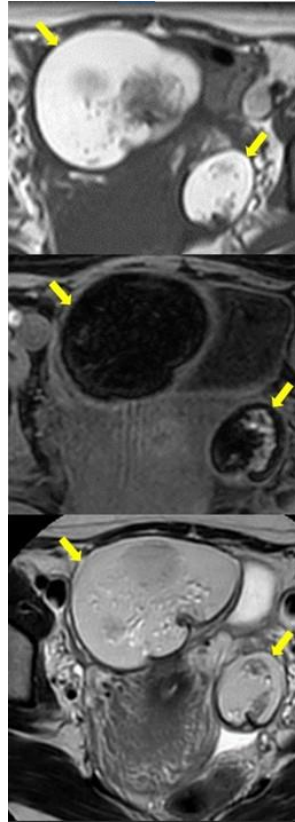
¹Department of Radiology, Karabük Training and Research Hospital

²Department of Radiology, Gülhane Medical School, Gülhane Training and Research Hospital

³Department of Radiology, Bolu Abant İzzet Baysal University, İzzet Baysal Training and Research Hospital

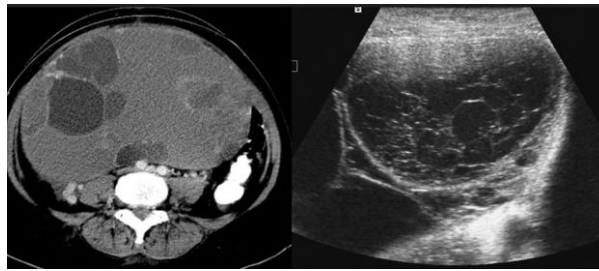
Abstract: INTRODUCTION: Ovarian masses are very common lesions, but most of them are benign and only a small part is borderline or malignant. TEACHING OBJECTIVES: 1.How to draw a road map in the diagnosis of ovarian masses 2.Being familiar to main sequences and what they tell us. REVIEW OF THE TOPIC: Before starting to look at MRI images we need to have information about the complaints of the patient, physical examination findings, if present, laboratory findings and previous radiologic examinations. Information about the patient's age, menopausal state, any kind of treatment history (medical, CRT, surgery), malignancies in her family available as well. Therefore gathering this information might take some time but means a lot for the patient diagnosis and the radiologist.MRI is the best radiologic modality for tissue characterisation. T1-, high-resolution T2 weighted both in small and big FOV images, fat-suppressed T1, diffusion-weighted imaging, and pre-post contrast T1 weighted images, in-out of phase imaging are used in ovarian MRI examination. Starting with T1w, fat-suppressed T1w, T2w, in out of phase signals are the main signals in the characterisation of ovarian mass content such as simple fluid, blood, microscopic or macroscopic fat, calcification, fibrosis, mucine, lymphoid tissue. Additionally, enhancement pattern and diffusion imaging characters might sometimes help to differentiate the benign and malign nature of the mass. CONCLUSION: As a result, ovarian mass diagnosis is a nice puzzle which we can solve when we put the pieces given above in the right places.

Figure 1



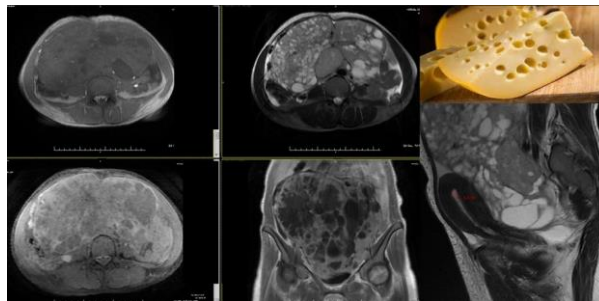
A 25-year-old woman was admitted with dull pelvic pain. T1-weighted TSE, fat-suppressed T1-weighted TSE, T2 weighted TSE axial images demonstrate two lesions hyperintense, hypointense and hyperintense respectively. Lesions are dermoid cysts containing macroscopic fat and hair.

Figure 2



A 38-year-old woman was admitted with weight gain and abdominal fullness. Axial CT and US images showed a mass with numerous thin septa in the small pelvis that is extending to upper abdomen with lots of locules containing different densities indicating different viscosity of mucine. Some of the septa are showing contrast enhancement. Histopathology revealed borderline mucinous cystadenoma.

Figure 3



A 52-year-old woman was admitted with a painless abdominal mass. Axial T1 weighted, axial and sagittal T2 weighted TSE, axial and coronal post-contrast fat-suppressed T1 weighted images demonstrate a huge mass filling most of the abdominopelvic cavity. The mass is prominently enhancing and composed of numerous T1 hypo- and T2 hyperintense multilocular cystic lesions like Swiss cheese.

Keywords: MRI, Ovarian Masses, Diagnostic Imaging of Ovarian Masses

A RARE CAUSE OF ILEUS IN ADULTS: INTUSSUSCEPTION- CASE REPORT

Onur Başdemirci¹, Merve Başdemirci¹

¹Department of Radiology, Karabük Training and Research Hospital

Abstract: INTRODUCTION and AIM: Intussusception is the interlocking of a bowel segment with an adjacent one. %95 of intussusception cases occur in children[1]. In adult population, it occurs less frequently (%5) and constitutes 1% of all intestinal obstruction cases[2]. Patients usually present to the emergency department with an intestinal obstruction[3]. In this case report, we aimed to give information and raise awareness about intussusception, a rare cause of ileus in adults. CASE: A 78-year-old male patient was admitted to the emergency department with complaints of abdominal pain. There was abdominal distension on physical examination. On direct graphy, there were air-fluid levels in the small bowel loops compatible with the ileus (Figure 1). In CT images, distension and air-fluid levels in the small intestine were observed (Figure 2). Axial CT images show ileoileal intussusception causing ileus (Figure 3a) and a hypodense lesion compatible with lipoma (lead point) causing intussusception in the adjacent area (Figure 3b). DISCUSSION and CONCLUSION: In 90% of cases of intussusception in adults, there is usually a lead point that triggers the intussusception. This lead point is an organic pathology, usually benign in the small intestine and usually malignant in the large intestine[1]. The most common organic cause of invagination in adults is colorectal carcinoma. Also, some benign pathologies can cause it such as GIST, polyp, lipoma and Meckel diverticulum[1,4]. The first radiological method for diagnosis is direct abdominal radiography and it can show intestinal dilations and air-fluid levels compatible with ileus. Other diagnostic imaging methods are ultrasonography and CT. CT is considered the most sensitive method for diagnosing intussusception[2,5]. Imaging findings vary depending on the imaging plane, the target sign is seen when viewed perpendicular to the lumen, and the sausage or "pseudokidney" sign is seen when viewed longitudinally[1,5,6]. In addition to the diagnosis of intussusception, CT can also identify the presence of lead factors, localization, and possible complications such as ischemia. Treatment in adult intussusception cases is usually surgical due to organic pathologies in its etiology and complications such as intestinal obstruction-ischemia. As a result, it's important to recognize intussusception in adults, define the presence of accompanying complications, and report the presence/absence of lead factor that may cause it.

Figure 1

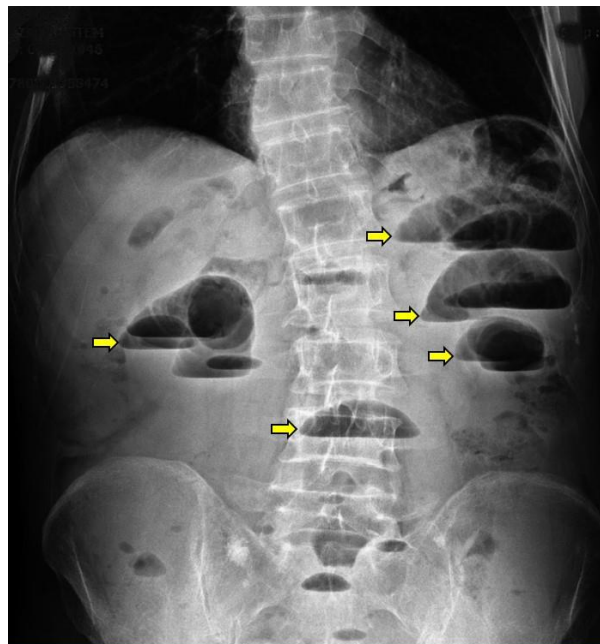


Figure 1: On direct graphy, air-fluid levels (arrows) in small bowel loops are compatible with the ileus.

Figure 2



Figure 2: In axial and sagittal CT images, show distension and air-fluid levels in the small intestine (asterisks).

Figure 3

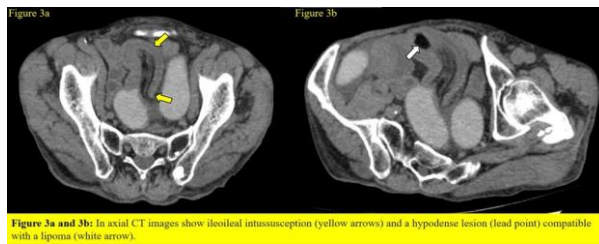


Figure 3a and 3b: In axial CT images show ileocecal intussusception (yellow arrows) and a hypodense lesion (lead point) compatible with a lipoma (white arrow).

Keywords: Ileus, Invagination, Lead Point, Intestinal Lipoma, Intussusception

MECKEL DIVERTICULUM PATHOLOGIES IN PEDIATRIC PATIENTS; CASE-BASED APPROACH

Serhat Akış¹, Fatma Ceren Sarıoğlu¹, Handan Gülerüz¹

¹Dokuz Eylul University

Abstract: INTRODUCTION Meckel's diverticulum is the most common congenital anomaly of the gastrointestinal tract. Even if it is generally asymptomatic it can lead to significant clinical complications such as gastrointestinal bleeding and diverticulitis. This abstract presents two distinct cases that illustrate the diverse presentations and imaging findings associated with Meckel's diverticulum. CASES In the first case, a pediatric patient presented with gastrointestinal bleeding. Initial imaging using technetium-99m pertechnetate scintigraphy was performed; however, the results were negative due to the presence of ectopic pancreatic tissue within the diverticulum, which complicated the diagnosis. CT findings included a tubular structure arising from the antimesenteric border of the ileum, with associated inflammatory changes indicative of bleeding. The second case involved a pediatric patient who experienced perforation of a Meckel's diverticulum. CT findings included a blind-ending, tubular structure arising from the ileum, with surrounding inflammatory changes and free air, consistent with perforation. DISCUSSION These cases emphasize the critical role of imaging techniques in the diagnosis and management of Meckel's diverticulum and its complications. Ectopic pancreatic tissue is the second most common ectopic tissue found in Meckel's diverticula after gastric mucosa. In cases where the ectopic tissue is pancreatic rather than gastric, the Meckel scan may be negative, as pancreatic tissue does not concentrate the radiotracer. This case highlights the importance of considering atypical presentations and the limitations of scintigraphy when ectopic pancreatic tissue is involved. Also one should consider Meckel's diverticulum in the differential diagnosis of acute abdominal pain, especially when complicated by diverticulitis or perforation. CONCLUSION Radiologists should maintain a high index of suspicion for this condition, as early recognition can significantly improve patient outcomes.

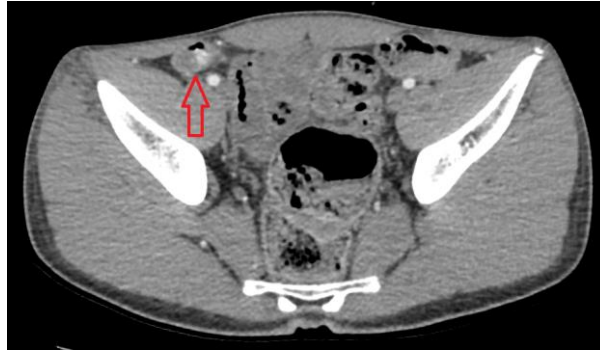
NEGATIVE SCINTIGRAPHY



NEGATIVE SCINTIGRAPHY FOR MECKEL'S DIVERTICULUM

In cases where the ectopic tissue is pancreatic rather than gastric, the Meckel scan may be negative, as pancreatic tissue does not concentrate the radiotracer.

GI BLEEDING ON CT



CT findings included a tubular structure with associated inflammatory changes indicative of bleeding.

3. MECKEL'S DIVERTICULUM PERFORATION



A blind-ending, tubular structure arising from the ileum, with surrounding inflammatory changes and free air, consistent with perforation.

Keywords: meckel's diverticulum, GI bleeding, ectopic pancreatic tissue, acute abdomen

ACCESSORY EXTENSOR CARPI RADIALIS LONGUS TENDON

İbrahim Çağrı Tural¹

¹*Necipfazıl State Hospital K.maras Turkey*

Abstract: Introduction: The hand, which performs the functions of grasping and grasping, requires the extensor and flexor muscles to work in harmony. Therefore, it is important to know the variations of the extensor and flexor muscles. Case: 42-year-old male suffering from pain in his wrist applied to ortopedics clinic. On physical examination the patient complained of pain with movement. He underwent an MRI. MRI was reported as accessory extensor carpi radialis longus tendon which was branching from the half of extensor carpi radialis longus tendon (Figure 1) Discussion: The muscle extensor carpi radialis longus (MECRL) originates from the distal 1/3 of the crista supracondylaris lateralis on the humerus, the epicondylus lateralis humeri, and the septum intermusculare brachii laterale. The muscle fibers tendonize in the upper 1/3 of the forearm. It passes deep to the abductor pollicis longus (MAPL) and the extensor pollicis brevis (MEPB) on the lateral side of the radius. It passes through the second canal with the tendon of the extensor carpi radialis brevis (MECRB) deep to the retinaculum extensorum and ends at the proximal dorsal surface of the second metacarpal bone (1). In previous studies, variations of the forearm muscles have been reported by many researchers (2). The incidence of variation in the extensor region muscles has been defined as 55%-75% (3). In the previously mentioned clinical studies, it has been emphasized that variations in the extensor region muscles are important in the development of upper extremity problems and that knowing these variations is clinically significant in diagnosis and treatment (4). In addition, forearm extensor region muscle tendon variations gain importance in tendon transfer procedures, and the importance of the tendons of these muscles or the bones they are attached to in terms of trauma repair is understood. In this study, it was aimed to create awareness for a rare variant of extensor wrist muscle and its MRI features. References 1- Andring N, Kennedy S, Iannuzzi N. Anomalous Forearm Muscles and Their Clinical Relevance. J Hand Surg Am. 2018;43(5):455-632-Williams PL, Bannister LH, Berry MM, Collins P, Dyson M, Dussek JE, Ferguson MWJ. Gray's Anatomy. 38th ed. New York: Churchill-Livingstone, 1998: 849-850

Figure1

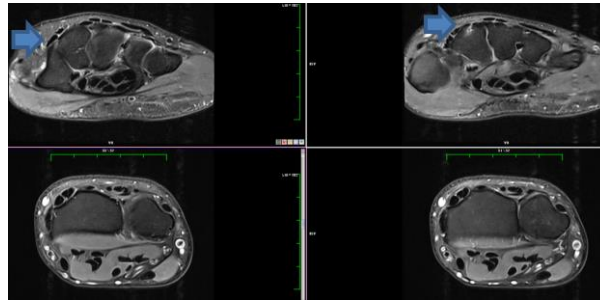


Figure1: MRI images of accessory extensor carpi radialis longus tendon

Keywords: Wrist muscles, anatomy, variation, MRI

THE ACCESSORY EXTENSOR CARPI RADIALIS INTERMEDIUS TENDON

İbrahim Çağrı Tural¹

¹Necipfazıl State Hospital

Abstract: Introduction: Having more muscles than normal in the arm muscles or the tendons of the muscles joining together in abnormal ways can sometimes cause pain. Accessory tendons suitable for transfer operations . Therefore it is important to know the variations of the extensor and flexor muscles (1,2). Case: 53-year-old female suffering from pain in his wrist applied to ortopedics clinic. On physical examination the patient complained of pain with movement. She was performed MRI. MRI was reported as The extensor carpi radialis intermedius tendon observed between extensor carpi radialis longus and brevis tendon (Figure 1) Discussion: The extensor radialis intermedius muscle and tendon has been first reported by the British surgeon, anatomist and physiologist John Wood in 1867. Extensor carpi radialis intermedius tendon's (ecrit) origin is between the extensor carpi radialis longus or extensor carpi radialis brevis muscles. It follows the trace between the extensor carpi radialis longus and extensor radialis brevis muscles, through the second or variably in a separate extensor compartment and inserts to the base of the second and/or third metacarpal bones. The incidence of the variation is high % 7-12. Accessory muscles in the wrist may cause pain. It may also cause diagnostic confusion with common pathologies such as ganglion cysts (3).The accessory tendinous band is worth looking for, particularly in patients with plegia, because it can be used to restore opposition to the flexor pollicis longus, or as a for the extensor pollicis longus (4). MRI is the major radiological modality due high to soft tissue discrimination. References 1- Andring N, Kennedy S, Iannuzzi N. Anomalous Forearm Muscles and Their Clinical Relevance. J Hand Surg Am. 2018;43(5):455-632-Williams PL, Bannister LH, Berry MM, Collins P, Dyson M, Dussek JE, Ferguson MWJ. Gray's Anatomy. 38th ed.New York: Churchill-Livingstone, 1998: 849-850.3-Jackson WT, Viegas SF, Coon TM, Stimpson KD, Frogameni AD, Simpson JM. Anatomical variations in the first extensor compartment of the wrist. A clinical and anatomical study. J Bone Joint Surg Am. 1986;68(6):923-6. 4-V E Wood .The extensor carpi radialis intermedius tendon J Hand Surg Am 1988 Mar;13(2):242-5.

Figure1

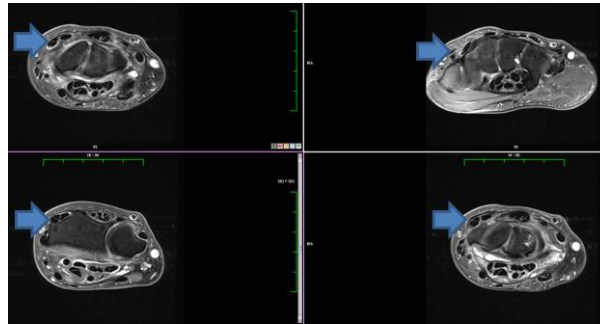


Figure1: MRI images of the extensor carpi radialis intermedius tendon

Keywords: wrist, muscle, accessory, MRI, extensor intermedius

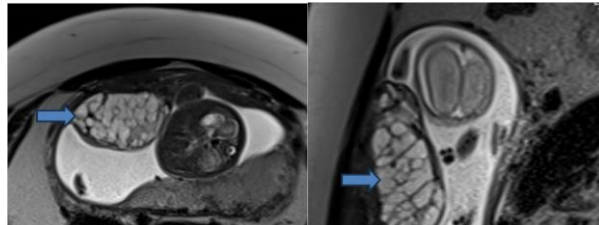
RADIOLOGICAL FEATURES OF PLACENTAL MESENCHYMAL DYSPLASIA

İbrahim Çağrı Tural¹

¹Necipfazıl State Hospital

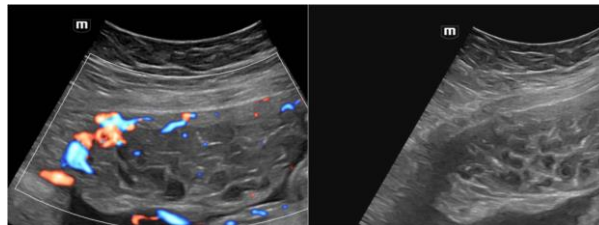
Abstract: Introduction: Placental mesenchymal dysplasia (PMD) is an uncommon disorder of the placenta, characterised by placentomegaly with diffuse hydropic stem villous, aneurysmally dilated vessels and lack of trophoblastic proliferation. Generalised vesicular lesions on ultrasonographic examination and gross appearance of placenta usually suggest a partial mole. Unlike partial moles, characterised by absent or malformed fetus, PMD can co-exist with a viable fetus. The common fetal complications reported in phenotypically normal fetuses associated with PMD are intrauterine growth restriction, intrauterine fetal demise or neonatal death. Case: A 33-year-old woman was admitted in her second pregnancy (first twin pregnancy) at 21 weeks' gestation in routine control. The described intrauterine mass was reported together with the MRI sections and USG performed on the same day. There is a lesion that protrudes towards the uterine cavity, in the anterior part of the uterus corpus, with a diameter measured as 67x40x100 mm at its widest point on T2 sequences, with widespread septa, and an appearance compatible with a thin hypointense capsule around it. In the sonographic examination, millimetric, punctate, vascular structures were observed within the lesion. Additionally, vascular structures extending vertically from the uterus into the lesion were detected. Observation of millimetric vascular areas within the lesion in Doppler examination supports placental mesenchymal dysplasia. Discussion: PMD is a rare benign condition. The fetus with PMD can develop normally without severe maternal complications. It is important to distinguish PMD from a partial mole with an abnormal triploid fetus, because this diagnosis may result in pregnancy termination. It is challenging to distinguish PMD from a complete mole with co-twin, which carries significant morbidity to the mother. The patient should be counseled on the potential associations of Beckwith-Wiedemann syndrome with prematurity, fetal growth restriction, or intrauterine fetal death. MRI has the advantage of very high image contrast with excellent contrast between the fluid and soft tissues. MRI findings of PMD have been described as an enlarged placenta with inhomogeneous signals and dilated placental vessels. As shown in our case, MRI with USG has the potential to be a useful tool for the differential diagnosis of PMD and should help inform appropriate management.

Figure 1



MRI images of placental mesenchymal dysplasia

Figure 2



Ultrasound images of placental mesenchymal dysplasia

Keywords: placental, mesenchymal, dysplasia, mri, ultrasound

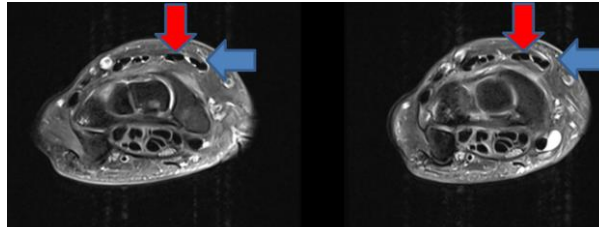
THE ACCESSORY EXTENSOR CARPI RADIALIS LONGUS AND BREVIS COINCIDENCE

İbrahim Çağrı Tural¹

¹Necipfazıl State Hospital

Abstract: Introduction: Accessory wrist muscles and tendons can sometimes cause pain. Accessory tendons are suitable for transfer operations. Therefore it is important to know the variations of the extensor and flexor muscles. Here we present a very rare coincidence of accessory extensor carpi radialis longus and brevis together (1,2). Case: 57-year-old female suffering from pain in his wrist applied to ortopedics clinic. On physical examination the patient complained of pain with movement. She was performed MRI. MRI was reported as accessory extensor carpi radialis longus and brevis together (Figure 1) Discussion: M extensor carpi radialis longus and brevis both have the same effect. They start from the crista supracondylaris lateralis and lateral epicondyle. Longus; attaches to the base of the 2nd metacarpal, brevis to the base of the 3rd metacarpal. Their nerves are n. radialis. Their function is to extend the hand. They help with radial abduction. In previous clinical studies, it has been emphasized that variations in the extensor region muscles are important in the formation of upper extremity-related problems and that knowing these variations is clinically significant in diagnosis and treatment (3,4). In addition, forearm extensor region muscle tendon variations are important in tendon transfer procedures (5). Accessory muscles in the wrist may cause pain. It may also cause diagnostic confusion with common pathologies such as ganglion cysts (3-5). MRI is the major radiological modality due high to soft tissue discrimination. References 1- Andring N, Kennedy S, Iannuzzi N. Anomalous Forearm Muscles and Their Clinical Relevance. J Hand Surg Am. 2018;43(5):455-632-Williams PL, Bannister LH, Berry MM, Collins P, Dyson M, Dussek JE, Ferguson MWJ. Gray's Anatomy. 38th ed. New York: Churchill-Livingstone, 1998: 849-850.3-Jackson WT, Viegas SF, Coon TM, Stimpson KD, Frogameni AD, Simpson JM. Anatomical variations in the first extensor compartment of the wrist. A clinical and anatomical study. J Bone Joint Surg Am. 1986;68(6):923-6. 4. West CT, Ricketts D, Brassett C. An anatomical study of additional radial wrist extensors including a unique extensor carpi radialis accessorius. Folia Morphol (Warsz). 2017;76(4):742-7 5. Albright JA, Linburg RM. Common variations of the radial wrists extensors. J Hand Surg Am. 1978;3(2):134-8.

Figure 1



PD MRI images of accessory Extensor carpi radialis longus (blue arrow) and brevis (red arrow), both are coupled

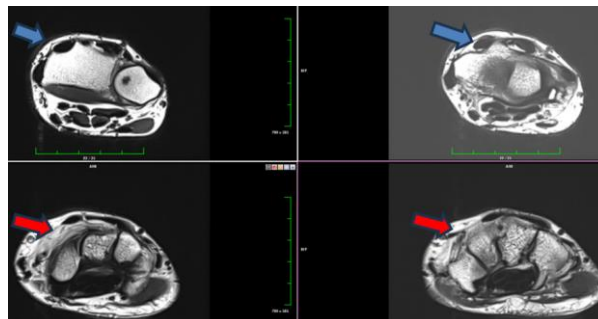
Keywords: wrist, accessory muscle, MRI

ABSENCE OF EXTENSOR CARPI RADIALIS LONGUS TENDON

İbrahim Çağrı Tural¹
¹Necipfazıl State Hospital

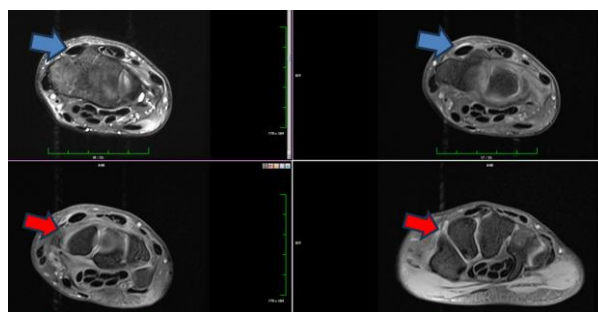
Abstract: Introduction: The second dorsal compartment of the wrist lies between the first compartment and the Lister tubercle and contains the extensor carpi radialis longus (ECRL) and extensor carpi radialis brevis (ECRB) tendons. The ECRL originates from the inferior third of the lateral epicondyle and supracondylar ridge and inserts onto the dorsal aspect of the second metacarpal base. The ECRB arises from the lateral epicondyle via the common extensor tendon origin and inserts onto the base of the third metacarpal. Case: 38-year-old male, suffering from pain in her wrist applied to ortopedics clinic. On examination, there was extension limitation on 2. finger. The patient complained of pain with movement With the current findings, the patient underwent an MRI. MRI was reported as extensor carpi radialis brevis tendon thickness increase and insertion in normal localization. The extensor carpi radialis longus tendon was not observed. Discussion: The extensor carpi radialis longus is a muscle within the superficial compartment of the posterior forearm. Its lateral position within the forearm produces abduction as well as extension at the wrist. The tendon of the extensor carpi radialis longus passes through the 2nd extensor compartment at the wrist. Extensor carpi radialis longus together with extensor carpi radialis brevis produce wrist extension and abduction (radial deviation). In addition extensor carpi radialis longus may help to flex the elbow joint and is active during fist clenching. The absence of the external carpi radialis longus tendons and thickening of the external carpi radialis brevis tendon, as in our case, is a very rare condition. This may cause limitation of extension and pain in the wrist. References 1. William PL, Warwick R, Dyson M, Bannister LH. Gray's Anatomy. 37. Edinburgh: Churchill Livingstone; 1989. The muscles of the fore arm; p. 6222. Palastanga, N., Field, D., & Soames, R. (2006). Anatomy and human movement: structure and function (Vol. 20056). Elsevier Health Sciences.

Figure 1



MRI images of absence of extensor carpi radialis longus tendon (red arrow) and thickening of extensor carpi radialis brevis tendon (blue arrow).

Figure 2



MRI images of absence of extensor carpi radialis longus tendon (red arrow) and thickening of extensor carpi radialis brevis tendon (blue arrow).

Keywords: wrist, mri, absence, ecrl, ecrb

RADIOLOGICAL FEATURES OF BORDERLINE SEROUS OVARIAN TUMOR

İbrahim Çağrı Tural¹

¹*Necipfazıl State Hospital*

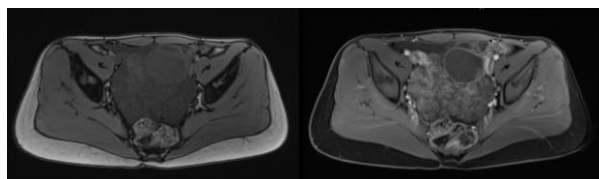
Abstract: Introduction: Borderline ovarian tumors (BOT) behave as intermediate lesions between benign cystadenomas and invasive carcinomas, making them a separate histologic and clinical entity. They represent 10 to 20 percent of all epithelial tumors of the ovary. They are characterized by an atypical epithelial cell proliferation without stromal invasion. These tumors are often diagnosed at an early stage while still confined to one or both ovaries, considered as stage I BOT according to the International Federation of Gynecology and Obstetrics (FIGO) classification. Serous borderline tumors often present as complex adnexal masses. Serous borderline tumors more commonly have papillary projections. Case: A 22-year-old nulligravid woman was admitted to our clinic complained with menstrual irregularity, abdominal pain and bloating abdomen. A large pelvi-abdominal multilocular complex cystic lesion was observed on computed tomography images. MRI sections seen eliciting low T1 and bright T2/SPAIR signal with thick internal septations and multiple papillary projections eliciting intermediate signal in T1 and T2 images with restricted diffusion in the DWI. They show heterogeneous enhancement in the post-contrast series. The described lesion filled the pelvic area and its borders from both ovaries could not be clearly distinguished. The postoperative pathological diagnosis was reported as serous borderline ovarian tumor. Discussion: Our study shows that borderline tumors often present as complex adnexal masses; none was a purely simple cystic lesion. Thus, although borderline ovarian tumors may appear to be benign masses clinically, their radiologic features require differentiation from early invasive disease. Borderline tumors are usually multiloculated with significant solid elements. The architecture of the solid component includes smooth round nodules, plaquelike thickening, and papilliform projections, with no tendency for any specific feature to predominate in malignancy. However, the thickness of the septations and the size of the nodules are greater in invasive tumors than in borderline tumors. Radiologic features of borderline tumors are similar to those of stage I ovarian cancers. The solid components are smaller and the septations are thinner in the borderline tumors, but although these features may be helpful in predicting likelihood of invasive tumors, neither feature allows confident differentiation of borderline from stage I disease.

Figure 1



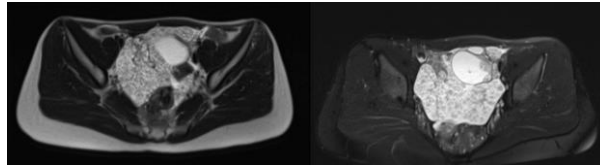
Contrast enhanced CT findings of serous borderline ovarian tumor (large pelvi-abdominal multilocular complex cystic lesion)

Figure 2



Axial T1-weighted MR image (left) and axial contrast enhanced T1-weighted MR image (right) shows large pelvi-abdominal multilocular complex cystic lesion

Figure 3



Axial T2-weighted MR image (left) and axial fat suppressed T2-weighted MR image (right) shows large pelvi-abdominal multilocular complex cystic lesion

Keywords: mri, serous, borderline, ovarian, tumor

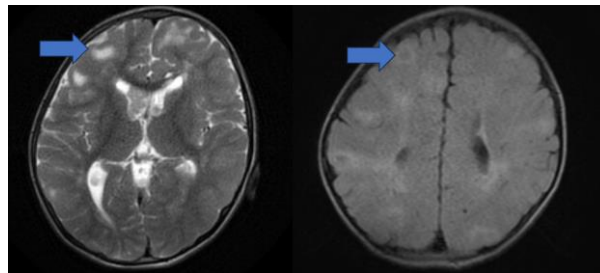
INTRACRANIAL LESIONS TUBEROUS OF SCLEROSIS

İbrahim Çağrı Tural¹

¹Necipfazıl State Hospital

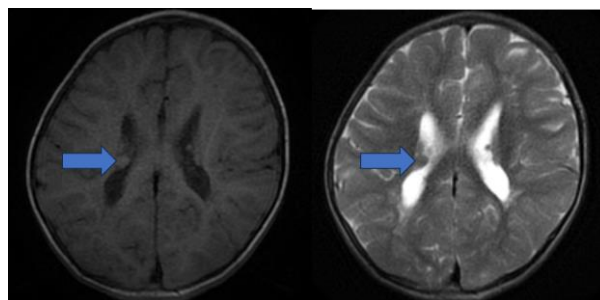
Abstract: Introduction: Tuberous Sclerosis Complex (TSC) is an autosomal dominant, multisystemic, hamartomatous, neurocutaneous disease. The most commonly affected organs include the brain, skin, kidney, lung, retina, and heart. Tuberous sclerosis complex (TSC) is a multisystem congenital syndrome with widespread CNS anomalies. The clinical neurologic manifestations include epilepsy and cognitive impairment. The intracranial features of TSC are cortical or subcortical tubers, subependymal nodules, subependymal giant cell astrocytomas, and white matter radial migration lines. Case: A 3 year-old male patient was admitted to the Pediatrics Clinic with complaints of ongoing seizures and and cognitive impairment. The patient was referred to the Radiology Clinic for a head MRI. Multiple hyperintense lesions in T2-weighted images in the both cerebral cortex and subcortical regions consistent with cortical tubers. Many subependymal nodules were observed, especially on the lateral ventricle walls. We observed an contrast enhancing lobulated solid mass contacts the lateral wall of the right lateral ventricle and near foramen Monro (subependymal giant cell astrocytoma). As of the current examination, hydrocephalus was not observed. Discussion: Advances in neuroimaging are improving the diagnosis of TSC and the treatment of children with this condition. Multiple-technique imaging with MRI, PET/MRI fusion, and magnetoencephalography/magnetic source imaging plays an important role in the noninvasive localization of epileptogenic tubers for possible surgical resection. Clinical presentation varies widely among the affected population, nevertheless distinctive clinical features include neurological anomalies, namely seizures, cortical tubers, subependymal tumors, neurodevelopmental anomalies and autism spectrum disorder, cardiac rhabdomyomas, renal angiomyolipomas and cysts, pulmonary lymphangioleiomyomatosis, retinal hamartomas, and typical cutaneous lesions including hypopigmented lesions, facial angiofibromas, ungual fibromas and shagreen patch. A timely diagnosis of TSC is essential, to allow early diagnostic assessments and therapeutic interventions to modify the natural progression of the disease and potentially prevent serious complications. References1-Curatolo, P., Bombardieri, R., & Jozwiak, S. (2008). Tuberous sclerosis. *The Lancet*, 372(9639), 657-668.2-Rodrigues, D. A., Gomes, C. M., & Costa, I. M. C. (2012). Tuberous sclerosis complex. *Anais brasileiros de dermatologia*, 87, 184-196.

Figure 1



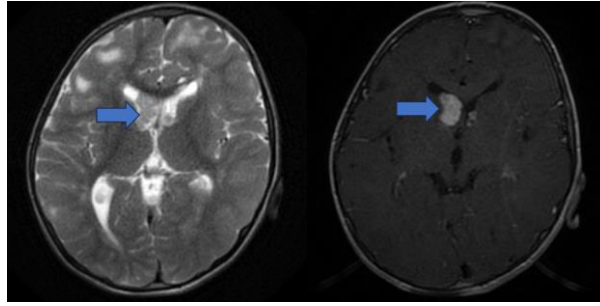
cortical tubers (blue arrows) on T2 weighted MR image (left) and T2 FLAIR MR image (right)

Figure 2



subependymal nodules (blue arrows) on T1 weighted MR image (left) and T2 weighted MR image (right)

Figure 3



subependymal giant cell astrocytoma (blue arrows) on T2 weighted MR image (left) and T1 contrast enhanced MR image (right)

Keywords: tuberous, sclerosis, intracranial, mri

IMAGING FINDINGS OF GRANULOSA CELL TUMOR: OVARIAN MASS AND ENDOMETRIAL HYPERPLASIA

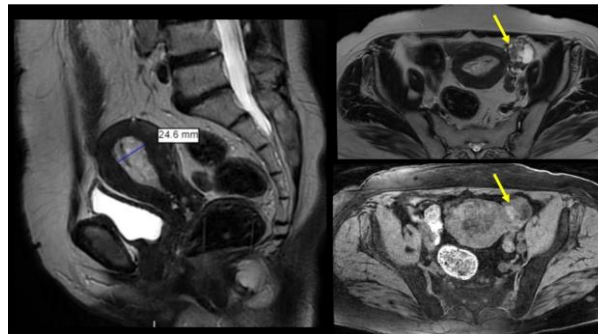
Elçin Aydın¹, Raşit Eren Büyüktoka², Hilal Şahin¹

¹Department of Radiology, Tepecik Training and Research Hospital, University of Health Sciences, Izmir, Turkey

²Department of Radiology, Izmir City Hospital, Izmir, Turkey

Abstract: Introduction: Granulosa cell tumor (GCT) is the most prevalent malignant ovarian sex-cord stromal tumor and is well-known for generating estrogen. There are two histopathological subtypes of GCT, adult and juvenile types with different clinics. Adult granulosa cell tumors are 95% of all granulosa cell tumors. Due to hyperestrogenism, endometrial hyperplasia, polyps or endometrial carcinomas may accompany to GCT. Solid masses, tumors with hemorrhagic or fibrotic alterations, multilocular cystic lesions filled with watery fluid or hemorrhage, or entirely cystic tumors are possible appearances for GCT. Objective: The clinical significance of magnetic resonance imaging (MRI) in diagnosing GCTs of the ovary. Material and methods: A 53-year-old postmenopausal woman was referred to our hospital for irregular vaginal bleeding lasting for 1 month. The patient had no history of hormone administration and surgery. Results: Laboratory tests showed that the associated tumor. The ultrasound showed a diffuse circumferential enlargement of the left ovary with heterogeneous tumoral involvement and endometrial thickening. Patient's abdominal MRI (1.5 Tesla, Siemens Magnetom Aera; Erlangen, Germany) was performed. MR imaging examination revealed the presence of a heterogeneous haemorrhagic solid & cystic pelvic mass originating from the left adnexa and endometrial thickening. Neither ascites nor pelvic lymphadenopathy was detected. Based on MRI findings, the presence of an early-stage ovarian malignancy was suggested. Conclusion: MRI is a reliable method for diagnosis of GCT. GCT should be considered first in the presence of hemorrhagic adnexal mass and endometrial thickening.

Figure



A 53-year-old woman with endometrial thickening and a hemorrhagic mass in the left adnexal area.
Histopathologically proven granulosa cell tumor.

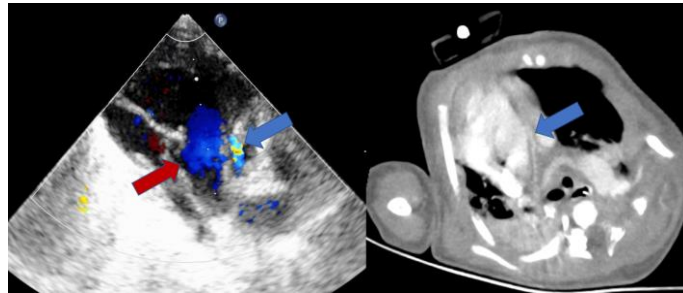
Keywords: Ovarian granulosa cell tumor, Sex-cord tumor, MRI, Diagnostic imaging

TETRALOGY OF FALLOT (TOF) AND MAJOR AORTOPULMONARY COLLATERAL ARTERIES (MAPCAS)

Aykut Teymur¹
¹*Antalya City Hospital*

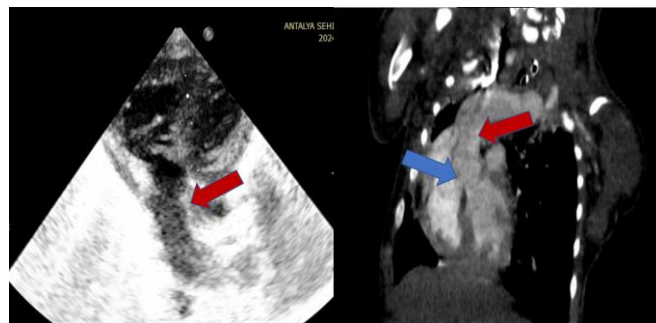
Abstract: Tetralogy of Fallot (TOF) is the most common cyanotic congenital heart disease (CHD) and represents 5% to 7% of all CHD (1). It has been classically characterised by the combination of pulmonary atresia with ventricular septal defect, biventricular origin of the aorta and late right ventricular hypertrophy. (2). Patients with tetralogy of Fallot and pulmonary atresia, the pulmonary blood supply arises from the ductus arteriosus or major aortopulmonary collateral arteries (MAPCAs) or from both (3–5). The MAPCAs may be relatively large arteries (3 to 20 mm in diameter), varying from one to five in number and arising most commonly from the descending thoracic aorta and less commonly from the subclavian arteries, the abdominal aorta or its branches or the left coronary artery (4,6). The clinical presentation of these patients is variable, depending on the magnitude of the pulmonary blood flow, which allows some patients to maintain an excellent functional status for many years (2).

image 1



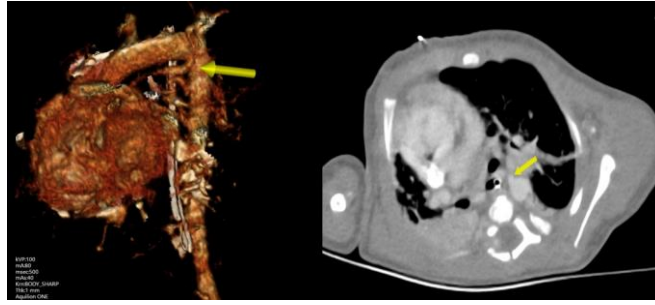
-Hypoplastic main pulmonary artery (blue arrow) -Aortic outlet (red arrow)

image 2



-Overriding aorta (red arrow) -Perimembranous VSD (blue arrow)

image 3



-MAPCA from descending thoracic aorta -MAPCA from arcus aorta

Keywords: fallot, MAPCAs, child, congenital heart disease, post-operative complication, CT

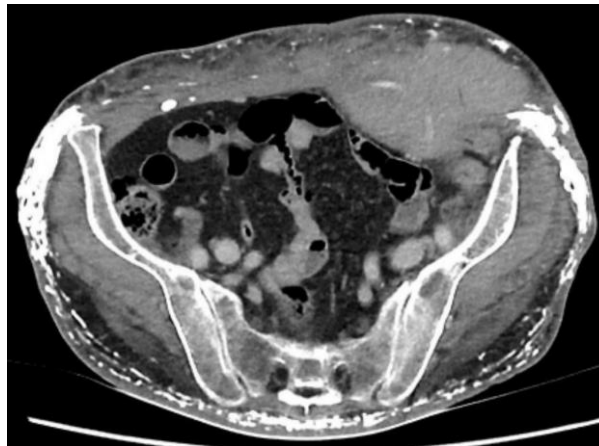
A CURIOUS TWIST: THE DISCOVERY OF EXTENSIVE CALCINOSIS UNIVERSALIS REVEALED IN A CASE OF RECTUS SHEATH HEMATOMA

Şule Özer¹, Saner Esmer¹

¹Çanakkale Onsekiz Mart University Hospital

Abstract: Calcinosis universalis is a rare condition characterized by extensive calcium deposition in the skin and subcutaneous tissues, often associated with connective tissue diseases such as dermatomyositis. Dermatomyositis primarily affects the muscles and skin, and while calcinosis can occur in these patients, its extent and distribution vary widely. Cases with extensive calcinosis offer valuable insights into the relationship between chronic inflammatory diseases and their dermatological manifestations. We present the case of a 47-year-old male who arrived at the emergency department with acute abdominal pain. A contrast-enhanced CT scan revealed a rectus sheath hematoma, a rare condition involving bleeding within the sheath of the rectus abdominis muscles. Additionally, widespread subcutaneous calcifications were incidentally discovered throughout the patient's body, later linked to his history of dermatomyositis. This connection allowed us to attribute the calcinosis universalis to the underlying dermatomyositis, unrelated to the hematoma. Dystrophic calcinosis cutis affects approximately 25% of systemic sclerosis patients and 11% to 20% of those with dermatomyositis. It can manifest as diffuse calcific deposits along the myofascial planes, as seen in this case, or as deep intramuscular tumoral deposits. The incidental discovery of significant calcifications in a patient initially assessed for an unrelated acute condition underscores the importance of a broad differential diagnosis and thorough imaging. This case highlights the complexities of diagnosing and managing calcinosis universalis, emphasizing the need for comprehensive evaluation in patients with systemic diseases like dermatomyositis. The concurrent findings provide a unique opportunity to explore and document a rare clinical presentation, enhancing clinical understanding and patient care.

Extensive subcutaneous coarse calcifications



Axial Section of Abdominal CT

Extensive Subcutaneous Calcifications



Coroner Section of Abdominal CT

Keywords: calcinosis, rectus sheath hematoma, calcinosis universalis

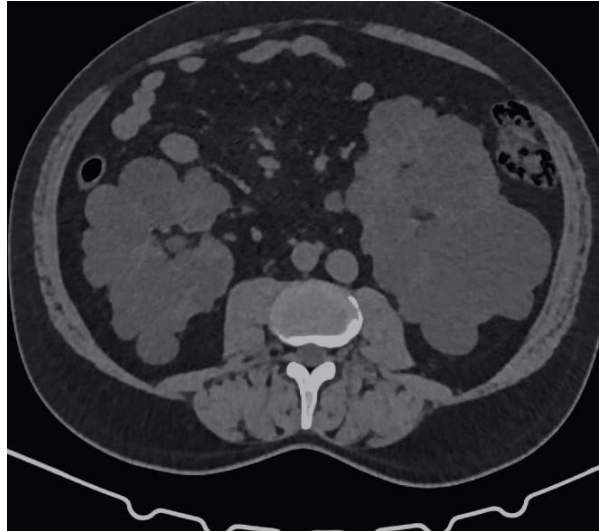
SITUS INVERSUS AND AUTOSOMAL DOMINANT POLYCYSTIC KIDNEY DISEASE IN AN ADULT PATIENT

Dursun Can KARAKUŞ¹, Hasan ERDOĞAN¹, Ömer Baran YAMAN¹, Elif Aybala
YILDIRIM¹, Esad Cihan LÜY¹

¹Kayseri Şehir Hastanesi

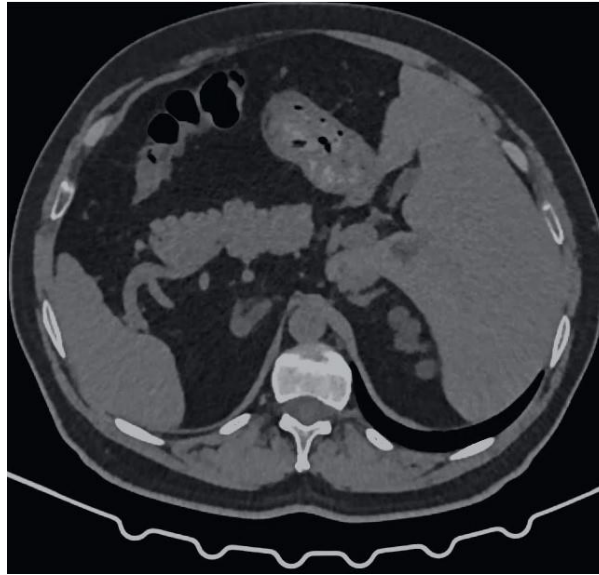
Abstract: INTRODUCTION AND PURPOSE: Situs inversus and Autosomal dominant kidney disease (ADPKD) are two rare conditions. Although there are a few similar pediatric cases in the literature regarding the coexistence of two conditions with cilia defects in their etiology, this condition is almost non-existent in adulthood. Our aim is to present the findings of this very rare condition through a case. CASE: A 52-year-old male patient was admitted to the hospital with abdominal pain. There was a known history of hypertension. On arrival at the hospital, blood pressure was 140/90 mm Hg. In the blood test, creatine was 1.4 mg/dL and was measured above normal. +1 hematuria was detected in the urinalysis. The patient was scheduled for non-contrast abdominal computed tomography (CT). ADPKD and situs inversus were detected in the non-contrast CT scan. DISCUSSION: Situs inversus totalis is a rare congenital abnormality characterized by mirror image transposition of both abdominal and thoracic organs. The frequency of situs inversus is 1:10,000. (1) Autosomal dominant polycystic kidney disease (ADPKD) is a disease characterized by the progressive increase of bilateral renal cysts, leading to chronic kidney disease (CKD) and often end-stage renal disease (ESRD). It is a systemic disease (2). There are many pathologies in the literature related to ADPKD. These may include hypertension, hepatic cysts, intracranial aneurysm, diverticulosis, and abdominal and inguinal hernias. (3) Situs inversus does not come to mind very often among the situations we have mentioned. The coexistence of the two conditions is rare and there are few pediatric case reports. (4) Situs inversus, as it is known, is a condition that occurs with cilia movement disorder. Several proteins encoded by ADPKD-associated genes have been identified in primary cilia in the renal tubular epithelium. These findings suggest that abnormalities in cilia formation and function may play a role in the pathogenesis of ADPKD. (5) Studies on this subject continue. CONCLUSION: With this very rare case of ADPKD and Situs Inversus; We touched upon the similarities and commonalities in the radiological findings and etiologies of both conditions. Recent studies shed light on the cause of both conditions being ciliary dysfunction.

picture 1



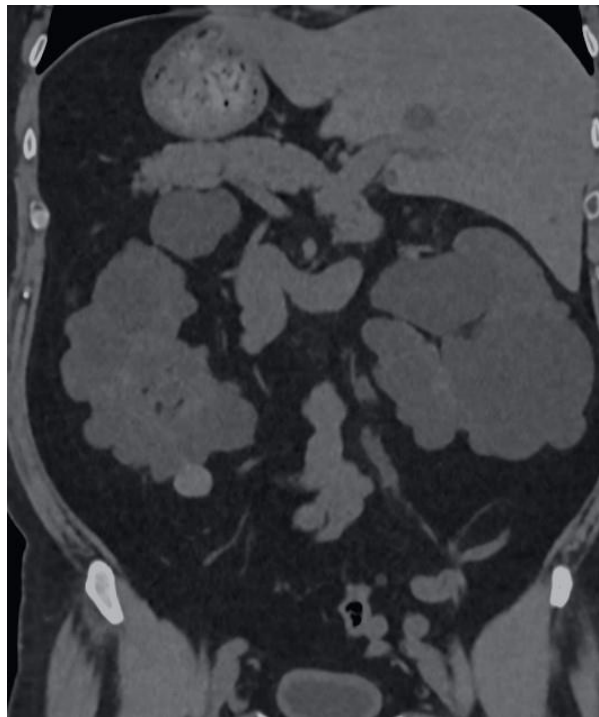
In axial non-contrast abdominal CT images, the size of both kidneys has increased and we see many hypodense cystic lesions. The appearance is compatible with ADPKD.

picture 2



Situs inversus is seen on axial non-contrast abdominal CT images

picture 3



The coexistence of situs inversus and ADPKD is seen in coronal non-contrast abdominal CT images.

Keywords: ADPKD, Situs inversus, Cilia Defect

INFERIOR MESENTERIC VEIN THROMBOPHLEBITIS SECONDARY TO ACUTE DIVERTICULITIS

Narmin Hüseyinli¹, Ezgi Güler¹, Laman Hüseyinzade¹

¹Ege Üniversitesi Tıp Fakültesi Radyoloji AD

Abstract: The inferior mesenteric vein (IMV) drains the distal transverse colon, descendant colon and the superior rectum. Inferior mesenteric vein thrombophlebitis is rare. Most cases of portal-mesenteric thrombophlebitis affect either the portal vein or superior mesenteric vein, only 6% of cases of portal-mesenteric thrombophlebitis affect the IMV exclusively. Thrombophlebitis typically occurs following inflammatory intra-abdominal processes, such as diverticulitis. Diverticulitis is often complicated by hemorrhage, obstruction, abscesses and fistulas. Thrombophlebitis is an uncommon complication of diverticulitis. We present a case of diverticulitis complicated by IMV thrombophlebitis. Case presentation: A 58-year-old male patient is presenting to the emergency department with a complaint of abdominal pain that started 5 days ago. On physical examination, widespread tenderness in the abdomen is observed. Laboratory results show elevated levels of liver enzymes and C-reactive protein (CRP). The CT scan reveals findings consistent with diverticulosis in the sigmoid colon and descending colon, as well as wall thickening and surrounding fat stranding at the level of the descending colon, indicative of diverticulitis. A thrombotic appearance in the inferior mesenteric vein and inflammatory changes in the surrounding fat tissue were observed, and these findings are evaluated as thrombophlebitis secondary to diverticulitis. Conclusion: Thrombophlebitis of the mesenteric veins and portal vein can occur secondary to intra-abdominal inflammation. Of the portal-mesenteric veins, the SMV is the most commonly affected by thrombophlebitis, however the IMV is the least commonly affected. Thrombophlebitis can develop secondary to intra-abdominal infectious processes such as diverticulitis, appendicitis, IBD and pancreatitis. Diverticular disease is very common in the Western world. Pylephlebitis is an uncommon sequela of diverticulitis, arising in only 3% of cases of diverticulitis. The inflammatory and infectious environment caused by diverticulitis induces hypercoagulability, leading to thrombosis in the veins. The symptoms are non-specific and include fever, chills, nausea and abdominal pain. The mortality rate is %25, and early diagnosis and treatment are important. Portal venous phase contrast-enhanced CT imaging is considered the “gold standard” imaging modality in diagnosing thrombosis and surrounding inflammatory changes.

Diverticulitis in the descending colon



Thrombophlebitis in the inferior mesenteric vein



Thrombophlebitis in the inferior mesenteric vein



Keywords: diverticulitis, thrombophlebitis, Inferior mesenteric vein

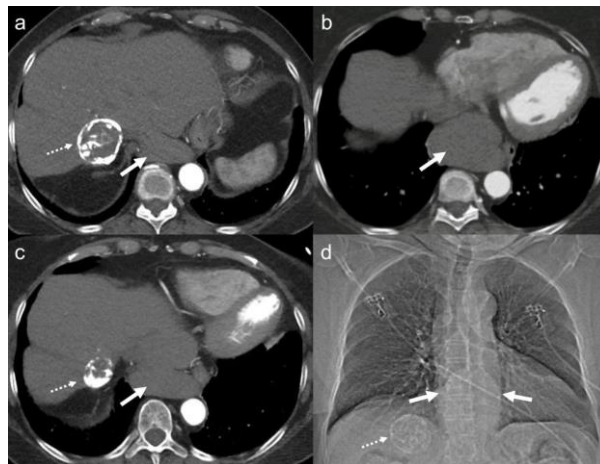
ISOLATED LIVER HERNIATION TO POSTERIOR MEDIASTINUM THROUGH GASTROESOPHAGEAL HIATUS

Vedat Yaman¹, Selin Ardali Duzgun¹, Tuncay Hazirolan¹

¹Hacettepe University, School of Medicine, Department of Radiology

Abstract: Liver herniation through the gastroesophageal hiatus is very rare and must be in the differential diagnosis of posterior mediastinal masses detected on chest X-ray. A 68-year-old man underwent coronary computed tomography angiography (CCTA) due to chest pain. The herniation of segment 1 and segment 3 of the liver through the gastroesophageal hiatus was incidentally noted (Fig.1). Type 4 hiatal hernia which is associated with a large defect in the phrenoesophageal membrane allows intraabdominal organs other than the stomach such as the colon, spleen, pancreas, and small intestine to herniate through the esophageal hiatus. Liver herniation through the esophageal hiatus is extremely rare and must be in the differential diagnosis of posterior mediastinal masses detected on chest X-ray. Apart from herniation through the gastroesophageal hiatus, intrathoracic liver tissue can be seen due to other reasons described by different pathophysiological mechanisms. Intrathoracic liver tissue is extremely rare and usually asymptomatic. It usually results from embryonic heteroplasia but it may occur after thoracic surgery and trauma. Adin et al. proposed a classification system for intrathoracic accessory liver tissue in their systematic review. In type 1, there is a direct extension of liver parenchyma through a diaphragmatic defect. In cases with type 1 intrathoracic accessory liver tissue, patients may have a history of trauma or thoracic surgery. Congenital diaphragmatic hernias morphologically belong to the type 1 group. Also, the herniation through the anatomical openings of the diaphragm such as inferior vena cava foramen or gastroesophageal hiatus can be included in type 1 morphologically. In type 2, the intrathoracic accessory liver tissue is connected to the orthotopic liver via a vascular pedicle. In type 3, the accessory intrathoracic liver tissue is completely isolated from the orthotopic liver. Although asymptomatic and incidentally detected as in our case, liver herniation through the gastroesophageal hiatus must be in the differential diagnosis of the posterior mediastinal masses detected on the chest or abdominal X-rays. Cross-sectional imaging studies such as computed tomography and magnetic resonance imaging can clearly demonstrate the mass as the herniated liver.

Fig.1



Axial CT angiography images at different levels (a-c) demonstrate the herniation of segment 1 (caudate lobe) and segment 3 of the liver through gastroesophageal hiatus (a-c, arrow). Also, a mostly calcified lesion compatible with a hydatid cyst is seen in the right posterior lobe of the liver (a, c, dashed arrow). On coronal CT scout image (d), the herniated liver is seen as a posterior mediastinal mass (arrows). The calcified hydatid cyst is also seen (dashed arrow).

Keywords: Gastroesophageal hiatus, liver herniation, intrathoracic, paraesophageal hernia, computed tomography

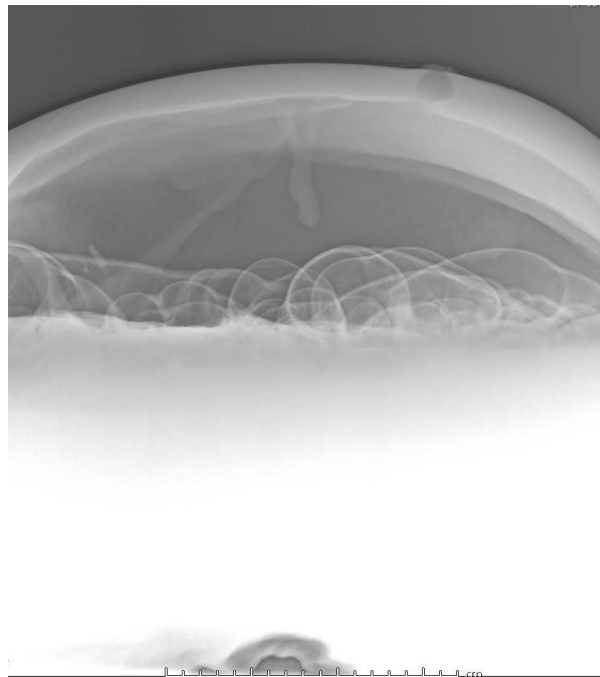
THE IMPORTANCE OF DORSAL (SUPINE) DECUBITUS X-RAY IN PNEUMOPERITONEUM

Catarina TRINDADE¹, Labrini ADAMOPOULOU¹, Afroditi KAROUTA¹, Foteini MERMIGKA¹, Anastasia TSAKIRI¹, Dimitrios FAGKREZOS¹, Charikleia TRIANTOPOULOU¹

¹*Konstantopouleio General Hospital*

Abstract: BACKGROUND AND PURPOSE: Pneumoperitoneum is defined by the presence of free air in the abdominal cavity, the most common cause being the disruption of the wall of a hollow viscus. In an emergency setting, the initial diagnostic method of choice is a simple X-ray, which should be performed in an erect position and can reveal alarming elements that will justify emergency surgery. However, what if our patient is unable to stand or lie on their side? In this case report we evaluate the importance of performing a supplementary projection, the abdomen dorsal decubitus view. PATIENT, METHODS AND FINDINGS: Female patient, 85 y.o presented to the Emergency Room of our hospital due to fever for the last 24 hours, loose stools for 10 days, and abdominal pain. Initially, a chest and abdomen X-rays, in an erect position, were ordered, however the patient was unable to stand. Both exams, performed in a supine position, revealed a noticeable dilated bowel with a double-wall appearance, compatible with the Rigler sign. Furthermore, displayed the presence of a crescent lucency, overlying the thoracic vertebrae, beneath the central part of the diaphragm described as Cupola sign. In order to exclude the presence of air-fluid levels, indicative of Ileus, a lateral decubitus view X-ray was requested. However, due to the inability of the patient to roll to her side, as a substitute, a dorsal decubitus was executed. The image showed the presence of free air intraperitoneally: A prominent radiolucent space between the abdominal wall and the pushed bowel, towards the spine, outlining the lateral aspect of the liver and the falciform ligament, as defined by the Silver Sign. The patient was rushed to CT, the diagnosis of pneumoperitoneum was confirmed, and finally an exploratory laparotomy revealed a very small, pinpoint, rupture of the cecum. CONCLUSION: When presented with an unstable patient whom is unable to stand or roll to their side, the abdomen dorsal (supine) decubitus X-ray can and should be used to promptly identify, when suspected, free intraperitoneal air, as it was done with our patient.

supine decubitus X-ray



Keywords: pneumoperitoneum, decubitus x-ray, Silver sign

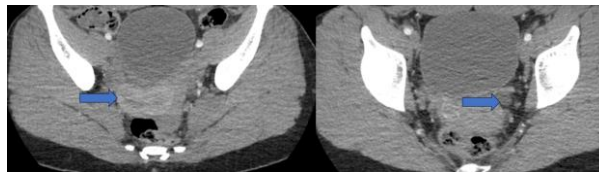
HERLYN-WERNER-WUNDERLICH SYNDROME

İbrahim Çağrı Tural¹

¹*Necipfazıl State Hospital*

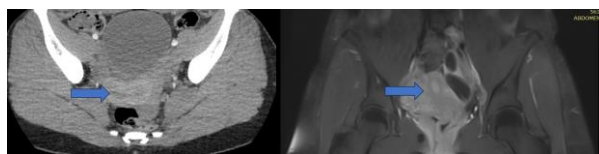
Abstract: Introduction: Herlyn-Werner-Wunderlich (HWW) syndrome is a combined anomaly of Mullerian and mesonephric ducts which includes a triad of didelphys uterus, obstructed hemivagina, and ipsilateral renal agenesis. HWW is rare with a reported incidence in the general population of approximately from 0.1% to 3.8%. Typical symptoms are pelvic pain, tenderness, pelvic mass due to blood collection in the obstructed hemi-vagina and uterus, and dysmenorrhea usually beginning shortly after menarche. MRI can accurately identify anatomic variants and obstruction sites of HWW syndrome. MRI can identify cervical communications, but is insensitive for detecting vaginal fistulas in HWW syndrome. Case: A 28-year-old female was admitted to our clinic complained with menstrual irregularity, menstrual cramps and progressive pain in the hypogastric region. Uterine didelphys and agenesis of left kidney was observed on computed tomography (CT). Additionally, loculated fluid was observed in the left hemivagina. Pelvic MRI was performed to better characterize the anatomy and confirmed the presence CT findings. The Magnetic Resonance Imaging (MRI) findings demonstrated a uterine-vaginal anomaly consisting in a dydelphys uterus and fluid accumulation in the obstructed hemivagina. Additionally, a tubular structure was observed in the left ureter trace ending in the left hemivagina (mullerian duct anomaly). Discussion: Herlyn-Werner-Wunderlich syndrome (HWWS) is a very uncommon congenital disorder of Müllerian and mesonephric duct development distinguished by the triad of uterus didelphys, obstructed hemivagina and ipsilateral renal agenesis. Renal agenesis on the same side of the obstructed vagina can be explained by embryological arrest at 8 weeks of pregnancy, simultaneously affecting the Müllerian (paramesonephric) and Wolffian (mesonephric) ducts. Patients with HWWS are often asymptomatic until menarche when they present with progressive pain due to hydrometrocolpos and hemivaginal obstruction within the first year of menstruation. Several complications may arise from this syndrome, the acute ones are usually pyohematocolpos, pyosalpinx, or pelviperitonitis, whereas long-term complications may be endometriosis, pelvic adhesions and increased risk of abortion or infertility. References 1- R. Del Vescovo et al. (2012). 'Herlyn-werner-wunderlich syndrome: MRI findings, radiological guide (two cases and literature review), and differential diagnosis', BMC Med Imaging vol. 12:4

Figure 1



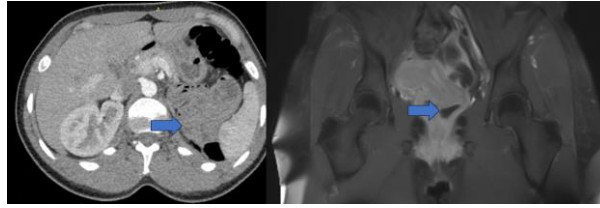
CT Findings uterin didelphys (left) and blunt-ended tubular structure (right)

Figure 2



Uterin didelphys in the contrast enhanced axial CT (left) and contrast enhanced T1 coronal MRI

Figure 3



Left renal agenesis on contrast enhanced axial CT (left) and left hemivagen fluid accumulation on contrast enhanced coronal MRI (right)

Keywords: renal agenesis, uterin didelphys, obstructed hemivagina, CT, MRI

AI IN RADIOLOGY: A ROBUST ASSISTANT OR A MISLEADING TOOL? PRIMARY RESULTS

Foteini MERMIGKA¹, Labrini ADAMOPOULOU¹, Vasileios CHATONIDIS¹,
Catarina TRINDADE¹, Chrysi CHATZIKONSTANTINO¹, Petros MANIATIS¹,
Charikleia TRIANTOPOULOU¹

¹Konstantopouleio General Hospital, Radiology Department

Abstract: INTRODUCTION Rayscape CXR is an artificial intelligence (AI) system developed to assist in diagnosing a range of conditions, both pathological and non-pathological, based on chest X-ray images. The aim of this study was to compare diagnoses made by radiologists with those provided by Rayscape CXR and to assess the system's efficacy as an adjunctive tool for radiologists. METHODS In our study we randomly selected digitally generated chest X-rays from 90 patients who visited the emergency department of our hospital on various dates. Our diagnoses were compared with those generated by an AI system, Rayscape CXR, across 17 specific categories supported by the system. Additionally, we assessed whether there were any other diagnoses identified by radiologists that were missed by the AI. RESULTS Following the data analysis using confusion matrices, two primary performance metrics were calculated: balanced accuracy (BA) and the F1 score. These metrics were assessed for atelectasis (BA=66.67%, F1=0.50), cardiomegaly (BA=95%, F1=0.73), cifo-scoliosis (BA=85.71%, F1=0.83), consolidation (BA=75%, F1=0.67), diaphragmatic disfunction (BA=93.48%, F1=0.83), hilar/mediastinal disease (BA=90.77%, F1=0.71), interstitial disease (BA=94.44%, F1=0.93), lung lesion (BA=70.98%, F1=0.31), lung opacity (BA=92.86%, F1=0.92), pleural effusion (BA=78.84%, F1=0.6), pleural abnormalities – pleural other (BA=90.28%, F1=0.86) and support devices (BA=99.43%, F1=0.89). It should be noted that there were not sufficient data to evaluate the system's performance for the diagnosis of edema, emphysema, fracture, pneumothorax, and tuberculosis. CONCLUSIONS Given the restrictions of the sample size, our results indicate that Rayscape CXR demonstrates high accuracy in detecting certain specific conditions, thereby serving as a valuable tool for radiologists. However, it has limitations in diagnosing pathologies that fall outside the predefined categories, such as pneumoperitoneum, which is critical for patient management. Moreover, the AI system is unable to assess variables such as patient body type or technical factors, including significant rotation, patient positioning (e.g., supine), or radiographic imaging during expiration. These limitations can lead to errors, such as the overdiagnosis of cardiomegaly. However, to accurately evaluate the full potential of AI systems in radiology, further analysis with a larger dataset is required.

Keywords: artificial intelligence, chest X-rays, accuracy

A CASE OF SUSPECTED FOREIGN BODY SWALLOWING: THE USE OF X-RAY AND ULTRASOUND AS SCREENING METHODS

Anastasios GIAPRAKIS¹, Afroditi KAROUTA¹, Anastasia PAPA¹, Konstantinos
VITZILAIOS¹, Dimitrios ARGYROPOULOS¹, Georgios ANASTOPOULOS¹,
Charikleia TRIANTOPOULOU¹

¹*Konstantopouleio General Hospital, Radiology Department*

Abstract: **PURPOSE:** Esophageal perforation is a rare but serious medical emergency which occurs when the wall of the esophagus is ruptured. Our aim is to present an interesting case of esophageal perforation after the swallowing of a foreign body. **METHOD:** A 42 years old female patient came to the emergency department of our hospital due to nausea, dysphagia and pain in the neck area after a reported swallowing of a foreign body (meat bolus) in the last 24 hours. The physical examination revealed cervical edema and the patient was referred for immediate assessment by an ENT doctor. A laryngoscopy revealed a free airway, without showing any signs of inflammation, and furthermore without the presence of a foreign body in the larynx and oropharynx. **RESULTS:** Following the diagnostic approach, a lateral x-ray of the neck was performed and showed a radiopaque foreign body in the middle section of the neck, behind the trachea, so the presence of a foreign body in the esophagus was suspected. Moreover, an ultrasound examination showed the presence of air in the soft tissues of the cervical area and in the thyroid gland along with an image of an intraparenchymal abscess as well. In order to confirm the findings, a CT scan was also performed, demonstrating the presence of a foreign body (bone) in the upper third of the esophagus, as well as the presence of air behind the esophagus and in the anterior cervical region. As a result, the diagnosis of esophageal perforation was made and a gastroenterological evaluation of the patient was requested immediately. After consultation with a specialized surgical center, she was transferred for immediate treatment. **CONCLUSION:** In order to establish a definitive diagnosis of esophageal perforation, a CT scan is the gold standard method used in an emergency setting. However, this case report emphasizes the importance of using Xray and Ultrasound when the presence of a foreign body in the esophagus is a suspicion.

Keywords: esophageal perforation, ultrasound, foreign body

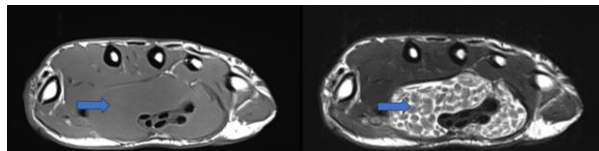
RICE BODIES IN THE WRIST

İbrahim Çağrı Tural¹

¹*Necipfazıl State Hospital*

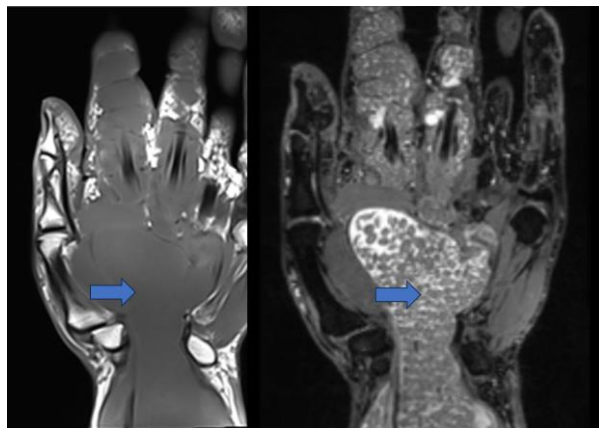
Abstract: Introduction: Rice body formation is an uncommon inflammatory process occurring in joints and tendon sheaths in systemic disorders. Microscopically, the rice bodies are composed of eosinophilic nuclei and fibrin due to a non-specific reaction to chronic joint inflammation. these have been described in various rheumatic diseases including rheumatoid arthritis, juvenile idiopathic arthritis, and seronegative inflammatory arthritis, in infections with atypical mycobacteria, and in subacromial bursitis. he diagnosis of rice bodies can be reached through proper history, thorough physical examination, and intensive radiological assessment through X-rays, computed tomography (CT), and magnetic resonance imaging (MRI).Case: A 47-year-old male came with progressive pain and isolated swelling of the right wrist, 2nd and 3rd finger. In magnetic resonance imaging, there is widespread fluid starting from the distal part of the forearm, extending to the metacarpophalangeal joint levels, in the vicinity of the exortend tendons, and also extending in the 2nd and 3rd fingers from the metacarpophalangeal joint level to the middle phalanx level in the distal part, and within this fluid, it is compatible with a millimetric-sized multiple rice body filling the cavity. views available. Widening of the carpal tunnel and widening between the flexor tendons and volar intercarpal ligament were observed. Discussion: Rice bodies are a rare condition that was first reported in patients with tuberculous arthritis. Thereafter, rice bodies have been reported in cases with a wide variety of rheumatic and inflammatory diseases, including but not limited to rheumatoid arthritis, juvenile idiopathic arthritis, and lupus erythematosus. The principal differential diagnoses of rice bodies are synovial chondromatosis and pigmented villonodular synovitis. Ultrasonography and MRI are the most effective diagnostic imaging modalities. On ultrasonography, rice granules appear as low-to-anechoic spherical intracapsular nodules but are almost indistinguishable from synovial chondromatosis. On MRI, rice bodies show low signal T1 and T2 weighted sequences. In contrast, the nodules of synovial chondromatosis show a high signal on the T2-weighted sequence because of the presence of cartilage components. Meanwhile, the signal cavity of pigmented villous nodular synovitis reflects hemosiderin deposition and the lack of sensitivity artefacts of the gradient echo sequence, which can be distinguished from rice bodies

Figure 1



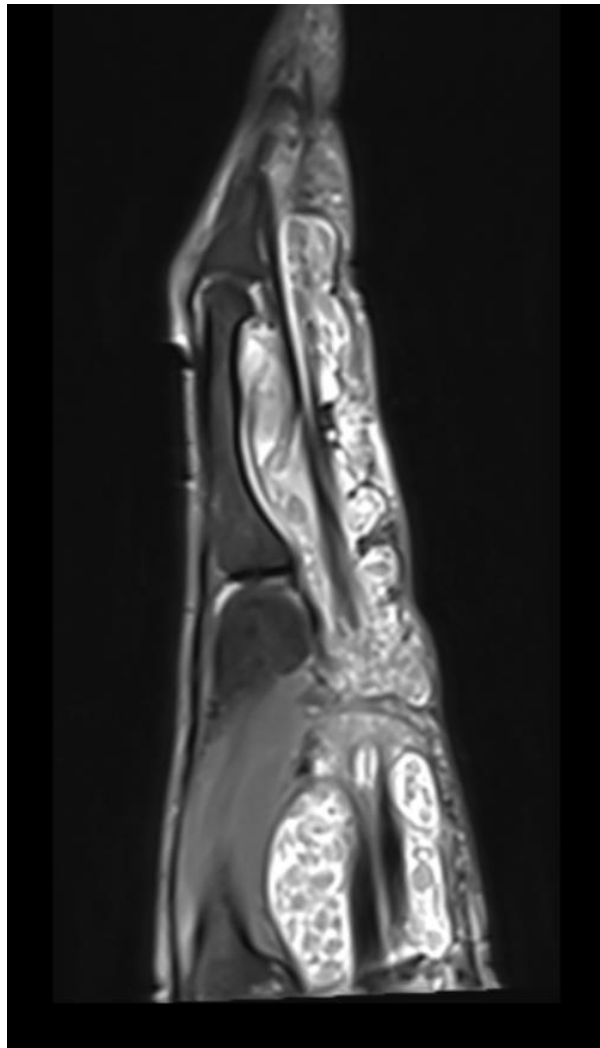
axial T1 (left) weighted MR imaging and axial T2 MR imaging (right) of rice bodies (blue arrows)

Figure 2



Coronal T1 (left) weighted MR imaging and Coronal T2 MR imaging (right) of rice bodies (blue arrows)

Figure 3



Sagittal T2 weighted MR imaging of rice bodies

Keywords: rice bodies, wrist, mri, inflammatory

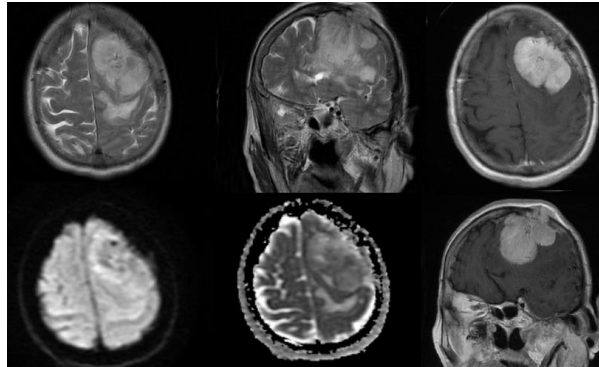
SOLITARY FIBROUS TUMOR IN THE CENTRAL NERVOUS SYSTEM: TWO CASES

Dilşah Oral¹, Ahmet Burak Kale¹, Gülgün Yılmaz Ovalı¹

¹Manisa Celal Bayar University Hafsa Sultan Hospital Radiology Department

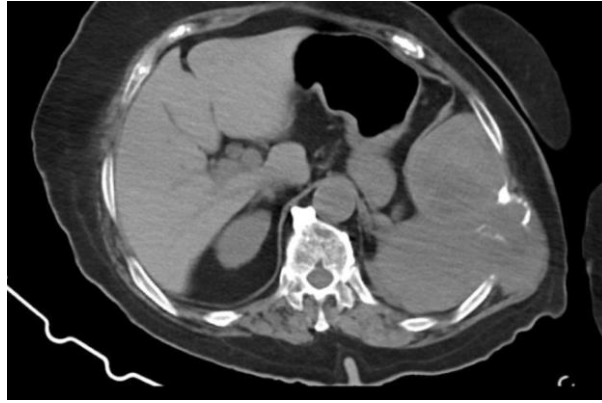
Abstract: Solitary fibrous tumors (SFTs) belong to the group of spindle cell neoplasms and are rarely observed and involvement of the central nervous system (CNS) is also rare. We'll present two cases diagnosed pathologically as SFT in CNS. The first patient is an 81-year-old female who presented with hemiplegia and headache. MRI revealed an extra-axial origin mass with intracranial and extracranial components. The lesion demonstrated linear hypointense structures and intense contrast enhancement. The patient was urgently operated on due to midline shift. The pathological findings were consistent with WHO Grade 2 SFT. Subsequent imaging revealed a large soft tissue lesion causing destruction of the 8th rib, suggestive of metastasis. The second patient is a 72-year-old male, presented with blurred vision and balance loss. MRI revealed an extra-axial mass originates from the interhemispheric surface. Lesion showed intense contrast enhancement, had heterogeneous internal structures and hypointense areas on T2-weighted images. The pathological findings were consistent with WHO Grade 1 SFT. Both of our patients were referred for radiotherapy after surgery. The first SFT case in CNS was reported in 1996. In 2016, WHO restructured the classification of both SFTs and hemangiopericytomas as variants of a single pathological entity. Approximately 0.09% of all meningeal tumors are SFTs. The most common location is the parasellar region. Mostly observed in the fourth decade in life and the most common symptom is headache. The differential diagnoses include meningioma, schwannoma etc. SFTs typically exhibit heterogeneity, containing T2 hypointense areas with intense contrast enhancement. Hypointense linear and curved structures can be seen. Bone erosion may also accompany. The absence of bone thickening can help in the differential diagnosis of meningioma. Although the radiological findings in our patients were consistent with SFTs, differentiation from meningioma could not be achieved radiologically. SFTs can metastasize extracranially, and although a standardized follow-up protocol is not established, regular monitoring is essential. The most common site of metastasis for SFTs is the bones. Surgical treatment is the primary option and also neoadjuvant radiotherapy should be considered. Due to the risk of recurrence, multidisciplinary approach is important and clinical and radiographic follow-up is essential.

Solitary Fibrous Tumor Case 1

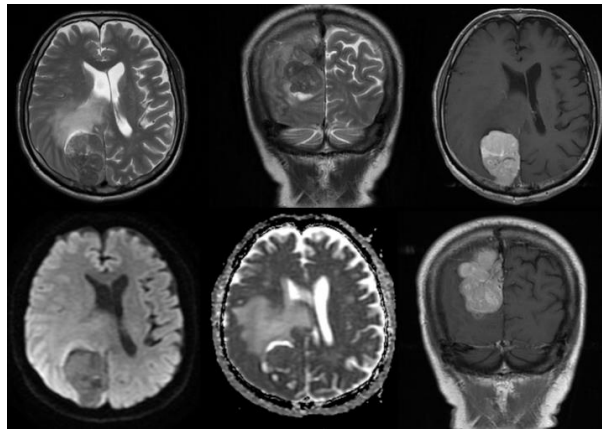


Sequences in Order: T2WI axial, T2WI coronal, T1WI contrast enhanced axial, DWI, ADC, T1WI contrast enhanced coronal

Solitary Fibrous Tumor Case 1 Bone Metastasis



Solitary Fibrous Tumor Case 2



Sequences in Order: T2WI axial, T2WI coronal, T1WI contrast enhanced axial, DWI, ADC, T1WI contrast enhanced coronal

Keywords: CNS, Solitary Fibrous Tumor, MRI, Hemangiopericytoma

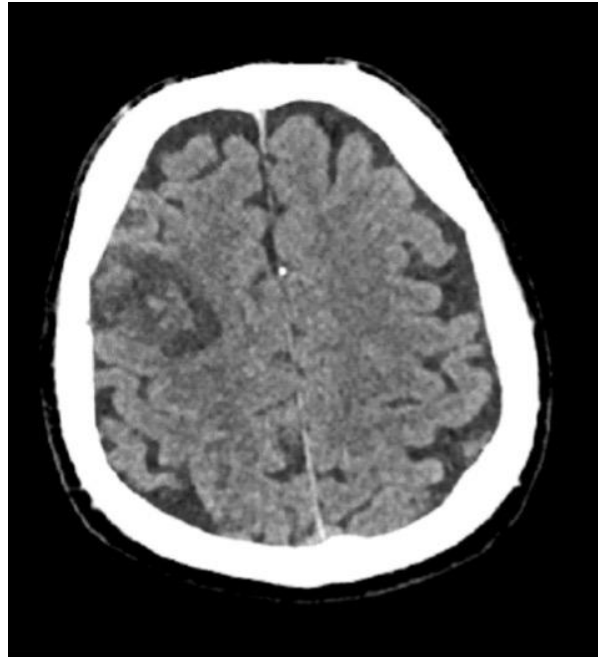
ISCHEMIC STROKE AS A RARE COMPLICATION OF A BEE STING: A CASE REPORT

Ahmet Burak Kale¹, Ozan Acar¹, Dilşah Oral¹, Gülgün Yılmaz Ovalı¹

¹Manisa Celal Bayar University, Radiology

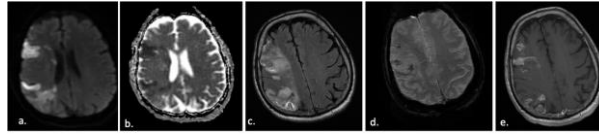
Abstract: Bee and insect stings primarily present as local skin reactions, but they can occasionally cause rare and serious outcomes in cardiac, neurological, immune, and ocular systems. The rare neurological outcomes reported include acute ischemic stroke, subarachnoid hemorrhage, acute encephalopathy and peripheral neuritis. The pathogenesis of these reactions remains unclear. Here, we present a 57-years-old male patient who was admitted to the emergency department with paresis and sensory impairment in the left upper extremity following a bee sting. A CT scan (Fig 1) revealed hypodensity in the right middle cerebral artery and borderzone areas, with hyperdense bleeding in some regions. MRI (Fig 2) showed acute diffusion restriction in the right sylvian fissure and parietal areas, suggesting hemorrhagic transformation. CTA identified (Fig 3) a soft plaque causing 70-80% stenosis in the right ICA. DSA confirmed (Fig 3) 50-70% stenosis due to an ulcerated plaque. The patient was recommended endarterectomy and was discharged with anticoagulant. Discussion: Acute ischemic stroke with etiology linked to bee and insect stings is rarely reported in the literature. According to the literature, bee and insect stings can cause ischemic stroke within a timeframe ranging from 15 minutes to 14 days. In our presented case, the bee sting occurred 4 days before the onset of symptoms. The mechanisms thought to play a role in the pathogenesis include hypotension caused by anaphylaxis, vasoconstriction aggravated by mediators released after the bee sting, and vasoactive substances in the bee venom that potentially lead to hypercoagulability (e.g., thromboxane A2, phospholipase). Literature states that epinephrine, dopamine, leukotrienes, and thromboxane in bee venom can cause not only stroke but also hemorrhage in the central nervous system. In our case, there was hemorrhagic transformation on the ischemic background. Conclusion: Given its rarity, bee and insect stings are an etiological factor that can sometimes be overlooked, particularly in central nervous system ischemia. The multifaceted etiology and unresolved molecular mechanisms necessitate an increase in our theoretical knowledge in this area. We present a case of ischemia in the right middle cerebral artery-right posterior cerebral artery irrigation area with an etiology linked to a bee sting.

Figure 1:



The right frontal region of the patient at the time of admission shows a hypodense area with occasional hemorrhagic transformation.

Figure 2:



DWI (a) and ADC (b) imaging of patient shows diffusion restriction in the temporal and occipital lobes. In FLAIR sequences (c), signal enhancement is observed in areas of ischemia. SWI sequences (d) reveal magnetic susceptibility findings consistent with hemorrhagic transformation. Post-contrast images (e) show gyral enhancement.

Figure 3:



CT angiography and DSA reveal 50-70% stenosis in the right internal carotid artery (ICA).

Keywords: Bee and insect stings, Acute ischemic stroke

A RARE CORONARY ARTERY ANOMALY: CONGENITAL ABSENCE OF THE LCX

Halil İbrahim Şara¹, Nusret Seher², Abdi Gürhan², Fatih Ateş³, Mustafa Azmi Eyio⁴

¹Konya Beyhekim Training and Research Hospital, Department of Radiology

²Selçuk University, Faculty of Medicine, Department of Radiology

³Konya City Hospital, Department of Radiology

⁴Konya Beyhekim Training and Research Hospital, Department of Cardiology

Abstract: Introduction: Coronary artery anomalies are rare and are often incidentally detected. The congenital absence of the left circumflex artery (LCX) is an extremely rare condition, with an incidence reported as 0.003% in one study. Computed Tomography Coronary Angiography (CTCA) plays a crucial role in accurately diagnosing this anomaly, as it can be mistakenly interpreted as an occluded LCX on catheter angiography. In this case report, we present the CTCA findings of LCX absence in a 59-year-old male patient. Case Report: A 59-year-old male patient presented to the cardiology clinic with complaints of chest pain. Both his electrocardiogram and echocardiogram were normal. Apart from a known history of hypertension, the patient had no chronic illnesses. The patient, a former smoker, underwent CTCA. The total calcium score was calculated as 1 according to the Agatston scoring system. Absence of the LCX was noted on the CTCA. The left anterior descending artery (LAD), diagonal branches, and right coronary artery (RCA) were well developed. A plaque causing less than 25% stenosis in the mid-LAD and superficial myocardial bridging in the distal LAD were observed. The RCA was found to supply the posterolateral wall of the left ventricle. Based on these findings, the patient was managed with medical therapy and scheduled for routine follow up. Discussion: Congenital absence of LCX is an exceptionally rare coronary anomaly. This condition often remains undiagnosed until patients undergo imaging for other cardiac symptoms. The importance of accurate diagnosis through advanced imaging techniques, particularly CTCA, can't be overstated, as it provides a detailed view of coronary anatomy. While the condition is generally benign, some patients may present with symptoms like exertional angina or even acute myocardial infarction. It is crucial for clinicians to recognize the potential for ischemic symptoms that may arise, particularly in patients with underlying risk factors such as hypertension or a history of smoking. Regular follow-up and monitoring are advised for these patients. In conclusion, congenital absence of the LCX is a rare but significant coronary anomaly that requires careful evaluation and management. Increased awareness and the use of advanced imaging techniques like CTCA can enhance diagnostic accuracy and improve patient outcomes.

Figure 1



Figure 1: (a) RCA (single arrow) and LAD (double arrow) are observed to be well-developed, while LCX is absent. (b) RCA is seen extending towards the localization of the LCX (double arrow).

Keywords: Coronary artery anomaly, Cardiac imaging, Computed Tomography Coronary Angiography

DOMINANT LCX ORIGINATING FROM THE RIGHT SINUS OF VALSALVA

Halil İbrahim Şara¹, Nusret Seher², Fatih Ateş³, Abdi Gürhan², Mustafa Azmi Eyio⁴

¹Konya Beyhekim Training and Research Hospital, Department of Radiology

²Selçuk University, Faculty of Medicine, Department of Radiology

³Konya City Hospital, Department of Radiology

⁴Konya Beyhekim Training and Research Hospital, Department of Cardiology

Abstract: Introduction: The incidence of coronary artery variations in the general population is reported to be approximately 2% . While these variations are often asymptomatic, early diagnosis is crucial as these anomalies can lead to myocardial ischemia. Computed Tomography coronary angiography(CTCA) allows for the identification of both coronary artery disease and variations. As the number of slices increases with technological advancements, image quality improves. Case Report: A 25-year-old male presented to the emergency department with sudden sharp chest pain. Laboratory tests revealed elevated levels of creatine kinase, troponin and C-reactive protein.he patient underwent an emergency CTCA evaluation. The CTCA findings showed a small-caliber right coronary artery (RCA) and the absence of the left main coronary artery. The left anterior descending artery (LAD) originated solely from the left sinus of Valsalva, while the left circumflex artery (LCX) originated separately from the inferior aspect of right sinus of Valsalva. The well-developed LCX coursed retroaortically. The LCX then followed a posterior course, supplying the posterolateral branch and the posterior descending artery. The patient, who had no evidence of stenosis, was diagnosed with acute myopericarditis.Discussion: The incidence of CAAs is relatively low, estimated at about 2% in the general population, yet they are the second most common cause of sudden cardiac death in young athletes. This underscores the importance of early detection of such anomalies.Anomalous origins of coronary arteries, especially those with an interarterial or retroaortic course, are associated with a higher risk of ischemic events due to potential compression during physical exertion. Recent advancements in imaging techniques, particularly CTCA have enhanced our ability to detect these anomalies . As the technology continues to improve, it is essential for clinicians to incorporate these diagnostic tools into routine evaluations for athletes, especially those with unexplained cardiac symptoms.In conclusion, this case exemplifies the critical nature of recognizing coronary artery anomalies in young athletes. While many individuals with CAAs may remain asymptomatic, the potential for life-threatening events necessitates a proactive approach in screening and monitoring. Continued research and awareness in this area are vital to prevent adverse outcomes and ensure the safety of athletes in competitive sports.

Figure 1

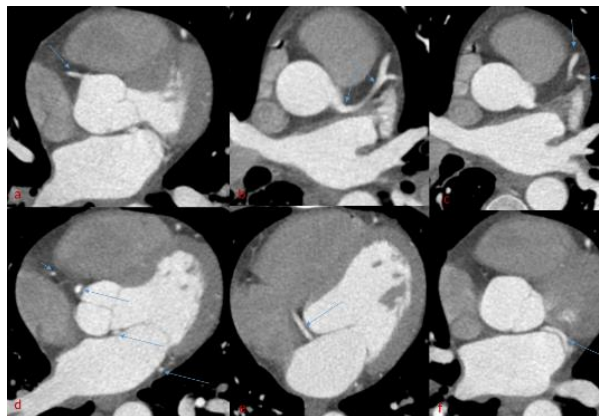


Figure 1: (a) RCA with a slightly small-caliber in its normal location. (b) LAD originating alone from the left sinus of Valsalva. (c) LAD (long arrow) and first diagonal branch (short arrow). (d) Small-caliber RCA (short arrow) and the course of the LCX originating from the right sinus of Valsalva (long arrows). (e) LCX passing retroaortically. (f) LCX returning to its normal location.

Figure 2



Figure 2: (a) Small-caliber RCA (thin arrow) and LAD (thick arrow). (b) LAD (thick arrow) and LCX (thin arrows). (c) RCA (thin arrow) and LCX originating from the inferior aspect of the RCA orifice in the right sinus of Valsalva, passing retroaortically, and coursing within the atrioventricular groove.

Keywords: Cardiac imaging, Computed Tomography Coronary Angiography, Coronary artery anomaly

A RARE CASE: UNROOFED CORONARY SINUS ASD AND PERSISTENT LEFT SUPERIOR VENA CAVA

Yeliz Akturk¹, Rasime Pelin Kavak¹

¹*Etlik City Hospital, Department of Radiology*

Abstract: Introduction Unroofed coronary sinus (UCS) atrial septal defect (ASD) is a rare congenital anomaly, accounting for less than 1% of all ASDs. It is frequently associated with persistent left superior vena cava (PLSVC). It is thought to be caused by failure to separate the superior wall of the coronary sinus from the left atrium. This leads to a direct communication between the coronary sinus and the left atrium, and a shunt may develop. It may also pose a risk for paradoxical embolization to the brain and other related complications. Case report: The heart size was significantly increased in the case. The pulmonary trunk diameter was 42 mm and dilated. PLSVC was present (Figure 1). The coronary sinus diameter was increased. Partial defect and ASD were detected in the terminal part of the coronary sinus (Figures 2,3). Discussion: PLSVC is a rare anomaly and its incidence in the general population with other cardiac abnormalities varies between 0.3% and 4.3%. However, in most cases, the left superior vena cava drains into the coronary sinus and remains asymptomatic. 8% of PLSVC cases drain into the left atrium. UCS-ASD is seen in 75% of patients with PLSVC draining into the left atrium. UCS is divided into four groups. Type I, complete UCS with PLSVC; Type II, UCS without PLSVC; Type III, partially unroofed midportion coronary sinus defect; Type IV, partially unroofed terminal portion coronary sinus defect. Type 4 UCS was detected in our case.

Figure 1

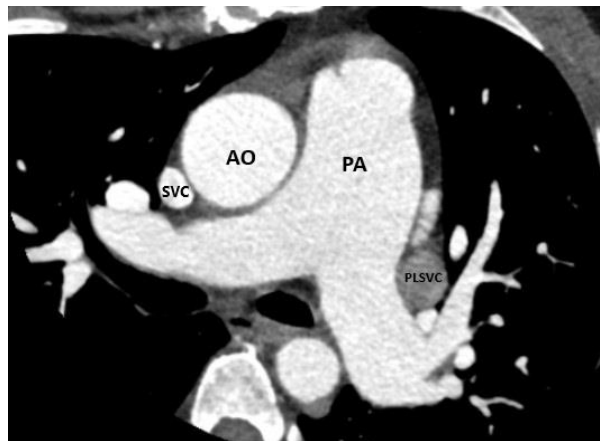


Figure 1. Axial image of coronary CT angiography. There is persistent left superior vena cava (PLSVC) and dilated pulmonary artery (PA) Ao:aorta, SVC: superior vena cava

Figure 2

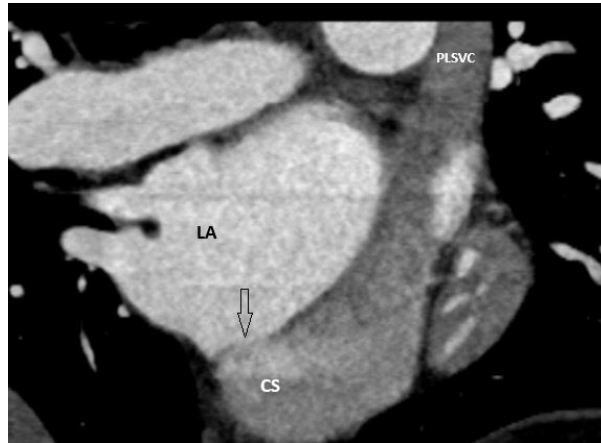


Figure 2. Sagittal oblique image of coronary CT angiography. LA: left atrium, PLSVC: persistent left superior vena cava, CS: coronary sinuse.

Figure 3



Figure 3. Axial image of coronary CT angiography. RA: right atrium, LA: left atrium, CS: coronary sinuse.

Keywords: Unroofed, coronary sinus, ASD, PLSVC

A RARE CORONARY ARTERY ANOMALY: LEFT MAIN CORONARY ARTERY ORIGINATING FROM RIGHT SINUS VALSALVA

Halil İbrahim Şara¹, Nusret Seher², Abdi Gürhan², Fatih Ateş³, Mustafa Azmi Eyiöl⁴

¹Konya Beyhekim Training and Research Hospital, Department of Radiology

²Selçuk University, Faculty of Medicine, Department of Radiology

³Konya City Hospital, Department of Radiology

⁴Konya Beyhekim Training and Research Hospital, Department of Cardiology

Abstract: Introduction: Coronary artery disease (CAD) is a significant health concern globally, characterized by the accumulation of atheromatous plaques in the coronary arteries. The clinical evaluation of chest pain, particularly in older adults, necessitates comprehensive diagnostic approaches. This case presentation discusses a 68-year-old female patient with a history of hypertension who presented with chest pain and early fatigue, focusing on the vascular anomaly observed in coronary CT angiography (CCTA). CASE: 68-year-old female patient presented to the clinic with complaint of chest pain. Her medical history included hypertension. Initial evaluations, including ECG and echocardiography, returned normal results. Given her symptoms and risk factors, CCTA was performed to assess for possible CAD. The CCTA findings were notable for the following: The LMCA originated from the right coronary sinus. The LMCA followed a retroaortic course, and the calibers of the LAD and LCX arteries were significantly reduced, raising concerns for obstructive CAD. These findings highlight the importance of advanced imaging techniques in diagnosing coronary artery anomalies and assessing the risk of ischemia. Discussion: The case underscores the role of CCTA as a non-invasive imaging modality. CCTA has gained recognition for its ability to visualize coronary artery anatomy and detect significant stenosis. The anatomical variant observed in this patient, where the LMCA arises from the right coronary sinus, is uncommon. Such anomalies can have significant clinical implications, including increased risk of myocardial ischemia due to mechanical compression. The retroaortic course of the LMCA is particularly concerning as it may lead to ischemic symptoms in increased cardiac workload. The significant reduction in caliber of the LAD and LCX arteries suggests the presence of obstructive disease, which could be attributed to atherosclerosis or the anatomical anomaly itself. Given the findings, it is crucial for clinicians to consider further evaluation and potential intervention. The management of patients with coronary artery anomalies may involve medical therapy, lifestyle modifications, and possibly revascularization procedures. Conclusion: This case illustrates the importance of thorough evaluation in patients presenting with chest pain, particularly in the context of atypical coronary anatomy. CCTA serves as a valuable tool in identifying coronary artery anomalies and assessing the risk of CAD, guiding management decisions to optimize patient outcomes.

Figure 1

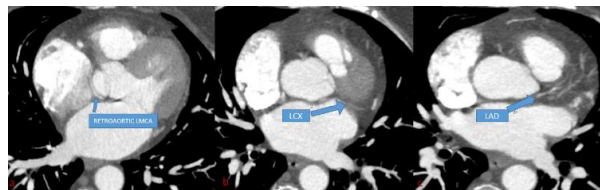


Figure 1: A retroaortic, narrow-caliber LMCA originating from the right coronary sinus, along with narrow-caliber LCX and LAD, is observed.

Keywords: Cardiac imaging, Computed Tomography Coronary Angiography, Coronary artery anomaly

A RARE CASE: PULMONARY CEMENT EMBOLISM

Halil İbrahim Şara¹, Nusret Seher², Abdi Gürhan², Fatih Ateş³, Öznur Güvenç Uzunay⁴

¹Konya Beyhekim Training and Research Hospital, Department of Radiology

²Selçuk University, Faculty of Medicine, Department of Radiology

³Konya City Hospital, Department of Radiology

⁴Konya Beyhekim Training and Research Hospital, Department of Chest Diseases

Abstract: Introduction: Percutaneous vertebroplasty is a simple and minimally invasive procedure used in cases of pain and spinal instability due to osteoporotic compression fractures or spinal osteolytic lesions. Complications may include bleeding, pain, infection, leakage of polymethylmethacrylate cement into the spinal canal or paravertebral soft tissues, perivertebral venous leakage, and, rarely, cement embolism into the pulmonary artery (1-3). In this report, we aim to present the imaging findings of a patient with cement embolization in the pulmonary artery. CASE: An 81-year-old female patient presented to the clinic with complaints of shortness of breath. Elevated D-dimer levels were detected, and the patient was evaluated with pulmonary CT angiography. Imaging revealed tubular and nodular hyperdense filling defects extending from the distal right pulmonary artery to the proximal lobar branches. A filling defect distal to the medial segment of the right lung's middle lobe was noted, showing a pulmonary infarction. Additionally, similar hyperdense filling defects were observed in the azygos vein and inferior vena cava during the examination. It was discovered that the patient had undergone vertebroplasty a week earlier. Based on the clinical history and imaging findings, the patient was diagnosed with pulmonary cement embolism. Discussion: Percutaneous vertebroplasty is the procedure that involves the injection of PMMA cement into the vertebral body under radiologic guidance. Its primary indications are painful compression fractures. Although it is a safe procedure, cement leakage into the venous system and the migration of cement into the inferior vena cava and subsequent development of pulmonary embolism is also always a potential risk. Additionally, the risk is higher in malignant tumors that have high vascularity. Pulmonary cement embolism can be asymptomatic during the procedure; however, fatal cardiopulmonary complications may also occur. The characteristic radiographic findings include multiple tubular or branching radiopacities, on non-contrast CT scans. In cases with focal filling defects, distinguishing between calcified granulomas and emboli can sometimes be challenging. If preoperative CT or direct radiographs are available, newly developed opacities are significant in this context. Well-defined opacities that are entirely surrounded by lung parenchyma, not associated with the pulmonary artery should be considered more likely to be calcified granuloma.

figure 1



Figure 1: Radiography reveals radiopaque tubulonodular appearances (a). In CT images, these opacities are observed to be intraluminal within the pulmonary artery branches (b,c).

Figure 2

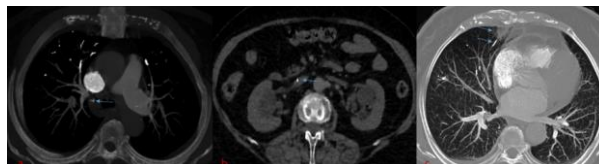


Figure 2: The hyperdense cement material is observed in the azygos vein (a) and the inferior vena cava (b). Cement material is seen in the distal segmental arterial branch of the medial segment of the middle lobe, with a pulmonary infarction appearance in the distal lung area (c).

Keywords: Pulmonary Embolism, Cement embolism, Vertebroplasty, thorax radiology

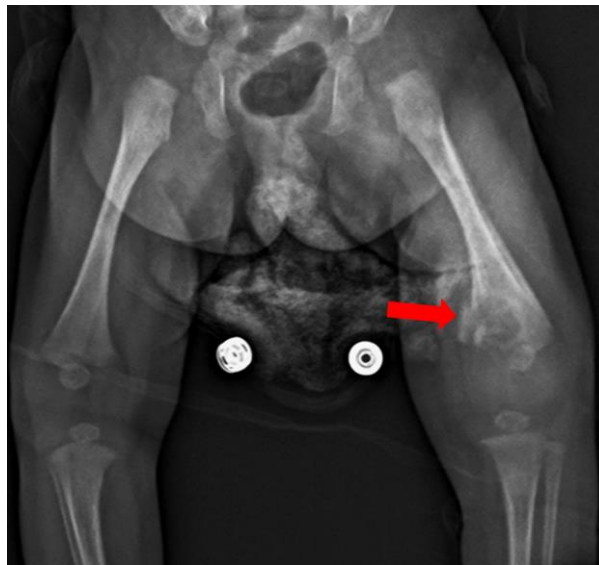
NEONATAL OSTEOMYELITIS: PLAIN RADIOGRAPHY AND ULTRASOUND FINDINGS

Nisa Serin¹, Abdi Gürhan¹, Mehmet Öztürk¹

¹Selcuk University, Faculty of Medicine, Department of Radiology, Division of Pediatric Radiology

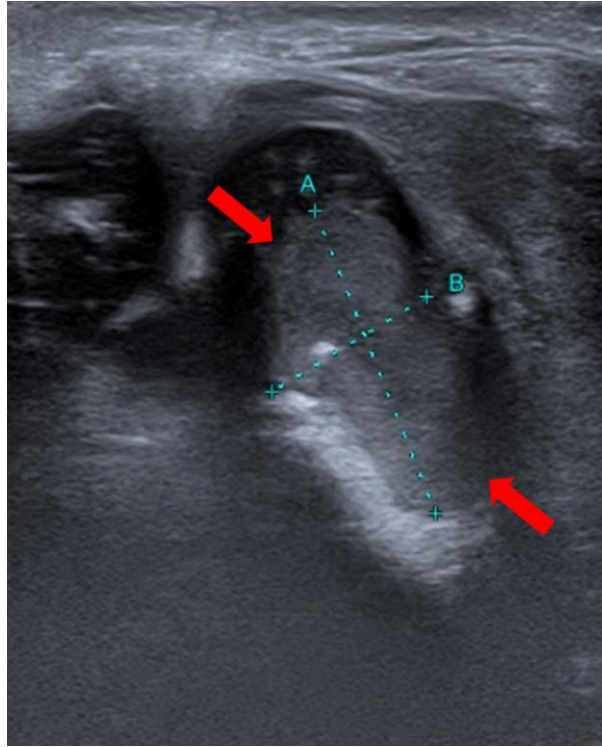
Abstract: Introduction: Acute osteomyelitis in neonates, though rare, presents significant diagnostic and therapeutic challenges. Neonates, particularly preterm infants, are more susceptible to osteomyelitis due to their immature immune systems and frequent invasive procedures. The well-perfused metaphyses of long bones, with limited functioning phagocytes, are the most common infection sites in hematogenous osteomyelitis. Diagnosis is often delayed due to non-specific symptoms and relies on clinical signs, laboratory findings, and radiological and microbiological criteria. Case: A 12-day-old male presented with redness and increased temperature in the left knee. Differential diagnoses included septic arthritis and osteomyelitis. Direct radiographs revealed a radiolucent, irregularly defined area in the left femur metaphysis. Ultrasound showed a dense fluid collection extending from the intramedullary cavity at the distal metaphyseal level of the left femur, disrupting cortical integrity and extending into the subperiosteal space. The intramedullary component measured 10x20 mm, with subperiosteal thickness up to 10 mm. Loss of integrity in the distal metaphysis was observed, along with a dense fluid collection in the knee joint space and edema-like echogenicity increases in surrounding tissues. Thus patient was diagnosed as osteomyelitis. Discussion: Neonatal osteomyelitis is a serious condition affecting the skeletal system, occurring more frequently in high-risk pregnancies, preterm infants, and with invasive device use. Staphylococcus aureus is the most common causative organism. Early diagnosis is challenging due to limited clinical signs but crucial for optimal outcomes. Radiological investigations play a vital role in confirming suspicion, defining infection sites, differentiating between unifocal and multifocal patterns, and identifying complications. Various imaging modalities, including CT, MRI, ultrasound, radiography, and bone scintigraphy, can detect osteomyelitis. However, considerations such as radiation exposure, sedation requirements, and patient transfer must be factored into technique selection. Radiographs, recommended as the initial diagnostic tool, offer high specificity (75-83%) but lower sensitivity (43-75%) for osteomyelitis detection. They can suggest the correct diagnosis and exclude other pathological conditions, making them a valuable first-line imaging option despite their limitations in early-stage detection.

Figure 1



Plain radiograph showing periosteal reaction and a lytic area consistent with osteomyelitis disrupting cortical integrity in the distal metaphysis of the left femur (red arrow).

Figure 2



Ultrasound image demonstrating abscess formation adjacent to the distal metaphysis of the left femur (red arrows).

Keywords: osteomyelitis, musculoskeletal imaging, neonatal radiology, metaphysis

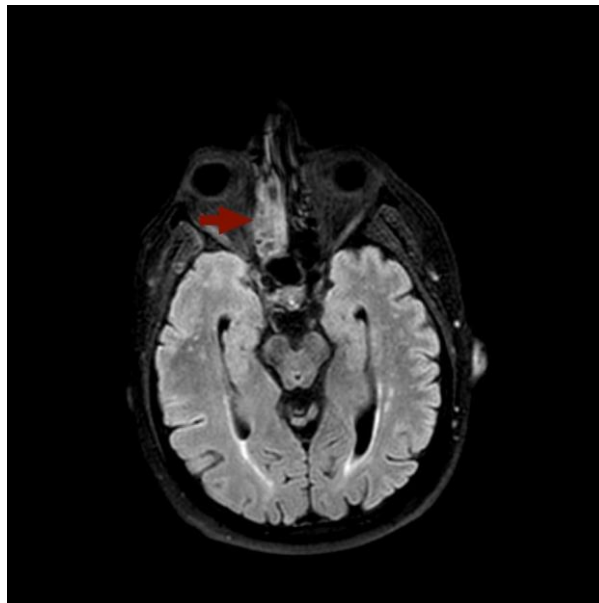
A RARE CASE; TRIGEMINAL NERVE ROOT INVOLVEMENT OF SINONASAL MUCORMYCOSIS IN AN IMMUNOCOMPROMISED PATIENT

Damla Arslan¹, Seda Sogukpınar Karaagac¹

¹Department of Radiology, Faculty of Medicine, Firat University, Elazığ, Turkey

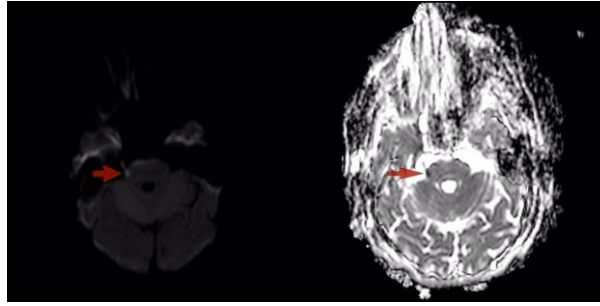
Abstract: A 61-year-old male presented to the emergency department complaining of facial numbness. The patient reported pain and tingling on the right side of his face. His past medical history includes diabetes mellitus, hypertension, p-ANCA + vasculitis and chronic kidney disease. He was undertreated of high dose prednisone due to acute vasculitis, however, his symptoms aggravated. On the initial examination, the patient was alert and oriented with a Glasgow Coma Scale (GCS) of 15/15. The pupils were 3 mm equal and reactive. There was sudden onset of right lower facial paralysis and decreased sensation to light touch, ptosis on the right palpebra. The extraocular muscle movement was intact. The visual fields were intact to confrontation with no gaze preference. The muscle power was 5/5 all over the limbs. Additionally, he described diplopia and developed dysarthria. Laboratory investigations showed the random blood glucose level was 221 mg/dL and creatinine was 2,92 mg/dL. During hospitalization, he developed limitations in the right eye movement. And acute phase reactants increased. Oropharyngeal examination demonstrated an ulcer black lesion on right middle concha and palatum drum. An endoscopic nasal examination biopsy revealed mucormycosis. Diffusion and contrast-enhanced brain magnetic resonance imaging (MRI) performed and showed soft tissue appearances compatible with inflammation, which filled the nearly right sinonasal region completely (Figure 1). In addition to, right trigeminal nerve root and trigeminal nerve nucleus in the right half of the pons showed enlargement and hyperintensity on T2 weighted images and restriction on diffusion images (Figure 2a, 2b). The patient underwent a wide debridement involving sinuses and conchas. The patient's hyperglycemia was controlled with insulin and intravenous antifungal treatment was begun. Mucormycosis, also known as black fungus, is a rare but aggressive fungal infection caused by the Mucorales fungi. This opportunistic infection predominantly affects immunocompromised individuals, with diabetes mellitus, chronic kidney disease (CKD) and under immunosuppressive treatment as a predisposing factor. The triad of diabetes, CKD, and mucormycosis presents a challenging clinical scenario, often leading to severe outcomes if not promptly diagnosed and treated. In advanced stages, mucormycosis may rarely present with cranial nerve involvement, as observed in our case.

Figure 1



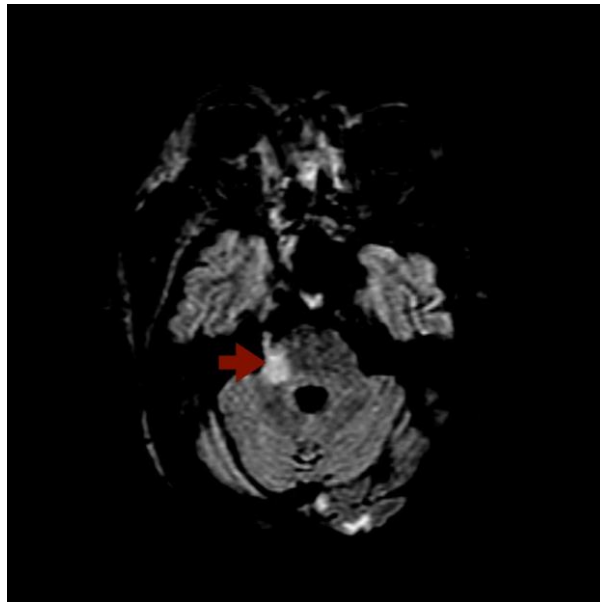
Soft tissue appearances filling the ethmoidal cells (arrow) and sinonasal space on the right (nasal sampling revealed mucormycosis)

Figure 2a



Diffusion restriction in the trigeminal nerve root and pons (arrow) (a) and high hyperintensity in the FLAIR image (b)

Figure 2b



Diffusion restriction in the trigeminal nerve root and pons (arrow) (a) and high hyperintensity in the FLAIR image (b)

Keywords: Mucormycosis, Trigeminal nerve, Immunocompromised

LUMBAR MRI FINDINGS IN CHILDREN AND ADOLESCENTS PRESENTING WITH NON-SPECIFIC LOW BACK PAIN

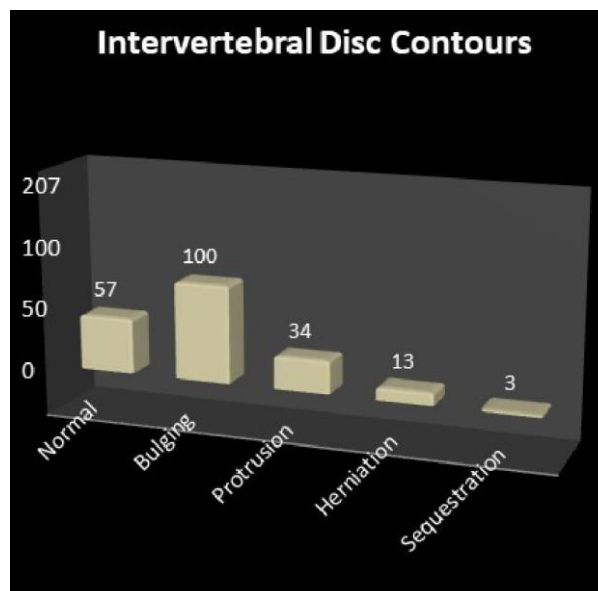
Ahmet Nedim Kahraman¹, Kamber Göksu¹, Ahmet Vural¹, Uğur Berk Akdağ²

¹Department of Radiology, Fatih Sultan Mehmet Training and Research Hospital, University of Health Sciences, Istanbul, Türkiye

²School of Medicine, Bahcesehir University, Istanbul, Turkey.

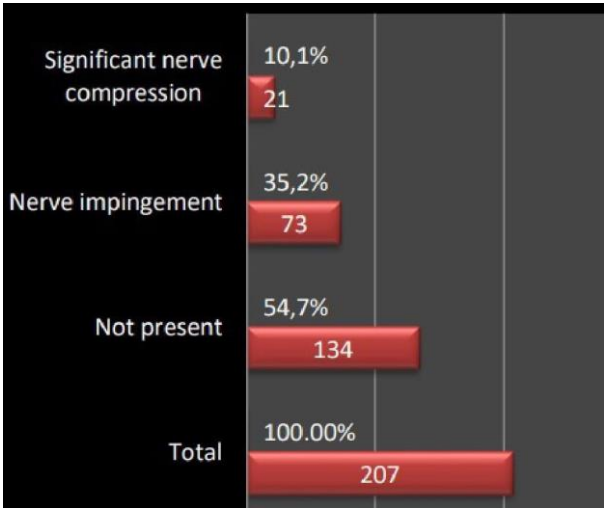
Abstract: Objectives: Low back pain (LBP) is recognized as a significant public health issue in children. LBP etiologies are categorized into mechanical, non-mechanical, and visceral causes, with benign mechanical factors accounting for over 80% of cases. Severe mechanical conditions, such as disc herniation, spinal stenosis, and spondylolisthesis, require further clinical investigations. Magnetic resonance imaging (MRI) plays a crucial role in evaluating LBP etiology, particularly in identifying lumbar spinal pathologies. Key MRI findings include intervertebral disc signal intensity, height, contours, endplate changes, and evidence of annular tears or nerve compression. Present study aims to assess lumbar MRI findings in children and adolescents with non-specific LBP and determine the prevalence of MRI findings related to mechanical LBP causes. Methods: This study retrospectively examined the MRI findings of 207 patients with non-specific low back pain. MRI scans (T1 WI, T2 WI, and T2 WI with FS) were performed in coronal, axial, and sagittal planes. The intervertebral discs were assessed by three experienced radiologists, who independently and blindly evaluated disc width, contours, signal intensities, annular tears, endplate changes, nerve impingement, spondylolisthesis, and scoliosis. Results: Totally normal disc contours were noted in 57 (27.5%) of the patients. Remaining 150 (72.5%) patients had at least one bulging, protruded, herniated or sequestered disc contour around their lumbar region. The most common disc change in the study group was bulging nucleus pulposus, and it was present in 100 patients (48.3%). 21 patients (10.1%) were found to have intervertebral space narrowing. Nerve impingement was present in 73 patients (35.2%), of which 21 patients (10.1%) had significant nerve compression. Conclusion: Non-specific low back pain in the pediatric and adolescent populations is prevalent and warrants careful consideration, often necessitating further evaluation. Radiological findings may be sufficiently pronounced to account for the clinical presentation, underscoring the need for regular and systematic assessments.

Intervertebral Disc Contours



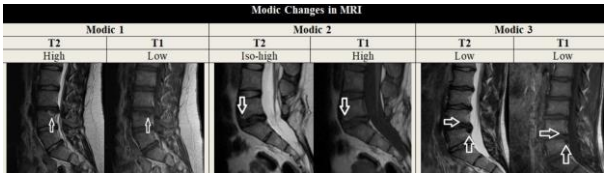
This photo demonstrates the presence of intervertebral disc contour irregularities including bulging nucleus pulposus, protrusion, herniation and sequestration

Presence of nerve compression



This photo demonstrates the presence of nerve compression in children and adolescents presenting with non-specific low back pain.

Modic Changes



This photo describes the Modic changes which are taken into consideration throughout the study

Keywords: Non-specific low back pain, intervertebral disc herniation, endplate changes, annular tear, scoliosis

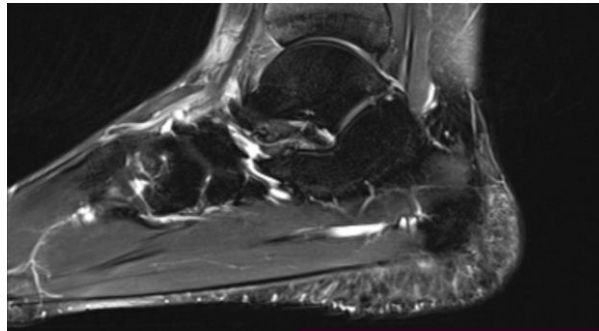
FIBROUS TALOCALCANEAL COALITION ON MRI

İbrahim Çağrı Tural¹

¹*Necipfazıl State Hospital*

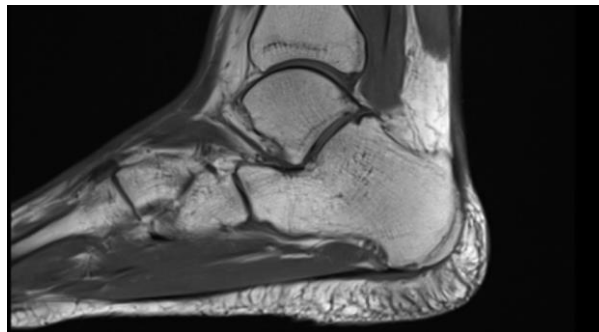
Abstract: Introduction: Tarsal coalition is defined as an abnormal union between two or more tarsal bones and is recognised as a common cause of rigid flatfeet. Tarsal coalition may be fibrous (synfibrosis or syndesmosis), cartilaginous (synchondrosis) or osseous (synostosis) in nature. The two most common coalitions are talocalcaneal and calcaneonavicular coalitions. The cause of tarsal coalition is reported to be a failure of segmentation of the primitive mesenchyme during development. Tarsal coalitions are clinically significant because they prevent normal joint motion, and they are frequently associated with non-traumatic pain and cavus foot deformity. The talocalcaneal coalition is one of the two most common subtypes of the tarsal coalition. Case: 27-year-old male was admitted with chronic joint pain. On MRI, talocalcaneal facet joint medial hypertrophy, narrowing and irregularities in joint space, irregularities on articular surfaces was detected. In the talocalcaneal joint, narrowing of the joint space in the posterior medial section, widening of the joint surfaces, cortical irregularity, and osteophyte in the posterior were observed. MRI findings are in favor of fibrous talocalcaneal coalition. Discussion: Tarsal coalitions are a not uncommon condition that may cause significant morbidity. While the diagnosis may sometimes be readily evident on clinical examination and/or imaging studies, unfortunately, the clinical examination and imaging findings can be difficult in many cases. In non osseous coalition; narrowing of the joint space and cystic reactive medium facet changes are monitored. Also it consists of hypertrophic changes in the underlying bone. Talocalcaneal coalitions are usually associated with overgrowth of the medial aspect of the talus and an abnormal morphology of the sustentaculum tali, readily detectable on CT or MRI. References 1. Jack, E. A. (1954). Bone anomalies of the tarsus in relation to "peroneal spastic flat foot". The Journal of Bone & Joint Surgery British Volume, 36(4), 530-542. 2. Kumar, S. J., Guille, J. T., Lee, M. S., & Couto, J. C. (1992). Osseous and non-osseous coalition of the middle facet of the talocalcaneal joint. JBJS, 74(4), 529-535. 3. Newman, J. S., & Newberg, A. H. (2000). Congenital Tarsal Coalition: Multimodality Evaluation with Emphasis on CT and MR Imaging 1: (CME available in print version and on RSNA Link). Radiographics, 20(2), 321-332.

Figure 1



Sagittal T2 weighted MR images of fibrous talocalcaneal coalition

Figure 2



Sagittal T1 weighted MR images of fibrous talocalcaneal coalition

Keywords: fibrous, coalition, tarsal, talocalcaneal, mri

A RARE ANOMALY: PARTIAL PERICARDIAL AGENESIS IMAGING FINDINGS

Abdi Gürhan¹, Nusret Seher¹, Mustafa Koplay¹

¹Selçuk University, Faculty of Medicine, Department of Radiology

Abstract: Introduction: The pericardium is a two-layered structure consisting of the visceral pericardium, which consists of a single layer of mesothelial cells and is and the parietal pericardium, which is a fibrous structure. The function of the pericardium is to stabilize the heart in the thorax, minimize friction, and act as a physical barrier against infection and trauma. Defective development of the pleurapericardial membrane, results in pericardial agenesis, most commonly on the left. In this report, Computed Tomography coronary angiography (CTCA) findings of a patient who diagnosed with partial pericardial agenesis will be presented. Case Report: A 43-year-old male patient was admitted to our hospital with a complaint of stinging chest pain. Right-axis QRS deviation associated with incomplete right bundle branch block (RBBB) was detected in the electrocardiogram (ECG). Due to long-term smoking history, the patient underwent CTCA. In CTCA, excessive levoposition and deviation of the apex to the left were observed. Additionally, it was observed that the pericardium was present on the right side of heart but absent on the left. Thus, the patient was diagnosed with congenital partial pericardial agenesis and was put under medical follow-up. Discussion: Pericardial agenesis is a very rare anomaly with an incidence of 0.002%. While the majority of patients are asymptomatic, some may present with chest pain or cardiac conduction problems. Even in some patients, the anomaly can result in mechanical impairment of cardiac function and even death. Although the diagnosis is usually incidental cardiac levoposition, abnormal septal motion and increased mobility of the heart can be seen on echocardiography. Developing MRI and CTCA technologies have enabled this defect to be recognized more frequently. In both examinations, the absence of pericardium, excessive levoposition, lung tissue entering the aortapulmonary window, or herniation of the left atrial appendage through the defect can be detected. Excessive movement of the heart can also be detected in cardiac MRI cine sequences. Although treatment is generally not required, surgery may be required if strangulation of cardiac structures develops. Conclusion: As radiologists, we need to be careful about this diagnosis, as pericardial agenesis can be easily detected by radiologists and unnecessary interventions and complications can be prevented.

Figure 1

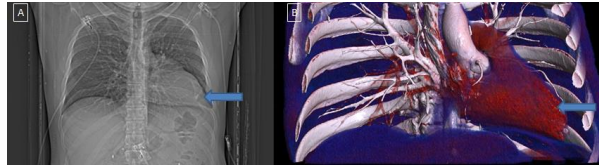


Figure 1: Excessive levoposition of the heart (blue arrow) is shown in the scenogram (A) and the 3D VRT image (B) created from the CTCA.

Figure 2

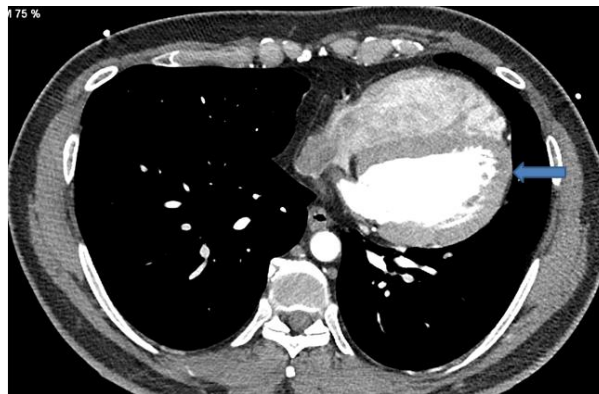


Figure 2: Excessive levoposition of the heart (blue arrow) is observed in the axial CTCA image.

Figure 3

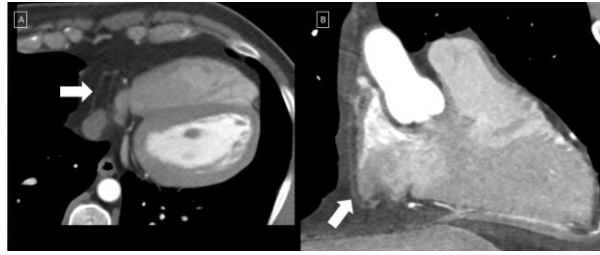


Figure 3: Axial CTCA (A) and Oblique coronal MPR CTCA (B) image shows that the pericardium (white arrow) is present on the right side of the heart, but it ends blindly and does not continue on the left side and the inferior border.

Keywords: Cardiac imaging, Computed Tomography Coronary Angiography, Pericardium, Congenital Cardiac Anomaly

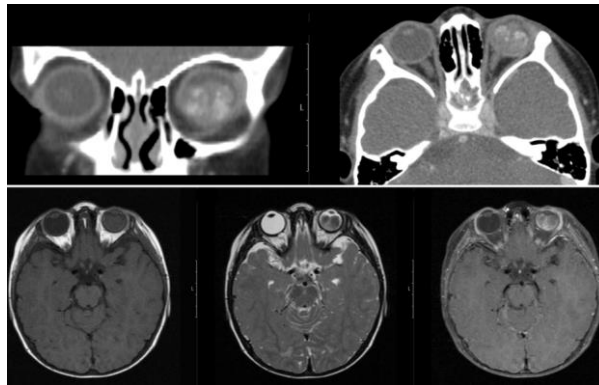
ORBITAL TUMORS

Melike Zeynep AYBAK¹, Süleyman Men¹

¹Dokuz Eylül University Hospital Radiology Department

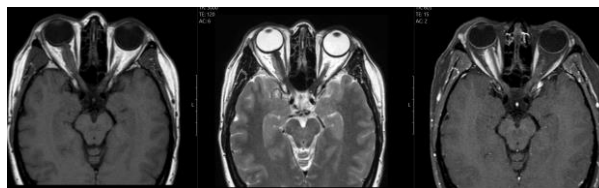
Abstract: ORBITAL TUMORSINTRODUCTIONThe orbit is a small anatomical space, but the wide range of structures present within it are often the site of origin of various tumors, both in adults and children. Imaging is mandatory for the detection, characterization, and mapping of these lesions. We herein describe orbital tumors as lesions of the globe (retinoblastom, uveal melanom, choroidal hemangiom), optic nerve sheath complex (schwannoma, optic nerve glioma, optic nerve meningioma), vascular structure of the orbit (capillary hemangioma, cavernous hemangioma, vascular malformation), conal-intraconal (lymphoma, rhabdomyosarcoma), and extraconal compartment (lacrimal tissue tumors).The purpose of this review is to describe imaging characteristics of each orbital tumor from our archives. DISCUSSIONWhen a lesion is seen in the orbit, one of the things to do is to decide whether it is an ocular or non-ocular lesion, meaning whether it affects the globe or structures outside the globe. If it is a non-ocular lesion, the next question is whether the lesion is located in the intraconal space, meaning the space bounded by the cone formed by the extraocular muscles, or in the conal or extraconal space. In this way, differential diagnoses can be made. Specific imaging patterns can aid in differentiating between tumor types. Common orbital tumors include lymphomas, meningiomas, retinoblastomas, and uveal melanoma, each exhibiting distinct imaging features. For instance, lymphomas typically present as homogenous soft-tissue masses with moderate enhancement, while meningiomas may show a characteristic dural tail on imaging. Retinoblastoma can appear with calcifications, and uveal melanoma shows variable intensity with the tumor's pigmentation. CONCLUSIONIn conclusion, benign and malignant orbital tumors can be challenging for image interpretation. Appropriate imaging modalities, knowledge of orbital anatomy, and being aware of characteristic appearances and key features on cross-sectional images (CT and MRI) of orbital tumors help to make the correct diagnosis. We hope that this pictorial review served the purpose of highlighting these points.

Reinoblastoma



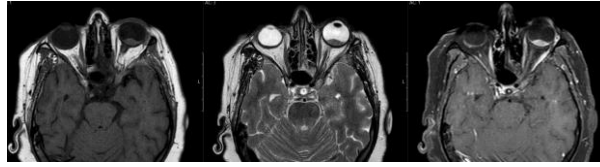
2 year old boy, there is a mass formation containing calcific areas in the left eyeball, filling nearly 90% of the eyeball. The lesion is hyperintense in T1W images and hypointense in T2W images compared to the vitreous and shows heterogeneous enhancement in contrast-enhanced series.

Optic Nerve Sheath Meningioma



54 year old woman. In the case, an appearance compatible with optic nerve sheath meningioma is observed on the right side, isointense with brain parenchyma in T1 and T2 weighted sequences, and shows homogeneous enhancement in contrast-enhanced series, surrounding the optic nerve (tram-track sign).

Uveal Melanoma



54 year old woman. A mass lesion compatible with choroidal melanoma, hyperintense in T1A series, isointense in T2A series, contrasting in the posterior part of the left bulbus oculi.

Keywords: orbital tumors, orbital lesions, orbit

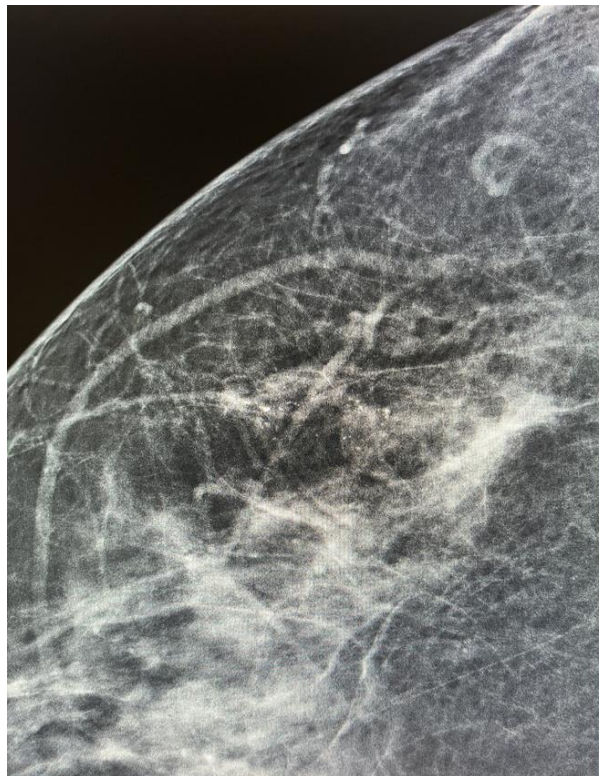
THE MAMMOGRAPHIC AND MRI APPEARANCES OF ULTRASONOGRAPHIC VISIBLE MALIGNANT BREAST MICROCALCIFICATIONS

Zeynep Banu Aydın¹

¹*Hitit University Faculty of Medicine, Radiology Department*

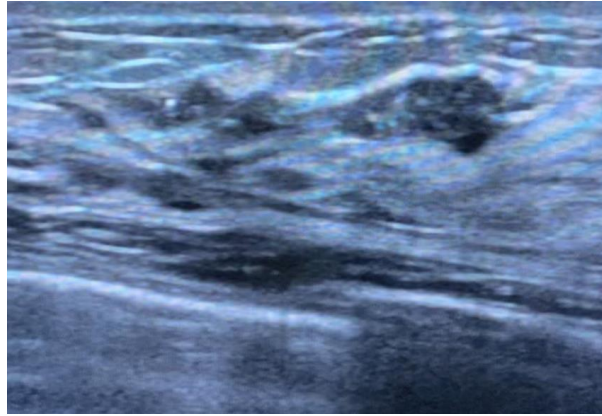
Abstract: Purpose: The aim of this study was to assess the benefits of ultrasonography on BIRADS 4-5 breast microcalcifications combined with MG and MRI. Methods: Between 2022 and 2024, 12 patients with mammographic BI-RADS 4 and 5 microcalcifications and diagnosed malignant by histopathologically were evaluated retrospectively. All our patients underwent US and MRI, and had biopsy performed after imaging work-up was finished. Results: In our study group, 12 patients aged between 44-81 years, with suspicious microcalcifications detected on mammography were evaluated. Seven patients had fine pleomorphic segmental microcalcifications, two had pleomorphic linear, and three of the patients had pleomorphic clustered. On MRI, non mass enhancement was seen in nine patients, and mass enhancement in three patients. Sonographic findings were heterogeneous hypoechoic paranchim with (4 patients) or without microcalcification (4 patients) and ductal segments with microcalcifications (4 patients). US guided core needle biopsy results were eight DCIS, two infiltrative ductal carcinoma, two combined DCIS and invasive carcinoma. Also, surgical excisional histopathologic results were added; three DCIS, seven invasive ductal carcinoma with DCIS, two infiltrative ductal carcinoma. In this study, the sonographic positive microcalsifications had significantly linear and segmental mammografic appearance (9 patients), and mostly viewed MRI finding was segmental or regional heterogeneous nonmass enhancement (9 patients). Conclusion: Sonographic approach is important for the diagnosis of suspicious breast microcalcifications, especially the ones distributed segmental and linear on MG. Additionally, with the support of MRI findings, the benefit of sonography increases, such as second look ultrasonography. As a result of this, US guided core needle biyopsi can be performed as a less invasive method than surgical excision for the histological diagnosis of breast suspicious microcalcifications before patients undergo surgery.

Figure 1



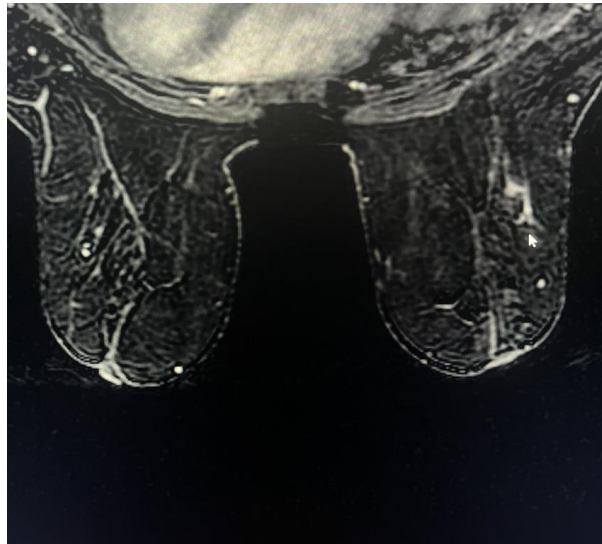
Mammografic appearance of fine pleomorphic linear microcalcifications

Figure 2



Ultrasonography of ductal segment with microcalcifications

Figure 3



MRI image after contrast administration, outer middle quadrant of right breast, linear non mass contrast enhancement.

Keywords: ultrasonography, microcalcification, breast

RADIOLOGICAL IMAGING CHARACTERISTICS OF TERATOMAS DETECTED DURING THE PRENATAL PERIOD

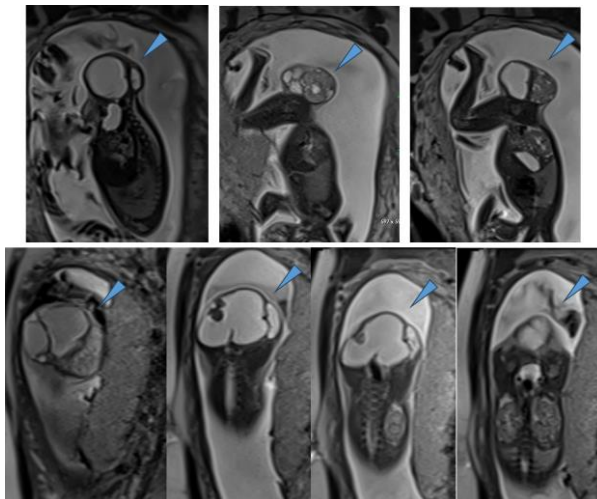
Fatih ATES¹, Mehmet Sedat DURMAZ²

¹Konya City Hospital, Radiology department

²Selcuk University, Faculty of Medicine, Radiology Department

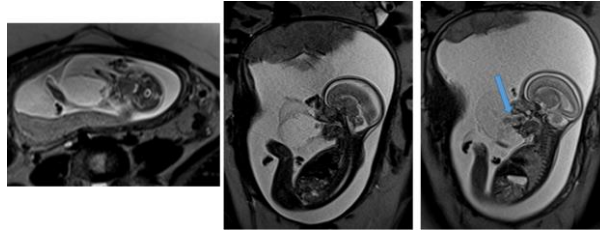
Abstract: Introduction and aim: Our aim was to examine and present the ultrasonographic (US) and fetal magnetic resonance imaging (MRI) findings of teratomas diagnosed during the prenatal period, in order to familiarize radiologists with these findings. Materials and methods: Between 2018 and 2023, an evaluation of the radiological imaging findings of patients diagnosed with teratomas in the postnatal period, which had been detected via fetal MRI or obstetric ultrasonography at a tertiary diagnostic and treatment center, was conducted using the hospital PACS system. The specified MRI and ultrasonographic examinations were reported by a physician with approximately 10 years of experience in fetal MRI and obstetric ultrasound (M.S.D). Results: A total of 8 patients were followed with a preliminary diagnosis of teratoma and underwent postnatal surgery. Among these, two were diagnosed with oropharyngeal teratomas, two with sacrococcygeal teratomas, one with an intracranial teratoma, one with a maxillofacial teratoma, one with a lumbar teratoma, and one with an umbilical cord teratoma. Discussion: The sacrococcygeal region is the most common site for teratomas and is the most frequently encountered neoplasm during fetal life. Its incidence is approximately 1 in 35,000 to 1 in 40,000 and is 3-4 times more common in female infants. In sacrococcygeal teratomas, the presence of certain factors is associated with a poor prognosis. These factors include: tumor size (greater than 10 cm), tumor growth rate, presence of solid components, tumor vascularization, polyhydramnios (which may indicate high-output cardiac failure), and increased placental thickness. In addition to sacrococcygeal teratomas, fetal teratomas can also be found in other regions, including the head-brain, face-neck, thorax-heart, abdominal-retroperitoneal, sacral-genital, extremities, skin, and placenta. Conclusion: US is an important non-invasive technique for early diagnosis and monitoring. Doppler imaging is used to assess the tumor's vascularity. MRI complements US by providing superior detail on: Tumor localization, Effects on surrounding tissues and structures, Tumor size and growth, The relationship between the mass and airway structures, including pressure on the esophagus and trachea. Additionally, MRI can aid in the selection of fetuses requiring respiratory support. MRI is a crucial imaging modality in treatment planning, including determining the timing and mode of delivery.

Figure 1



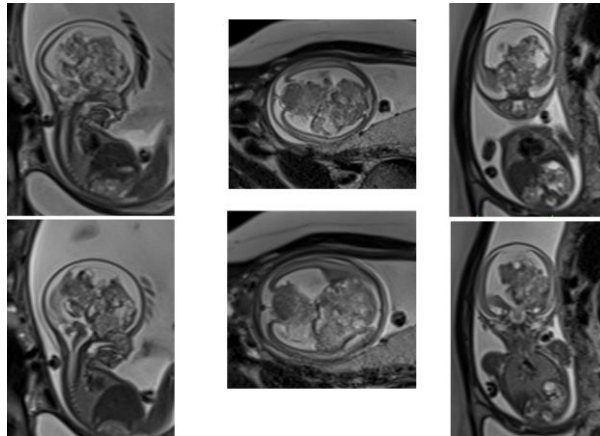
A teratoma observed in the sacrococcygeal region is typically visualized on fetal MRI sections as a mass with heterogeneous cystic components. This diagnosis was made via ultrasound. Ultrasound images and postnatal imaging are also available for this patient.

Figure 2



Axial and coronal sections of a cervicofacial teratoma case are presented with MRI findings. The patient's images from 12 weeks ago are available, showing a mass with significant size increase on follow-up. Additionally, fetal MRI was crucial for determining the delivery method and for prenatal monitoring in this case.

Figure 3



In a 19-week pregnant patient, a heterogeneous, irregularly defined mass occupying space in the intracranial area was observed. This diagnosis of an intracranial mass was made via ultrasound. Ultrasound images are available. The patient unfortunately expired in the early postnatal period.

Keywords: Sacrococcygeal teratoma, Fetal MRI, Obstetric US, Oropharyngeal teratomas

TART (TESTICULAR ADRENAL REST TUMORS)

Laman Huseynzade¹

¹Ege University Faculty of Medicine Hospital

Abstract: Introduction: Congenital adrenal hyperplasia (CAH) describes a group of inherited autosomal recessive disorders characterized by enzymatic defects in the steroidogenic pathways. Therefore that leads to decreased biosynthesis of steroid hormones such as cortisol, aldosterone, and androgens. 21-Hydroxylase deficiency is the most common cause of CAH. ACTH synthesis results in hyperplasia of ACTH sensitive tissues in adrenal glands and other sites of ectopic adrenal tissue such as the testes. Aberrant adrenal tissue that has become hyperplastic because of elevated ACTH causes testicular masses known as testicular adrenal rest tumors (TARTs). Here we report a case of TART in a 16-year-old man with CAH. Case report: A 16-year-old male patient applied to us because he was taller than his peers and he started growing hair in the armpit and genital areas when he was 3 years old. He was referred to the endocrinology outpatient clinic. Genkort treatment was started with the preliminary diagnosis of CAH, concomitant HT was detected, but no treatment was given. He could not receive Genkort treatment regularly, there were occasional interruptions in the treatment, and he did not go for regular check-ups. At the age of 10-11, he became shorter compared to his peers. The patient, who was diagnosed with CAH 3 months ago because he was shorter than his peers, was referred to us for further examination and treatment with suspicion of 11-beta hydroxylase. MRG with These lesions are isointense (on T1) and hypointense (on T2 weighted images) to the remaining testicular parenchyma. No restricted diffusion is seen in these lesions. These lesions show avid enhancement (more than the normal testicular parenchyma) on post-contrast images. Conclusion and discussion :ARTs are the most recognized tumors in CAH. Their reported prevalence varies between 0 and 94%, and they may already appear during childhood. They occur in patients with CAH and poor hormonal control, due to high levels of ACTH and angiotensin II (AII) that stimulate the ectopic adrenal tissue within the testicles. They are bilateral and benign. In some cases, TARTs cause compression of the seminiferous tubules that may lead to obstructive azoospermia, irreversible damage of the surrounding testicular tissue, and consequently infertility.

Keywords: tart.testikuler tumors

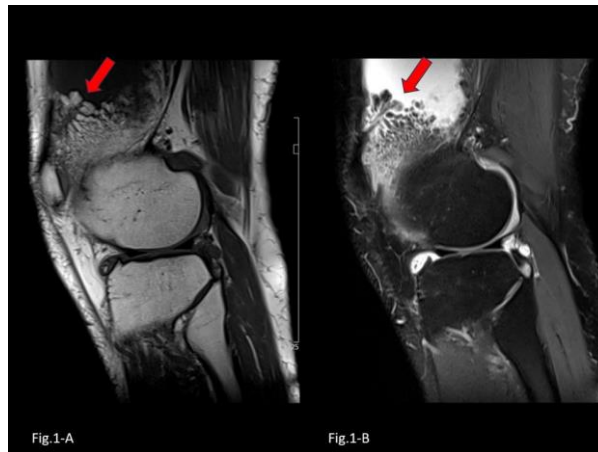
LIPOMA ARBORESCENS OF THE KNEE ON MRI: A RARE CASE REPORT

Kübra Bozkurt¹, Hüseyin Bozkurt¹, Hanife Özdemir¹, Abdullah Soydan Mahmutoğlu¹

¹Istanbul Training And Research Hospital, Department Of Radiology

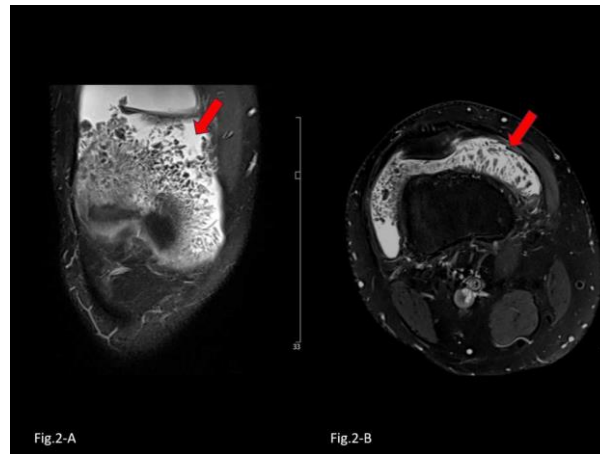
Abstract: **INTRODUCTION:** Lipoma arborescens (LA) is a benign condition where mature fat cells proliferate in the synovium, primarily affecting the knee. It is an uncommon cause of intermittent knee pain and effusion. Magnetic resonance imaging (MRI) is crucial for diagnosis, revealing the characteristic tree-like projections, and is improving recognition of this condition. **CASE PRESENTATION:** We report a case of LA in a 35-year-old male with 3 years of knee pain and swelling. The patient had no significant surgical history, family history of disease or chronic conditions. Laboratory results showed no inflammatory changes and were negative for rheumatoid factors. MRI revealed frond-like villous projecting from the synovium into the joint, with high signal intensity on T1-weighted images and low signal on PD-weighted images with fat saturation (FS), predominantly in the suprapatellar pouch. Additionally, the MRI examination showed minimal degenerative changes (Figure 1,2). **DISCUSSION AND CONCLUSION:** Synovial lipomatosis is a rare benign condition with tree-like projections of fat cells in the synovium, first described by Dr. Albert Hoffa in 1904. It typically affects adults, though cases in children have been reported. The etiology is considered idiopathic but may be linked to chronic synovial irritation and inflammatory conditions. MRI helps differentiate it from other synovial pathologies and identifies associated conditions like joint effusion and meniscal tears. MRI is the gold standard for diagnosis, showing hyperintense leaf-like projections on T1WI/T2WI and fat suppression on STIR sequences. No blooming is seen on gradient imaging. While subsynovial tissue doesn't enhance with contrast, the inflamed thickened synovium may show diffuse enhancement. While these lesions may be missed on plain radiographs, ultrasonography and CT can provide diagnostic information. Lipoma arborescens typically affects the suprapatellar region of the knee but can involve other joints. Treatment usually involves open or arthroscopic synovectomy, allowing for complete lesion removal and promoting early recovery. Early intervention is crucial to prevent joint degeneration and achieve excellent outcomes with rare recurrence.

Figure 1



MRI images, including sagittal T1-weighted (1-A) and PD-weighted with FS (1-B), demonstrate several frond-like villous projecting from the synovium into the joint and joint effusion (Red Arrow).

Figure 2



MRI images, coronal PD-FS (2-A) and axial PD-FS (2-B), show frond-like villous projecting from the synovium into the joint and joint effusion (Red Arrow).

Keywords: Lipoma Arborescens, Magnetic Resonance Imaging, Knee, Synovial Lipomatosis

MRI OF OVARIAN CYSTADENOMAS

Mete Sezer¹, Merve Başdemirci², Onur Başdemirci², Safiye Gürel³, Samet Töken³

¹Department of Radiology, Bolu Abant İzzet Baysal University, İzzet Baysal Training and Research Hospital

²Department of Radiology, Karabük Training and Research Hospital

³Department of Radiology, Gülhane Medical School, Gülhane Training and Research Hospital

Abstract: INTRODUCTION: Epithelial neoplasms of the ovary account for 60% of all ovarian tumors and 40% of benign tumors. They are classified as benign, borderline, and malignant tumors. Ovarian cystadenomas are common benign epithelial neoplasms with an excellent prognosis. The two most frequent types of cystadenomas are serous and mucinous cystadenomas whereas endometrioid and clear cell cystadenomas are rare. Despite advances in imaging studies, the establishment of a definitive diagnosis of cystadenomas is primarily by histopathological examination of the surgical specimen [1]. TEACHING OBJECTIVE: 1. To Review MRI findings of ovarian cystadenomas REVIEW OF THE TOPIC: Imaging Studies: Several imaging techniques are useful for the diagnosis of ovarian cystadenomas. They include Pelvic ultrasonography (US), Computed tomography (CT) and Magnetic resonance imaging (MRI). Benign epithelial ovarian neoplasms are predominantly cystic, in contrast to malignant epithelial neoplasms which comprise both cystic and solid components. Cystic lesions containing simple fluid have prolonged T1 and T2 relaxation times and very high signal intensity on T2-weighted images. The features that are more suggestive of a benign cystic neoplasm include: Unilocularity of cysts, minimal septations, thin walls and absence of papillary projections. Complications: Cystadenomas of the ovary are benign lesions that rarely recur after incomplete resection. Rare complications of ovarian cystadenomas include: Ovarian torsion and cyst rupture. There is a risk of the development of pseudomyxoma peritonei if a mucinous cystadenoma ruptures. CONCLUSION: Cystadenomas are among the most common tumors of the ovary, and it is important to be familiar with the imaging findings in diagnosis.

Figure 1

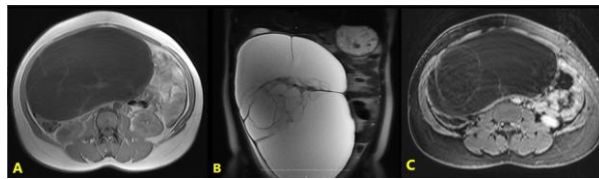


Figure 1: On MRI images, a multilocular cystic lesion originating from the pelvic region and extending to the subhepatic and epigastric region appears hypointense on T1-weighted images (A) and hyperintense on T2-weighted images (B). The lesion contained multiple septa which show contrast enhancement on postcontrast images (C). The pathology report was compatible with mucinous cystadenoma.

Figure 2

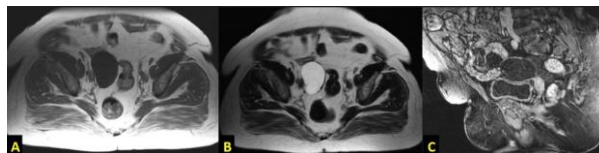


Figure 2: In the right adnexal region, there is a cystic lesion that appears homogeneous hypointense on T1-weighted images (A), homogeneous hyperintense on T2-weighted images (B) and has mild contrast enhancement in the wall and septa on the postcontrast images (C). The pathology was reported as compatible with mucinous cystadenoma.

Figure 3



Figure 3: On MRI images, a complicated cystic lesion in the left adnexal region extending superiorly to the level of the lower poles of the kidney appears hypointense on T1-weighted images (A) and hyperintense on T2-weighted images (B). The lesion contained multiple septa and its wall and septa showed minimal contrast enhancement on postcontrast images (C). The pathology was reported as compatible with mucinous cystadenoma.

Keywords: MRI, Magnetic Resonance Imaging, Ovarian Cystadenoma, Ovarian Masses

ADENOMA MALIGNUM OF UTERIN CERVIX: MAGNETIC RESONANCE IMAGING FINDINGS

Abdi Gürhan¹, Nusret Seher¹

¹Selcuk University, Faculty of Medicine, Department of Radiology

Abstract: Uterine cervix cancer is the 4th most commonly diagnosed cancer in women. Cervical cancer is generally associated with chronic HPV infections, and Squamous cell carcinoma is the most common histological type. Adenoma malignum is a rare type of cervical carcinoma and accounts for 1%-3% of cases. In this report magnetic resonance imaging (MRI) findings of a patient who diagnosed with adenoma malignum will be presented. **Case Report:** A 53-year-old postmenopausal female patient was admitted to our hospital with complaints of lower abdominal pain and watery vaginal discharge that had been going on for 2 months. An MRI was performed on the patient whose transvaginal ultrasonography revealed a multiloculated cystic lesion in the cervix and whose pap smear test result was normal. In the MRI examination, a multiloculated cystic lesion with a diameter of approximately 6 cm was observed in the uterine cervix location. (The lesion appeared to have dense content in places. In addition, nodular contrast enhancement was observed in the septae in the images taken after intravenous contrast material. Histopathological sampling was recommended to the patient whose radiological findings were compatible with adenoma malignum. **Discussion:** Adenoma malignum is a difficult diagnosis because it is rare and usually does not show any findings in pap smear. The major symptoms of adenoma malignum are abnormal vaginal discharge and vaginal bleeding as menometrorrhagia or post-menopausal bleeding. Imaging has an important place in diagnosis. On ultrasonography, a grape-like multiloculated cystic lesion and accompanying solid areas may be seen. In MRI examination, a multiloculated mass with enhanced solid components and cystic areas that is isointense relative to the uterus on the T1-weighted image and hyperintense on the T2-weighted image can be seen. Multiple nabothian cysts and tunnel cluster are included in the differential diagnosis, enlargement of the cervix and contrast enhancing solid component are not observed in these lesions. Although the prognosis is controversial, current studies report that it is quite good. The standard treatment method is surgery. **Conclusion:** Since adenoma malignum, which is a very rare entity, is a disease that can be treated with early diagnosis, we, as radiologists, must be careful about this issue.

Figure 1

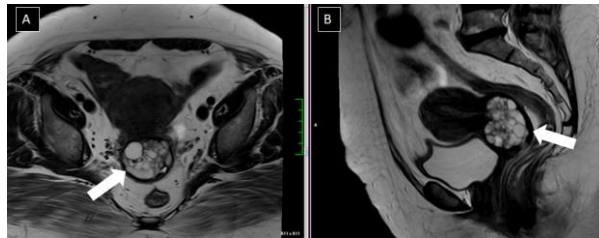


Figure 1: A hyperintense multiloculated cystic lesion (white arrow) is observed in the cervix on axial (A) and sagittal (B) non-fat suppressed T2-weighted images.

Figure 2

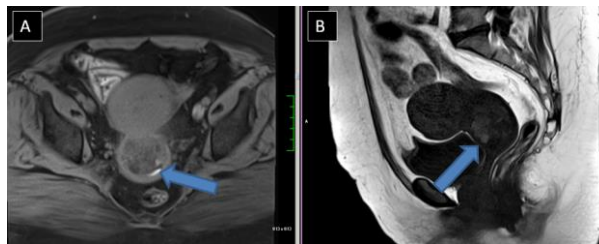


Figure 2: Axial fat-suppressed T1-weighted (A) and Sagittal non-fat-suppressed T1-weighted (B) images show hyperintense areas (blue arrow) compatible with dense content within the lesion.

Figure 3

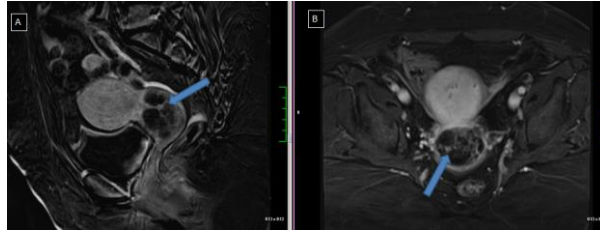


Figure 3: Sagittal (A) and Axial (B) T1-weighted Subtraction images obtained in the venous phase show a multiloculated cystic lesion which is located at uterine cervix with nodular contrast enhancement (blue arrow).

Keywords: Cervical carcinoma, Urogenital imaging, Magnetic resonance imaging

RARE ACCESSORY BONE OF THE FOOT; OS CALCANEUS SECUNDARIS

Gulseher Saylan¹, Seda Sogukpınar Karaagac¹

¹Department of Radiology, Faculty of Medicine, Firat University, Elazığ, Turkey

Abstract: The presence of accessory ossicles at the level of the foot is common; most are asymptomatic and are usually detected incidentally by radiologic imaging. However, due to the particularly complex biomechanical system of the foot, they may gain clinical significance through trauma or chronic stress. A 41-year-old man presents to the orthopedics and traumatology outpatient clinic with chronic foot pain symptoms. Non-contrast computed tomography (CT) examination of the left foot performed with suspicion of a fracture showed an accessory bone articulating with the anterosuperior aspect of the calcaneus and medially with the navicular bone. The smoothly contoured bone structure was interpreted in favor of the sesamoid ossicle of the os calcaneus secundaris (CS) (Figure 1). Intense degenerative changes and subchondral cystic degenerations were observed in the identified bone and adjacent calcaneus (Figure 2). Os calcaneus secundarius is an accessory bone that can be located in the anteromedial aspect of the calcaneus, cuboid bone, talus head and tarso-navicular space, and is often detected incidentally. However, since a CS can alter biomechanics and cause restriction in joint motion and foot sprain, it can cause secondary findings such as chronic pain, flat feet and inversion limitation. Differential diagnosis with physical examination or conventional X-rays is very difficult. CT images are helpful in demonstrating the bone structure with blunt edges and smooth contours. If there is still doubt on CT images, magnetic resonance imaging may be used to demonstrate bone marrow edema and absence of fracture. Since the benefit of surgical treatment has not been clearly established, conservative approaches such as immobilization or steroid injections are recommended in symptomatic cases.

Figure 1



3D image of the accessory bone of the os calcaneus secundaris (CS) articulating with the anterosuperior calcaneus and navicular bone

Figure 2



CT image showing intense degenerative changes and subchondral cystic degenerations in the calcaneus secundaris (CS) accessory bone and adjacent calcaneus

Keywords: Calcaneus Secundaris, Accessory bone, Sesamoid

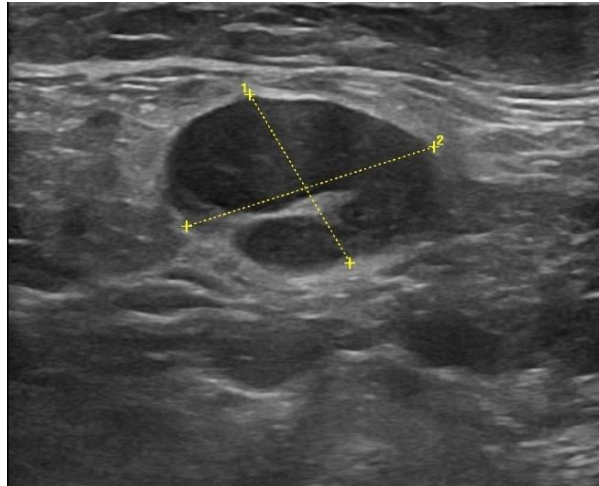
RARE INVOLVEMENT OF SARCOIDOSIS: INTRAMAMMARIAN AND BILATERAL AXILLARY MULTIPLE LYMPHADENOPATHIES

Atakan Kurt¹, Deniz Esin Tekcan Şanlı¹

¹Gaziantep University Faculty of Medicine, Department of Radiology

Abstract: Introduction: Sarcoidosis is a multisystemic, chronic granulomatous disease of unknown etiology. Although it most commonly involves the lung and mediastinal lymph nodes, breast involvement is quite rare (1,2). Granulomas occurring in the breast usually mimic inflammatory diseases such as tuberculous mastitis, granulomatous mastitis, especially breast cancer in the form of masses with irregular spiculated contours, or lymphoproliferative diseases such as lymphoma with axillary lymph node involvement, or may coexist with these in the same patient (1). However, it may suggest occult breast cancer with isolated axillary lymph node involvement (2). No case of sarcoidosis in the form of intramammary lymphadenopathy (LAP) was found in the literature. Therefore, it was aimed to share this case report with its clinical and radiological features. Case: A 39-year-old female patient presented to our clinic with a new painless mass in the left axilla. On ultrasonographic examination, multiple LAPs with bilateral thick cortex, fatty hiluses and pathological appearance, the largest of which was 35x20 in the left axilla (Figure 1). No significant sonographic findings suspicious for malignancy were found in both breasts. However, multiple hypoechoic solid lesions with smooth contour, oval and spherical shape, the largest of which was 18x10 mm in size, showing internal vascularisation on colour doppler ultrasonography (RDUS) were observed in the upper outer quadrant of the left breast at 2-3 o'clock and evaluated in BIRADS 3 category (Figure 2). Core needle biopsy was performed from the axillary lymph nodes and the lesions in the left breast due to a possibility of occult breast cancer or lymphoma. Histopathological results of both axillary lymph nodes and hypoechoic solid lesions in the breast were compatible with non-necrotising granulomatous tissue reaction. The hemogram of the patient was normal. When the patient's past history and investigations were evaluated, it was learned that multiple mediastinal LAPs were detected incidental in the non-contrast thorax Computed Tomography (CT) examination performed due to a traffic accident in 2018, transbronchial needle aspiration (TBNA) was performed from these lymph nodes with endobronchial ultrasonography (EBUS) and Sarcoidosis was diagnosed and the patient was followed up without treatment since then.

Figure 1



Left axillary lymphadenopathy

Figure 2



Left intramammary lymph node

Keywords: breast cancer, occult breast cancer, axillary lymphadenopathy, Sarcoidosis, intramammary lymph node

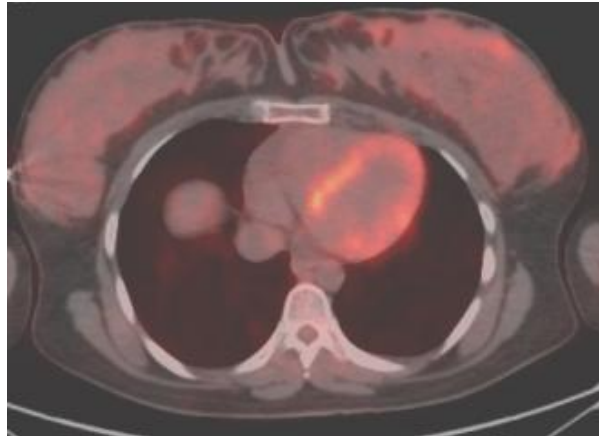
A RARE AND INTERESTING CASE REPORT: INVASIVE BREAST CARCINOMA WITH SPONTANEOUS REGRESSION AFTER LABOUR

Deniz Esin Tekcan Şanlı¹

¹Gaziantep University, Faculty of Medicine, Radiology Department

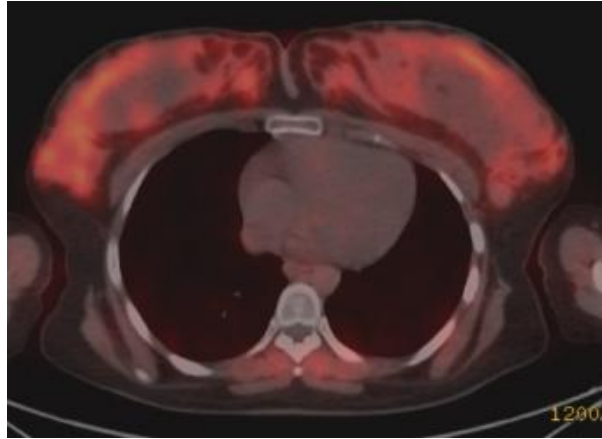
Abstract: Introduction: Approximately 70% of breast cancers are hormone receptor (Estrogen Receptor, Progesterone Receptor) positive and hormone sensitive (1). Due to increased hormonal activity during pregnancy or breastfeeding, these tumours may show faster progression and a more aggressive course (2). The interesting aspect of our case is that breast cancer was diagnosed in the 3rd trimester and the tumour could not be visualised in all imaging methods performed in the early post-partum period. Such a case has never been encountered in the literature. However, it has been reported that breast cancer may be spontaneously partially or completely regressed in 1/60.000-100.000 cases (3). In this case, the possibility of spontaneous disappearance of a highly hormone positive breast tumour due to decreased estrogen concentration after delivery comes to mind. Case: A 31-year-old woman in her 33rd gestational week presented to our clinic with a palpable hardness in the right breast for about 2 weeks. On ultrasonography examination, a heterogeneous, irregularly contoured hypoechoic solid lesion of approximately 35x20 mm in size was observed in the upper inner quadrant of the right breast at 2-3 o'clock and evaluated in BIRADS 4c category and core biopsy was performed from the mass on 24 July 2024. Histopathology result was invasive ductal carcinoma (IDC, Estrogen Receptor: 90%, Progesterone Receptor: 90%, Ki-67: 60%, Luminal A). In addition, 2 lymph nodes with slightly thick cortex were observed in the right axilla and fine needle aspiration biopsy was performed with low suspicion for metastasis and the histopathological result was benign. Post-partum neoadjuvant chemotherapy was decided for the patient due to the large tumour size. FDG-PET for staging was also postponed until after delivery. The malignant lesion in the right breast could not be visualised in the breast magnetic resonance imaging (MRI) on 13 September 2024, FDG PET-CT on 16 September 2024, control ultrasonography on 18 September 2024 and FAPI-PET CT on 20 September 2024. PET-CT examinations showed no evidence of distant metastasis in both axillae. The skin and nipple sparing mastectomy was recommended to the patient because the tumour in the breast could not be localised despite all imaging methods.

Figure 1



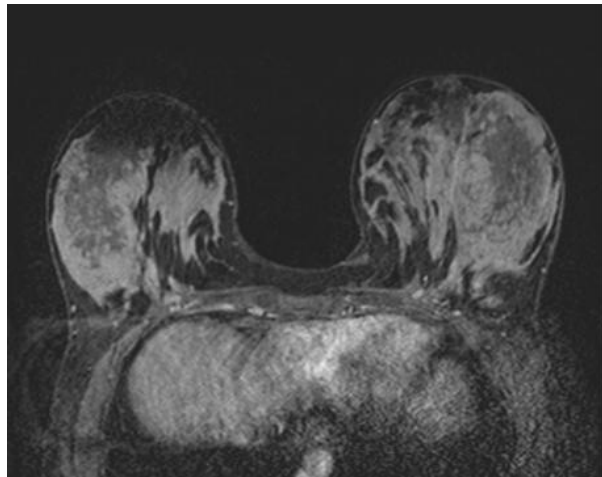
FDG PET-CT image taken in the post-partum period

Figure 2



FAP PET-CT image taken in the post-partum period

Figure 3



Breast MRI image taken in the post-partum period

Keywords: breast cancer, breast cancer during pregnancy, breast cancer during lactation, spontan regression

LEFT CIRCUMFLEX AORTA -CASE REPORT

Dragana Nikolić², Fahad Al Abdughani¹

¹*Amiri Hospital Kuwait City*

²*Al Salam Hospital Kuwait*

Abstract: A left circumflex aorta (LCA) is a rare variation of the thoracic aorta. It is distinguished by a retroesophageal descending aorta that subsequently travels down the right side of the thoracic vertebrae towards the aortic hiatus. This study presents a description of a LCA in a 69-year-old male patient. The CT study revealed the descending aorta posteriorly from the trachea and oesophagus and then laterally on the right from the thoracic vertebral bodies. The branching pattern of the aortic arch was typical, so was the course of the. Due to the normal appearance of the ascending part and the arch of the aorta, it is safe to presume that the variation originated from the persistent right dorsal aorta, with the retroesophageal part from the persistent left dorsal aorta. Detailed understanding of the variations of the thoracic aorta, and the anomalies associated with the LCA, can help to improve management of these conditions, and with that, improve patients' overall outcomes. Patients with a LCA, or another vascular ring, can either be asymptomatic or present with oesophageal and/or tracheal compression symptoms.

Keywords: Left circumflex aorta, CT, Embriology

A RETROSPECTIVE ANALYSIS OF CASES AND RADIOLOGICAL EVALUATION OF PATHOLOGICAL FINDINGS BASED ON 13 YEARS OF EXPERIENCE IN FETAL MRI AT A TERTIARY CARE CENTER.

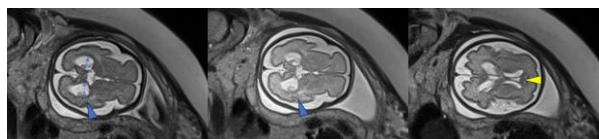
Fatih ATES¹, Mehmet Sedat DURMAZ², Mustafa KOPLAY²

¹Konya City Hospital

²Selcuk University, Faculty of Medicine, Radiology Department

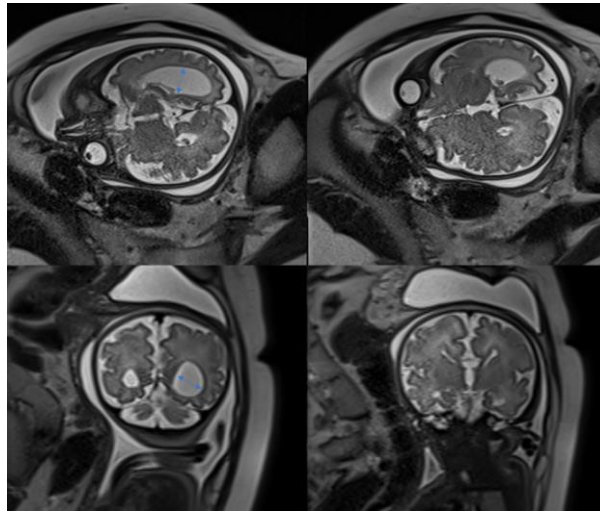
Abstract: We aimed to investigate the most common anomalies in fetuses, the associated radiological findings, and the most frequent indications for fetal MRI in pregnant patients referred to our clinic for fetal imaging. A retrospective review was conducted of all fetal MRI (fMRI) examinations performed at our center over a 13-year period. The pathological findings, preliminary diagnoses, patient age, and gestational age of the patients were recorded. We identified that 613 fetal MRI examinations were conducted at our center over the course of 13 years. In these cases, the three most common preliminary diagnoses were ventriculomegaly (n=240), unspecified preliminary diagnoses (n=48), and agenesis/dysgenesis of the corpus callosum (n=47). After fetal MRI was performed, the most frequently noted anomaly in the preliminary diagnosis was again ventriculomegaly (n=243). The second most common diagnosis was completely normal cases (n=105). The third most common diagnosis observed was agenesis or dysgenesis of the corpus callosum (n=69). The other diagnoses exhibited a wide distribution, including mega cisterna magna, hypoplastic left heart, intraventricular hemorrhage, hemivertebra anomaly, occipital meningocele, bilateral hydronephrosis, adrenal hemorrhage, cleft lip and palate, pulmonary sequestration, placental accreta spectrum, lissencephaly, cystic hygroma, microcephaly, schizencephaly, sacrococcygeal teratoma, Dandy-Walker malformation, alobar holoprosencephaly, congenital pulmonary airway malformation, and other subgroups. The patients who underwent the examinations were between 18 and 32 weeks of gestation. The age range of the patients was between 17 and 40 years. Ultrasonography (US) may be insufficient for detecting fetal anomalies in maternal obesity, oligohydramnios, neurological disorders, and those other anomalies. Although US is always performed first, in such cases, fetal MRIs should be used to evaluate the midline structures of the brain. fMRI provide detailed intrauterine imaging of the developing fetus. Fast sequences are required because of fetal movement. fMRIs are most commonly used when US findings are unclear. Using fMRI, fetal anatomy can be evaluated in detail, including the brain, upper respiratory-digestive system, thorax, pelvis, and abdomen. fMRI are usually done during and after the second trimester. we aimed to present the radiological imaging findings of fetal pathologies identified during the prenatal period that were suspected in obstetric care.

Figure 1



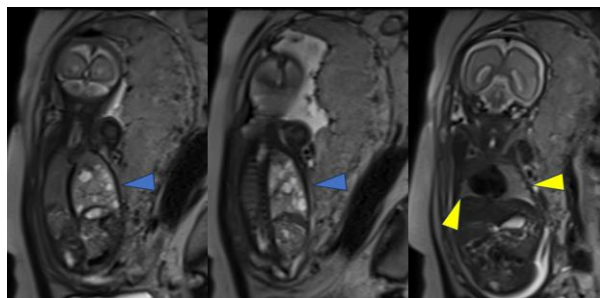
A 31-year-old woman, 28 weeks pregnant, was evaluated with fetal MRI following the detection of bilateral ventriculomegaly on ultrasound. Axial T2-weighted images revealed that both lateral ventricles were enlarged, measuring 12 mm at the atrium level (indicated by blue triangles). An accompanying cavum veli interpositi was also observed (indicated by the yellow triangle). No other anomalies were identified upon examination of the other systems aside from the ventriculomegaly.

Figure 2



A 22-year-old woman, 32 weeks pregnant, was referred due to asymmetric ventricular width observed on ultrasound. Fetal MRI revealed that the right ventricle was asymmetrically enlarged, measuring 18 mm. The corpus callosum was not visualized, and this was reported as corpus callosum agenesis.

Figure 3



A 28-year-old woman, 26 weeks pregnant, underwent fetal MRI for further evaluation due to the observation of bowel loops in the lung on ultrasound. The MRI revealed a diaphragmatic defect in the left hemithorax with herniation of the bowel loops (indicated by blue arrows). Additionally, a congenital pulmonary airway malformation consistent appearance was noted in both lungs, with more extensive involvement on the left side (indicated by yellow triangles).

Keywords: Ventriculomegaly, Fetal MRI, Corpus callosum agenesis, Prenatal diagnosis

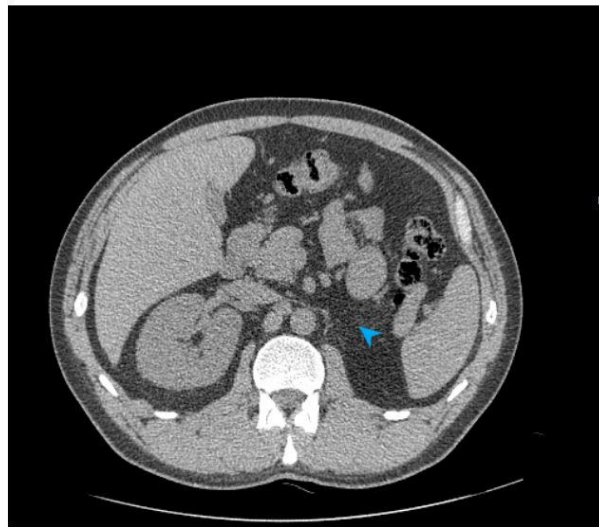
A RARE UROGENITAL ANOMALY: ZINNER SYNDROME

Dilara Budak¹, Kubilay Kağan Budak¹, Esat Kaba¹, Hande Melike Bülbül¹, Gülen Burakgazi¹

¹*Recep Tayyip Erdoğan Üniversitesi Eğitim ve Araştırma Hastanesi*

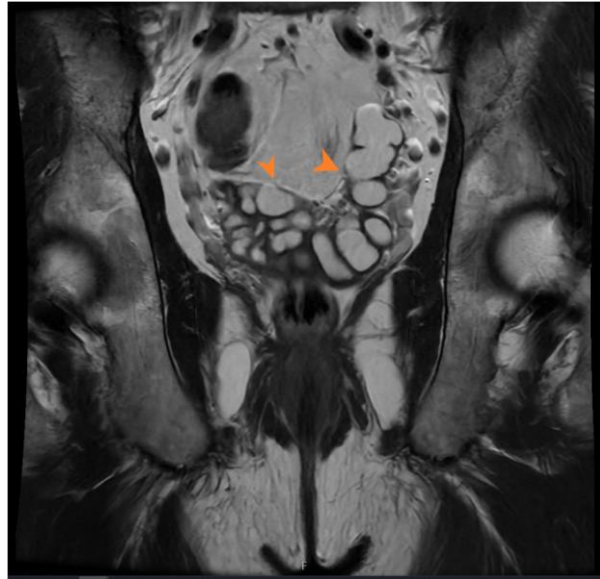
Abstract: INTRODUCTION Zinner syndrome is a rare congenital urological entity with an incidence of 0.005% of the population, defined by the triad of unilateral renal agenesis, ipsilateral cystic dilatation of the seminal vesicle and ipsilateral ejaculatory duct obstruction. This male condition is caused by the failure of ureteric buds to migrate from the mesonephric duct. Patients with Zinner syndrome are usually asymptomatic until the 2nd or 3rd decades of life. Clinically, patients generally come with dysuria, epididymitis, hematospermia, ejaculatory disturbances and infertility. Symptoms generally begin after the individuals become sexually active, in which the accumulation of seminal fluid will result in increased seminal vesicle size, and it may lead to seminal vesicle abscess, other developmental abnormalities or neoplasms. CASE A 42-year-old male patient presented with complaints of pain and swelling in the left testicle at the emergency department. Scrotal ultrasound examination revealed left sided epididymitis and vas deferens dilatation with mucosal thickening. Following antibiotic therapy, the patient continued to present with dysuria, mild hematuria and recurrent prostatitis. Abdominal ultrasound examination revealed the absence of the left kidney and focal dilatation in the distal ureter. A non-contrast-enhanced computed tomography (CT) scan was performed for further evaluation regarding urinary tract pathologies. The CT scan showed left renal agenesis and cystic tubular dilatations on the left side of the prostate. Subsequently, a pelvic magnetic resonance imaging (MRI) was conducted, which confirmed the presence of cystic areas observed in the CT as cystic dilatation of the seminal vesicles, thus confirming the diagnosis of Zinner syndrome. DISCUSSION We have presented a patient with Zinner syndrome with typical urogenital symptoms. The condition used to be rare but is now more frequently encountered due to the advent of MRI and CT. Imaging techniques play an essential role in the diagnosis of Zinner syndrome. Ultrasound and abdomino-pelvic CT scan shows the absence of ipsilateral kidney and may reveal a cystic mass or formation near the prostate. Pelvic MRI is the gold standard imaging technique as it confirms the diagnosis by identifying the cystic dilatation of the seminal vesicles in its characteristic periprostatic location. Cyst contents may vary depending on its contents, which are normally hypointense on T1 and hyperintense on T2 when they are pure liquid. In conclusion, radiologists should keep Zinner syndrome in mind in patients with recurrent urogenital symptoms and unilateral renal agenesis.

CT



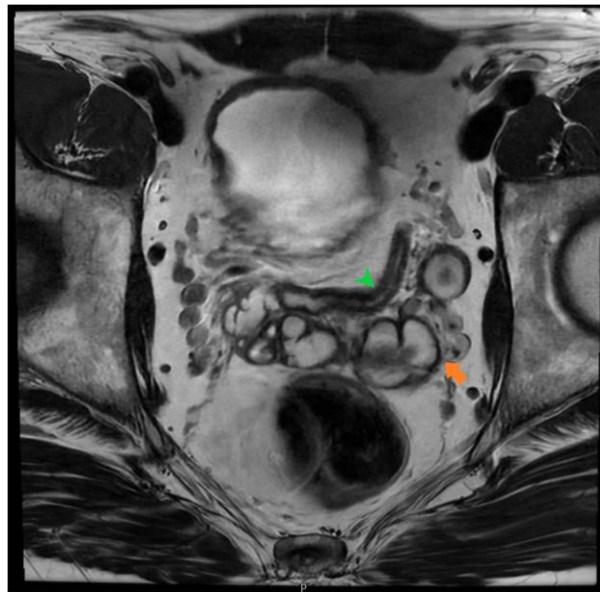
Non-enhanced CT scan showing renal agenesis

MRI



Orange arrows showing cystic dilatations of seminal vesicles on T2 image

MRI



T2 image, green arrow showing dilated ductus deferens

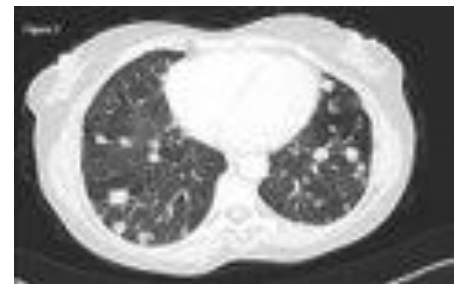
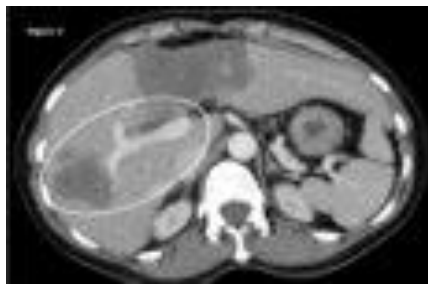
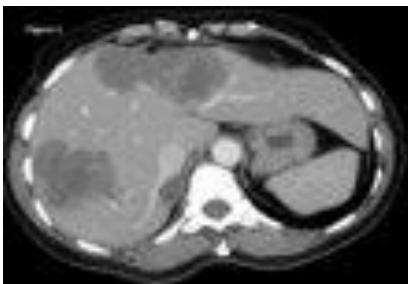
Keywords: Zinner Syndrome, Urogenital Anomaly, Renal Agenesis, Seminal Vesicles, Ejaculatory Duct Obstruction

A RARE CASE: HEPATIC EPITHELIOID HEMANGIOENDOTHELIOMA WITH LUNG METASTASIS

Aytekin Erol¹, Zülküf Akdemir¹, Saim Türkoğlu¹, Ensar Türko¹, Bulut
Tuğal¹, Muhammed Bilal Akıncı¹, Mesut Özgökçe¹

¹Van Yüzüncü Yıl University, Dursun Odabas Medical Center

Abstract: Epithelioid hemangioendothelioma (EH) is an extremely rare tumor, which originates from the vascular endothelium, and liver is the most commonly primary site. We aim to discuss computed tomography (CT) imaging of EH. A 44-year-old female patient presented to the outpatient clinic with abdominal pain and dyspnea. A decision was made to perform a contrast-enhanced abdominal CT scan. The contrast-enhanced abdominal CT revealed hypodense lesions in both lobes of the liver, extending to the capsule, with lobular contours and retraction in the capsule, exhibiting minimal vascularity (Figure 1). A lollipop sign was observed in the lesion in the right lobe (Figure 2)(Circle). Additionally, the scan showed scattered metastatic nodules of varying sizes in the lungs (Figure 3). A biopsy of the liver lesions confirmed a diagnosis of epithelioid hemangioendothelioma. Hepatic epithelioid hemangioendothelioma (HEH) is an extremely rare liver tumor and patients could have different long-term prognoses due to the disparity in tumor malignancy. Several studies have reported the radiological features of HEH, such as subcapsular lesion, coalescent lesion, capsular retraction, lollipop sign and target sign. Lollipop sign was depicted as hepatic or portal vein tapering and terminating at the edge of a well-defined peripherally lesion, which was previously reported to be a characteristic feature of HEH. Target sign which was depicted as two or multiple concentric layered “target-like” appearance was also reported to be a specific radiological feature of HEH. However, target sign could also appear on the radiological image of patients with hepatic metastatic tumor (HMT). The results of studies showed that capsular retraction and lollipop sign were more specific CT features of HEH, which could be used for distinguishment from HMT. One of thoracic involvement imaging pattern is a multinodular pattern. It is characterized by multiple discrete nodules, predominantly seen in a peribronchovascular distribution. The nodules are usually subcentimeter but might range from punctuate to 2 cm in size. However, because of the indolent nature of the disease, little or no growth is observed on serial examinations. Tumor calcifications or cavitation is rare. Although the radiological appearance of the tumor is non-specific, knowing the radiological features allows the tumor to be considered in the differential diagnosis.



XIX.

BALKAN CONGRESS
OF RADIOLOGY



OCTOBER 23-26, 2024
ALTIN YUNUS HOTEL, ÇEŞME
izmir

